Fire Dynamics Simulator (FDS) Pyrolysis Model Analysis of Heavy Goods Vehicle Fires in Road Tunnels

by

Xiaoyun Wang

Supervised by

Professor Charles Fleischmann

and

Associate Professor Michael Spearpoint

August 2017

A thesis presented as partial fulfilment of the requirements for the degree of the Doctor of Philosophy in Fire Engineering

Department of Civil and Natural Resources Engineering

University of Canterbury

Private Bag 4800

Christchurch, New Zealand

Abstract

Heavy goods vehicle (HGV) fires cause more serious fire safety problems than other vehicle fires in road tunnels due to the large fire size. The fire size is a critical parameter in road tunnel fire safety design and this parameter varies considerably under different environmental conditions. It is impractical to experimentally measure heat release rate (HRR) for HGV fires under different tunnel conditions because of the large experimental cost. There is a desire to use a cost-effective computational fluid dynamics (CFD) modelling method to study tunnel fires, such as fire dynamics simulator (FDS). The pyrolysis model in FDS can predict HRR based on fuel properties and environmental conditions. Therefore, the FDS pyrolysis model is adopted in this research to simulate a large-scale tunnel simulated HGV cargo experiment, which was carried out on behalf of the Land Transport Authority (LTA), Singapore. There are three major objectives in this research: to understand fuel properties for the application of the pyrolysis model; to understand influence of forced ventilation on the HRR of tunnel fires; and to assess the predictive capability of the pyrolysis model in FDS to simulate tunnel fires.

The material properties of the fuels (plastic and wood) adopted in the LTA experiment are investigated. A simple hand calculation method using multiple-component schemes is proposed in this research to analyse the kinetic properties for the LTA materials through a series of material-scale experiments. Favourable FDS predictions of decomposition behaviour are obtained based on the derived kinetic properties. Following the studies of the kinetic properties, a manual optimisation process is used to determine other thermal properties for the application of the FDS pyrolysis model. The results from FDS simulations for a series of cone calorimeter experiments reveal that the use of component schemes and thermal property settings are critical in accurately predicting burning behaviour in FDS.

A series of small-scale tunnel experiments are conducted which is scaled at a ratio of 1:20 on the basis of the LTA large-scale tunnel experiment. Medium density fireboard (MDF) cribs are used as fuel source to investigate the influence of forced ventilation on tunnel fires. It is found that the forced ventilation affects fire spread rate and burning efficiency which ultimately affects the peak HRR. In addition, the influence of forced ventilation on burning efficiency is affected by the crib length. A mathematical model to predict peak HRR for crib fires is proposed based on the observed influences on crib fires from these different factors.

The ultimate objective is to assess the ability of the FDS pyrolysis model to predict the HRR in the small-scale and large-scale tunnel experiments. In the simulations, the decomposition reactions are described. The ventilation influences on burning efficiency are accounted for

through heat of combustion. Unfortunately, FDS considerably under predicts the HRR and fire growth behaviour for both experiments. These results suggest that the FDS pyrolysis model is unable to predict fire burning behaviour for complex fuels with sufficient accuracy to be used in practical tunnel design.

Overall, this research reveals an effective hand calculation method to derive kinetic properties; a manual optimisation process to determine thermal properties; a mathematical model to describe forced ventilation influence on fire size and to further estimate peak HRR for tunnel crib fires. In addition, the results from the application of FDS pyrolysis model to simulate tunnel fires reveal that the pyrolysis model is unable to accurately predict fire burning behaviour for complex fuels.

UNIVERSITY OF CANTERBURY
Te Whare Wānanga o Waitaha
CHRISTCHURCH NEW ZEALAND

Deputy Vice-Chancellor's Office
Postgraduate Office

Co-Authorship Form

This form is to accompany the submission of any thesis that contains research reported in co-authored work that has been published, accepted for publication, or submitted for publication. A copy of this form should be included for each co-authored work that is included in the thesis. Completed forms should be included at the front (after the thesis abstract) of each copy of the thesis submitted for examination and library deposit.

Please indicate the chapter/section/pages of this thesis that are extracted from co-authored work and provide details of the publication or submission from the extract comes:

Chapter 3

Wang, X., Fleischmann, C., Spearpoint, M. and Li, K. (2015) A Simple Hand Calculation Method to Estimate the Pyrolysis Kinetics of Plastic and Wood Materials. 10th Asia-Oceania Symposium on Fire Science and Technology (10th AOSFST), 5/10/2015.

Please detail the nature and extent (%) of contribution by the candidate:

Xiaoyun Wang carried out the experiments and analysis under supervision of the co-authors.

Xiaoyun Wang was responsible for 80% of this published work.

Certification by Co-authors:

If there is more than one co-author then a single co-author can sign on behalf of all

The undersigned certifies that:

- The above statement correctly reflects the nature and extent of the PhD candidate's contribution to this co-authored work
- In cases where the candidate was the lead author of the co-authored work he or she wrote the text

Name: *Charles Fleischmann* Signature: Date: *02 Feb 2017*

UNIVERSITY OF CANTERBURY
Te Whare Wānanga o Waitaha
CHRISTCHURCH NEW ZEALAND

Deputy Vice-Chancellor's Office
Postgraduate Office

Co-Authorship Form

This form is to accompany the submission of any thesis that contains research reported in co-authored work that has been published, accepted for publication, or submitted for publication. A copy of this form should be included for each co-authored work that is included in the thesis. Completed forms should be included at the front (after the thesis abstract) of each copy of the thesis submitted for examination and library deposit.

Please indicate the chapter/section/pages of this thesis that are extracted from co-authored work and provide details of the publication or submission from the extract comes:

Chapter 3

Wang, X., Fleischmann, C. and Spearpoint, M. (2015) The effect of using lids in differential scanning calorimeter experiments for determining the heat of reaction of wood. Coimbra, Portugal: 2015 International Fire Safety Symposium (IFireSS), 20-22 April 2015.

Please detail the nature and extent (%) of contribution by the candidate:

Xiaoyun Wang carried out the experiments and analysis under supervision of the co-authors.

Xiaoyun Wang was responsible for 80% of this published work.

Certification by Co-authors:

If there is more than one co-author then a single co-author can sign on behalf of all

The undersigned certifies that:

- The above statement correctly reflects the nature and extent of the PhD candidate's contribution to this co-authored work
- In cases where the candidate was the lead author of the co-authored work he or she wrote the text

Name: *Charles Fleischmann* Signature: Charles M Fleischmann Date: *02 Feb 2017*

UNIVERSITY OF CANTERBURY
Te Whare Wānanga o Waitaha
CHRISTCHURCH NEW ZEALAND

Deputy Vice-Chancellor's Office
Postgraduate Office

Co-Authorship Form

This form is to accompany the submission of any thesis that contains research reported in co-authored work that has been published, accepted for publication, or submitted for publication. A copy of this form should be included for each co-authored work that is included in the thesis. Completed forms should be included at the front (after the thesis abstract) of each copy of the thesis submitted for examination and library deposit.

Please indicate the chapter/section/pages of this thesis that are extracted from co-authored work and provide details of the publication or submission from the extract comes:

Chapter 4

Wang, X., Fleischmann, CM. and Spearpoint, MJ. (2016) Parameterising study of tunnel experiment materials for application to the Fire Dynamics Simulator pyrolysis model. Journal of Fire Sciences 34(6): DOI:10.1177/0734904116667738.

Please detail the nature and extent (%) of contribution by the candidate:

Xiaoyun Wang carried out the simulations and analysis under supervision of the co-authors.

Xiaoyun Wang was responsible for 80% of this published work.

Certification by Co-authors:

If there is more than one co-author then a single co-author can sign on behalf of all

The undersigned certifys that:

- The above statement correctly reflects the nature and extent of the PhD candidate's contribution to this co-authored work
- In cases where the candidate was the lead author of the co-authored work he or she wrote the text

Name: *Charles Fleischmann* Signature: Charles M Fleischmann Date: *02 Feb 2017*

UNIVERSITY OF CANTERBURY
Te Whare Wānanga o Waitaha
CHRISTCHURCH NEW ZEALAND

Deputy Vice-Chancellor's Office
Postgraduate Office

Co-Authorship Form

This form is to accompany the submission of any thesis that contains research reported in co-authored work that has been published, accepted for publication, or submitted for publication. A copy of this form should be included for each co-authored work that is included in the thesis. Completed forms should be included at the front (after the thesis abstract) of each copy of the thesis submitted for examination and library deposit.

Please indicate the chapter/section/pages of this thesis that are extracted from co-authored work and provide details of the publication or submission from the extract comes:

Chapter 5

Wang, X., Spearpoint, M. and Fleischmann, C. (2017) Comparison of results from large-scale and small-scale tunnel experiments submitted to Fire Safety Journal.

Please detail the nature and extent (%) of contribution by the candidate:

Xiaoyun Wang carried out the experiments and analysis under supervision of the co-authors.

Xiaoyun Wang was responsible for 80% of this work.

Certification by Co-authors:

If there is more than one co-author then a single co-author can sign on behalf of all

The undersigned certifies that:

- The above statement correctly reflects the nature and extent of the PhD candidate's contribution to this co-authored work
- In cases where the candidate was the lead author of the co-authored work he or she wrote the text

Name: *Charles Fleischmann* Signature: Charles M Fleischmann Date: *02 Feb 2017*

UNIVERSITY OF CANTERBURY
Te Whare Wānanga o Waitaha
CHRISTCHURCH NEW ZEALAND

Deputy Vice-Chancellor's Office
Postgraduate Office

Co-Authorship Form

This form is to accompany the submission of any thesis that contains research reported in co-authored work that has been published, accepted for publication, or submitted for publication. A copy of this form should be included for each co-authored work that is included in the thesis. Completed forms should be included at the front (after the thesis abstract) of each copy of the thesis submitted for examination and library deposit.

Please indicate the chapter/section/pages of this thesis that are extracted from co-authored work and provide details of the publication or submission from the extract comes:

Chapter 6

Wang, X., Spearpoint, M. and Fleischmann, C. (2017) Investigation of the effect of tunnel ventilation on crib fires through small-scale experiments Fire Safety Journal DOI: 10.1016/j.firesaf.2017.01.002.

Please detail the nature and extent (%) of contribution by the candidate:

Xiaoyun Wang carried out the experiments and analysis under supervision of the co-authors.

Xiaoyun Wang was responsible for 80% of this published work.

Certification by Co-authors:

If there is more than one co-author then a single co-author can sign on behalf of all

The undersigned certifies that:

- The above statement correctly reflects the nature and extent of the PhD candidate's contribution to this co-authored work
- In cases where the candidate was the lead author of the co-authored work he or she wrote the text

Name: *Charles Fleischmann* Signature:  Date: *02 Feb 2017*

UNIVERSITY OF CANTERBURY
Te Whare Wānanga o Waitaha
CHRISTCHURCH NEW ZEALAND

Deputy Vice-Chancellor's Office
Postgraduate Office

Co-Authorship Form

This form is to accompany the submission of any thesis that contains research reported in co-authored work that has been published, accepted for publication, or submitted for publication. A copy of this form should be included for each co-authored work that is included in the thesis. Completed forms should be included at the front (after the thesis abstract) of each copy of the thesis submitted for examination and library deposit.

Please indicate the chapter/section/pages of this thesis that are extracted from co-authored work and provide details of the publication or submission from the extract comes:

Chapter 7

Wang, X., Fleischmann, CM. and Spearpoint, MJ. Applying the FDS pyrolysis model to predict heat release rate in small-scale tunnel experiments accepted by International Symposium on Tunnel Safety and Security (ISTSS), 2018.

Please detail the nature and extent (%) of contribution by the candidate:

Xiaoyun Wang carried out the simulations and analysis under supervision of the co-authors.

Xiaoyun Wang was responsible for 80% of this work.

Certification by Co-authors:

If there is more than one co-author then a single co-author can sign on behalf of all

The undersigned certifys that:

- The above statement correctly reflects the nature and extent of the PhD candidate's contribution to this co-authored work
- In cases where the candidate was the lead author of the co-authored work he or she wrote the text

Name: *Charles Fleischmann* Signature: Charles M Fleischmann Date: *02 Feb 2017*

UNIVERSITY OF CANTERBURY
Te Whare Wānanga o Waitaha
CHRISTCHURCH NEW ZEALAND

Deputy Vice-Chancellor's Office
Postgraduate Office

Co-Authorship Form

This form is to accompany the submission of any thesis that contains research reported in co-authored work that has been published, accepted for publication, or submitted for publication. A copy of this form should be included for each co-authored work that is included in the thesis. Completed forms should be included at the front (after the thesis abstract) of each copy of the thesis submitted for examination and library deposit.

Please indicate the chapter/section/pages of this thesis that are extracted from co-authored work and provide details of the publication or submission from the extract comes:

Chapter 8

Wang, X., Fleischmann, C. and Spearpoint, M. (2016) Assessing the influence of fuel geometrical shape on fire dynamics simulator (FDS) predictions for a large-scale heavy goods vehicle tunnel fire experiment. Case Studies in Fire Safety 5: 34-41. DOI: 10.1016/j.csfs.2016.04.001.

Please detail the nature and extent (%) of contribution by the candidate:

Xiaoyun Wang carried out the simulations and analysis under supervision of the co-authors.

Xiaoyun Wang was responsible for 80% of this published work.

Certification by Co-authors:

If there is more than one co-author then a single co-author can sign on behalf of all

The undersigned certifys that:

- The above statement correctly reflects the nature and extent of the PhD candidate's contribution to this co-authored work
- In cases where the candidate was the lead author of the co-authored work he or she wrote the text

Name: *Charles Fleischmann* Signature:  Date: *02 Feb 2017*

Acknowledgement

I would like to acknowledge the valuable assistance and support of the following people I have received throughout this research project:

My supervisors, Professor Charles Fleischmann and Associate Professor Michael Spearpoint for their patience, guidance and invaluable advice throughout the development of this research.

Dr. Mun Kit Cheong for providing the experimental data and the cone calorimeter experimental data for the LTA large-scale tunnel experiments. Dr. Kaiyun Li and Dr. Dennis Pau for their valuable discussion and suggestions on kinetic properties analysis in my research. Dr. Anthony Abu for his ongoing encouragement and support over the time.

Grant Dunlop and Bob Wilsea-Smith for their help with the design and construction of the experimental apparatus in this research. Brandon Hutchison for providing me the technical support to access computers for conducting simulations in the computer lab. Mike Van der Colk, from Chemistry for allowing me to spend extensive time using the SDT machine in their laboratory.

The University of Canterbury, New Zealand, for awarding the UC Doctoral Scholarship.

The New Zealand Fire Service Commission for their continued support of the Fire Engineering programme at the University of Canterbury.

My officemates and colleagues from university for all the coffee talks and chats in my PhD study time.

My family for all the support they had given me during my overseas studies over the years.

I would also like to thank for the support and encouragement from my colleagues (Melbourne fire team, Arup) over my thesis defence period, thank David Graham for allowing me to take extra time from work to prepare for the defence and thank Jarrod Alston and Peter Johnson for the valuable discussion and help.

Table of Content

List of Figures

List of Tables

Nomenclature

A	pre-exponential factor (s^{-1})
A_{cross}	Tunnel cross section area (m^2)
A_{sur}	surface area of fire (m^2)
A_v	ventilation area (cm^2)
A_s	exposed surface area (cm^2)
b	wood stick thickness (mm)
c	component mass fraction
C	fuel property constant ($g\ s^{-1}\ cm^{1.5}$)
C	heat capacity ($J\ K^{-1}$)
c_p	specific heat ($J\ g^{-1}\ K^{-1}$)
D^*	characteristic fire diameter
E	activation energy ($J\ mol^{-1}$)
F_{rc}	critical Froude number
Fr	Froude number
g	acceleration of gravity ($m\ s^{-2}$)
$grade$	tunnel gradient (%)
h	heat transfer coefficient ($W\ m^{-2}\ K^{-1}$)
H	tunnel height (m)
ΔH_c	heat of combustion ($MJ\ kg^{-1}$)
ΔH_e	effective heat of combustion($MJ\ kg^{-1}$)
Δh_r	heat of reaction ($kJ\ kg^{-1}$)
dh/dt	kinetic heat flow (mW)
k	thermal conductivity ($W\ m^{-1}\ K^{-1}$)
k	conversion factor of fire size
K_1	constant for critical Froude number
K_g	grade factor
k_0^{30}	thermal conductivity along the panel thickness at 30 ˚C
Δk	the correction term for k_0^{30} due to moisture
l	length (m)
L	thickness (m)
m	mass (g)
$\dot{m}''$	mass flux ($kg\ m^{-2}\ s^{-1}$)
MC	moisture content

n	reaction order
N	number of components
P	porosity factor (mm)
$\dot{q}''$	heat flux (kW m^{-2})
$\dot{q}'''$	heat flow rate per unit volume (kW m^{-3})
Q	energy (kJ or MJ)
$\dot{Q}$	heat release rate (kW)
dq_b/dt	heat flow for an empty crucible(mW)
$\dot{Q}_{nat}$	heat release rate for a tunnel fire with natural ventilation (kw)
dq_s/dt	total heat flow (mW)
$\dot{Q}_{vent}$	heat release rate for a tunnel fire with forced ventilation (kW)
r	decomposition reaction rate (% K^{-1})
R	universal gas constant, 8.314 (J K^{-1} mol^{-1})
S_p	hydraulic diameter of the ventilation area (mm)
t	time (s)
T	temperature (K or ˚C)
T_f	average temperature near fire site (K)
T_0	temperature at ambient condition (K)
u_c	critical velocity for tunnel back layering (m s^{-1})
v	ventilation velocity (m s^{-1})
v	yield of residue in solid phase reaction
Y	mass conversion fraction

Greek symbol

α	conversion fraction
β	heating rate (K min^{-1})
γ	enhancement factor
ε	emissivity
σ	Stefan-Boltzmann constant, 5.6×10^{-8} (W m^2 K^{-4})
ρ	density (kg m^{-3})
ρ_0	ambient density (kg m^{-3})
φ	HRR enhance coefficient

Subscripts

be	burning efficiency
c	convective
CAL	calculation results

ce	cellulose
ch	char
e	end of reactions
$engulfed$	engulfed fire
FDS	FDS results
fs	fire spread
fv	forced ventilation
h	hemicellulose
i	i^{th} component
j	j^{th} second
ig	ignition
l	lignin
L	large-scale
nv	natural ventilation
$open$	free burning
p	peak value
pl	plastic
w	wood
r	radiative
rc	reference crucible
re	residue
rea	reactants
s	solid
S	small-scale
sc	sample crucible
sp	solid products
ss	sample
vs	virgin sample
0	Initial state

Acronyms

DSC	differential scanning calorimeter
DTG	derivative thermogravimetric curve
GA	genetic algorithm
HC	hand calculation
HGV	heavy goods vehicle
HOC	heat of combustion
HRR	heat release rate
HRRPUA	heat release rate per unit area
HRRPUV	heat release rate per unit volume
MDF	medium density fireboard
MLR	mass loss rate
TG	thermogravimetric
TGA	thermogravimetric analysis
SDT	simultaneous DSC and TGA

Chapter 1 Introduction

1.1 Background

Vehicle incidents are the most common reasons for road tunnel fires. The fire types and sizes depend on types of vehicles involved, as well as the goods carried by them. When heavy goods vehicles (HGVs) are involved in a fire, more extensive damage and serious consequences are far greater than other types of vehicle fires in tunnels. Carvel and Marlair listed the tunnel fire incidents for the past decades in [1]. Some incidents are introduced here to demonstrate the significant cost of life and property by HGV road tunnel fires: In 1949, a fire involved ten HGVs and sixty-six people were injured in the Holland tunnel in New York, USA [2]; The Mont Blanc Tunnel fire in 1999 [3], where thirty-four vehicles were destroyed (twenty-three HGVs) and the tunnel had severe damage; the same year another fire happened in Tauern Tunnel, Austria [4], in which sixteen HGVs were caught on fire and twelve people died. The Frejus Tunnel fire in 2005, four HGVs destroyed and two fatalities, and in October 2007, Newhall pass tunnel fire in the USA [5] was caused by the collision of two HGVs and a total of thirty HGVs were involved.

In order to understand HGV fires in tunnels and to further minimise the severe consequences caused by the fires, the heat release rates (HRRs) of tunnel HGV fires need to be investigated. HRR is an important parameter to evaluate the development, severity and consequences of a tunnel fire [6]. This parameter is the basis of tunnel fire safety design, such as the ventilation, evacuation and structural design for a tunnel. In the past decades, many large-scale road tunnel HGV and simulated HGV cargo fire tests have been carried out to measure the HRR for HGV tunnel fires. In 1992, two tests to investigate HGV fire size were conducted in the EUREKA test programme [7]. An authentic HGV and an HGV-trailer were used for the testing under different ventilation conditions, where peak HRR of 128 MW for the real HGV and 23 MW for the trailer were obtained. In 2000, 23 MW peak HRR was obtained in the fire test of the Mont Blanc tunnel by using an HGV consisting of 400 kg of margarine [8]. In the Second Benelux tunnel fire test in 2001 [9], three different peak HRRs of 13, 19, and 16 MW were obtained using HGV mock-ups at three different ventilation conditions. Following that, four large-scale simulated HGV cargo tests were conducted in the Runehamar tunnel in 2003 [10], where different loadings were used and different ventilation conditions were applied. The recorded peak HRRs from these tests varied from 66 to 202 MW depending on different conditions and different fire loads used. In addition to the recorded experimental HRR data, the design fire size can also be obtained from the tabulated values in different road tunnel fire

safety standards. Cheong [11] summarised the fire sizes from NFPA 502 (2004), BD78/99, CETC and PIARC (1999), where 20-30 MW was suggested for an HGV fire, and a value up to 100 MW was recommended from BD78/99 for a HGV fire. In the latest version in NFPA 502 (2014) [12], the fire size for HGV fire has been changed to 150 MW.

Although there are available tunnel fire testing data and there is guidance for the recommended fire sizes for HGV tunnel fires, one question is whether these HRR data from a particular tunnel fire test or the standardised fire sizes from regulations can effectively represent the real tunnel fires under different conditions.

As introduced by Ingason [13], tunnel fires are different from open fires and compartment fires. Tunnel fires are affected by the geometry of tunnels (such as cross-sectional area, height, length etc.) The development of tunnel fires is also effected by the ventilation rate. In the EUREKA 499 tunnel tests, the significant ventilation influence on fire sizes was observed after the fan was turned off from 5-6 m/s then restarted after 3 min period to 2-3 m/s. Carvel and Beard [14] used a probabilistic method to quantify the ventilation influence on fire size based on a few different tunnel fire tests under different ventilation conditions. For example, they found that HRR could increase up to a factor of 2 at 3 m/s ventilation compared to the scenario under natural ventilation for a two-lane HGV tunnel fire. Ingason [15] obtained a factor of ~1.55 based upon a series of small-scale tunnel experiments results, which are lower than the values calculated by Carvel and Beard. Even though there are some inconsistent magnitudes of the influence on fire size in these studies, the pronounced impacts of ventilation on the fire size are recognised. Due to these significant influences on tunnel fire sizes, the HRR data from a tunnel test or a fixed fire size value suggested in regulations may have limitations to cover all different tunnel fire scenarios.

Fire Dynamics Simulator (FDS) [16] is a widely used computational fluid dynamics (CFD) modelling software in fire engineering. There are different approaches to model a fire in this software. One is to use a single ‘gas burner’ method to specify it with a given HRR curve or to specify multiple ‘gas burners’ with the ignition temperature and burning rate for the fuel materials. Most tunnel modelling studies carried out so far were based on this ‘gas burner’ approach. Li and Ingason [17] used a single gas burner to represent the HGV fire in the Runehamar tunnel and investigated the temperature predictions in FDS. Cheong et al [18] adopted the multiple gas burner method to predict the HRR for the Runehamar tunnel fire test 1 based on the ignition temperature, fuel burning surface area and cone calorimeter burning rate of the fuel, where the growth rate and peak HRR were effectively predicted in the simulations. However, these applications are controlled by the user defined ignition

temperature and burning rate in FDS, the use of the gas burner method has limitations to actually reflect the reactions in a fire and the spread of a fire. Another method in FDS is to simulate a fire based on the pyrolysis model in FDS. By using this method, there is no need to define the HRR values for the fire as the HRRs can be predicted instead. The ignition and spread of the fire can also be simulated based on this method. The material properties of the fuel are required (including the kinetic properties for the decomposition reactions, heat of combustion, heat of reaction, thermal properties). These properties are not always available and experimental analyses for these properties are often required. However, based on this method, FDS can predict HRR for fires under different circumstances when the properties of the fuel and environmental conditions are specified.

1.2 Motivation and Objectives for the Research Project

As introduced above, the HRR values of HGV tunnel fires vary considerably due to different environmental conditions and it is impractical to measure the fire size for the different scenarios through large-scale experiments. Since the pyrolysis model in FDS is able to predict HRR, based on material properties, one cost-effective solution to investigate HGV tunnel fires is to apply the pyrolysis model in FDS to model the fires under different conditions and to predict the corresponding HRRs. However, the actual application of the pyrolysis model to predict the HRR for tunnel fires is very limited. Most current applications of the model to predict HRRs are for material or bench-scale experiments [19, 20], where heat transfer can be assumed to be only in dimension, such as cone calorimeter experiments. In order to evaluate whether the pyrolysis model in FDS is able to effectively predict fire phenomenon for actual tunnel fires, it is important to perform some studies to assess the prediction capabilities.

In 2012, a series of large-scale (simulated HGV cargo) tunnel fire experiments were conducted in Spain on behalf of the Land Transport Authority (LTA), Singapore (Note: the HGV term for the LTA experiments used in this work refers to simulated HGV cargo). The aim of this programme was to investigate HGV tunnel fire behaviour in the presence of water suppression and longitudinal ventilation rate. A total of seven experiments, six with a water suppression system and one without, were conducted in this programme. Gas temperature, thermal radiation, velocity profile and gas concentrations of O_2, CO_2, CO and HRR were monitored in all experiments. With the permission from the LTA, the wood and plastic samples used in the large-scale experiments were sent to the University of Canterbury for material property studies.

Since the available large-scale HGV tunnel experimental data from the LTA and the available samples for material property analysis, it is proposed to apply the pyrolysis model in FDS to

simulate the LTA HGV tunnel fire experiment and to further study the tunnel ventilation influence on HGV fires for this research.

The objectives of this research are to understand fuel material properties for the application of the pyrolysis model in FDS version 6 (FDS6); to understand the influence on HRR of tunnel fires from varied ventilation conditions; to provide validations for the application of the pyrolysis model to simulate tunnel fires. Four tasks involving both experimental work and modelling work are designed in this research in order to achieve these objectives:

Task 1 is to conduct a parameterisation study for the materials used in the LTA large-scale tunnel experiments to obtain the corresponding material properties for the application of the pyrolysis model in FDS. In this task, thermogravimetric analysis (TGA) and differential scanning calorimetry (DSC) experiments are adopted to study the kinetic properties of the materials for the decomposition reactions.

Task 2 is to understand the ventilation influence on tunnel fire behaviour based on a series of small-scale tunnel fire experiments. The small-scale tunnel experiments in this task are based on the data from the large-scale tunnel experiments, in order to understand the influence of the different fuel sources and varied ventilation velocities on the HRR in the tunnel.

Task 3 is to apply the pyrolysis model to simulate the series of small-scale tunnel experiments under different ventilation conditions and to evaluate the limitations in applying the FDS pyrolysis model to predict HRR. In this task, the material properties of the fuel source are studied and different factors affecting the modelling results are investigated with the purpose of understanding the predictive ability of the pyrolysis model.

Task 4 is to simulate the LTA large-scale tunnel experiment. The aim of this task is to apply the pyrolysis model to predict HRR for a large-scale tunnel fire. The material properties of the fuel in the simulations are based on the results from Task 1. Due to the complex fuel geometry in the large-scale tunnel, this task is also to demonstrate a practical method to represent the complex fuel geometry in using the pyrolysis model. The predicted HRR and fire spread behaviour are investigated.

1.3 Thesis Structure

This thesis consists of ten chapters including two conference papers and three published journal papers and two submitted papers.

List of published and submitted papers including in this thesis:

- Wang, X., Fleischmann, C., Spearpoint, M. and Li, K. (2015) A Simple Hand Calculation Method to Estimate the Pyrolysis Kinetics of Plastic and Wood Materials. 10th Asia-Oceania Symposium on Fire Science and Technology (10th AOSFST), 5/10/2015.

- Wang, X., Fleischmann, C. and Spearpoint, M. (2015) The effect of using lids in differential scanning calorimeter experiments for determining the heat of reaction of wood. Coimbra, Portugal: 2015 International Fire Safety Symposium (IFireSS), 20-22 April 2015.

- Wang, X., Fleischmann, C. and Spearpoint, M. (2016) Assessing the influence of fuel geometrical shape on fire dynamics simulator (FDS) predictions for a large-scale heavy goods vehicle tunnel fire experiment. Case Studies in Fire Safety 5: 34-41. DOI: 10.1016/j.csfs.2016.04.001.

- Wang, X., Fleischmann, CM. and Spearpoint, MJ. (2016) Parameterising study of tunnel experiment materials for application to the Fire Dynamics Simulator pyrolysis model. Journal of Fire Sciences 34(6): DOI:10.1177/0734904116667738.

- Wang, X., Spearpoint, M. and Fleischmann, C. (2017) Investigation of the effect of tunnel ventilation on crib fires through small-scale experiments Fire Safety Journal DOI: 10.1016/j.firesaf.2017.01.002.

- Wang, X., Spearpoint, M. and Fleischmann, C. (2017) Comparison of results from large-scale and small-scale tunnel experiments submitted to Fire Safety Journal.

- Wang, X., Fleischmann, CM. and Spearpoint, MJ. Applying the FDS pyrolysis model to predict heat release rate in small-scale tunnel experiments accepted by International Symposium on Tunnel Safety and Security (ISTSS), 2018.

In addition to the above papers included in this thesis, the paper listed below is relevant to the research and included in appendix A:

- Wang, X., Fleischmann, C. and Spearpoint, M. (2015) The application of different component schemes to predict wood pyrolysis and fire behaviour. 2015 International Fire Safety Symposium (IFireSS), 20/4/2015.

Chapters that are reproduced from these papers also include some additional information that was not presented in the original papers, which is to provide readers with a more comprehensive knowledge of the research work.

The second chapter is the literature review. There are three major parts in this review which include: available HGV tunnel fire tests, tunnel ventilation studies and FDS simulation studies in tunnel fires.

Chapter 3 and 4 are the fundamental material property studies for the fuel used in the LTA experiments. Chapter 3 introduces a methodology to derive the decomposition kinetic properties for different fuel materials. In addition, the determination of heat of reaction is discussed in this chapter. Chapter 4 presents an overall parametrising study for the material properties and the predictions in HRR for the simulations of cone calorimeter experiments.

Chapter 5 and 6 present the work on the small-scale tunnel experiments. In chapter 5, the experimental results of using different fuel sources are demonstrated. The comparisons between the results obtained from the small-scale experiments and the results from the large-scale experiment are discussed. Chapter 6 addresses the ventilation influences on tunnel fires based on the results obtained from the small-scale experiments. A mathematical model is derived to explain the effect of the forced ventilation velocity on the spread of fire and the burning efficiency.

Chapter 7 introduces the simulation results of the small-scale tunnel experiments. The FDS pyrolysis model and multiple gas burner methods are adopted to simulate the experiments. Some limitations in the predictions are presented in this chapter.

Chapter 8 and 9 are the simulations for the LTA large-scale tunnel experiment based on different methodologies. Chapter 8 demonstrates the influence from HGV geometrical shape on the simulation results, where the single gas burner method is adopted to model the HGV fire. Chapter 9 discusses the application of the pyrolysis model to simulate the large-scale simulated HGV cargo tunnel fire.

The conclusions for this research project are provided and the recommendations for future research are introduced in chapter 10.

Chapter 2 Literature Review

In this literature review chapter, there are three major sections: current HGV tunnel fire tests, studies of ventilation influence on tunnel fires, applications of the pyrolysis model, and FDS tunnel fire simulations. In addition, the LTA tunnel experiments which are used in this research work are also presented in this chapter. However, the literature reviews relating to some specific topics in this research are separately discussed in individual chapters.

2.1 Heat Release Rates in HGV Road Tunnel Fires

HRR is known as a key parameter in tunnel fire safety design. The determination of suitable HRR values is crucial to tunnel design works. In this section, the HRR measured from different HGV fire test programmes are introduced and the design fire sizes recommended from varied guidance and some empirical design fire curves are summarised.

2.1.1 HRRs in Large-scale Tunnel HGV Fire Tests

In order to quantify the design fire HRR for tunnels, fire tests are used to measure the HRRs for different types of tunnels. There are different measuring techniques to determine HRRs in tunnel tests. The most commonly used method is oxygen-consumption calorimetry. Four HGV tunnel fire tests are introduced to demonstrate the measured HRR values in different tests. The influence on HRRs from environment conditions and the fuel source itself are discussed. A summary of the four testing programmes can also be found in Table 2.1.

The first tunnel fire test to study HGV fires was the EUREKA EU499 test programme (1990 to 1992) [7]. The test programme included 21 large-scale tests and the aim was to investigate the fire behaviour for different road and rail vehicles. In the tests, the oxygen consumption calorimetry was for the first time adopted in large-scale tunnel tests [7]. Two tests to investigate HGV fire size were performed in this programme. One test used an HGV loaded with 1994 kg mixed furniture (75% cellulose material and 25% plastic) where the total heat content was 87.4 GJ. In this test, initial ventilation velocity was 5-6 m/s for 13.5 min then the fan was turned off. The estimated HRR at the time was 120 MW. After three minutes the fan was turned on at 2-3 m/s velocity and the HRR reach to a peak value of 128 MW. Another test of using a simulated HGV cargo was conducted under a ventilation of 0.5 m/s, which represented a natural ventilation scenario. Wood cribs combined with rubber tyres and plastic materials were used as fuel, where the ratio between the cellulosic and plastic materials was 78% to 22% and the estimated energy content was 63.7 GJ. A peak HRR of 16 MW was obtained at 13 min after ignition.

The Mont Blanc tunnel fire tests were conducted following the disastrous fire in 1999 [8] with the aim of investigating the consequences from the fire. One test was conducted using a real HGV tuck and a trailer equipped with 400 kg margarine. The total energy was about 76 GJ. 1.5 m/s ventilation velocity was used in the test. HRR reached 23 MW around 40 min after ignition as fire spread to the trailer with the goods after 40 min.

The second Benelux tunnel test 2002 [9] was another tunnel testing programme involving three tests . In the three tests, wood pallets and four tyres were mounted in the truck. The total energy for the fire load was about 10 GJ. Different ventilation conditions of natural ventilation, a velocity of 5 m/s and 5.3 m/s were used in the tests to observe the effects of longitudinal ventilation on the fire growth rate. The corresponding recorded peaks HRR were 13.2 MW, 16.2 MW and 19.5 MW, respectively. Based on the results from the tests, the peak HRR obtained in the scenarios with forced ventilation were 1.2 to 1.5 times higher than the scenario with natural ventilation.

The Runehamar 2003 tunnel tests [10] were carried out with HGV-trailer cargos in the Runehamar tunnel in Norway. Four HGV-trailer mock-up tests were conducted. In Test 1, the fire load consisted of wooden and plastic pallets and a target consisting of a pile of 21 wood pallets located 15 m downstream away from the trailer. The target was used to evaluate the risk for fire spread. The total energy content was 242 GJ in Test 1 and the peak HRR obtained was 202 MW. In Test 2, the fire load consisted of wood pallets and mattresses and a target was at 15 m. The total energy content was 141 GJ. The peak HRR recorded in this test was 141 MW. In Test 3, the fire load included furniture and fixtures, and 10 tyres to represent a real HGV trailer and a target was also used. The estimated total energy in this test was 131 GJ. 119 MW peak HRR was recorded in this test. In the final test, corrugated paper cartons, polystyrene cups and 40 wood pallets were used. There was no target in this test. The total energy of the fuel in the test was 62 GJ, and 67 MW peak HRR was recorded. In all the tests, longitudinal ventilation velocity of 2.4 to 3 m/s was provided by two jet fans positioned near the tunnel portal.

Table 2-1: Testing programme summary.

Testing programme	Fuel description	Ventilation Velocity	Peak HRR
EUREKA 499 (1992) [7]	HGV-trailer (mock-up) (64 GJ)	0.7 m/s	23 MW
	HGV-truck and trailer (87 GJ)	5-6 m/s 2-3 m/s	128 MW
Mont Blanc tunnel (2000) [8]	HGV(truck and trailer) (35 GJ)	1.5 m/s	23 MW
Second Benelux tunnel (2001) [9]	Standardized wood pallets (10 GJ and 20 GJ)	0.5 m/s 4-5 m/s 5 m/s	13 MW 19 MW 16 MW
Runehamar tunnel (2003) [10]	Wood pallets and PE pallets (242 GJ)	2.4-3 m/s	202 MW
	Wood pallets and mattresses (141 GJ)	2.4-3 m/s	157 MW
	Furniture and fixtures with ten truck rubber tyres (131 GJ)	2.4-3 m/s	119 MW
	Paper cartons and polystyrene cups (62 GJ)	2.4-3	67 MW

2.1.2 Design Fires

In road tunnel fire safety design, the design fires are usually represented as a steady-state value or a time dependent fire curve.

The constant values can be found from different guidelines or standards for road tunnels. These values usually are determined from tunnel fire testing data and the agreement from relevant technical committees [21]. Table 2-2 gives the recommended fire size for HGV tunnel fires from different regulations or guidelines for different countries [11, 21].

Table 2-2: Design fires for HGV fires in road tunnel in different regulations or countries.

Regulations	PIARC (1999)	BD 78/99	France	Germany	NFPA 520 (2004)	NFPA 520 (2014)
HGV (MW)	20-30	30-100	20-30	20-30	20-30	150

Instead of using constant maximum design fire values in tunnels, time dependent design fire curves provide more information to describe fires, which include the long periods of the fire growth, constant maximum HRR values and fire decay phases. According to the study of [21], there are three different mathematical expressions for the design fire curves: linear curve (linear growth and decay with constant maximum period), quadratic curve (quadratic growth and exponential decay with constant maximum period), and exponential curve (exponential growth and decay). These mathematical expressions can effectively give a time-dependent description of fire development; however, the determinations of the maximum HRR and time to maximum HRR in these correlations are still strongly dependent on the information from tunnel testing.

Overall, the use of design fires is a simple approach for engineering practice. However, these values have limits when representing different fire scenarios. For instance, for the scenario with forced ventilation, the design fire size may be undersized; for the scenario with fire suppression systems, these values may be oversized. It is also important to bear in mind that constant design fire values from different design guidelines or the mathematical expressions based design fire curves still largely rely on available tunnel fire testing data. The design fires for the different fire scenarios with ventilation systems or with fire suppression systems also need further experimental investigation.

2.2 Tunnel Ventilation

Tunnel fires are affected by multiple factors such as, the ignition source, fuel involved, vehicle types, tunnel geometry, and ventilation conditions. In this section, the influence of tunnel ventilation is particularly discussed.

2.2.1 Tunnel Ventilation Design

There are three major tunnel ventilation systems: longitudinal, semi-transverse and fully transverse [22, 23].

For longitudinal ventilation, the airflow blows in a longitudinal direction along with the incoming fresh air through the tunnel to move the pollutants away. Three means are usually adopted to achieve this ventilation system by using jet fans mounted at the tunnel ceiling or by injecting air through a nozzle at one end of the tunnel or by employing a push-pull concept to create a longitudinal airflow in the tunnel. A semi-transverse is a system which either has a uniform distribution or collection of air throughout the full length of a tunnel. A fully transverse ventilation system provides not only a uniform supply air but also a uniform collection of air with a full-length supply duct and a full length supply exhaust duct in the tunnel. The different tunnel ventilation systems are illustrated in Figure 2-1.

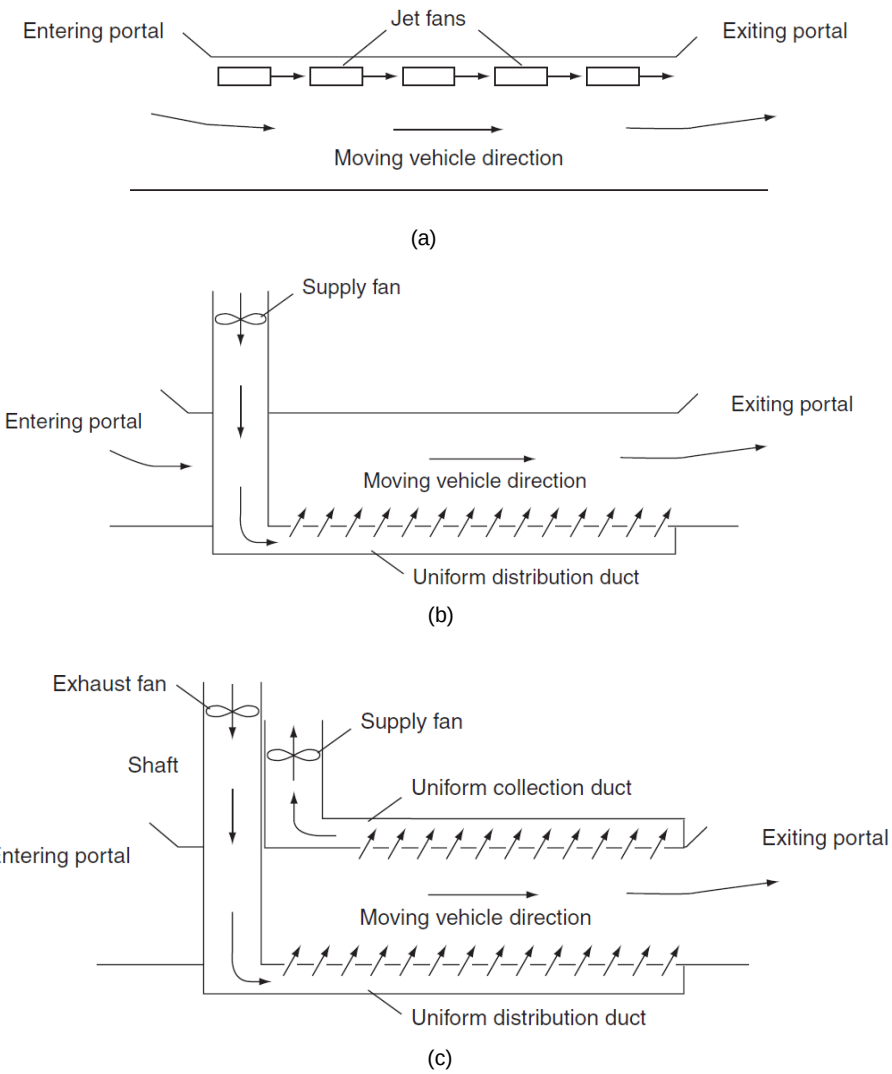

Figure 2-1: Tunnel ventilation systems: (a) jet fan longitudinal ventilation system; (b) semi-transverse ventilation system; (c) fully-transverse ventilation system (Reproduced from [23]).

Among the three types of ventilation systems, the longitudinal ventilation system is relatively inexpensive and easy to install compared with the other two systems as it does not need extra

space for ducts [22]. However, many countries have restricted the application of the longitudinal system. According to PIARC (1999) [24], Germany only allows the longitudinal system for bidirectional tunnels up to 2 km and 4 km for one-way traffic tunnels. France limits the length to 1 km for two-way tunnels and 4 km for one-way tunnels in non-urban area. The USA only permits tunnels less than 900 m to install longitudinal ventilation. With the development of cleaner vehicles, well-designed longitudinal ventilation is also suitable for long tunnels to maintain acceptable air quality [25]. Australia has widely applied this system to most road tunnels in the past two decades [25].

2.2.2 The Smoke Control in a Longitudinal Ventilation System

When a forced ventilation system is used to control smoke in a fire event, it requires that the system must be designed to achieve a sufficient capacity to effectively control the smoke. The Memorial Tunnel Fire Ventilation Test Programme (MTFVTP) 1995 [23, 26] has given an overall review on the use of varied ventilation systems in controlling smoke movement. The results from the tests showed that the use of jet fans to create a longitudinal ventilation could be capable of controlling the movement of smoke and heated gases from a fire up to 100 MW, while a fully transverse ventilation system would not be able to control smoke and gases from a large fire. In this research, the use of longitudinal ventilation systems to control smoke flow is adopted for the analysis.

The concept of using a longitudinal ventilation system to control smoke [22] is to produce a longitudinal flow to blow smoke towards one direction and to create a smoke-free path at the upstream direction of the fire for evacuation, rescue, and firefighting purposes. The limitation in using this ventilation system in fire scenarios is that the occupants on the downstream side of the fire will be exposed to heat and smoke.

In the design of a longitudinal ventilation system to control smoke, it is important to achieve a minimum ventilation velocity defined as the critical velocity, which can prevent the spread of smoke towards the upstream side of a fire (termed as ‘back layering’). The minimum velocity to prevent back layering is quantified as the critical velocity [27, 28], which is commonly calculated through [29]:

$$u_c = K_1 K_g \left(\frac{g\dot{Q}H}{\rho_0 c_p T_f A_{cross}} \right)^{1/3} \quad (2.1)$$

$$K_1 = F_{rc}^{-1/3} \quad (2.2)$$

$$K_g = 1 + 0.0374(grade)^{0.8} \quad (2.3)$$

$$T_f = \frac{\dot{Q}}{\rho_0 c_p A u_c} + T_0 \quad (2.4)$$

When the designed ventilation velocity is higher than the calculated critical velocity, the designed system is considered to be acceptable. As recommended by the PIARC (1999) [24], a maximum limit of 8 to 10 m/s also needs to be considered in the system, which is a cost-effective value and without disturbing vehicles and the staff operating in the tunnel.

2.2.3 Longitudinal Tunnel Ventilation Influence on Fires

Although the increase of ventilation velocity can effectively prevent the back layering in a fire and create a smoke-free path on the upstream side of a fire, it has been noted that the forced air flow has a significant influence on fire size. In one of the HGV fire tests in EUREKA (1992) [7], significant influences on fire development were observed by applying different ventilation velocities at different fire development stages. In the Second Benelux tunnel test series for HGV fires in 2001, the HRR obtained with forced ventilation was 1.2 to 1.5 times larger than the HRR with natural ventilation [9].

Carvel and Beard [14] adopted the Bayesian probabilistic method to quantify the ventilation influence on tunnel fire size based on a number of experimental fire tests in tunnels. An equation of the influence was given:

$$\dot{Q}_{vent} = k\dot{Q}_{nat} \quad (2.5)$$

where $\dot{Q}_{vent}$ is the HRR of a given fire in a tunnel with forced ventilation and $\dot{Q}_{nat}$ is the HRR of a similar fire in a naturally ventilated tunnel and k is a variable parameter representing the change in the HRR between natural and forced ventilation.

Different vehicle fires at different fire growth stages were investigated in their study. The k values for HGV fires in single-lane tunnels and in two-lane tunnels at the growth phase and fully developed phase are shown in Figure 2-2. The results shown in their study demonstrated that the ventilation in a tunnel fire significantly enhanced fire size.

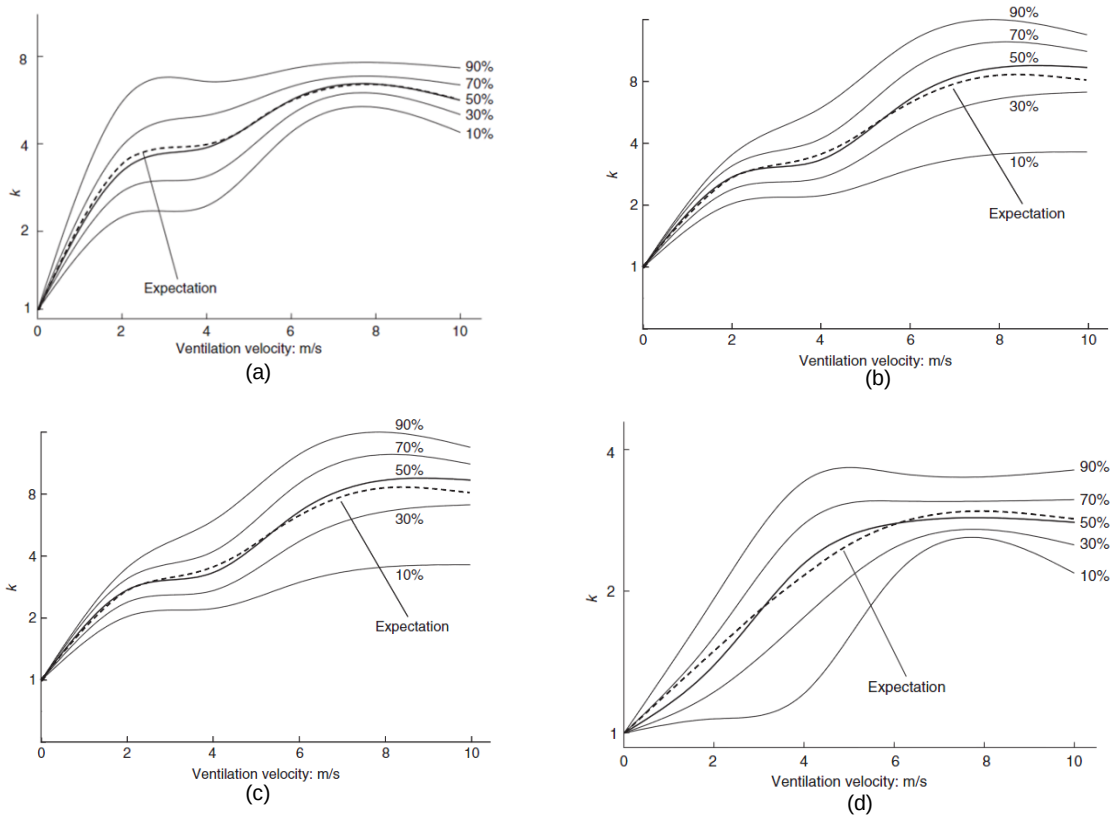

Note that the vertical axis of the graph is presented on a logarithmic scale.

Figure 2-2: k values for a HGV fire: (a) in a single-lane tunnel at fire growth phase; (b) in a single-lane tunnel at fully developed phase; (c) in a two-lane tunnel at fire growth phase; (d) in a two-lane tunnel at fully developed phase (reproduced from [14]).

Ingason [15] used a series of small-scale tunnel experiments to investigate the tunnel ventilation influence on HGV fires. All the experiments were carried out in a 1:23 small-scale tunnel, which was 10 m long, 0.4 m wide and with two heights of 0.2 m and 0.3 m. Two different sizes of wood cribs were used to represent HGVs. The longitudinal ventilation was provided by an electric fan attached to the entrance of the small-scale tunnel. Longitudinal velocities in the experiments were 0.42 m/s, 0.52 m/s 0.62 m/s and 1.04 m/s (Corresponding to the large-scale velocities are 2 m/s, 2.5 m/s, 3 m/s and 5 m/s.)

In the work, the porosity of wood cribs (P) was considerably discussed, which can be obtained from the equation below:

$$P = \frac{A_v}{A_s} s_p^{1/2} b^{1/2} \tag{2.6}$$

where A_v is the ventilation area, A_s is the exposed surface area, S_p is the hydraulic diameter of the ventilation area and b is the thickness of wood stick. According to the discussion in [15], the fire became independent of the influence of wood crib geometry, when the P value was larger than 0.7 mm. In Ingason's experiments, the P values of the two wood cribs were 0.94 mm and 1.24 mm.

The analysis from Ingason [15] showed that the ventilation velocity enhanced the maximum HRR per unit fuel surface area in the range of 1.4 to 1.55 times compared with the value for the free burning scenario, where wood crib was placed in an open space without influence from tunnel surrounding walls and ventilation.

In 2007, the tunnel ventilation influence on fire growth and maximum HRR were further investigated by Lonnermark and Ingason [30] through another series of small-scale tunnel experiments at a scale of 1:20. The tunnel was 10 m long with three different widths of 0.3 m, 0.45 m and 0.6 m and with two different heights of 0.25 m and 0.4 m. In this work, they particularly investigated the air velocity influence on fuels with different porosities. The wood cribs adopted in the experiments had porosities of 2.1 mm and 0.62 mm. Velocities of 0.22 m/s, 0.45 m/s, 0.67 m/s and 1.12 m/s were used in experiments, which corresponds to 1 m/s, 2 m/s 3 m/s and 5 m/s at the large-scale. A total of 19 wood crib experiments were conducted.

In this series of experiments, they found that the ventilation had more significant influence on the enhancement of maximum HRR when low porosity wood cribs were used. The increase in maximum HRRs at different velocities compared with the result in free burning experiment is in the range of 1.4 to 1.7 for high porosity wood cribs. The effects increase from 1.8 to 2.2 when low porosity wood cribs are used.

Overall, these studies all demonstrate the significant influence of ventilation on fire size in HGV tunnel fires. HGV tunnel fires are considerably larger compared with other type of vehicle fires, the fire will burn more fiercely and cause serious consequences with the effects of the ventilation conditions.

2.3 Fire Dynamics Simulator (FDS)

The one of the main objectives of this research is to establish a simulation methodology using the pyrolysis model in FDS6 to predict HRR for tunnel fires. In this section, the basic features of FDS6, the existing studies using the pyrolysis model to predict HRR for fires and the current work of using FDS to model tunnel fires are discussed.

2.3.1 Basic Features

FDS6 [16] is a computational fluid dynamics (CFD) model of fire-driven fluid flow. In CFD modelling, the motion of fluid can be described by a set of partial differential equations (called as the Navier-Stokes equations) to resolve the conservation of mass, momentum and energy for a flowing fluid. In FDS6, the form of the Navier-stoke equations are numerically solved for low-speed, thermally-driven flow with an emphasis on smoke and heat transport from fires.

In FDS, turbulence is treated through Large Eddy Simulation (LES) method, where turbulences in the flow are only averaged at scales smaller than the cell size. The large scale eddies are resolved directly. When the mesh size is extremely well resolved, FDS6 is able to perform a Direct Numerical Simulation (DNS). The LES is the default model.

Combustion model is defined by two approaches in FDS6, which are mixing controlled combustion and the combustion under DNS model. The first approach is used in most applications, the reaction of fuel and oxygen is infinitely fast and controlled only by mixing. The fuel in this mixing-controlled combustion can be defined as a single fuel species consisting of C, H, O and N to react with oxygen. Alternatively, the fuel can be defined in a more complicated manner, which requires the specification of the detailed reaction stoichiometry in FDS. In addition, multiple chemical reactions are allowed in FDS6. The use of multiple fuels in FDS6 only works when the mass flux of each fuel can be specified. For the DNS model approach, a very fine grid resolution (a millimetre or less in size) is required.

In FDS6, the radiative heat transfer is calculated by the radiation transport equation for a gray gas, and in some limited cases a wide band model is adopted. This solver in the FDS6 costs 20% in CPU time. The default radiative fraction in FDS6 is 0.35 and this value is also allowed to be specified by users.

2.3.2 The Pyrolysis Model

In order to simulate a fire in FDS6, one can use a gas burner with a specified HRR, where the fire spread rate or burning rate can be defined. One can also simulate a fire by using the complex pyrolysis model in FDS6, from which the HRR and the spread of fire can be predicted rather than using pre-defined values.

In a fire, the pyrolysis is the thermal decomposition process for a heated solid material to release gaseous fuel. In the presence of oxygen, the combustible gaseous fuel released in the decomposition will be burnt above the solid material and the charring residue may be oxidised. In FDS6, this pyrolysis process is described through an Arrhenius-like equation, which gives a relationship between reaction rates and temperatures. The decomposition rate for a material undergoing one or more reactions can be written as below.

$$r_{ij} = A_{ij}\left(\frac{\rho_{s,i}}{\rho_s(0)}\right)^{n_{s,ij}}_{s,i} \exp\left(-\frac{E_{ij}}{RT_s}\right) \tag{2.7}$$

FDS6 adopts a one-dimensional heat conduction equation to compute the temperature gradients in solid phase, which further determines the changes in the decomposition rate with the increase in temperatures. Based on the two key equations, the release rate of gaseous fuel can be calculated and the corresponding heat release rate can be obtained. The detailed derivation of all the equations for the prediction in HRR will be further introduced in Chapter 4.

2.3.3 Kinetic Properties Analysis in Literature for the Pyrolysis Model

In order to apply the pyrolysis model, the three kinetic properties of A_{ij}, E_{ij} and n_{ij} listed in Equation 2.7 need to be defined. The TGA experimental method is commonly used to obtain the kinetic properties for materials. In TGA experiments, only small amount of the material is required (e.g.10 mg), the samples are placed in a cup (~ 5 mm in diameter) and the cup is heated at a constant heating rate under a nitrogen environment. The mass losses due to the thermal decomposition are recorded during the heating up process. In this thesis, this type of experiment is defined as the material-scale experiment. Based on the TGA mass loss curves, different methods have been developed to derive the kinetic properties. Such as: analytical methods [31, 32], genetic algorithm (GA) optimisation methods [33], graphical analysis methods [34] and combining methods [35]. In addition to TGA experiments, cone calorimeter experiments under ambient air environment (defined as bench-scale experiments) are useful

to validate the solid phase decomposition and to further refine the estimate of the material parameters.

Matala and Hostikka [36] applied the analytical method proposed in [32] and the GA optimisation method to analyse the kinetic properties for PVC cable materials. In the use of the analytical method, the reaction order was simplified to one, and the A and E were derived from simple analytical calculations based on the TGA results. The GA optimisation method was based on a random set of parameters testing against TGA experimental curves in order to find the parameters which give the best fitting to the experimental curves. In addition, they compared the differences in using different reaction paths (parallel and consecutive) to estimate the kinetic properties. The kinetic properties obtained from the two different methods gave effective predictions in simulating TGA experiments. The results in the simulations of cone calorimeter experiments were significantly different if the same set of thermal properties was used. However, good fits to the experimental data were achieved when the thermal properties were optimised based on the two different sets of kinetic properties. In terms of the effect of using different reaction paths, the effect on the TGA predictions was very minor. However, a considerable effect was obtained in the predictions for the cone calorimeter experiment. In their paper, they highlighted the findings that the kinetic properties were not fixed values for a complex material, while these properties were significantly dependent on the analysis methods, the selection of reaction paths and the properties sets.

Pau et al. [34] introduced the applications of three graphical techniques (the kinetic analysis method, the Arrhenius plot method and the inflection point method) to determine kinetic properties of polyurethane foam. These three methods are built upon different correlations, which describe the relationships between the kinetic properties and the changes in mass during the decomposition of a material. Based on the TGA experimental data for the polyurethane foam, the correlations can be obtained graphically and the values of A, E and n can be derived subsequently. In Pau's thesis [20], he evaluated five different reaction schemes with different level of complexity including: single reaction scheme, multi reaction scheme, multi layers scheme, mass fraction scheme and residue formation scheme. These schemes were all applied to simulate the cone calorimeter experiments for polyurethane foam samples using the corresponding kinetic properties analysed from the graphical methods. The best cone calorimeter simulation results were obtained based on the multi reaction scheme, which was a scheme that the polyurethane foam was assumed to have two different decomposition reactions and each reaction had its own kinetic properties. The thermal properties in the two decomposition reactions were assumed to be the same. However, the predictions based on this scheme also resulted in overpredictions under high external heat flux.

Li et al. [35] applied the Kissinger method combined with the GA searching method to determine kinetic properties for medium density fireboard (MDF), which is a wood-based material with a complicated decomposition behaviour. Due to the complexity of the decomposition for MDF, the graphical methods are not applicable to an analysis of the TGA curves consisting of overlapping reactions, while the use of the GA method requires a long computational time to conduct blind searching of the results. Therefore, the Kissinger method was firstly applied to narrow the searching range and the GA method was used to locate the final results, which give the best fit the experimental curves. A four-component scheme was used to represent MDF and each component had its own decomposition reaction [35]. Four different heating rates were used to obtain the TGA experimental results. The initial values of A and E for each component were estimated using the Kissinger method based on the TGA experimental results at different heating rates. The final kinetic properties were optimised through the GA searching method. This combination method proposed by Li et al. demonstrated an advanced technique to quickly obtain the kinetic properties using multiple heating rates to analyse the kinetic properties. However, there is no further validation in applying these properties to conduct FDS simulations for material-scale or bench-scale experiments.

As introduced above, a common way to obtain the kinetic properties of materials is to derive these values from TGA experimental results. The kinetic values are dependent not only on the methods adopted in the calculations but also on the reaction paths/schemes chosen in the analyses.

2.3.4 Applications of the Pyrolysis Model to Predict HRR

Most applications of the FDS pyrolysis model are for the simulations of material and bench scale experiments. There are only a few available studies using the pyrolysis model to predict HRR for small-scale or large-scale experiments. In this section, some studies for these applications are reviewed. The predictions in these papers exhibit the limitations in using the pyrolysis model to predict the actual experimental results. However, these studies are still valuable in demonstrating the approaches of using the pyrolysis model to simulate different scale fires and the possible reasons behind the limited predictions.

McGrattan et al. [32] used Lagrangian particles, which is a method to define a particle as an element of fluid with assigning one or more property values, to represent two complex fuel geometry experiments (burning cables and burning trees). FDS allows the use of Lagrangian particles to simulate a wide variety of subgrid-scale objects, from office clutter to vegetation in

FDS [16]. The pyrolysis properties for cables and trees were calculated using an analytical method. In the simulations of the experiments, the cable and tree were simulated through the Lagrangian particle approach, in which the particles were randomly inserted in a defined volume. The pyrolysis properties were assigned to the surface for each particle, where only one-dimensional heat conduction was computed. The predictions in HRR for the cable fire and mass loss rate for the tree burning were presented in the paper, where the results obtained from the simulations can only partially represent the actual burning for both scenarios. The limitations in the prediction were attributed to the lack of a comprehensive set of material properties to accurately reflect the pyrolysis reactions. Overall, the main interest in the paper was to use the particle-based method to model complex fuel geometries.

Pau [20] applied the pyrolysis model to simulate experiments of fire spread on polyurethane foam mattress. In the experiments, two foam slabs were used, the dimensions being 1000 mm in width and 2000 mm in length and of two thicknesses of 100 mm and 120 mm. A line burner was set at one end of the mattress to ignite the foam and the burner was turned off after 120 s. In the simulations, FDS failed to produce the fire spread on 120 mm and 100 mm foam slabs when the material properties adopted the inputs, which were experimentally developed or refined through a material property estimation software: Gpyro. However, FDS was only able to represent the fire spread on the two foam slabs when value of activation energy is reduced by a factor of 20 to 30%.

Another application came from a recently published SP report by Li [37]. In the report, Li used two methods in FDS to simulate a train carriage fire in a tunnel. One of his simulation methods was the pyrolysis model method. The material properties used in the simulations were estimated and calibrated based on the data from TGA experiments and cone calorimeter experiments. By applying the pyrolysis model, the prediction in the peak HRR for the train fire was much lower than the test data and the total energy content was also significantly lower than the result in the test. The main reasons introduced in the report for the significant underpredictions in the simulations were due to the inappropriate kinetic properties and insufficient representation form some combustible materials. However, there was no detailed introduction in the report regarding the derivation of kinetic properties and the relevant material properties. It is difficult to justify whether the simulation results were based on correct material properties.

Overall, the predictions obtained by applying the pyrolysis model in FDS to simulate some medium or large-scale fire cases had different degrees limitations. Based on the discussion from these studies, the reason is mainly attributed to the use of insufficient information of fuel

properties to describe decomposition reactions. Therefore, a comprehensive study of fuel properties prior to any further applications of the pyrolysis model is a crucial step to obtain more positive results.

2.3.5 FDS Simulations for Tunnel Fires

A common approach to simulate a fire in a tunnel is to use a gas burner with a specified HRR to represent the fire. This representation of a fire can effectively predict the temperature profiles and the backlayering phenomena in the tunnel for a pool fire scenario with the appropriate use of grid size and boundary conditions, such as the simulations carried out by Kim et al. [38], where simulations were conducted for a pool fire test (with approximately 100 MW HRR) in the Memorial Tunnel Ventilation Test Program (MTVTP). However, for HGV fire tests, this representation may have some limitations to fully represent HGV fire burning behaviour due to the influence of vehicle shapes.

Li and Ingason [17] adopted a dimension of 3 m (W) x 10 m (L) gas burner with specified HRR inputs to simulate the Runehamar tunnel T1 test, where an HGV mock-up was used in the experiment. They found that the predictions in ceiling gas temperatures correlated well with the experimental results from 10 m to 150 m on the downstream side of the fire, while the temperatures obtained for further downstream locations (250 m, 350 m and 450 m) in the simulation were significantly overestimated. In addition, the predicted incident heat fluxes at the downstream side of the fire in the simulation did not match well with the experimental results.

Apart from the use of the known HRR as input to simulate a two dimensional gas burner fire, the HRR can also be predicted by dividing the surface up into individual element with specified ignition temperature and burning rate history.

In Cheong's simulations for Runehamar tunnel T1 test [18], the gas burner approach was also adopted. Instead of using the HRR obtained from the T1 test directly, he specified burning rates and ignition temperatures for individual surface elements based on the cone calorimeter results for different materials. In the simulation, the HGV fuel surface would only be ignited when the set-up ignition temperature was reached and the corresponding surface would burn at a specified rate as defined. Because of the limitation in the available computational capability, the fuel geometry in the simulation was simplified by obtaining the equivalent burning surface area to the burning area of the mock-up HGV in the test. The predicted HRR curve from the

simulation showed the similar growth rate history and peak heat release rate to the fire test produced, while the fire decay phase was not predicted.

In Li's report [37], the gas burner with specified burning rates and ignition temperatures was also adopted to predict the HRR for a train carriage fire. The HRR for different fuels were measured through cone calorimeter experiments and single item tests and the burning rates were specified accordingly for each fuel. Good predictions were obtained in using this method. In his work, the selections of ignition temperature and the modifications of burning rate from experimental data were specifically discussed. Li highlighted the fact that there were auto-ignition and pilot-ignition temperatures involved in the actual ignition scenarios. He used a temperature in between the two ignition temperatures in the simulations. When the cone results were applied to specify the burning rate, the HRR results were measured under incident heat fluxes from 25 kW/m^2 to 50 kW/m^2 were adjusted proportionally as the incident heat flux in the actual burning were about 33 kW/m^2 to 150 kW/m^2, which are much higher than the values in the cone experiments. Li increased the HRR values from cone results by a factor of 2 to compensate for the use of insufficient energy from cone results representing the actual burning scenario. As demonstrated in Li's work, the uncertainties in choosing the ignition temperatures and the burning rates have significant influences on the final predictions. The burning prediction in this method is controlled by the pre-defined ignition temperatures and burning rates, where the fuel is assumed to ignite at the same temperature and to burn at the same rates. Because of these assumptions, this method has limitations to represent the actual fire spread and burning in a real fire.

The alternative solution to predicting a fire burning is to use the pyrolysis model, where the ignition, fire spread and HRR of a fire can be predicted based on the fuel material itself and the environment influences instead of giving pre-defined values. A more realistic fire can be modelled using the pyrolysis model. Currently, there are only very limited applications to model tunnel fires based on this method. As introduced, the pyrolysis model was applied to simulate a train carriage fire in a tunnel [37], where HRR predictions were significantly underestimated.

2.4 The LTA Tunnel Simulated HGV Cargo Fire Experiment

As summarised In Chapter 1, one of the main objectives in this research is to apply the pyrolysis model to simulate one LTA large-scale simulated HGV cargo tunnel fire experiment. The material properties for the fuels used in the LTA experiment are analysed and evaluated in Chapter 3 and 4. The LTA experimental data and specifications have been used to design the small-scale tunnel experiments described in Chapter 5 and 6. The corresponding

simulations for the LTA experiment are carried out in Chapter 8 and 9. Because of the significant reliance of the LTA experiment in this research, it is necessary to have an overview of the LTA experiment, which can give the reader a better understanding of the following chapters.

This LTA programme involved a series of large-scale fire experiments, which were carried out in a test tunnel facility in Spain in 2012. The heat release rates generated by a simulated HGV cargo fire were investigated in the circumstances with and without a fire suppression system in a ventilated tunnel [39]. The aims of this programme were to study the influences on fire size and temperatures from water suppression in the presence of a tunnel ventilation system, and to obtain appropriate design data for the most probable fuel load used in the road tunnels. Seven experiments were conducted; one with a ventilation system only and six with both a ventilation system and fixed water based fire-fighting system. In this thesis, the experiment with only a ventilation system is adopted as the main interest of this work lies in the ventilation influence on tunnel fires.

2.4.1 Tunnel Geometry and Positions of Instrumentation

The tunnel was a two-lane road tunnel built in concrete. The total length of the tunnel was 600 m with a longitudinal gradient of 1%. The original tunnel was in a horseshoe shape and a length of 445 m portion of the tunnel was modified to a rectangular shape for fire tests. At the location of the fire source, a minimum dimension of 7.3 m wide and 5.2 m height was measured. In order to protect the concrete against damage from fire, walls over 120 m were constructed inside the tunnel. The overview of the longitudinal cross section for the tunnel is shown in Figure 2-3 (a).

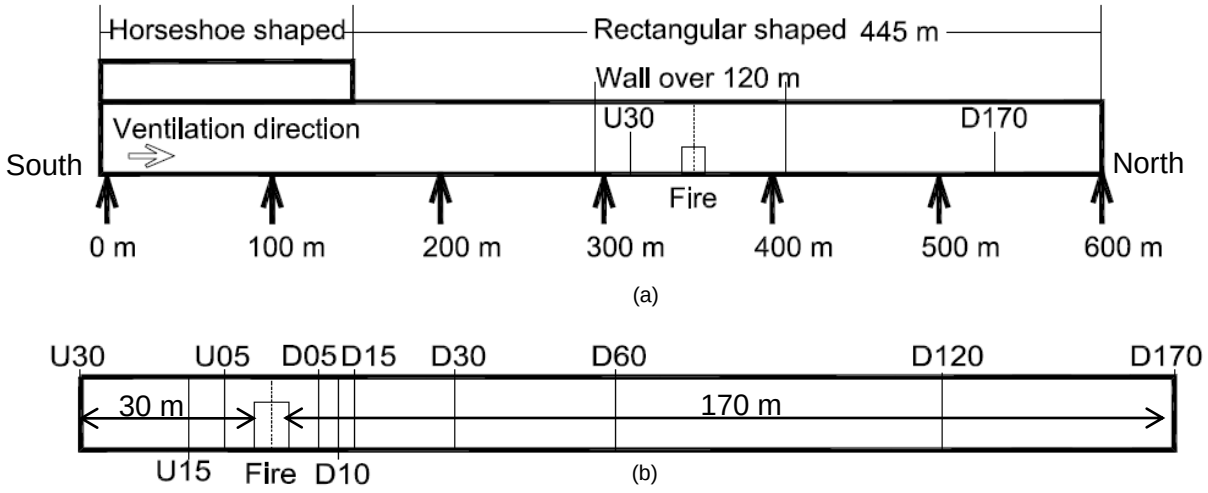

Figure 2-3: Tunnel longitudinal cross section: (a) overview of the tunnel (b) detailed measurement locations and fire location in the tunnel (reproduced from [39]).

A series of temperature and heat flux data were recorded during the experiment from 30 m away from the upstream edge of the fire to 170 m away from the downstream edge of the fire. Figure 2-3 (b) presents the longitudinal locations of measurement in the tunnel, where Ux/Dx denotes a position x m away from the upstream/downstream edge of the fire. Based on the information provided by the LTA, water spray was used 9 min after ignition at 45 m downstream away from the fire location for the experiment only with the operation of the ventilation system to cool down the tunnel structure. It is assumed that the water discharge had no influence on the temperature results at locations before this point and no influence on the HRR results in the experiments.

According to the data presented in Cheong et al. [39] and the available data information provided by the LTA, the detailed arrangements of instrumentation at the cross-sections of U30, U10, D5, D10, D15 and D30 are shown in Figure 2-4. The oxygen depletion calorimetry method, where the heat release rate is measured based on the amount of oxygen consumed, was adopted in the test. The corresponding gas concentrations at location D170 were measured. The positions of gas sensors are also show in Figure 2-4. It is noted that there are other measurements in the tests at different locations. However, the corresponding data for these measurements are not available. Therefore, these measurements are not introduced in this research.

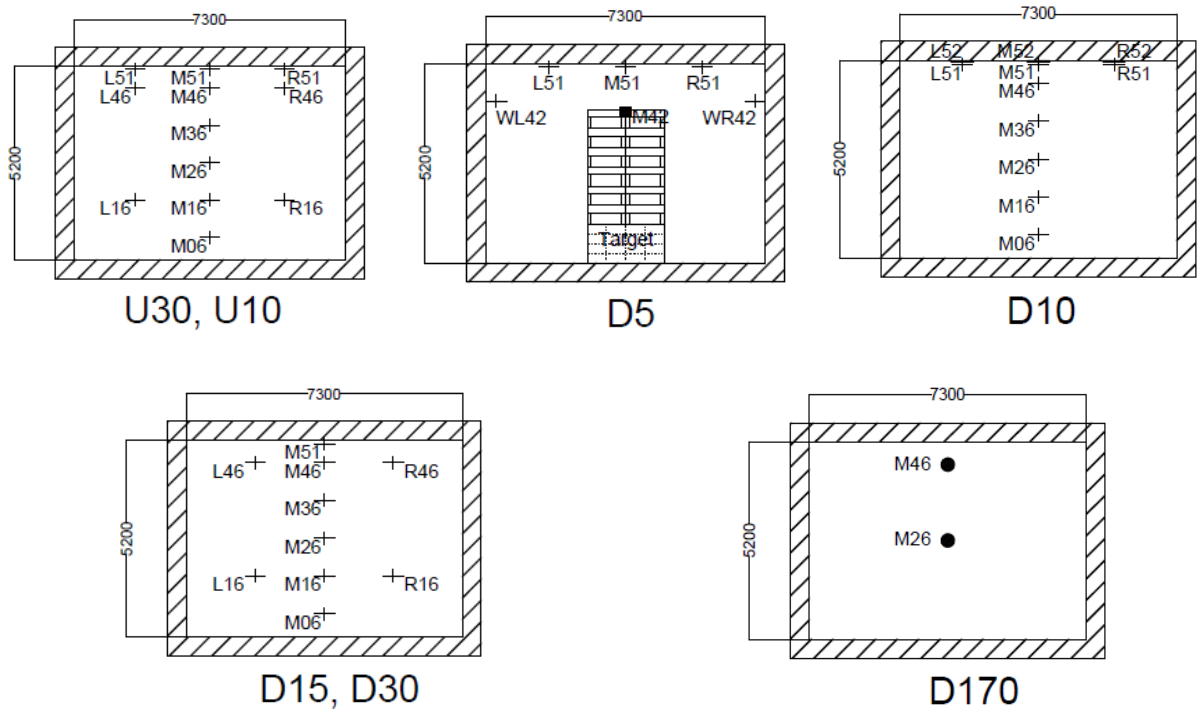

Figure 2-4: Cross section of instrumentation at different locations (reproduced from [39]).

In Figure 2-4, W denotes a position near the wall. M means the centreline of the cross section, L/R means that 2 m away from the centreline towards left/right side. The numbers indicated in the figures denote the relative height (in cm) of a sensor above the floor of the cross section. For instance, M46 is a sensor on the centreline of the cross section at 4.6 m above the floor.

2.4.2 Tunnel Ventilation System

The longitudinal ventilation system in the experiment was applied by using jet fans at the southern end of the tunnel to provide an air velocity of approximately 3 m/s. The velocity data was measured upstream 45 m away from the fire location. The corresponding results for the test only with ventilation system are plotted in Figure 2-5.

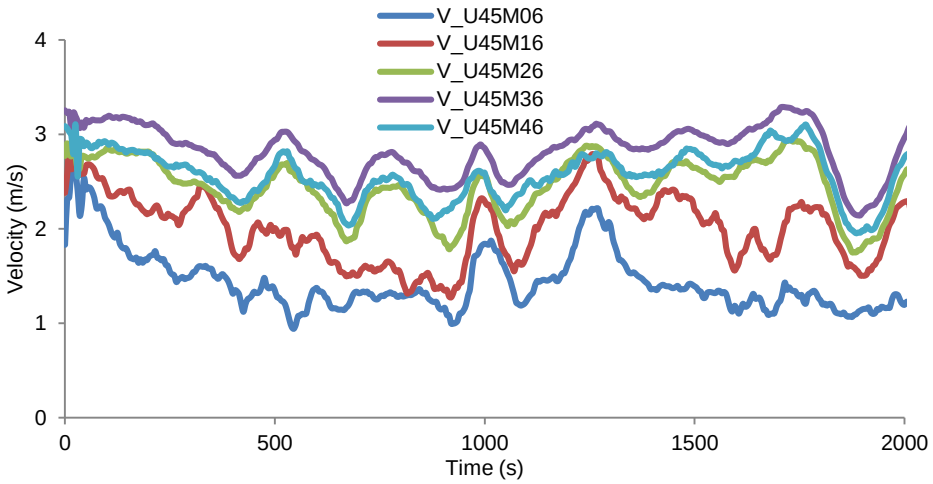

Figure 2-5: Velocity data at 45 m upstream of fire for test only with ventilation system (reproduced from [39]).

As shown in the figure, an average of 3 m/s is maintained at upper cross section positions (M46, M36, M26), while slightly lower velocities occurred at the lower cross section positions, where sensors of M06 and M16 were installed. The reason for the lower velocities at low position was explained in [39] that was due to obstacles in the lower part of the tunnel.

2.4.3 Fire Source

The configuration of the fuel in the experiments was based on a typical rigid HGV fully loaded with pallets, as shown in Figure 2-6 (a). A total 228 pallets, with 48 plastic pallets (20%) and 180 wood pallets (80%) were used to represent an HGV fuel load in the experiments [39] (shown in Figure 2-6 (b)). The pallets were in 12 stacks, 19 layers high on a 1 m elevation, with a steel frame around them. The top, front and back sides of the entire fuel load were covered with 1 mm thick steel plates, and a thin plastic tarpaulin was used to cover the left and right sides of the fuel load. The pallets used were the standard euro pallet size with dimensions of 1.2 m x 0.8 m.

The pallets were distributed so that every four layers of wood pallets were followed by one layer of plastic pallets until the 15th layer, which was followed with three layers of wood pallets only. Then, the 19th layer was for a layer of plastic pallets. Two trays with dimensions of 0.35 m x 0.70 m, which contained about 1 L of gasoline were located on the second layer of pallets at the most upstream stacks. The distribution of the pallets and the location of the ignition source are indicated in Figure 2-6 (b). A target with two full pallet stacks was placed 5 m downstream from the rear end of the fire source.

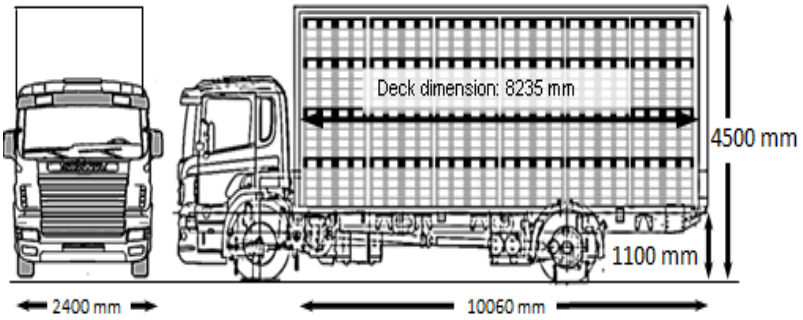

(a)

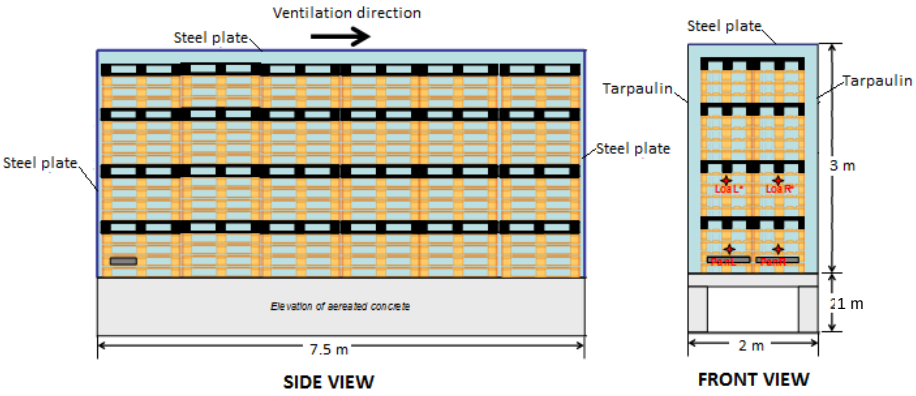

(b)

Figure 2-6: (a) a typical rigid HGV fully loaded with pallets; (b) distribution of the pallets and the location of the ignition source (reproduce from [39]).

2.4.4 Heat Release Rate

The HRR curve obtained from the experiment without operation of fixed water suppression system is plotted in Figure 2-7. As discussed in Cheong et al.'s paper [39], the HRR for the test without the operation of water suppression system showed a ultra-fast fire growth rate in the first 7 min and the fire grew even more rapidly after 7 min.

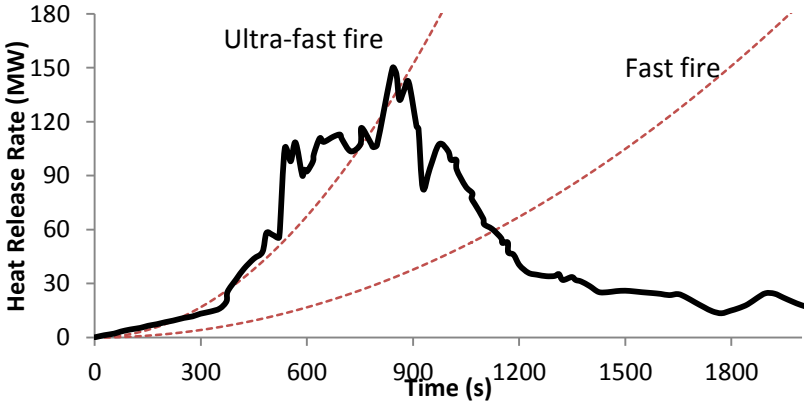

Figure 2-7: HRR curve for the LTA test without operation of water suppression system (reproduce from [39]).

As shown in the figure, there is a sudden increase in HRR from a steady value of 100 MW to a peak value 150 MW at 12.8 min. According to the observation from the test [39], the reason for the rapid increase in HRR was due to the collapse of pallets stacks during the burning process increasing a large amount of exposed surface area to the fire. The target at 5 m away from the fuel was ignited in this test and a peak heat flux value of 220 kW/m^2 was obtained at the target location [39]. Further results obtained from the LTA experiment are shown in Chapter 5 and Chapter 8.

Chapter 3 Experimental Analytical Studies of Decomposition Properties for Tunnel Experiment Materials

This chapter introduces the analyses of kinetic properties and heat of reaction for the LTA materials. Two published paper are included in this chapter

3.1 Introduction

As introduced in Chapter 1, one of the aims in this thesis is to apply the pyrolysis model in FDS6 to model the LTA large-scale tunnel simulated HGV cargo fire experiment. In order to apply the pyrolysis model to predict HRR, a series of properties such as kinetic properties, heat of reaction, thermal properties and heat of combustion of the fuel need to be used as inputs in FDS[16, 19, 20]. Hence, a detailed study of fuel properties is carried out.

Two samples (refer as the recycled plastic and wood samples in this research) shown in Figure 3-1 are investigated which are the same materials used to make wood and plastic pallets representing HGVs in the large-scale tunnel experiments. However, the given information of these samples from the pallet manufacture is limited: the recycled plastic samples are composed of a mixture of recycled plastics, while other possible additives are not specified, and the species of the wood samples is unknown. It is very challenging to specify the properties for these unknown materials.

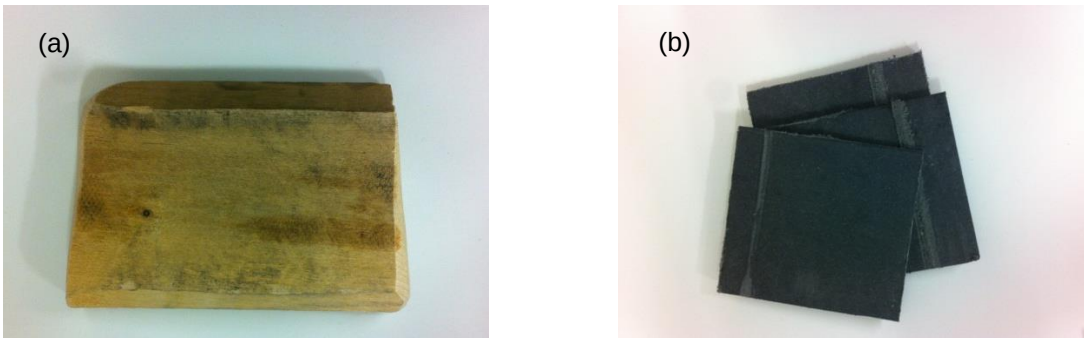

Figure 3-1: Fuel samples: (a) wood; (b) plastic.

In this chapter, TGA and DSC experiments are adopted to investigate the properties of activation energy (E), pre-exponential factor (A) and reaction order (n), and heat of reaction (Δh_r). A DSC-TGA Q series™ instrument (SDT600) manufactured by TA instruments is employed in this work, which simultaneously records the changes in mass [40] and in enthalpy during sample decomposition.

3.2 Kinetic Properties in the Pyrolysis Model

3.2.1 Mathematical Theory of Pyrolysis Model

The concept of pyrolysis reactions has been introduced in Chapter 2. A more detailed discussion in terms of the mathematical theory of pyrolysis model is carried out in this section.

Pyrolysis is a decomposition process that occurs in the solid phase of a heated material before going to the combustion phase. Gaseous products are released during the pyrolysis for a material. When air is present in the pyrolysis process, the combustible gaseous products may be ignited undergoing combustion reactions. The generated heat from combustion reactions keeps the pyrolysis continuing to release more gaseous products maintaining the fire. As can be seen, the pyrolysis rate significantly determines the generation of gaseous products and further affects the heat release rate for the corresponding fire. The reaction rate in the pyrolysis model is often numerically described in a form of the Arrhenius-like equation:

$$r = \frac{d\alpha}{dt} = A\exp\left(-\frac{E}{RT}\right)(1-\alpha)^n \tag{3.1}$$

where R is the universal gas constant, T the temperature and A, E and n are known as the kinetic triplet. The volatile conversion fraction is defined as [35]: $\alpha = 1 - m/m_0$, where m_0 is the initial mass and m is the mass at temperature T.

3.2.2 Kinetic Triplet Influences on Reaction Rate

Mathematically, the kinetic triplet (A, E and n) in Equation 3.1 are the key properties to describe a pyrolysis process. These three properties have significant influences on the decomposition reaction rate. Reaction rate can be calculated based on Equation 3.1, when A, E and n are known.

An example of decomposition rate (defined as DTG) curve for a single reaction at a constant heating rate of 5 K/min is plotted in Figure 3-2 with the values for that A is 1.5 x 10^{14} s^{-1}, E is 2 x 10^5 J/mol and n is 1. As shown, when the pyrolysis range for this reaction is from 550 K to 670 K, the peak reaction rate occurs at 636 K.

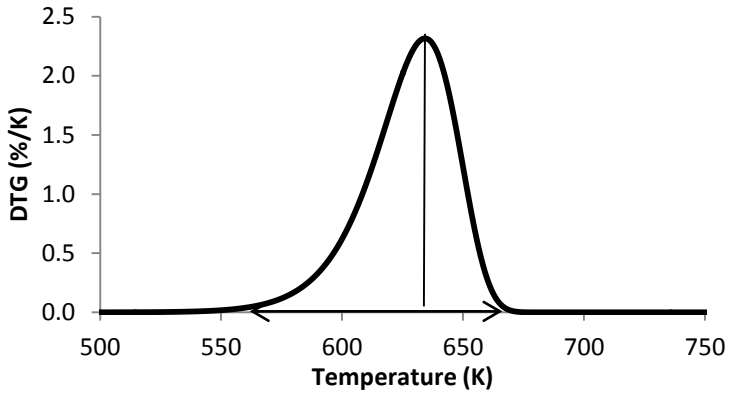

Figure 3-2: Reaction rate curvature for a pyrolysis process.

3.2.3 Influence from Reaction Order

According to Equation 3.1, reaction order is present in the term of $(1-\alpha)^n$. From a mathematical point of view, n has a significant effect on the results of reaction rate. Figure 3-3 plots the DTG curves for the scenarios that n are changed to different values of 2, 4 and 6, while A and E are kept as 1.5 x 10^{14} s^{-1} and 2 x 10^5 J/mol.

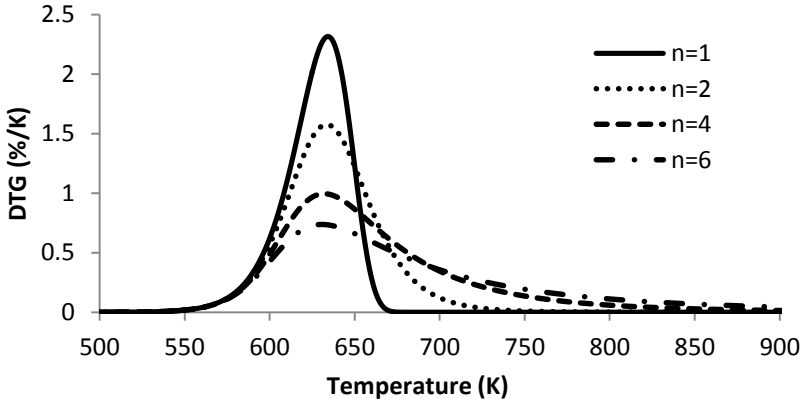

Figure 3-3: Reaction rate curvatures at different reaction orders.

As illustrated, the value of peak reaction rate reduces with the increase of the value of n, and the completion of the reaction ends towards high temperatures when a high reaction order is applied. The influences on the reaction rate curves suggest that a higher reaction order slows down the reaction and requires higher temperatures to complete the reaction. However, the temperature for the peak reaction rate is not affected by the changes in reaction order.

3.2.4 Influence from Activation Energy

When different values of activation energy (E) are applied to Equation 3.1, such as 2.0 x10^5 J/mol, 2.1 x10^5 J/mol, 2.4 x10^5 J/mol and 2.6 x10^5 J/mol. The corresponding curves of reaction rate are plotted in Figure 3-4.

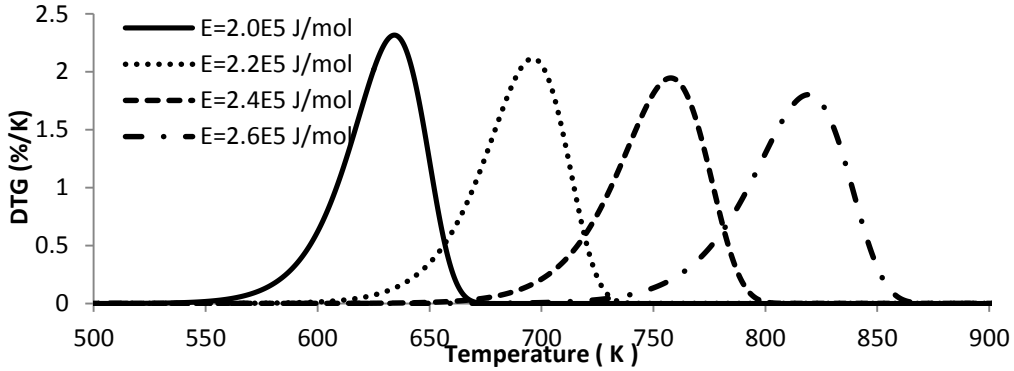

Figure 3-4: Reaction rate curvatures at different values of E.

As shown, the increase of E significantly increases temperatures for the peak reaction rates and the temperature range for the pyrolysis (from the start temperature to the completion temperature) shifts considerably towards higher temperatures. The relationship between the temperature and activation energy indicates that more energy is required to activate a reaction with the increase of E. However, the values of peak reaction rate are only slightly affected by the changes in activation energy.

3.2.5 Influence from Pre-exponential Factor

In terms of the pre-exponential factor (A), the influence on reaction rate curve is relatively limited compared with the other two properties. When the values of 1.5 x10^{14} s^{-1}, 3.0 x10^{14} s^{-1}, 6.0 x10^{14} s^{-1} and 9.0 x10^{14} s^{-1} for A are used, the corresponding DTG curves are plotted in Figure 3-5:

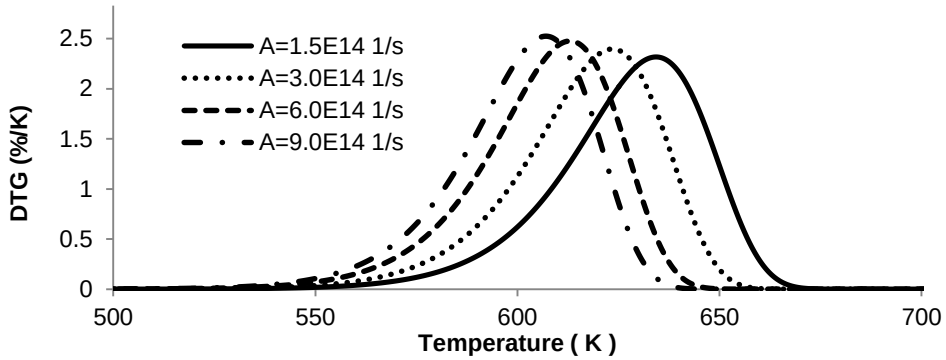

Figure 3-5: Reaction rate curvatures at different values of A.

As illustrated in Figure 3-5, the changes in peak reaction rate are negligible with the increase of pre-exponential factors. The temperatures for reaching the peak reaction rate and the temperatures for completing the reaction decrease with the increase of the A values.

According to the above comparisons, reaction order majorly determines the reaction rate and the pyrolysis range of a reaction, activation energy mainly controls the reaction temperatures required for a reaction and the pre-exponential factor also determines reaction temperatures although the influence from this property is not as significant as activation energy. The connection between A and E may be explained by a so-called 'compensation effect' [41]. According to the influences of the three properties on reaction rate curves, it can be concluded that A and E determines the location of a reaction curve, while n is the parameter to define the sharpness and the shape of the curve.

3.3 Derivation of Kinetic Properties

This part of work is reproduced from a published paper in the 10th Aisa-Oceania Syposium inn Fire Science and Technology:

The A, E and n have significant influences on the decomposition reaction for a material. However, the kinetic triplets are often to be unknown properties for most materials. TGA experiments which are used to record the changes in mass during decomposition under a controlled environment are commonly applied to obtain decomposition rate curves and the corresponding kinetic properties can be derived reversely.

As introduced in Chapter 2, there are many varied methods available in the literature to derive kinetic properties from the TGA experimental data, such as graphical techniques [34], analytical methods [31, 32] and even more advanced computational optimization methods

such as genetic algorithm (GA) searching methods [33]. However, these methods may have different limitations in their practical applications. The graphical techniques may not be suitable for analysing multiple overlapped reactions [35]; the analytical methods may have limitations in determining the values of reaction order [36]; and the complexity of the analysis procedures and required advanced programming skills may disadvantage the computational optimization methods.

In order to overcome the limitations with the various methods and to achieve simplicity and accuracy in the estimation of kinetic parameters for engineering practice, a hand calculation searching method combining the Kissinger analysis [31] with a simplified optimization process is proposed in this chapter. A series of TG experiments on the wood and recycled plastic samples are carried out to analyse the kinetic properties. Furthermore, the estimated kinetic parameters are used as inputs to FDS6 [16, 42] to predict the pyrolysis behaviour in order to evaluate the suitability of the proposed hand calculation method.

3.4 Introduction of the Hand Calculation Method

A multiple component scheme, which has been used to describe a complex decomposition [35], is adopted in the hand calculation method proposed in this study. If i is defined as the i^{th} component, the mass fraction of the i^{th} component is $c_i = m_{i0}/m_0$; the mass conversion fraction for the reaction of i^{th} component is denoted by $Y_i = 1 - \alpha_i = m_i/m_{i0}$, which starts from unity. The mass fraction of the residue of the component is represented by v_{si}, which can be obtained from TG experimental results. The decomposition rate of gaseous products r_i for the i^{th} component can be converted from Equation 3.2 into

$$r_i = -\frac{dY_i}{dt} = (1 - v_{s,i}) c_i A_i \exp\left(-\frac{E_i}{RT}\right)(Y_i)^{n_i} \tag{3.2}$$

The global decomposition rate of a material is the lumped result of the reaction rate for each component such that

$$r = \sum_{i=1} r_i = \sum_{i=1} (1 - v_{s,i}) c_i A_i \exp\left(-\frac{E_i}{RT}\right)(Y_i)^{n_i} \tag{3.3}$$

In order to determine the four unknown parameters A_i, E_i, n_i and c_i in Equation 3.3, an analytical calculation step to estimate the values of A_i and E_i, and a searching calculation step to find the values for n_i and c_i are applied.

In the first step, the Kissinger analysis method [31] is adopted to obtain the parameters A_i and E_i. The concept is to seek the temperature $T_{i,p}$ for the maximum reaction rate in a reaction at different heating rates β and then to identify a linear relationship between $\ln(\beta/{T_{i,p}}^2)$ and $1/T_{i,p}$ to further calculate the values of A_i and E_i such that

$$\ln\left(\frac{\beta}{{T_{i,p}}^2}\right) = -\frac{E_i}{RT_{i,p}} + \ln\left(\frac{A_i R}{E_i}\right) \tag{3.4}$$

After A_i and E_i are determined, the reaction temperature range of the reaction can also be confirmed, which has been discussed earlier. The adjustment of n_i and c_i can result in a change in the shape of the curves [19, 35]. Therefore, a simple searching model is proposed to find the value of n_i and c_i for a reaction based on the comparison of curve fitness between the model curve and the experimental curve. The searching model can be easily set up in a data analysis tool (such as a spreadsheet). The concept of the searching model is illustrated in the flow chart shown in Figure 3-6:

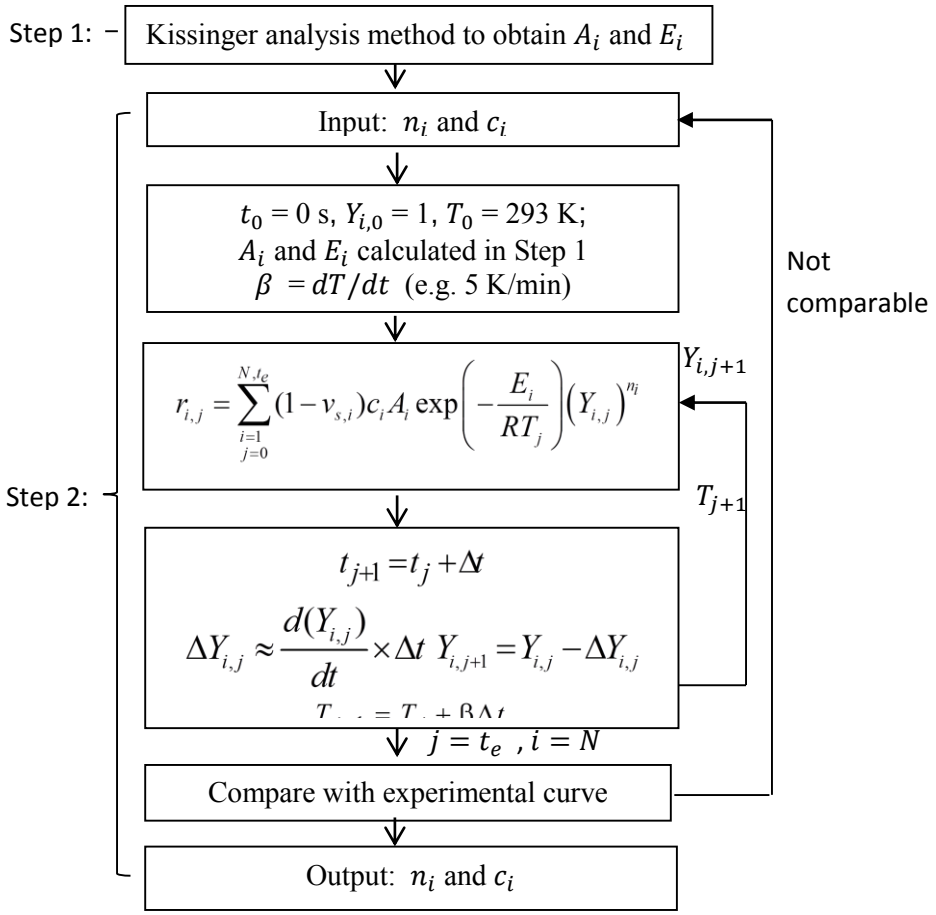

Figure 3-6: Flow chart for the searching method.

where j denotes the j^{th} second, i is the i^{th} component, t_e is the total time to complete reactions and N is defined as the total number of components. When the initial values of mass conversion fraction $Y_{i,0}$, temperature T_0, time t_0 at the zero second are defined and the heating rate β is chosen, the decomposition rate r_i can be calculated from Equation 3.3 by using the initial given input of n_i and c_i. Subsequently, the values of mass conversion fraction $Y_{i,j}$, temperature T_j and time t_j for the next time step can be derived as shown in Figure 3-6. According to these step by step calculations, the curve of decomposition rate for a material can be plotted based on the summation results of the decomposition rates for each assumed component. In terms of the initial value of n_i and c_i, one is used as the initial value of n_i, which is a value commonly used in chemical reactions [19], and the initial value of c_i can be estimated from literature values or from experimental curves. The determination of the final values of these two properties can be achieved by the visual comparisons between model and experimental results. It is noted that the values derived from this method are mathematical outcomes.

3.4.1 Materials and Experimental Method

The SDT Q600 thermal analyser was employed to conduct TGA experiments. Real fire environments may involve oxygen in the reaction zone which increases the complexity of the decomposition reactions. Similar to previous work [34], this study assumes a fire scenario in which the oxygen has been consumed before it reaches the pyrolysis front. The decomposition only refers to the scenario without oxygen. Therefore, all experiments were performed in a nitrogen environment by flowing nitrogen gas at 100 ml/min into the furnace. In experiments, the plastic and wood samples were all shredded into fine fragments. A sample (~10 mg) was loaded into a 90 *μL* alumina crucible (about 5 mm in diameter) and heated together with an empty crucible from ambient temperature to 850 K at three different constant rates of 5, 20 and 60 K/min.

3.4.2 Results and Discussion for the Kinetic Properties Analysis

3.4.2.1 Kinetic Properties Analysis for Plastic

Figure 3-7 (a) illustrates an example of DTG curves for the plastic samples at 5, 20 and 60 K/min heating rates. Since the main decomposition reactions for plastic start from 500 K or above and the changes in reaction rate between 400 to 500 K are negligible, the data for lower temperatures (less than 400 K) is not included in Figure 3-7 (a). As shown, decomposition rate are approximately same at all heating rates, decomposition starts at a higher temperature for a higher heating rate. The two decomposition rate peaks on each reaction curve clearly indicate the existence of two reactions for the decomposition. The peak value of the first reaction is about eight times smaller than the peak value of the second reaction, which demonstrates the second reaction is the dominant reaction. In order to simplify the complicated components for the plastics, two components (‘P1’ and ‘P2’) undergoing two reactions at distinct temperature ranges, which are illustrated in Figure 3-7 (b)

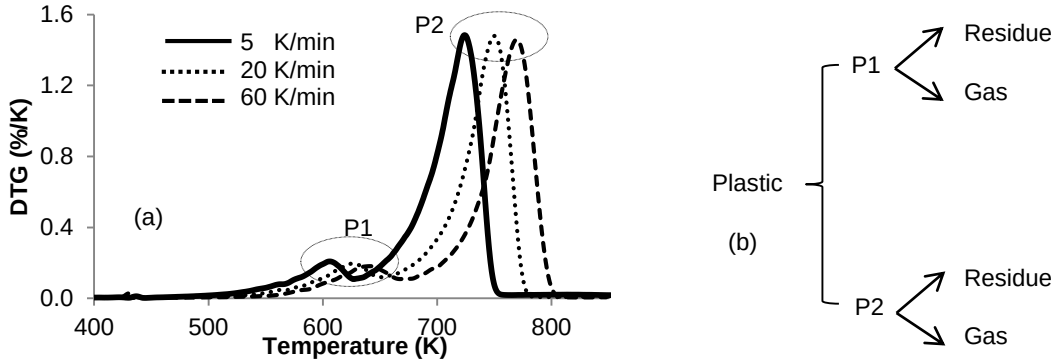

Figure 3-7: Plastic decomposition behaviour: (a) decomposition rate at different heating rates (b) decomposition steps.

Based on $T_{i,p}$ for each reaction at the three heating rates shown in Figure 3-7 (a), the linear lines of $\ln(\beta/T_p)$ against $1/T_p$ for the two reactions are plotted in Figure 3-8. The calculated values of E_i and A_i for each reaction are shown in Table 3-1 based on the indicated slope and intercept of the lines in Figure 3-8.

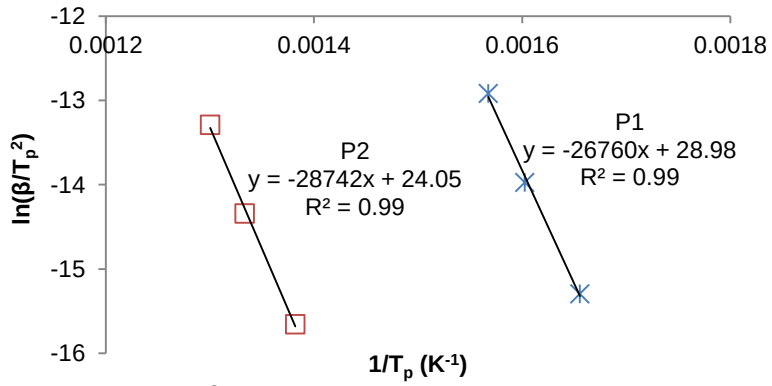

Figure 3-8: $ln(\beta/{T_{i,P}}^2)$ versus $1/T_{i,P}$ for each component of plastic.

Table 3-1: E_i and A_i for each component of plastic.

Components	E_i (J/mol)	A_i (s^{-1})
P1	2.22×10^5	1.04×10^{17}
P2	2.39×10^5	7.99×10^{14}

The mass fractions of the two components, 0.11 for P1 and 0.89 for P2, are initially estimated based on the ratios of the first peak value (0.18) and second peak value (1.48), which are the values shown in Figure 3-7 (a) to the summation of the two peak values(1.66). The values of v_{si} for the two reactions are assumed to be the same, which is about 4% for the remaining

residue from the mass recorded in TG experiments of the plastic samples when the sample is fully reacted.

When n_i = 1 is applied to the two components the initial reaction rate curves can be plotted. Figure 3-9 illustrates this example for the comparison between the experimental curve and the model curve based on the initial input of n_i and c_i listed in Table 3-2 at 5 K/min.

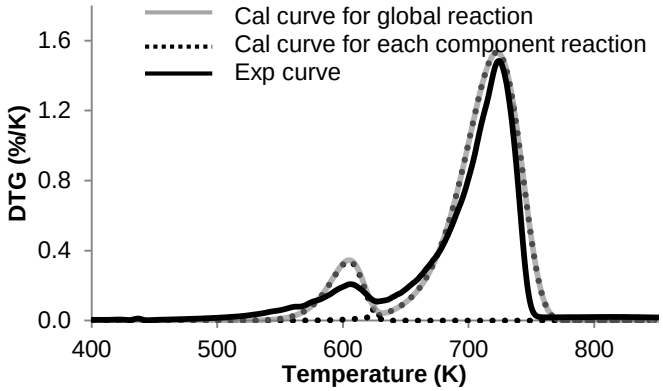

Figure 3-9: Experimental curve and initial model outputs at 5 K/min.

As discussed, reaction order n_i has significant influences on the sharpness of reaction curves [19, 35] and curve shape. In addition to the influences from n_i, c_i affects the magnitude of the reaction. The influences of n_i and c_i on the shape of the DTG curve are demonstrated in Figure 3-10. The reaction of P1 is used as the example to demonstrate the influences. It is found that a flat curve with low peak value reaction can be obtained by means of increasing n_i and decreasing c_i.

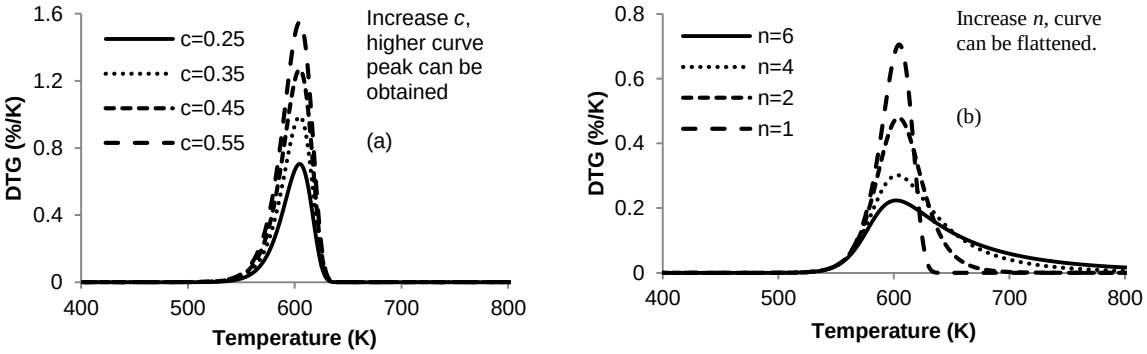

Figure 3-10: Influences on curve shape from: (a) c_i ; (b) n_i.

In order to achieve a better fit to the experimental curve for the results shown in Figure 3-10, the reaction curve of component P1 needs flattening and component P2 needs a slight

reduction in magnitude of the peak for a better fit to the experimental curve. Therefore, the n value of P1 is increased from 1 to 7.5 and the c value of this component is also changed from 0.11 to 0.25. In terms of the component P2, the c value is slightly reduced from 0.89 to 0.75, while n is kept as 1.

All the results for n_i and c_i are listed in Table 3-2. The final model curves at the three heating rates are plotted in Figure 3-11, which demonstrates an excellent fit to the experimental curves.

Table 3-2: The values of n_i and c_i for each component of plastic.

Item	Component P1		Component P2	
	Initial	Final	Initial	Final
n_i	1.0 →	7.5	1.0 →	1.0
c_i	0.11 →	0.25	0.89 →	0.75

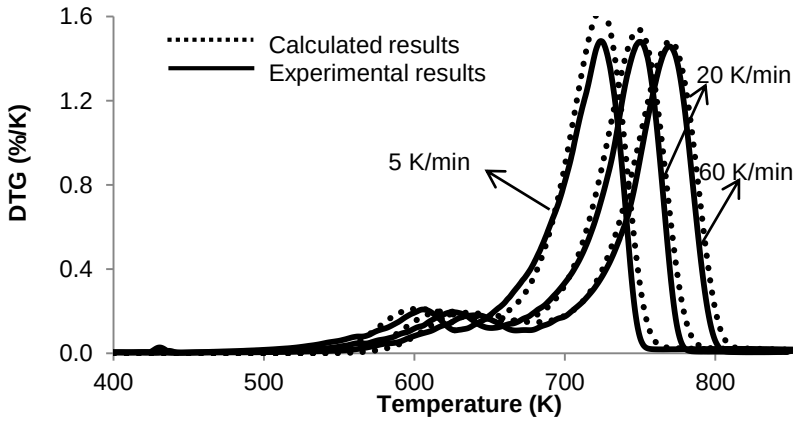

Figure 3-11: Comparison of experimental curve and final model outputs.

3.4.2.2 Kinetic Properties Analysis for Wood

Compared with the decomposition of plastic, wood has more complicated decomposition features. An example of the DTG curves for wood samples from TG experiments at the three different heating rates (5, 20 and 60 K/min) are plotted in Figure 3-12 (a). Because the interest of this study is to address kinetic properties for wood decomposition, the temperature before 400 K, which is mainly for the vaporization of moisture content, is not included in this study. As shown, the three curves at the three heating rates all demonstrate a shoulder part, a noticeable peak and a long tail part over different temperature ranges, which are commonly identified as three reaction regions: hemicellulose, cellulose and lignin reaction regions [43]. In this work, only three components for the three major reaction regions are assumed to represent wood decomposition, which is illustrated in Figure 3-12 (b).

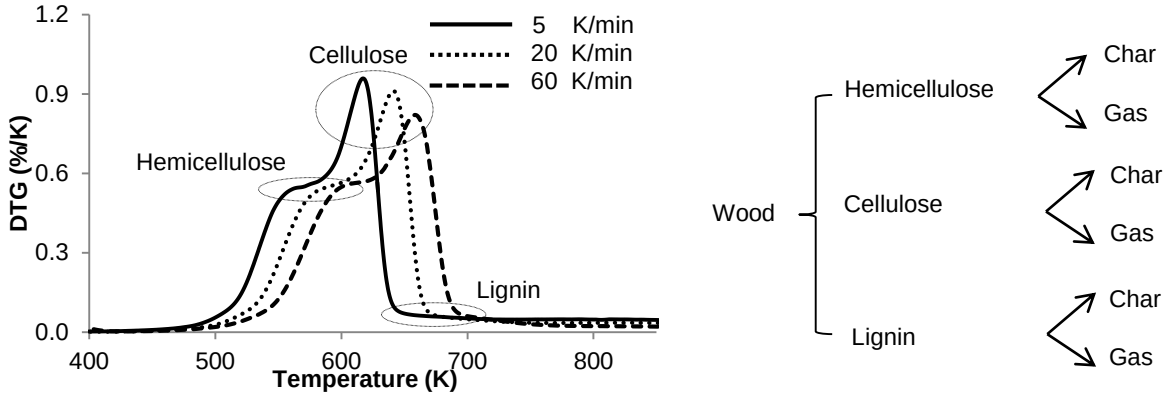

Figure 3-12: Wood decomposition behaviour: (a) Decomposition rate at different heating rates; (b) Decomposition steps.

In order to derive the values of A_i and E_i for each component, the $T_{i,p}$ for the peak reaction rate of each component needs to be identified. In Figure 3-12, the T_p values for the cellulose reaction region can be clearly found on the curves. However, there are no obvious indications for the T_p values for the hemicellulose and lignin on the DTG curves. One approach is to use a second derivative of the DTG (DDTG) curve to locate zero values where the temperatures correspond to the T_p values [35]. Hence, as an example, a plot of DDTG curve and DTG curve for the heating rate of 5 K/min is illustrated in Figure 3-13. Three T_p values are found at approximately 560 K, 618 K and 649 K for the hemicellulose, the cellulose and the lignin reaction regions respectively. Subsequently, the $T_{i,p}$ values of each component at the three heating rates are identified and summarised in Table 3-3.

Table 3-3: $T_{i,P}$ for each component at different heating rates.

Components	5 K/min	20 K/min	60 K/min
Hemicellulose	560 K	580 K	600K
Cellulose	618 K	636 K	685 K
Lignin	649 K	659 K	706 K

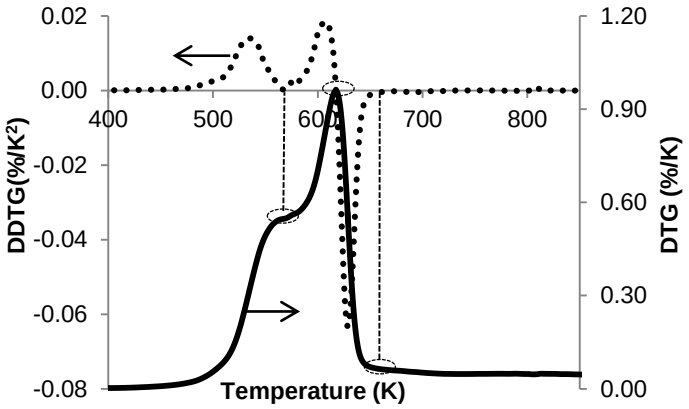

Figure 3-13: Curves DDTG & DTG at 5 K/min.

The linear relationships of $\ln(\beta/{T_{i,P}}^2)$ and $1/T_{i,P}$ for the three components are plotted in Figure 3-14. Accordingly, the E_i and A_i for each component are calculated from the slope and the intercept of each line based on Equation 3.4. All the results are listed in Table 3-4.

Table 3-4: E_i and A_i for each component.

Components	E_i (J/mol)	A_i (s^{-1})
Hemicellulose	1.64×10^5	1.09×10^{13}
Cellulose	1.98×10^5	3.23×10^{14}
Lignin	1.52×10^5	5.52×10^9

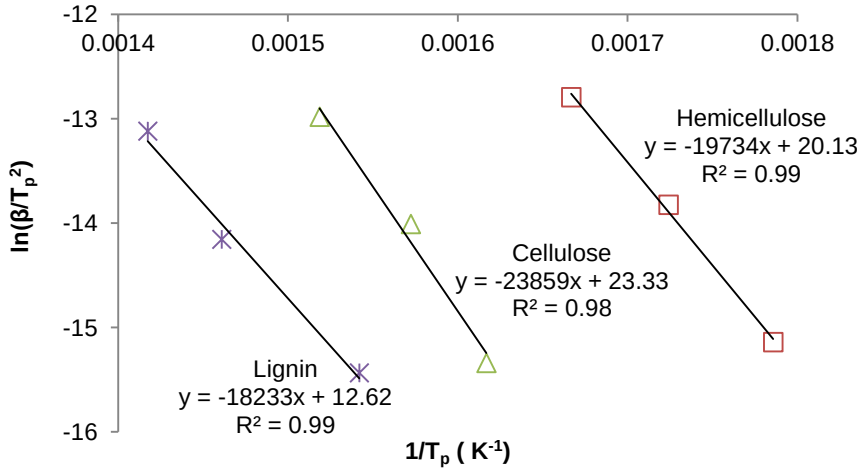

Figure 3-14: $\ln(\beta/{T_{i,P}}^2)$ versus $1/T_{i,P}$ for each component of wood.

In order to search for the appropriate n_i and c_i for each component, 30% hemicellulose, 45% cellulose and 15% lignin [44, 45] are considered as the initial c_i values for the components. A moisture content of 10 % is assumed in this study based on the average measured moisture

content in the wood samples at an ambient environment. The initial value of n_i is set to be one. The values of v_{si} is ~13% for the wood sample, which is determined by the stable remaining mass fraction results from TG experiments.

The 5 K/min data is used to demonstrate the searching process for the values of n_i and c_i to fit the experimental curve. Figure 3-15 illustrates the comparison of the initial model curves to the experimental curve.

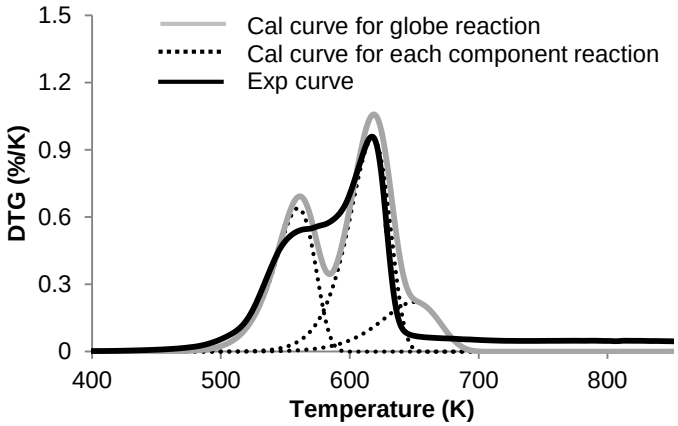

Figure 3-15: Experimental curve and initial model outputs at 5 K/min.

As the discussion on the sensitivity analysis of n_i and c_i in Figure 3-10, a flat curve with a low peak value can be achieved by increasing n_i and decreasing c_i, while the decrease of n_i and the increase of c_i can result a high peak and sharp curve. In Figure 3-15, the reaction curves of all of the components need to be flattened and the magnitude of reactions needs to be adjusted. Therefore, the n value of hemicellulose is increased from 1 to 2.1 to flatten the initial curve and the c value is also increased from 0.3 to 0.37 for a better fit to the experimental data. The value of n and c for cellulose are changed from 1 to 1.1 and from 0.45 to 0.44, respectively. Similarly, the final values of n and c for the lignin component are adjusted to be 5 and 0.09. All the results are summarized in Table 3-5.

Table 3-5: The values of n_i and c_i for each component of wood.

Item	Hemicellulose	Cellulose	Lignin
	Initial Final	Initial Final	Initial Final
n_i	1.0 → 2.1	1.0 → 1.1	1.0 → 5.0
c_i	0.3 → 0.37	0.45 → 0.44	0.15 → 0.09

The model curves based on the final inputs are plotted in Figure 3-16, which illustrates a more comparable result to the experimental curve than the initial result in Figure 3-15.

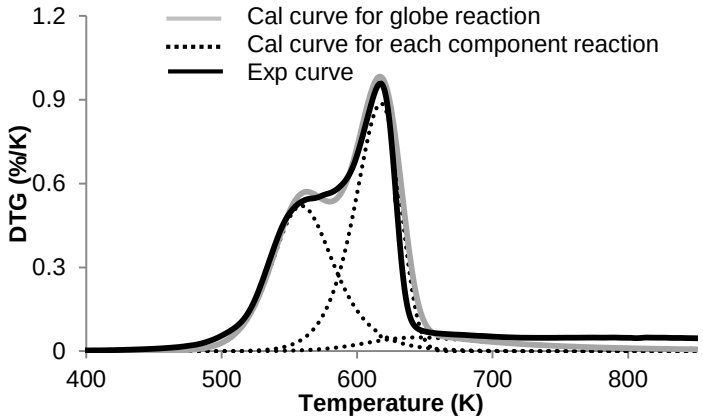

Figure 3-16: Experimental curve and final model outputs at 5 K/min.

The model curves at 20 K/min and 60 K/min are calculated based on the inputs from the analysis at 5 K/min. The comparison of the model curves and the experimental curves at the three heating rates are depicted in Figure 3-17.

Overall, the curves obtained from the hand calculation method can effectively present the features of wood decomposition. The model curves give very good fits with the experimental curves at the hemicellulose and the cellulose regions, while results for the reaction of lignin region are slightly higher than the experimental results.

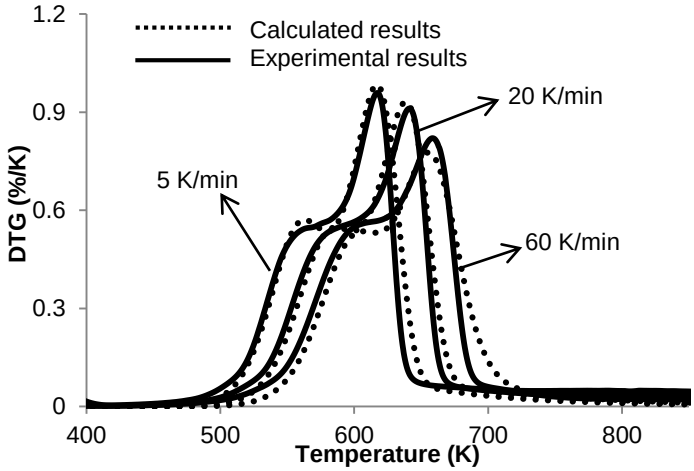

Figure 3-17: Comparison of experimental curve and final model outputs.

3.4.2.3 FDS6 Simulations Based on the Kinetic Properties

In order to verify the suitability of these parameters derived from the hand calculation method, the pyrolysis model in FDS6 is applied to simulate the plastic and wood TG experiments based on the kinetic parameters obtained from the hand calculation method.

In these FDS6 simulations, a solid material is assumed to be a single layer and the layer consists of different components[16]. When the reaction of a component produces a residue, the decomposition rate for a component is defined as [16] :

$$-\frac{dY_i}{dt} = (1-v_{si})A_{i,FDS}\exp\left(-\frac{E_i}{RT}\right)\left(Y_{i,FDS}\right)^{n_i} \tag{3.5}$$

where $Y_{i,FDS} = m_i/m_0$, and this is different from the definition of Y_i in Equation 3.2. When more than one component is assumed in the material, the value of $Y_{i,FDS}$ in Equation 3.5 does not start from one. In order to have consistent mathematical meaning in Equations 3.2 and 3.5, the difference between them can be attributed to the pre-exponential factor, which is written as:

$$A_{i,FDS} = A_{i,CAL}\left(\frac{m_{i0}}{m_0}\right)^{1-n_i} = A_{i,CAL}(c_i)^{1-n_i} \tag{3.6}$$

The corrections to the pre-exponential factors for each component of wood and plastic are listed in Table 3-6:

Table 3-6: Corrections to the pre-exponential factors.

Material and components		$A_{i,FDS}$ (original) $\longrightarrow$ $A_{i,CAL}$(corrected)
Wood	Hemicellulose	$1.09\times10^{13} \longrightarrow 3.25\times10^{13}$
	cellulose	$3.23\times10^{14} \longrightarrow 3.51\times10^{14}$
	Lignin	$5.52\times10^{9} \longrightarrow 8.41\times10^{13}$
Plastic	P1	$1.04\times10^{17} \longrightarrow 8.48\times10^{20}$
	P2	$7.99\times10^{14} \longrightarrow 7.99\times10^{14}$

Figure 3-18 is an example (wood at 5 K/min) using derived kinetic parameters from the hand calculation method but with the different pre-exponential values listed in Table 3-6 as inputs to an FDS6 simulation to demonstrate the significant difference and the importance of distinguishing between the definitions of mass conversion fractions in different kinetic models. The curve denoted as ‘original parameters’ is the result of using the parameters derived from the hand calculation method without corrections for pre-exponential factor, which suits for the kinetic model in Equation 3.2. The curve of ‘corrected parameters’ is the results with using the corrected pre-exponential factor values, which suits for the kinetic model in Equation 3.5.

Therefore, in the simulations in FDS6, the corrected pre-exponential factor of each component based on Equation 3.6 must be applied.

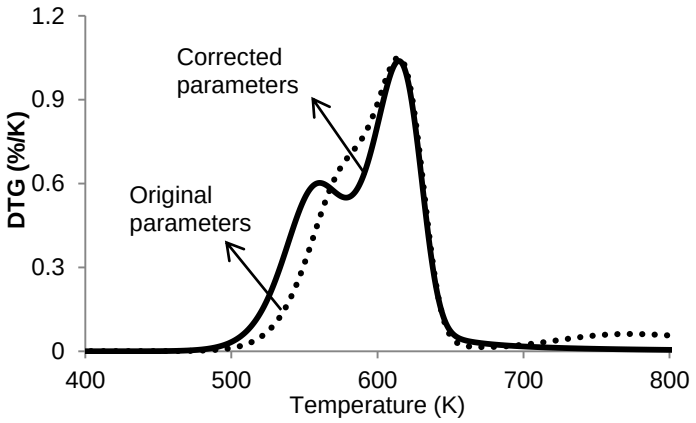

Figure 3-18: FDS6 results with and without corrections for wood at 5 K/min.

The TG experiments are under a nitrogen environment, which means no oxidation reaction is involved. Therefore, the gas phase calculations need to be turned off by setting the solid phase only [16] in the simulations for all the experiments in FDS6. A much larger domain than the actual size of the crucible is set up in each simulation, which has been found to give a much more stable numerical solution when the solid phase computation only is involved [19]. The sample is mimicked by the use of a very thin solid surface with an insulated back boundary. The gas temperature in simulations is set to increase from 293 K to 1093 K at a rate of 5, 20 and 60 K/min. The outputs from the simulations are recorded in the form of a normalised mass loss rate and are all converted to consistent units for the purpose of comparison. In the simulations, two components are applied to represent for plastic samples and three components are used for wood samples.

The final comparisons for the FDS simulation results and experimental results at the three different heating rates, for plastic and for wood, are illustrated in Figure 3-19 and Figure 3-20, respectively. Curves FDS6 (Hand calculation) represent the FDS6 simulations based on the parameter obtained from the hand calculation method (corrected).

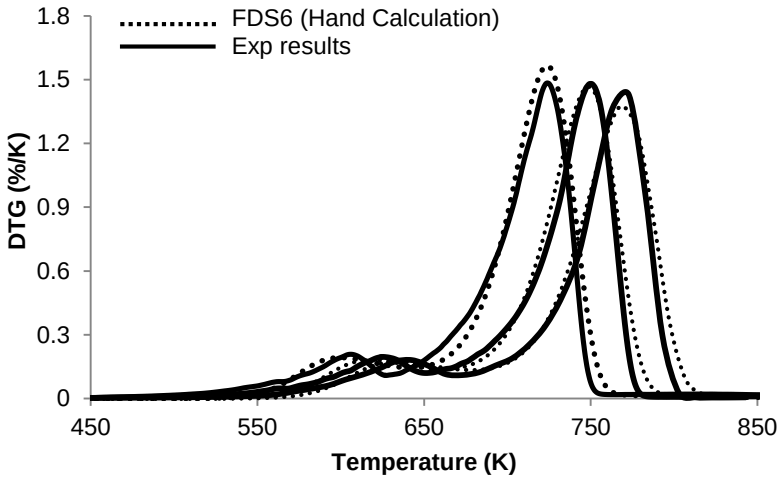

Figure 3-19: FDS6 simulation results and experimental results for plastic.

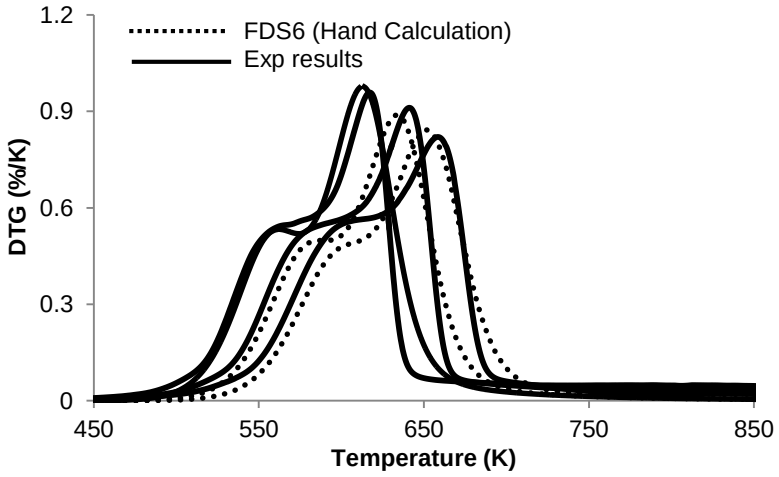

Figure 3-20: FDS6 simulation results and experimental results for wood.

The results for plastic and wood TG experiment predictions in FDS6 based on the hand calculation method can effectively match the experimental results. This suggests that the kinetic parameters derived from the hand calculation method are sufficient to represent the thermal decomposition features of plastic and wood in FDS6 and this method can give reliable kinetic parameters of different materials for the further applications in FDS6.

3.5 Heat of Reaction

In FDS6, the amount of energy consumed in solid phase pyrolysis reactions is specified as heat of reaction [16]. DSC is a technique which has been widely used to determine the heat of reaction by measuring the energy differences between a crucible containing a sample of the material and an empty reference crucible during the decomposition of the sample. The measured data from DSC experiments are represented by heat flow in mW.

3.5.1 Determining Heat of Reaction for Plastic Samples

The results of heat flow from DSC are commonly affected by the heating rates, the sample itself, and the measuring equipment [46, 47]. A baseline correction to the raw DSC data is a common approach to mitigate the effects during the measurement [20].

Pau [20] suggested an approximation method to obtain the corresponding baseline for materials without sufficient information of the governing correlations of the heat capacity. Because of the lack of information about the plastic compositions, the heat of capacity correlations are not available for the plastic sample, the approximate baseline method proposed by Pau is adopted to analyse the DSC heat flow data.

The simultaneously recorded heat flow data at 5 K/min for the recycled plastic samples from the SDT experiments are used for analysis. The weight of the samples (10 mg) and the heating rate of 5 K/min are within the recommended practice range for DSC experiments in [48]. The original heat flow data from the three repetition experiments are plotted in Figure 3-21.

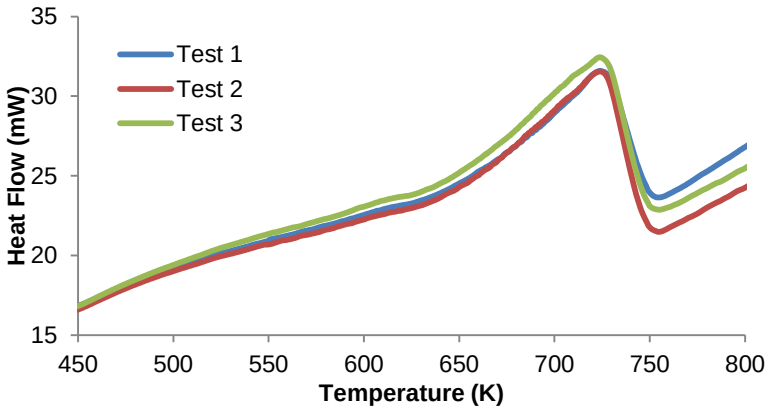

Figure 3-21: DSC heat flow data for plastic sample.

Since the interest of this analysis is to obtain the heat of reaction for decomposition reactions, only the heat flow data within the decomposition temperature range are used for the baseline reduction. The heat flow results from Test 1 are used as an example to demonstrate the data reduction. Figure 3-22 depicts the details of the data reduction procedure and the corresponding DTG curve is plotted to illustrate the decomposition reaction range.

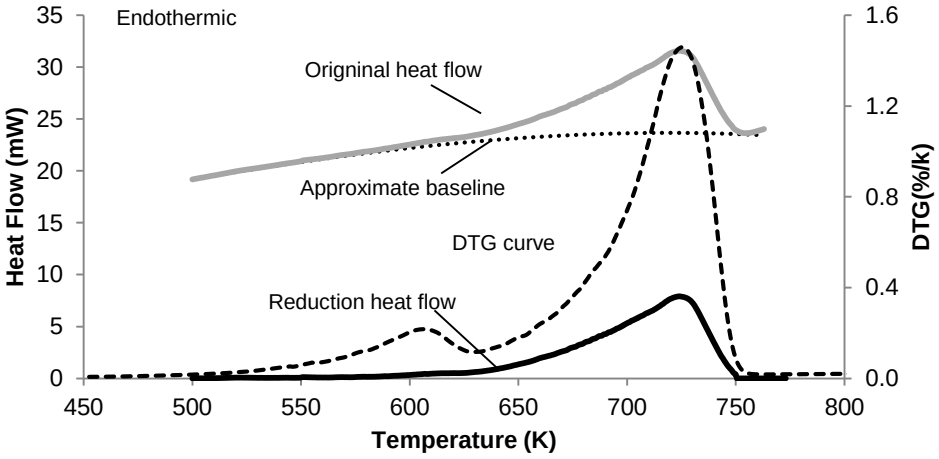

Figure 3-22: DSC data reduction for plastic sample.

As shown, the DTG curve indicates the decomposition of the sample starts from 500 K and ends at 750 K. The approximate baseline can therefore be developed according the observed heat flow trend over the non-decomposition regions. After removing the baseline influence, the reduction heat flow curve is obtained. The energy changes indicated on the curve is mainly located at the second decomposition temperature region, while the energy changes in the first reaction is almost negligible.

The heat of reaction (Δh_r) is mathematically defined as energy required for pyrolysis per unit mass of reactants [16], which can be written as:

$$\Delta h_r = \frac{1}{m_{rea}}\left(\int_{T_{start}}^{T_{end}} \left(\frac{dh_{vs}}{dT}\right) dT\right) * \frac{1}{dT/dt} \tag{3. 7}$$

where m_{rea} is the mass of reactants within the temperature range of a reaction and T_{start} and T_{end} denote the initial and the final temperature for the reaction. The term within the parentheses is determined by integrating the heat flow curve within the reaction temperature range and the last term dT/dt is the heating rate (5 K/min). Based on Equation 3.7, the heat of reaction for the decomposition of the plastic sample in Test 1 is 670 J/g. The same procedures are applied to heat flow data from Test 2 and Test 3 to derive the heat of reaction value. The values are 740 J/g for Test 2 and 875 J/g for Test 3.

3.5.2 Determining Heat of Reaction for Wood Samples

This part of work is reproduced from a published conference paper in 'International Fire Safety Symposium, 2015':

As discussed earlier, DSC technique can determine the heat of reaction by measuring the energy differences between two crucibles used in the experiments. Rath et al. highlighted that there is significant influence of using lids on heats of reaction for wood samples [49]. However, there is no specific guidance on whether the crucibles in experiments involving the decomposition of wood should be closed with lids or open without lids.

Based on the results from Rath et al's experimental results, different DSC results for wood were obtained from the experiments with and without lids. It was considered that the differences in emissivity between the formed char and the reference crucible caused an extra radiation effect in the experiments without lids [49]. However, by taking out the radiation effect, the results for the heat of reaction for the experiments without lids were still inconsistent with the results with lids. It is questionable whether the formed char only affects the scenarios without lids, whether the radiation is the only factor causing the difference in the results, and whether the difference will cause significant influence on the application of the DSC results in other analyses. In this section, a further investigation is conducted on the influence of using and without using lids in the DSC experiments for determining the heat of reaction.

3.5.3 Method for Analysing Heat of Reaction for wood sample

The DSC technique involves the measurement of the difference in heat flow rate dq_s/dt between a sample crucible and an empty reference crucible while they are heated at a constant rate within a controlled environment [50], where a nitrogen environment is used in this study. During the decomposition of virgin wood in nitrogen, it is expected that the sample generates gaseous products, a remaining solid product and that a residue is leftover at the end of the process. When thermal lag is negligible, the heat flow is [50]:

$$\frac{dq_s}{dt} = \frac{dh_s}{dt} + (C_{ss} + C_{sc} - C_{rc})\frac{dT}{dt} \tag{3.8}$$

where dh_s/dt is the kinetic heat flow rate produced by transformations and reactions of the sample; C_{ss} and C_{sc} denote the heat capacity of the sample and the heat capacity of the crucible on the sample side, while C_{rc} denotes the heat capacity for the crucible on the reference side, and dT/dt is the heating rate. In order to calculate the heat of reaction for a wood based on dh_s/dt, three DSC runs are required to extract the kinetic heat flow from dq_s/dt, which are: an empty crucible run, a virgin sample run and a residue run. These runs are used to assess the influence of the empty crucible on the heat flow rate, to exclude the

heat capacity of the virgin sample and to examine the heat flow rate of the residue respectively. According to Equation 3.8, the measured total heat flow rate for an empty crucible run is:

$$\frac{dq_b}{dt} = (C_{sc} - C_{rc})\frac{dT}{dt} \tag{3.9}$$

When using Equation 3.8 to subtract Equation 3.9, the heat flow rate without the thermal effect of the empty crucible is obtained such that:

$$\frac{dq_s}{dt} - \frac{dq_b}{dt} = \frac{dh_s}{dt} + C_{ss}\frac{dT}{dt} \tag{3.10}$$

In Equation 3.10, $\mathrm{C_{ss}}$ combines the heat capacity of the virgin sample ($\mathrm{m_{vs}(t)c_{p_{(vs)}}}$) and the heat capacity of the solid product ($\mathrm{m_{sp}(t)c_{p_{(sp)}}}$) generated during the decomposition. Similarly, $\mathrm{dh_s/dt}$ also consists of the kinetic heat flow rate for the virgin sample ($\mathrm{dh_{vs}/dt}$) and for the solid product (dh_{sp}/dt). Therefore, Equation 3.10 can be expanded as:

$$\frac{dq_s}{dt} - \frac{dq_b}{dt} = \frac{dh_{vs}}{dt} + (m_{vs}(t)c_{p_{(vs)}})\frac{dT}{dt} + \frac{dh_{sp}}{dt} + (m_{sp}(t)c_{p_{(sp)}})\frac{dT}{dt} \tag{3.11}$$

where $c_{p_{(vs)}}$ and $c_{p_{(sp)}}$ refer to the specific heat of the virgin sample and solid product; $m_{vs}(t)$ and $m_{sp}(t)$ are the mass for the virgin sample and solid product at time t. The term $dh_{sp}/dt + (m_{sp}(t)c_{p_{(sp)}})dT/dt$ represents the heat flow rate for the solid product generated during the run. The exact value of this term can be obtained through an extra run for the residue remaining from the sample run, the heat flow rate for this extra run without the thermal effect of the crucible is expressed as:

$$\frac{dq_{re}}{dt} - \frac{dq_b}{dt} = \frac{dh_{re}}{dt} + (m_{re}c_{p(re)})\frac{dT}{dt} \tag{3.12}$$

where dq_{re}/dt denotes the measured heat flow rate for the residue; dh_{re}/dt and m_{re} refer to the kinetic heat flow rate and the mass for the remaining residue. When the dimensionless product conversion fraction α is defined the relationship between the heat flow rate of the solid product in the sample run and Equation 3.12 can be written as: $\alpha(dq_{re}/dt - dq_b/dt) \approx dh_{sp}/dt + (m_{sp}(t)c_{p(sp)})dT/dt$. Therefore, the kinetic heat flow rate of the virgin sample based on the three experiments can be written as Equation 3.13, where a positive value is for an endothermic reaction and a negative value is for an exothermic reaction.

$$dh_{vs} / dt = (dq_s / dt - dq_b / dt) - \alpha(dq_{re} / dt - dq_b / dt) - m_{vs}(t)c_{P(vs)} dT / dt \quad (3.13)$$

3.5.4 Experimental Procedure

The same equipment SDT Q600 thermal analyser was employed for the experiments. Two series of experiments using two 90 *μL* aluminium crucibles (~5 mm in diameter), with and without lids, were carried out. Figure 3-23 shows a crucible and a lid for the experiments.

Figure 3-23: Crucible and lid for DSC experiments

To ensure the repeatability of all experimental data, three sets of experiments under identical conditions were conducted for the series with lids, and the series without lids. All experiments were conducted at a heating rate of 5 K/min in a pure nitrogen environment by flowing nitrogen gas at 100 ml/min into the furnace. Fine fragment wood samples were evenly placed within the crucible and the mass of the samples in each experiment were controlled at ~10 mg. Each run started from ambient temperature heating up to 873 K. The furnace was cooled down to ambient temperature in a nitrogen gas environment at the end of each run to prevent any residue remaining in the crucibles being oxidised.

3.5.5 Results of TGA-DSC

The DTG curves and the mass loss curves are shown in Figure 3-24 (a) and Figure 3-24 (b) for runs with and without lids. As shown in Figure 3-24 (a), three major reaction regions can be identified for both scenarios: the hemicellulose reaction region, from the initial increase of decomposition rate (~400 K) to the shoulder part (~575 K); the cellulose reaction region, which is mainly for the range of the peak of the curve and the lignin reaction region, from the sharp decay in the rate after the peak (~640 K) to the wide long tail part (~850 K) [5]. However, the decomposition rates behave slightly differently based on the DTG curves for the two scenarios. Figure 3-24 (b) also shows that less residue remains when the lids are not used. The

differences in the two figures are possibly due to the different heat exchange mechanisms caused by the presence and absence of lids.

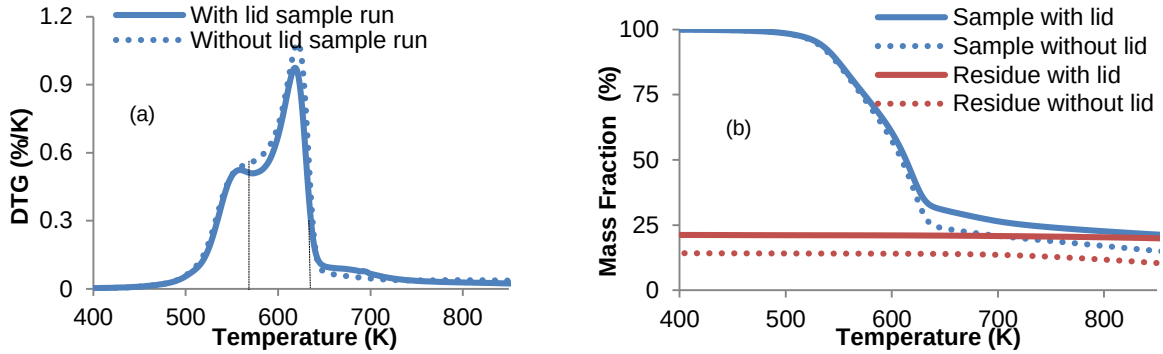

Figure 3-24: TG curves: (a) DTG curves for wood; (b) Mass loss curves for wood and residues.

Figure 3-25 (a) and Figure 3-25 (b) illustrate the heat flow rates for the empty crucible, sample and residue runs with and without lids. The heat flow rate curves recorded from the empty crucible runs determine the baselines for the sample and residue runs, as explained in Equation 3.10 and Equation 3.12. The results from the heat flow rate from the residue runs and from the empty crucible runs almost overlap between 400 K and 600 K, indicating the heat flow rate generated from the residue is negligible within this range.

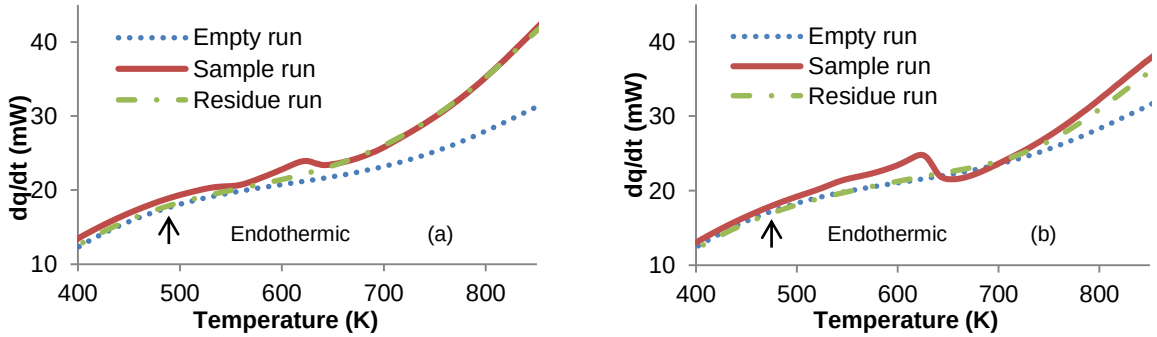

Figure 3-25: DSC experimental curves: (a) with lids; (b) without lids.

However, at the high temperature range, i.e. above ~720 K, the heat flow rate curve for the residue run overlays the sample run when lids are used (Figure 3-25 (a)). This means the heat flow rate for the sample run, recorded at high temperatures, is mainly determined by the heat capacity of the residue. For the scenario without lids, the heat flow rate curve for the residue run is slightly lower than the curve for the sample run at the high temperature range, which suggests further reactions or transformations may have occurred during the residue run. The reduction in mass from ~ 720 K onwards for the residue run without lids (Figure 3-24 (b)) also reflects the residues have possibly undergone reactions at this high

temperature range. However, the formed residue is not expected to have any further decomposition in a pure nitrogen environment. Therefore, it is reasonable to assume that samples are fully decomposed during the sample run in this study. Based on this, the heat flow rate curve for the sample run in Figure 3-25 (b) is manually shifted to overlap heat flow rate curve for the residue run at a temperature of ~720 K onwards.

3.5.6 Heat Flow Rate for Virgin Samples

Equation 3.13 is applied to extract the kinetic heat flow rate for the decomposition of virgin wood, where an equation for the specific heat of dry wood is used to determine the heat capacity of the virgin sample: $c_{p(vs)} = 3.867(T + 273) + 103$ [51] and the $m_{vs}(t)$ is defined as: $(1 - \alpha)m_0$. Figures 3-26 (a) and 3-26 (b) show the kinetic heat flow rate of the virgin sample for runs with and without lids along with the corresponding DTG curves for a better interpretation of the thermal decomposition process.

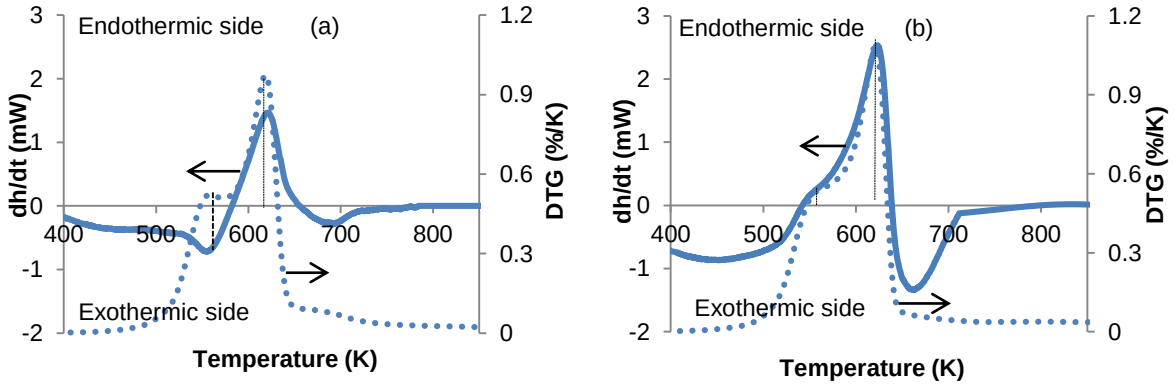

Figure 3-26: Heat flow rate & DTG curves for wood: (a) with lids; (b) without lids.

There is no obvious change of decomposition rate on DTG curves at the temperature range from 400 K to 450 K, suggesting no apparent gas or solid product is generated. However, exothermic behaviour is indicated on the heat flow rate curves in both lid scenarios at this temperature range, which suggests exothermic reactions have still occurred without obviously changing the mass of the samples.

In the scenario with lids (Figure 3-26 (a)), concave upward and downward peaks (at ~ 555 K and 620 K, respectively) on the heat flow curve correspond to the regions for hemicellulose and cellulose, suggesting hemicellulose decomposes exothermically, while the decomposition of cellulose is endothermic. However, in the scenario without lids (Figure 3-26 (b)), there is no clear concave upward peak in the region dominated by hemicellulose, while a pronounced concave downward peak can still be found on the heat flow rate curve for the

cellulose region. This illustrates that the decomposition of cellulose is still dominated by an endothermic reaction even though no lid is present. However, it is difficult to conclude that the reaction in the hemicellulose region still behaves exothermically in this scenario. Rath et al. [49] also observed similar reaction behaviours in their DSC experiments.

The possible reason for the differences in these two scenarios could be attributed to the different decomposition mechanisms occurring during the reactions. As explained in the literature [44], there are two competitive reactions during wood decomposition: the exothermic charring reaction and the endothermic volatile reaction. Hence, in the hemicellulose and cellulose reaction regions, when no lid is used, the generated volatiles are efficiently diffused into the nitrogen environment and heat is efficiently exchanged with the heated environment. Due to the supplement of heat from the environment, the reaction is then pushed toward the endothermic volatilisations which have an opposite cooling effect to balance the heat gained from the environment. Therefore the global heat flow behaviour moves extensively toward the endothermic side, as indicated in Figure 3-26 (b). On the contrary, the presence of a lid keeps the generated volatiles within the crucible which may slow down the reaction rate due to the cooling effect from volatile reactions: this results in the decomposition moving toward the charring reaction which is an exothermic reaction generating more heat to compensate for the loss of heat due to the cooling effect.

The third concave peak (at ~ 680 K) followed by a noticeable rising trend shown on the heat flow curve in Figure 3-26 (a) corresponds to the lignin decomposition region. A similar correspondence is also found in Figure 3-26 (b) at ~ 650 K. The upward concave curve on the exothermic side in these scenarios indicates the decomposition of lignin is dominated by an exothermic charring reaction. When lids are used, the heat generated from the charring reaction is kept within the crucible, which speeds up the decomposition rate and the overall reaction gradually moves toward the volatile reaction side to balance the heat. However, when no lid is used, the generated heat from the charring reaction is efficiently diffused into the nitrogen environment, thus less heat remains within the crucible compared with the scenario leaving lids on. Therefore, for the case without the use of lids, the charring reaction still dominates the overall reaction until sufficient heat is gained from the heated nitrogen environment to accelerate the volatile reaction. Therefore, a much larger concave upward curve is obtained on the exothermic side in Figure 3-26 (a) than in Figure 3-26 (b).

3.5.7 Calculation of Heat of Reaction

The mathematical form for heat of reaction (Δh_r) is written in Equation 3.7. In order to estimate the mass of reactants from each reaction region, heat flow curves and the corresponding mass curves for runs with and without lids are plotted in Figure 3-27 (a) and Figure 3-27 (b).

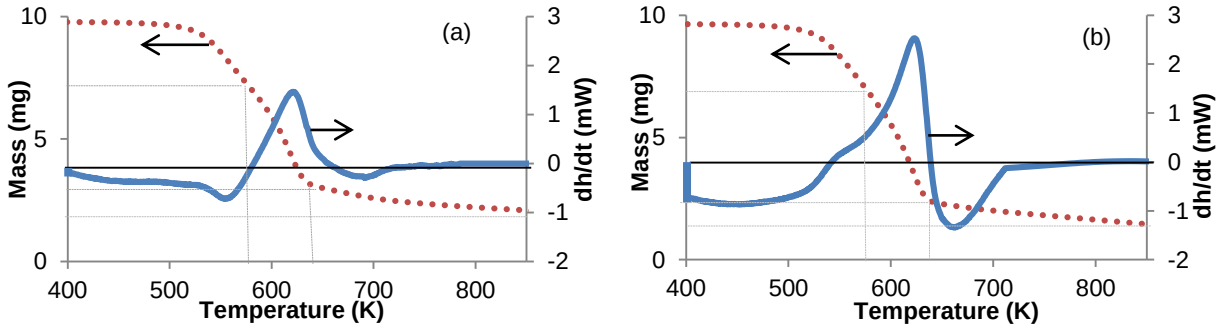

Figure 3-27: Derivation of heat of reaction for wood: (a) with lids; (b) without lids.

The changes in mass for reactants within each reaction region and the final heat of reaction results for the cases in Figure 3-27 (a) and 3-27 (b) are listed in Table 3-7 as L1 and NL1. In addition, the heats of reaction for other sets of experiments are calculated and listed in Table 3-7, where $\Delta h_{r,h}$,$\Delta h_{r,ce}$, and $\Delta h_{r,l}$ are the heat of reaction for the reaction regions of hemicellulose, cellulose and lignin.

Table 3-7: Results for heat of reaction.

Items		Hemicellulose region			Cellulose region			Lignin region		
		$\int(\frac{dh_{vs}}{dT})dT$ (mW·K)	m_r (mg)	$\Delta h_{r,h}$ (J/g)	$\int(\frac{dh_{vs}}{dT})dT$ (mW·K)	m_r (mg)	$\Delta h_{r,ce}$ (J/g)	$\int(\frac{dh_{vs}}{dT})dT$ (mW·K)	m_r mg)	$\Delta h_{r,l}$ (J/g)
With lids	L1	-72	3.24	-273	49	5.27	111	-12	1.30	-114
	L2	-65	3.47	-223	33	5.88	68	-56	1.48	-456
	L3	-104	3.08	-405	48	5.13	113	-21	1.26	-199
With-out lids	NL1	-93	3.05	-366	92	5.43	204	-69	1.09	-759
	NL2	-110	3.17	-418	61	5.52	133	-92	1.09	-1017
	NL3	-117	3.22	-438	54	5.32	122	-79	1.15	-828

The calculated results clarify the decomposition of cellulose is endothermic and the decomposition for hemicellulose and lignin is exothermic in both lid scenarios. These findings agree with the analysis of Yang et al. [52]. However, the differences in results are significant from experiment to experiment, which are possibly due to the experimental variability. Nevertheless, the values still quantitatively indicate some general phenomena: more energy is absorbed or generated in each decomposition region in the absence of lids than in the presence of lids. This is due to the improved heat exchange with the environment in the absence of lids pushes reactions toward the side of endothermic or exothermic reaction to balance the heat in the decomposition.

From a practical point of view, it is worth observing whether the differences in heats of reaction obtained for the different lid scenarios will cause significant differences in HRR prediction through FDS6, where heat of reaction is used to describe energy changes caused by chemical reactions in the heat transfer equation.

A cone calorimeter experiment at 35 kW/m^2 incident heat flux is simulated in FDS6 based on different heat of reaction inputs from Table 3-7, while all other parameters are kept the same. The cone calorimeter experimental data comes from experiments on the same wood material that has been used in the LTA tunnel testing programme previously mentioned (More details regarding the cone calorimeter experiments and simulations are introduced in Chapter 4). The comparisons of predicted HRR curves with the experimental curve are shown in Figure 3-28 (a) and Figure 3-28 (b). In this section, the experimental data is used for a reference comparison to demonstrate the differences in HRR predictions by using the two sets different values of heat of reaction.

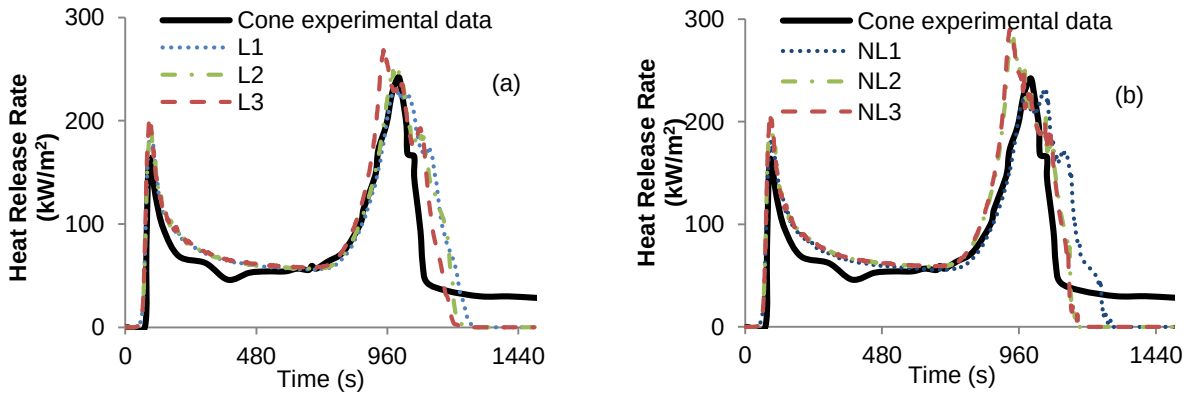

Figure 3-28: HRR using Δh_r: (a) with lid; (b) without lid.

The predicted HRR curves in the scenarios with lids fit to the experimental data slightly better than the scenario without lid, which indicates the differences of heat of reaction caused by the absence and presence of lids only have a weak effect on the prediction of HRR. Mathematically the contribution of the energy from the chemical reactions to the overall heat transfer is minor compared to the energy gained from front surface based on the equation of heat transfer in FDS6. Therefore the quantitative differences in the heat of reaction in this study, due to equipment uncertainties or experimental conditions, are still within an acceptable range and do not significantly affect the heat release rate predictions in FDS6.

3.6 Conclusion

In this chapter, a simple hand calculation method is proposed to estimate the kinetic properties from a series of TG experiments for wood and plastic materials. According to the applications, it is found the method to estimate the kinetic properties is suitable for a decomposition consisting of several separated reactions (such as the decomposition for the recycled plastic samples in this chapter) and a decomposition having several overlapped reactions (such as the decomposition for the wood samples). This work also highlights the different definitions of normalised mass for each component between the proposed method and FDS6 which will result in a difference in the values for the kinetic properties. The favourable comparison to the experimental data for the TG simulations in FDS6 demonstrates the accuracy of the hand calculation method to determine kinetic properties.

In the analysis of heat of reaction for the plastic samples, an approximate baseline method is adopted to correct the measured DSC heat flow data. It is found that the change in energy is negligible for the first plastic decomposition reaction and the heat of reaction for the second plastic decomposition reaction is ~ 670 to 875 J/g.

In the study of heat of reaction for the wood samples, an analytical method is applied to investigate the influence of using lids in DSC experiments. The experiments with lids and without lids result in different heat exchange dynamics which lead to differences in the absorption and release of energy during the decomposition of wood. The values of heats of reaction obtained with and without lids differ from experiment to experiment. However, these values still quantitatively indicate more energy is gained and released in the scenario without lids than with lids and these values also have a qualitative consistency in revealing the endothermic and exothermic reaction behaviour in the decomposition process. The predictions of HRR for cone calorimeter simulations in FDS6 are only slightly affected by the differences of heat of reaction in the experimental methods, suggesting the variations of the heat of

reaction in this study are within an acceptable range in the application of the pyrolysis model in FDS6.

Chapter 4 Parameterising Study of Tunnel Experiment Materials for Application to the FDS Pyrolysis Model

This chapter is reproduced according to the published paper titled ‘Parameterising study of tunnel experiment materials for application to the FDS pyrolysis model’ in Journal of Fire Sciences.

The information regarding the details of hand calculation to derive kinetic properties is not included in this chapter since extensive analyses of the method have been introduced in Chapter 3.

4.1 Introduction

As introduced in the previous chapters, the modelling of tunnel fires in FDS can often rely on specifying the energy release rate on the basis of experimental fires or standard growth fire curves. However, different tunnel conditions can have a significant influence on the energy release rate of a fire in a tunnel, such as tunnel geometry, ventilation conditions, etc. [53]. These influences may not be modelled through the application of prescribed fire growth methods. It has been said that this research aims to apply the new approach of using the pyrolysis model in FDS6 to predict HRR for the LTA tunnel fire experiment. In order to apply the pyrolysis model to predict HRR, the kinetic parameters, heat of reaction, thermal properties and heat of combustion of the fuel are required to describe the decomposition and the heat transfer in solid fires [16]. Hence, an important step prior to carrying out the simulation of the large-scale tunnel experiment is to investigate the fuel properties, where plastic and wood were used to make pallets representing an HGV.

In this work, the pyrolysis model in FDS6 is applied to simulate the decomposition and burning behaviour of the recycled plastic and wood samples obtained from the LTA large-scale experiment. Although samples of the materials used to construct the pallets are used in this study, detailed information on the plastic is not available and the species of wood is unknown. As such this work illustrates a practical application of the modelling approach where in many real-world situations the exact materials that are likely to burn are not known and only a general assessment can be made.

Since the decomposition of a solid material is described by an Arrhenius equation in FDS6, the kinetic properties (activation energy, pre-exponential factor and reaction order) are the key parameters to describe the decomposition reaction of a fire. However, it is a challenge to define them due to the unknown number of reactions in the decomposition of a solid fire. In order to simplify the complex decomposition, one-component and multi-component decomposition schemes have been used to analyse kinetic properties for solid materials, which have been introduced by Di Blasi [44].

The one-component scheme regards a solid material as a single component undergoing a single reaction to generate products. The multiple-component scheme assumes that a solid material is composed of several components and each component undergoes a single independent reaction to generate products. The overall reaction rate is the summation of the reaction rate of each component. In the study of Li et al. [35] an optimised searching method was proposed which combines the Kissinger's method with genetic algorithm (GA) to analyse

kinetic properties. In their study, four components (resin, hemicellulose, cellulose and lignin) were used to represent the decomposition of medium density fireboard (MDF). This method has an advantage in analysing the complex decomposition process of solid materials. In Chapter 3, a simple hand calculation method has been developed to derive kinetic properties for a more practical engineering application. The same two materials are investigated using a three component scheme to represent the wood and a two component scheme to represent the recycled plastic in this chapter.

In this chapter, both one-component and multi-component schemes are used to describe the decomposition behaviour for the plastic and wood materials used in the large-scale tunnel experiments. The hand calculation method and the GA searching method are adopted for the analysis of the kinetic properties, which are defined as a GA one-component scheme, a GA multi-component scheme and a hand calculation multi-component scheme.

In addition to kinetic properties, another major part in the use of the pyrolysis model is to obtain the properties which are for the heat transfer within solids. Stoliarov et al. [54, 55] demonstrated the experimental based methodology to parameterise both charring and non-charring of known polymer materials. Due to the limited information on the materials, the thermal properties of the wood and recycled plastic samples are determined from a series of manual optimisation studies.

In order to examine the ability of the pyrolysis model to predict the decomposition and burning behaviour of the materials, simulations of TG and laboratory scale cone calorimeter experiments are conducted using the properties derived in this study. Some modelling work for both TG and cone experiments have been conducted for various materials in the literature [20, 56, 57]. The specific aim in this study is to get sufficiently representative kinetic and thermal properties of the wood and plastic materials to enable the simulation of the LTA full-scale experiment by:

1. Deriving the kinetic parameters from the TG experiments for the two materials by applying the three decomposition schemes: GA one-component, GA multi-component and hand calculation multi-component.
2. Characterising material properties through parametric sensitivity analyses.
3. Validating the FDS6 predictions of the burning behaviour based on the three decomposition schemes and the corresponding material properties.

A discussion regarding the use of different multiple-component schemes to predict the wood pyrolysis and burning behaviour is attached in Appendix A as this work is not directly relevant to the remainder of this thesis.

4.2 Materials and Methods

4.2.1 Experiments

The TG experimental results at three different constant heating rates of 5, 20 and 60 K/min introduced in Chapter 3 are adopted in the analysis in this Chapter directly.

The cone calorimeter experiments were performed on behalf of the LTA by a third party prior to the inception of this paper. In the experiments all but the top surface of the sample was covered with aluminium foil, and the sample was placed on thermal insulation blanket of unreported thermal properties. Four sets of incident heat flux of 25 kW/m^2, 35 kW/m^2, 50 kW/m^2 and 75 kW/m^2 were applied in the experiments and three repetitions were conducted for each incident heat flux. The dimensions of the plastic and wood samples used in the experiments were 100 mm × 100 mm × 3 mm thick and 100 mm × 100 mm × 21.5 mm thick, respectively.

4.2.2 Reaction Schemes and Kinetic Properties

Both hand calculation method and GA searching method are used to derive the kinetic properties.

Since the detailed derivation of the kinetic properties for the recycled plastic and wood samples based on the hand calculation method have been extensively discussed in Chapter 3, the results are directly adopted for further analysis in this chapter. The kinetic properties for the plastic and wood samples are listed in Table 4-1.

The GA searching method, which is a heuristic searching method based on Darwinian survival-of-the fittest theory [35], is used to seek the kinetic properties for plastic and wood samples based on the two and three components, respectively. The kinetic results from the GA method are built upon a large search space to seek the outputs which can produce the fittest curves to the experimental curves. The details of the GA-based methods can be found in [33, 35]. Due to the advantage in analysing a large amount of data, the GA searching method is also able to simplify the complex decomposition of the plastic and wood to a single component with a single reaction and to find the most suitable kinetic properties for the single component for

the plastic and wood, which are denoted by P-component and W-component respectively. The results of these kinetic properties from the GA method are also listed in Table 4-1. (The GA analysis was performed by Dr. Xinyan Huang at Imperial College, London under the supervision of Dr. Guillermo Rein. Dr. Xinyan Huang currently works as a postdoc at the University of California at Berkeley.)

Table 4-1: Kinetic parameters for different component schemes.

Materials		Components		E_i (J/mol)	A_i (s^{-1})	n_i	ρ_{i0}/ρ_0
Hand calculation method	Plastic	Two components	P1	2.22×10^5	8.48×10^{20}	7.5	0.25
			P2	2.39×10^5	7.99×10^{14}	1.0	0.75
	Wood	Three components	Hemicellulose	1.64×10^5	3.25×10^{13}	2.1	0.37
			Cellulose	1.98×10^5	3.51×10^{14}	1.1	0.44
			Lignin	1.52×10^5	8.41×10^{13}	5.0	0.09
GA searching method	Plastic	Two components	P1	1.47×10^5	1.12×10^{13}	5.6	0.29
			P2	2.37×10^5	5.51×10^{14}	0.8	0.71
		One component	P-component	2.01×10^5	1.68×10^{12}	0.92	1.00
	Wood	Three components	Hemicellulose	1.41×10^5	1.54×10^{11}	1.5	0.37
			Cellulose	1.87×10^5	3.36×10^{13}	0.9	0.40
			Lignin	1.19×10^5	2.14×10^{10}	4.4	0.13
		One component	W-component	1.23×10^5	5.80×10^8	2.2	0.90

Note: From TG experiments, the moisture content of wood was determined to be approximately 10%.

Although there are other reported kinetic property values for wood and plastic based on different component schemes, the literature values give limited comparable results to the findings in this work. This might be expected because of the differences in the material itself where the two materials in this work are those specifically used in the LTA large-scale tunnel fire experiment. In addition, variations in heating conditions and mathematical formulations are also likely to be factors. For instance, the kinetic properties reported by Anca-Couce et al. [58] for dry pine uses a different pyrolysis model than that in FDS6.

4.2.3 Heat Release Rate Calculation in FDS6

To model a fire, several other processes need to be included into the simulation and these are: the combustion of the generated gases, heat generated from the fire transferring back to the solid and the heat transfer within the solid which maintains the continuous generation of gases. In FDS6 the temperatures inside the solid are found using a one-dimensional heat conduction

equation to compute the solid phase temperature gradient at x depth, which is expressed as [16, 42]:

$$\rho_s c_{p,s} \frac{\partial T_s}{\partial t} = \frac{\partial}{\partial x}(k_s \frac{\partial T_s}{\partial x}) + \dot{q}'''_{s,r} + \dot{q}'''_{s,c} \tag{4.1}$$

In Equation 4.2 the term $\dot{q}'''_{s,r}$ is the radiation absorption in a solid, and $\dot{q}'''_{s,c}$ is the heat production (loss) rate within the chemical reactions, which is explained in Equation 4.2

$$\dot{q}'''_{s,c} = -\rho_0 \sum_i r_i(x) \Delta h_i \tag{4.2}$$

The temperature of the front surface of a solid is defined by a convective heat flux ($\dot{q}''_c$) and radiative flux ($\dot{q}''_r$) [42] where

$$-k_s \frac{\partial T_s}{\partial x}(0,t) = \dot{q}''_c + \dot{q}''_r \tag{4.3}$$

Equation 4.3 is also used for the back surface of the solid material in which it can be open to an ambient void or to another part of the computational domain. For a perfectly insulated back surface the term $-k_s \frac{\partial T_s}{\partial x}$ is defined as 0.

The heat release rate per unit area generated from the ignited combustible gases can be described from the mass flux and heat of combustion (ΔH_c) of the material by

$$\dot{q}'' = \dot{m}'' \Delta H_c = \Delta H_c \rho_0 \int_0^L \sum_i (1 - v_{s,i}) A_i (\frac{\rho_i}{\rho_0})^{n_i} \exp(\frac{-E_i}{RT(x)}) dx \tag{4.4}$$

Therefore, in order to calculate the heat transfer in a solid, and thus to simulate the solid phase reaction to predict HRR, the parameters required for the pyrolysis model in FDS6 are not only the kinetic properties of each component but also the properties to conduct heat and handle combustion (such as heat of reaction, thermal properties and heat of combustion) The selection of values for these properties is as important as the kinetic properties. However, a challenge in obtaining these properties is the lack of detailed information of the plastic and wood used in the LTA experiments. The method proposed in Matala's work [56] in which changing one property at a time to observe how the it affects the model behaviour to further

estimate the properties is applied here. Parameters that give the best fitting to the experimental curve are determined based on the influences from different properties on the model curves.

For the properties of the materials in this particular work some of them are obtained from the cone calorimeter experiments conducted on behalf of the LTA such as the density, heat of combustion and sample thickness; some of them can be analysed through experimental methods, such as the kinetic properties; while there are some properties which are unable to be obtained due to the limitations in carrying out experimental analyses. For the unavailable properties of the LTA materials, literature values for the corresponding representative materials (typical recycled plastics, such as PE, PP, PS, PET, PVC and etc. to represent the plastic samples and the general wood to represent the wood samples) are adopted to conduct cone calorimeter simulations at one incident heat flux. Based on the cone calorimeter simulation results, the suitability of the properties to represent the LTA samples are determined. Where the simulation results cannot represent the actual burning behaviour of the samples, the approximation procedure proposed by Matala [56] combining with the properties from the representative materials are adopted to conduct sensitivity studies and to seek appropriate properties for the simulations. The analysis procedure for the properties for the samples in this study is illustrated in Figure 4-1.

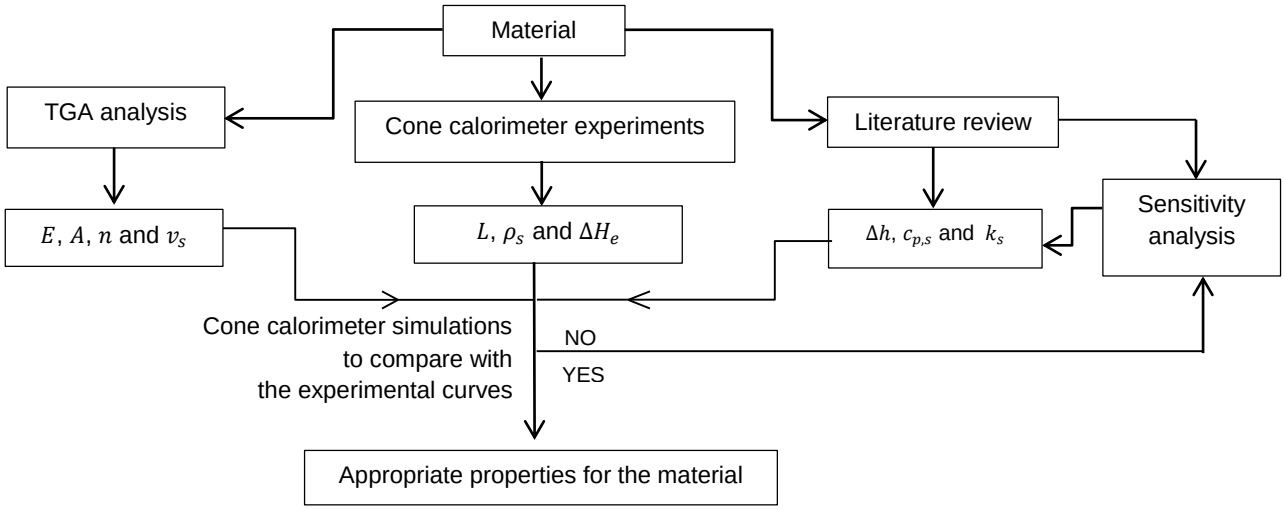

Figure 4-1: Flow chart for material property analysis procedure.

It is noted that the use of parametric sensitivity analyses to seek properties based on the concept of curve matching is not rigorous and the estimated properties may not in agree with literature values. However, this approach demonstrates a logical procedure to derive properties for materials in many real world situations where only general information on the burning materials is available. Some other approaches can also be adopted, such as the

methods in Stoliarov and Li [59], where a more sophisticated method is introduced to analyse the material properties.

4.3 Simulation Results and Discussion

4.3.1 TG Simulations in FDS6 for Plastic and Wood Samples

The simulation method for the TG experiments has been discussed in Chapter 3. In this section, simulations are carried out by applying the kinetic properties derived from different methods and different component schemes shown in Table 4-1. In the simulations for the TG experiments the changes in temperatures are strictly controlled by the set-up of a constant heating rate corresponding to the experiments. The heat transfer in solids is not included in the algorithms in the TG simulations and there is no effect from the combustion phase. Therefore, the TG simulation results can fully represent the prediction capability of the decomposition rates in FDS6. Figure 4-2 (a) and (b) are DTG results of plastic and wood at the decomposition ranges from 450 K to 850 K and from 400 K to 800 K, respectively. The TG simulation results at heating rates of 5, 20 and 60 K/min are presented in the figure based on the kinetic properties from the hand calculation and the GA method. Multiple component schemes and one component scheme (GA-1) for both materials are applied in the simulations. The experimental results at each heating rate are also plotted in the figure.

As shown in Figure 4-2 (a), two significant reaction peaks are indicated in the experimental decomposition curves of the plastic samples. The first reaction temperature range is from 575 K to 675 K and the temperature range for the second reaction is from 675 K to 800 K depending on different heating rates. According to the literature [60], the DTG curves for PE, PP, PS and PET only have one significant reaction and the DTG curve of PVC demonstrates two significant reactions. The temperatures for the decomposition reactions at 10 K/min are around 450 K to 750 K for PS, about 650 K to 850 K for PE, PS and PET, about 450 K to 650 K for the first major reaction of PVC and 650 K to 850 K for the second major reaction of PVC. The decomposition temperature range of the plastic sample is within the decomposition temperatures for these typical plastic materials. However, it is not possible to exclude other unknown additives in the plastic sample that contribute to the decomposition reactions. In terms of simulations, the FDS results using either the hand calculation or GA method two-component schemes can effectively describe the DTG curves at all three heating rates. The results of using the one-component scheme demonstrate the second reaction peak occurring at high temperatures during the decomposition, while the first reaction at low temperature range is not modelled.

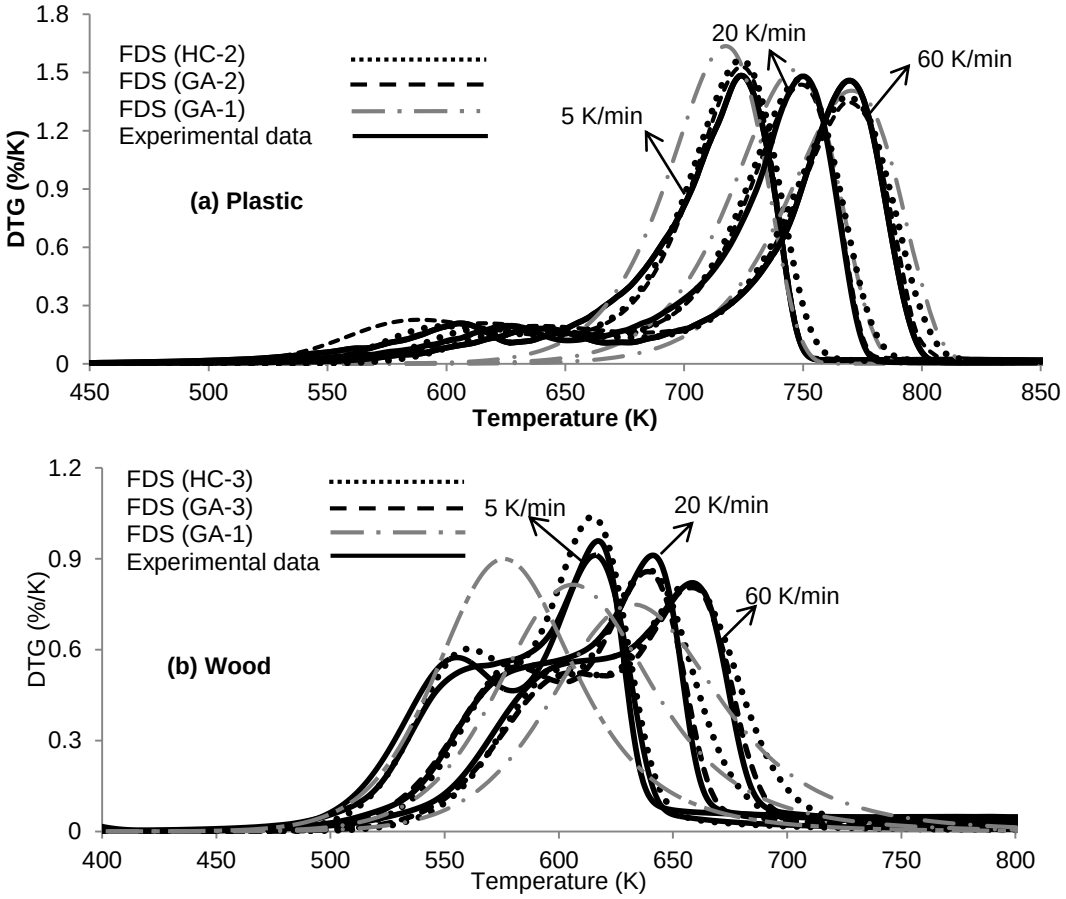

Figure 4-2: TG simulations in FDS6: (a) plastic; (b) wood. (HC = hand calculation; GA = genetic algorithm; n is the number of components simulated).

For wood, the experimental DTG results demonstrate the basic features of wood decomposition [43], which are characterised by a shoulder part for hemicellulose reaction, and a pronounced peak and a long tail for the reactions of cellulose and lignin. The FDS predictions based on the three-component scheme give comparable results to the experimental DTG curves. The predicted DTG curves from simulations all reflect the three major parts of the wood decomposition curve. The limits in the predictions of HC-3 and GA-3 are in the shoulder and tail parts which have slight differences from the experimental curves. However, the GA-1 curves at the three different heating rates can only show an 'averaged' reaction in between the reaction regions of hemicellulose and cellulose.

4.3.2 Cone Calorimeter Experiments Simulations in FDS6

In the FDS simulation of a cone calorimeter experiment, the cone heater could be simulated as a complex cone shape with the assignment of temperatures to surfaces so that a corresponding heat flux is directed to the target sample. However, this approach is

unnecessarily complex as the selection of the correct temperatures to achieve the desired heat fluxes is crucial in this method. Alternatively, an external heat flux can be directly added to the sample surface representing the cone heater. Matala et al. [36] adopted the 'external heat flux' method to represent the cone heater in their research and this method is adopted here. A domain with dimensions of 220 mm × 220 mm × 1200 mm is used to ensure that the entire flaming region of the fire plume can be fully captured and the loss of heat to the outside of the domain is minimised. In the simulations, the sample is represented by the top surface of a solid block (100 mm × 100 mm) with properties derived from the experiments and analysis presented in this paper. The side surfaces of the simulated sample are defined as inert. The surface opposite the exposed face in the experiment, referred to here as the back face, is simulated either as a second layer according to the properties of insulation materials or as different boundary conditions available in FDS, which are discussed in section 4.3.3 and 4.3.4.

A 10 mm cubic cell is applied to the gas phase computations which gives results comparable to those produced using a cell size of 5 mm but within a reasonable computational time. The cell size in the solid phase is determined through grid sensitivity analyses which are discussed later. Figure 4-3 illustrates the simulation of a cone calorimeter experiment for wood at 35 kW/m^2. The detailed parameter set-ups are further discussed in the following sections for the simulation of the cone calorimeter experiments of the plastic and wood samples.

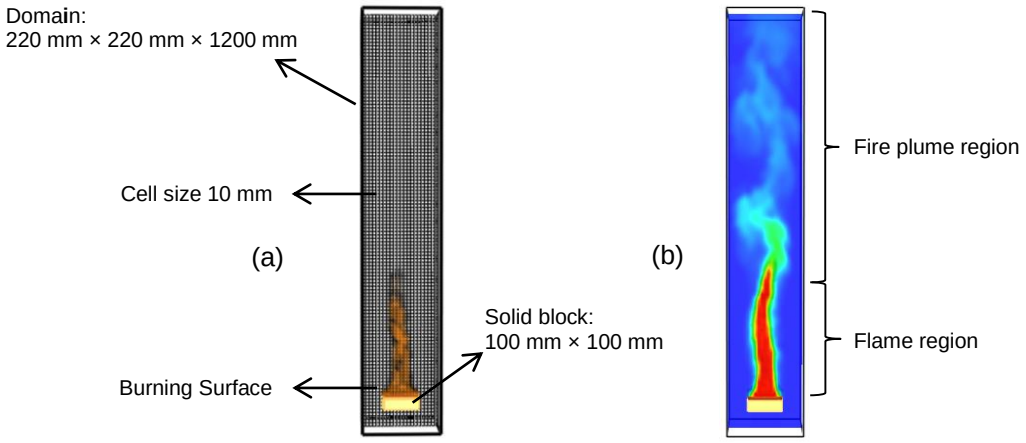

Figure 4-3: Burning of a cone calorimeter simulation in FDS6 for wood at 35 kW/m^2 at 1000 s (a) dimensions of set-up; (b) temperature slice.

4.3.3 Plastic Samples

According to the cone calorimeter experiments conducted by a third party on behalf of the LTA, the recycled plastic samples have physical properties of density (1376 kg/m^3) and thickness (3 mm) and the effective heat of combustion (35 MJ/kg). The density has been verified using

samples provided by the LTA since an examination of information provided by various manufacturers of pallets using recycled plastics suggests that PE and PP are the most common materials used. Since PE and PP typically have densities in the order of 925 to 950 kg/m^3, the measured value suggests there are other unidentified materials in the mixture.

In addition to the above properties, the parameters of heat of reaction and thermal properties of the plastic are needed to conduct cone simulations. Based on the DSC data obtained from the SDT experiments, the heat of reaction of the plastic is investigated. Since there is insufficient information for the temperature correlation governing the heat capacity of the plastic sample and no information on the radiation effects in the heating process, a simplified method proposed by Pau [20] is applied to analyse the heat of reaction for the plastic. According to the reduced DSC data, it is found the heat of reaction for the first reaction is negligible and the heat of reaction for the second reaction is ~ 670 to 875 J/g. The reported heats of reaction in Stoliarov and Walters [54] for PP, PE and PS is 800 to 1400 J/kg, for PET it is 1800 J/g and the heat of reaction of PVC for the decomposition at low temperatures is 0 to 340 J/g whereas at high temperatures it is 150 to 930 J/g. As mentioned in Pau [20], the amount of energy absorbed for decomposition is negligible when it is compared with the energy released in combustion. According to the heats of reaction listed above and the 35 MJ/kg effective heat of combustion for the plastic sample, it is considered that the heats of reaction for the plastic decomposition only have limited effects on the final HRR. The final heats of reaction for the plastic sample in FDS are determined to be 150 J/g for the reaction at the low temperature range and 1000 J/g for the reaction at high temperature range, which are the averaged results based on the measurement and literature values.

The thermal properties of the plastic samples cannot be simply determined from typical recycled plastic materials such as PP, PE, PS and etc. since it appears that additional elements may be present in the mixture which may not contribute to the decomposition reactions but affect the overall thermal behaviour. Due to the 3 mm thickness and the limited amount of residue (4%), the heat generated during the burning process could easily penetrate through the sample itself and the partial heat feedback at the back face of the sample is possibly lost. Therefore the burning predictions in cone calorimeter simulations may be sensitive to the boundary conditions on the back face. In order to choose a set of appropriate thermal properties for the plastic samples and to decide on a suitable boundary condition for the back face in FDS, a series of simulations at an incident heat flux of 35 kW/m^2 are carried out to conduct the corresponding sensitivity studies. In these simulations, the HC-2 scheme is adopted as it gives a better prediction of the pyrolysis behaviour than the one component scheme.

The cone calorimeter data from three replicate experiments at the 35 kW/m^2 incident heat flux are plotted in Figure 4-4. Results for the other incident heat fluxes show similar repeatability and therefore any curve obtained at a given incident heat flux effectively represents the experiment.

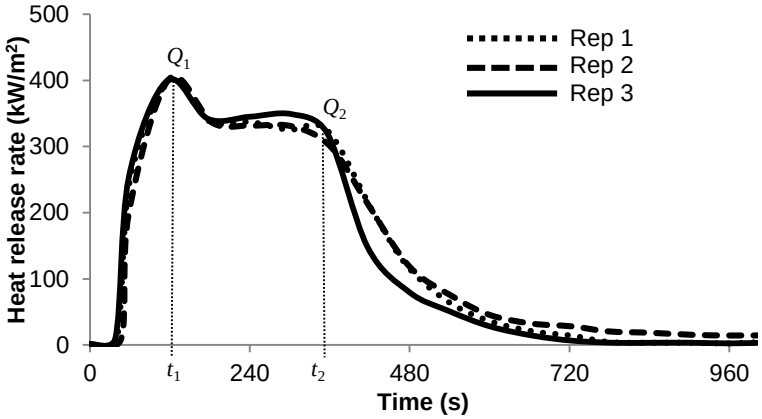

Figure 4-4: Measured HRR from three replicate cone calorimeter experiments of plastic at 35 kW/m^2.

As shown in the three curves in Figure 4-4, the first peak appears after the ignition, which is defined as Q_1. Following on from the peak there is a combustion period with a slowly decreasing trend which is maintained by the heat from the burning surface and the external heat flux provided by the cone heater. When the reaction front reaches the back face of the sample, the HRR starts to decay until the fuel is burnt out. The HRR just prior to the decay phase is defined as Q_2. Both t_1 and t_2 indicated on the curve represent the time to reach Q_1 and Q_2 respectively.

A sensitivity analysis to select the appropriate thermal properties is carried out by applying different values to the cone calorimeter simulations. The initial values for the inputs (2 J/g/K for c_p and 0.25 W/m/K for k) are based on the thermal properties of typical recycled plastics at ambient condition, which are listed in Table 4-2.

Table 4-2: Thermal properties for plastics at ambient condition [51, 61].

Item	c_p (J/g/K)	k (W/m/K)
PP	1.7-1.9	0.10-0.22
PE	1.9-2.3	0.30-0.40
PET	1.2-1.35	0.15-0.40
PS	1.2	0.10-0.13
PVC	0.98-1.38	0.17-0.19

It is observed that the 4% residue set-up in FDS only has very limited influence on the overall HRR predictions based on a preliminary study on the simulations with/without the residue. In order to minimise the number of parameters for the sensitivity analysis, the thermal properties of residue of 0.06 W/m/K for k_{re}, 2.5 J/g/K for $c_{p,re}$ and 390 kg/m^3 for $\rho_{pl,re}$ are adopted, taken from ref. [56] and the back face is set to an insulted condition. Table 4-3 lists the proposed thermal property values for the plastic samples and the corresponding cone calorimeter simulation results using these properties are plotted in Figure 4-5.

Table 4-3: Thermal properties used in the plastic sample sensitivity study.

Item		S1	S2	S3	S4
Sample	$c_{p,pl}$ (J/g/K)	2	2.5	2.5	3.2
	k_{pl} (W/m/K)	0.25	0.1	0.06	0.06

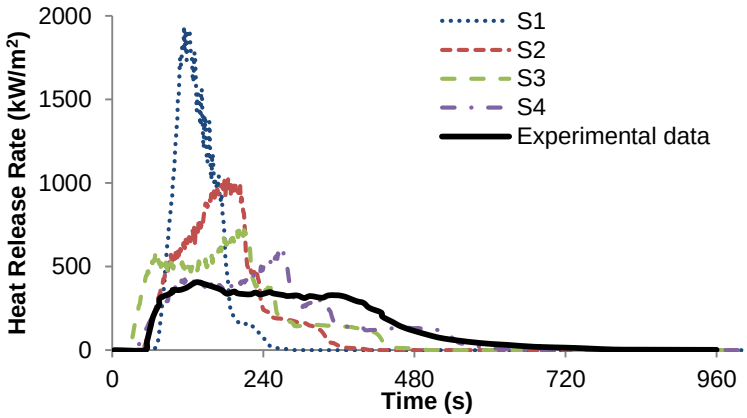

Figure 4-5: HRR predictions for plastic with different thermal properties schemes.

A comparison between S1, S2, S3 and S4 given in Figure 4-5 shows the predicted HRR results are affected by the values of $c_{p,pl}$ and k_{pl}. When k_{pl} and $c_{p,pl}$ are within the values listed in Table 4-2, the HRR curves are significantly over-predicted, which indicates that the thermal behaviour of the plastic sample is not determined by assumed values for PP and PE only but it is also affected by other elements in the sample. When k_{pl} is changed from 0.25 to 0.1 W/m/K and $c_{p,pl}$ is changed from 2 to 2.5 W/m/K, the predicted peak HRR in S2 is reduced to half of the value in S1. When k_{pl} is changed from 0.1 W/m/K in S2 to 0.06 W/m/K in S3, the first peak is clearly shown on curve S3. When $c_{p,pl}$ is increased from 2.5 J/g/K in S2 to 3.2 J/g/K in S4, Q_1 is reduced from ~600 kW/m^2 to ~400 kW/m^2, while t_1 is extended from ~70 s to ~140 s. Due to the adiabatic condition for the insulation layer, the heat feedback at the back face results in very high values for Q_2 in the three simulations. Overall, the HRR curve based on S4 inputs (3.2 J/g/K for the specific heat and 0.06 W/m/K for the thermal conductivity) is the most comparable result to the experimental result. However, neither of these values represents the

typical thermal properties for recycled plastics at ambient conditions. What was observed in the research by Fujino and Honda [62] was that the specific heat capacity for a recycled plastic composite consisting of PP, PE and fly ash increased with the increase of temperature. Fujino and Honda [63] also found that the thermal conductivity for their recycled plastic composite decreased with the increase of temperature. Based on the findings in refs. [62, 63], the values proposed in S4 may represent the values of thermal properties at high temperatures. It is noted that the LTA plastic is not thought to be a single pure material but a mixture with other unknown additives which may affect the overall thermal behaviour of the plastic.

In addition to the thermal property effects, the different back face boundary conditions influence the cone calorimeter simulation results as suggested by Pau [20]. Three different back face scenarios are used to examine the influence of boundary conditions on the simulation results, where the two-component scheme is adopted. First, an insulation material with a low conductivity, namely fibre blanket [64] is used for the back of the sample. The specific heat, thermal conductivity, and density values used for the material are listed in Table 4-4, which are based on suggestions from the AS/NZS3837 [65] and manufacturer's specifications [64]. The second condition is the 'INSULATED' set-up in FDS to represent a perfectly insulated back face. The last one is for an unexposed boundary condition where in FDS this represents an air gap at ambient conditions next to the inner-most layer for an obstruction more than one cell thick [16]. This final setting may represent a scenario where there might not have been perfect contact between the insulation layer and the sample.

Table 4-4: Different back face conditions in FDS cone calorimeter simulations.

Item		fibre blanket	adiabatic	air gap
Insulation layer	c_p (J/g/K)	1.0	Perfectly insulated, no heat loss	Default setting: air gap
	k (W/m/K)	0.06		
	ρ (kg/m^3)	65		

The cone calorimeter simulation curves using different boundary materials are plotted in Figure 4-6. As seen from the comparison, the values of second peak Q_2 are sensitive to the different back face conditions. When an insulation material (fibre blanket) is used, an over-predicted Q_2 results from the feedback heat from the back face. In the perfectly insulated back face condition, a higher value of Q_2 is obtained. For air gap, the Q_2 value is significantly reduced compared with another two scenarios and the heat loss behaviour in FDS is similar to the heat decay behaviour in the experiment. Since the fibre blanket was used in the actual experiments, the use of fibre blanket for the insulation layer is adopted for further simulations to correspond to the experimental set-up.

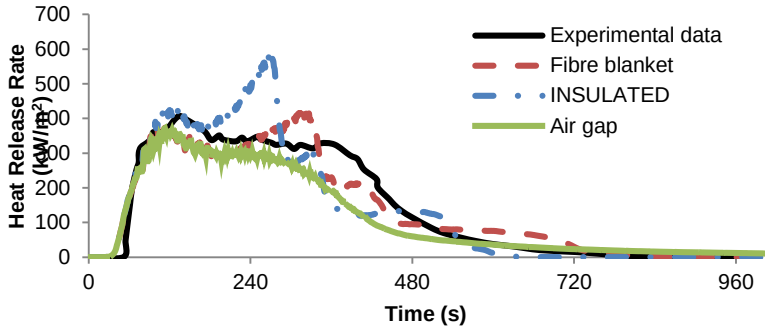

Figure 4-6: Comparison of back face conditions in cone calorimeter simulations.

As discussed, the first peak of the cone calorimeter HRR curve in FDS is most sensitive to the thermal properties of the plastic and the second peak is affected by the back face conditions. Table 4-5 summarises the main parameters which are suitable to use as inputs to FDS using the comparison against the cone calorimeter HRR experimental curve at an incident heat flux of 35 kW/m^2. Since the one-component scheme only represents the major decomposition behaviour, the heat of reaction for the major decomposition is considered. The energy consumed for the decomposition will be ~15% less. However, as discussed earlier, the overall energy released from the combustion will not be significantly affected by this loss.

Table 4-5: Summary of thermal properties for the recycled plastic sample.

Item		Two components		One component
		P1	P2	P-component
Plastic	Δh (kJ/kg)	150	1000	1000
	ρ_{pl} (kg/m^3)	1376		
	$c_{p,pl}$ (J/g/K)	3.2		
	k_{pl} (W/m/K)	0.06		
	L (m)	0.003		
	ΔH_c(MJ/kg)	35		
	ε_{pl}	0.9		
Residue yield	v (%)	4%		

According to Pau [20], the set-up for the cell size is sensitive to schemes with multiple layers and with the formation of residues. Therefore, it is necessary to carry out a grid sensitivity analysis for the solid phase. The default sizes of mesh cells for the solid phase in FDS are non-uniform values, which are smaller than the values of $\sqrt{k/\rho c_p}$ [16], while the numerical accuracy and stability for the computations in the solid phase is possible to be improved by changing settings in FDS. A setting of STRETCH_FACTOR=1 and a CELL_SIZE_FACTOR less than 1 can make the mesh density more uniform and mesh size smaller [16]. The changes in cell size settings used here are listed in Table 4-6.

Table 4-6: Cell size limits at solid phase sensitivity analysis for plastic cone calorimeter simulations.

Cells in solid phase	Computational time	Remark
0.12 mm	10.2 hr	Non-uniform
0.12 mm	12.0 hr	STRETCH_FACTOR=1, cell size is uniform
0.06 mm	12.1 hr	STRETCH_FACTOR=1 and CELLSIZE FACTOR=0.5
0.012 mm	14.1 hr	STRETCH_FACTOR=1 and CELLSIZE FACTOR=0.1

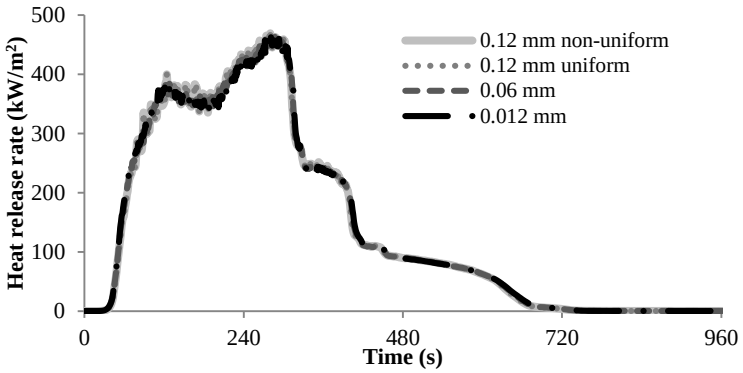

Figure 4-7: Comparison of cone calorimeter simulations of plastic samples in using different grid cell size limits.

The variances in using different grid cell size limits in the solid phase shown in Figure 4-7 are minor which demonstrates there is no difference in the overall prediction of the burning behaviour. The computational time for the default setting is shorter than other settings which have smaller and uniform cell sizes.

FDS simulations for cone calorimeter experiments at incident heat fluxes of 25 kW/m^2, 35 kW/m^2, 50 kW/m^2 and 75 kW/m^2 are conducted by defining the kinetic properties from the two-component hand calculation scheme (HC-2), GA method (GA-2), and from the one-component GA scheme (GA-1). Results for HRR and the change in mass are plotted in Figure 4-8. From an overall comparison point of view, the differences in using kinetic properties from the HC-2 and GA-2 schemes to predict burning behaviour are negligible, while the use of the GA-1 scheme behaves differently under the different heat flux conditions.

For the results at the 25 kW/m^2 incident heat flux shown in Figure 4-8(a), the Q_1 values in the simulations are not as high as in the experiment which suggests that heat flux set-up in the simulation is not sufficient to ignite the plastic. There are pronounced second peaks in all the FDS HRR curves which are the result of the over-predicted heat feedbackon the back face. The mass remaining in the simulations using the HC-2 and GA-2 schemes is similar to the

mass remaining in the experiment. In terms of the GA-1 scheme the reaction behaviour is significantly delayed.

When the incident heat flux is raised to 35 kW/m^2 (shown in Figure 4-8(c) and (d)) the simulations can effectively predict the values of Q_1 under the HC-2 and GA-2 schemes. The predicted burning behaviour (both the HRR and mass loss curves) is very similar to the experiment over the time period 0 to ~ 240 s. The major difference between the simulation curves using HC-2 and GA-2 and the experimental curve is after ~280 s where the HRR jumps to a second peak and the mass starts to reduce quicker in the simulations than in the experiment. The final mass remaining in the simulations is less than 3%, while the remaining mass in the experiment was ~6%. Significant delays are found in the GA-1 simulation results compared to the experimental curves.

For the cases using incident heat fluxes of 50 kW/m^2 and 75 kW/m^2, as shown in Figure 4-8(e) to (h), the values of Q_1 in all simulations are over-predicted. The heat feedback on the back face is still high in the simulations which results in an over-predicted Q_2 as well. The mass loss rate in the simulations for HC-2 and GA-2 are still faster than the measured mass loss rate. The final mass fraction in the corresponding simulations under these two heat fluxes are less than 3%.

The predictions based on the one-component scheme at the two high heat fluxes (50 kW/m^2 and 75 kW/m^2) demonstrate slight delays in the results of Q_2, which is different to the scenarios using lower heat fluxes. The time to reach the first peak Q_1 in the simulations is similar to the time in the experiments even though the values of Q_1 are over-predicted in both scenarios. The simulated mass loss rate curves are faster than in the experiments under the one-component scheme, while the final remaining mass in the two simulations are less than 3%.

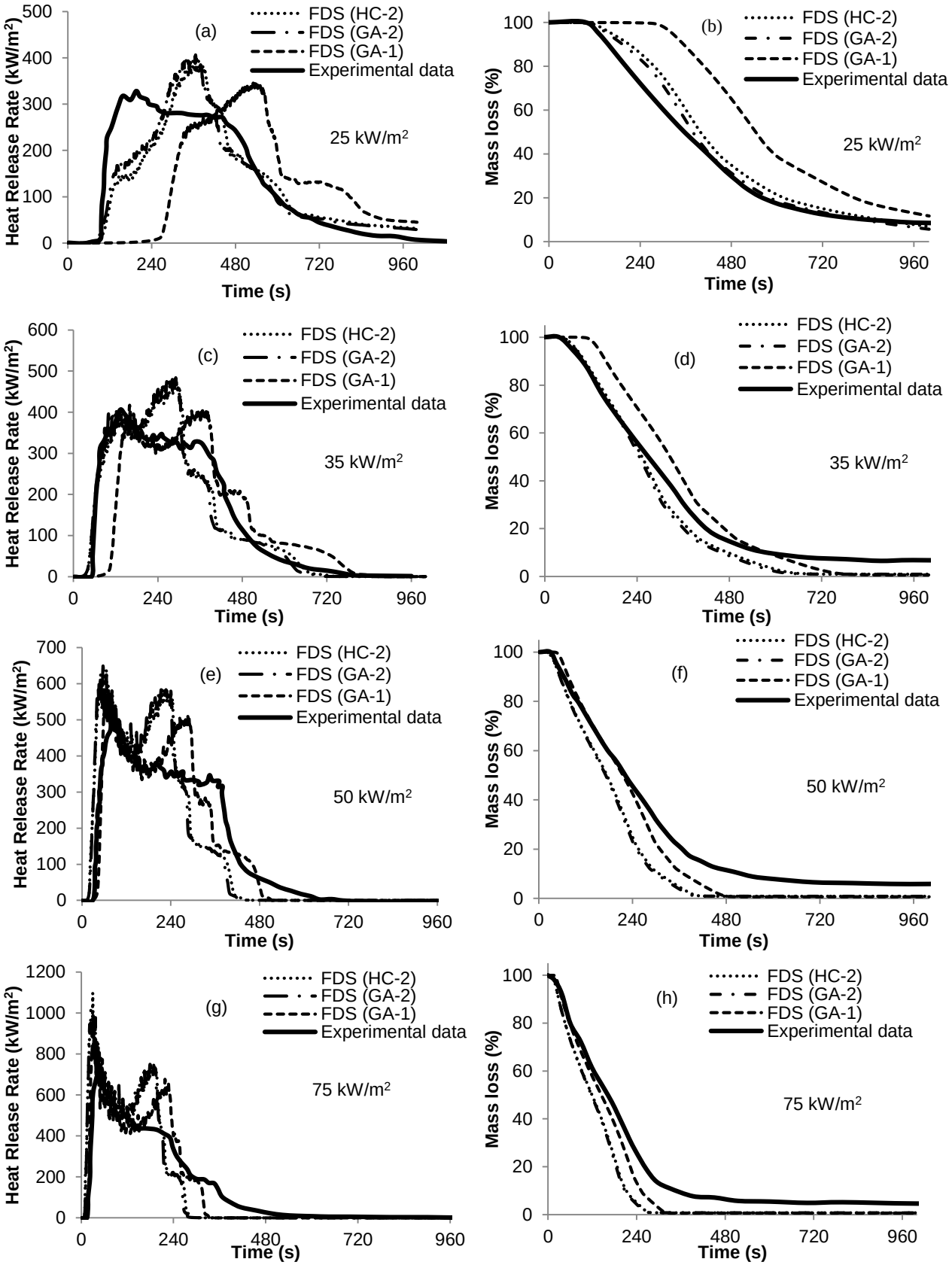

Figure 4-8: Comparison of HRR and mass fraction curves from the recycled plastic sample cone calorimeter simulations using the different schemes and experimental results at the indicated incident heat fluxes.

The predictions based on the one-component scheme at the two high heat fluxes (50 kW/m^2 and 75 kW/m^2) demonstrate slight delays in the results of Q_2, which is different to the scenarios using lower heat fluxes. The time to reach the first peak Q_1 in the simulations is similar to the time in the experiments even though the values of Q_1 are over-predicted in both scenarios. The simulated mass loss fraction curves still shows are faster loss in mass in the simulations than in the experiments under the one-component scheme, while the final remaining mass in the two simulations are less than 3%.

4.3.4 Wood Samples

The wood samples used in the experiments had a thickness of 21.5 mm, an average density 566 kg/m^3 and an effective heat of combustion of 12.1 MJ/kg from the cone calorimeter experimental data provided by the LTA. It is important to note that the residues obtained from the TG experiments for wood samples were mainly char, which has significant thermal effects on the burning behaviour of wood. Therefore the definition of the thermal properties of char is as important as the properties of wood in the simulations.

Due to the wide applications of wood materials, the thermal properties of wood and char have been investigated through various studies in past decades, Table 4-7 summarises the relevant information of wood and char for this work. The values heat of reaction (Δh_w) for each component are based on the discussions in Chapter 3. According to TenWolde et al [66], the specific heat ($c_{p,w}$) is a temperature-dependent property as described in Equation 4.5 shown as part of Table 4-7. The specific heat for wood char ($c_{p,ch}$) is also dependent on temperature. The model defined in Equation 4.6 [51] is adopted in this work and also shown in Table 4-7. In terms of thermal conductivity of wood (k_w), the proposed model by TenWolde et al. [66] is determined by temperature, moisture content and density. Thus, a value of 0.21 W/m/K at ambient temperature for the k_w can be obtained from the model, which is based on a wood sample with 10% moisture content and a density of 566 kg/m^3. Although the k_w value of wood increases with the increase of temperature [67], the use of a constant value without considering the influence of the rising of temperature has been applied to the studies of pyrolysis models [68-70], therefore, this simplification is also adopted in this work. The value for the thermal conductivity of wood char (k_{ch}) is more difficult to determine as there is no mathematical model available to describe k_{ch}. However a summary of k_{ch} for wood char provided in the work of Li et al. [71] gives an idea of the possible values of k_{ch} with a range of 0.07-0.14 W/m/K where 0.1 W/m/K for k_{ch} is used in this work. The density of the char (ρ_{ch}) is estimated as 150 kg/m^3 based on [72] 26% of the density of original wood, which is consistent to the bulk density value estimated from cone experimental results. The emissivity ε_{ch} is taken as 1 in this study.

Table 4-7 Properties of wood and char.

	Item	Hemicellulose	Cellulose	Lignin	W-component
Virgin wood	Δh_w (kJ/kg)	~ -200 to - 400	~ 100 to 200	~ -400 to -800	100
	ρ_w(kg/m^3)	566			
	$c_{p,w}$(J/g/K) [66]	(3.87T+101.3)/1000 (T in K) (4.5)			
	k_w(W/m/K)	0.21			
	L_w(m)	0.0215			
	ΔH_c(MJ/kg)	12.1			
Char	ρ_{ch} (kg/m^3)	150			
	$c_{p,ch}$(J/g/K) [51]	(714+2.3T- 8×10$^{-4}T^2$ - 3.7×10$^{-7}T^3$)/1000 (T in ˚C) (4.6)			
	k_{ch}(W/m/K)	0.1			
	ε_{ch}	1			
Residue yield	v (%)	13%			

As introduced, three repeated cone calorimeter experiments for the wood samples were conducted for each heat flux. The results at 35 kW/m^2 are plotted in Figure 4-9, where curves Rep 1, Rep 2 and Rep 3 are from the three replicate experiments. As seen, only two sets of results from the three repetitions show sufficiently consistent burning behaviour. Therefore, the two consistent results under each incident heat flux are selected for further analysis. In Figure 4-9, the 'average' curve is plotted that combines the HRR and time values from the two consistent experimental results (Rep 1 and Rep 2). As demonstrated from these curves, there are two distinct peaks during the burning process. The first peak Q_1 comes immediately after ignition and thereafter the HRR quickly decreases with time because the char layer formed in between the exposed surface and pyrolysis front in the virgin wood slows down the pyrolysis progress [19]. Due to the thickness of the wood and the constant external heat flux from the cone heater the stable burning of wood is maintained for a few minutes (from t_1 to t_2). When thermal penetration front reaches the back of the sample the heat feedback increases the HRR which then reaches a second peak Q_2.

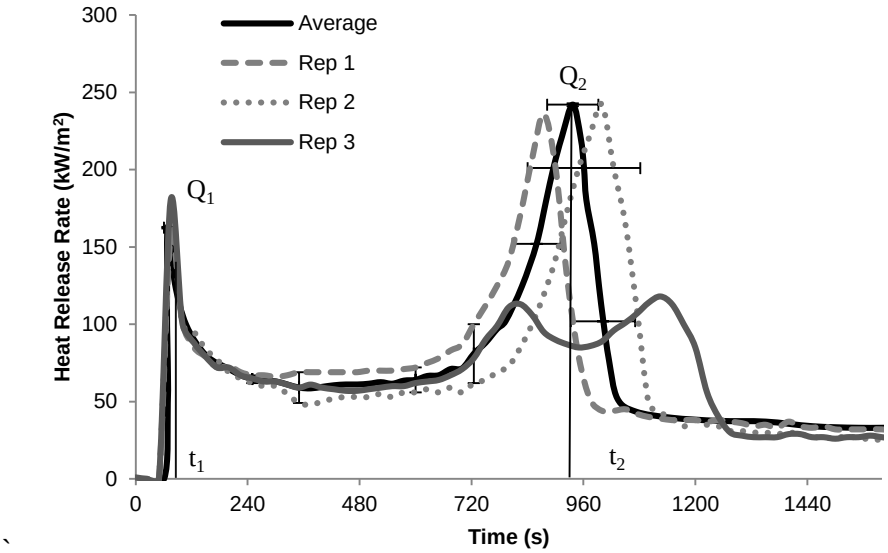

Figure 4-9: HRR from wood sample cone calorimeter experiments at 35 kW/m^2.

The heat feedback from the back face of the sample has an important effect on the form of the second peak in the cone calorimeter experiments. To examine the effect of the back face in the simulations, three different conditions are applied to simulate the case of the cone calorimeter experiment at the external heat flux 35 kW/m^2 using the three-component scheme. The first condition sets the back face to be adiabatic; the second condition uses the same insulation material (fibre blanket) as used in the plastic sample cone calorimeter simulations; and the third condition uses the default FDS setting, for which it is assumed that the defined surface of wood is sitting on an air gap at ambient temperature. All of the simulation results for the three boundary conditions are plotted in Figure 4-10. As seen, using the different properties most affects the second peak Q_2, where the use of adiabatic condition demonstrates the result of using a perfect insulated back face compared with the cases with heat losses when settings of back surface are changed to fibre blanket or an air gap. In order to be consistent with the actual experimental condition, the use of fibre blanket for back surface insulation is adopted for the following analysis.

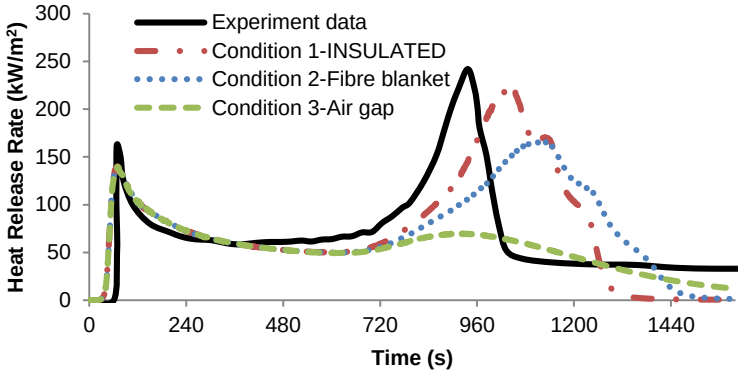

Figure 4-10: Comparison of wood sample cone calorimeter simulations with different back face boundary conditions.

Similar to the plastic material, a sensitivity study for the solid phase cell size showed that the HHR curves are not sensitive to the limits with the result a 0.14 mm cell size for solid phase is used.

After confirming all of the relevant settings for the FDS simulations, four series of simulations for wood experiments at 25, 35, 50 and 75 kW/m^2 external incident heat fluxes are carried out using the HC-3, GA-3 and GA-1 schemes; the corresponding simulation results are plotted in Figure 4-11 for the different heat fluxes. The experimental data used in these comparisons are the averaged results as discussed previously. All of the HRR results from simulations are able to effectively illustrate the major features of the wood experimental results. The predictions using the three-component scheme demonstrate some over- and under-predicted results at different heat flux scenarios, while there are only minor differences in the results between the HC-3 and GA-3 schemes. However, results for the one-component scheme show significant variations compared to the experimental results in all simulations under all heat fluxes. It is also noted that the predictions in FDS do not account for the combustion phase beyond flaming combustion at the end of the cone calorimeter experiments. Once the flame self-extinguishes, glowing combustion on the surface of the charred fuel can be seen in the experiments but is not included in simulations.

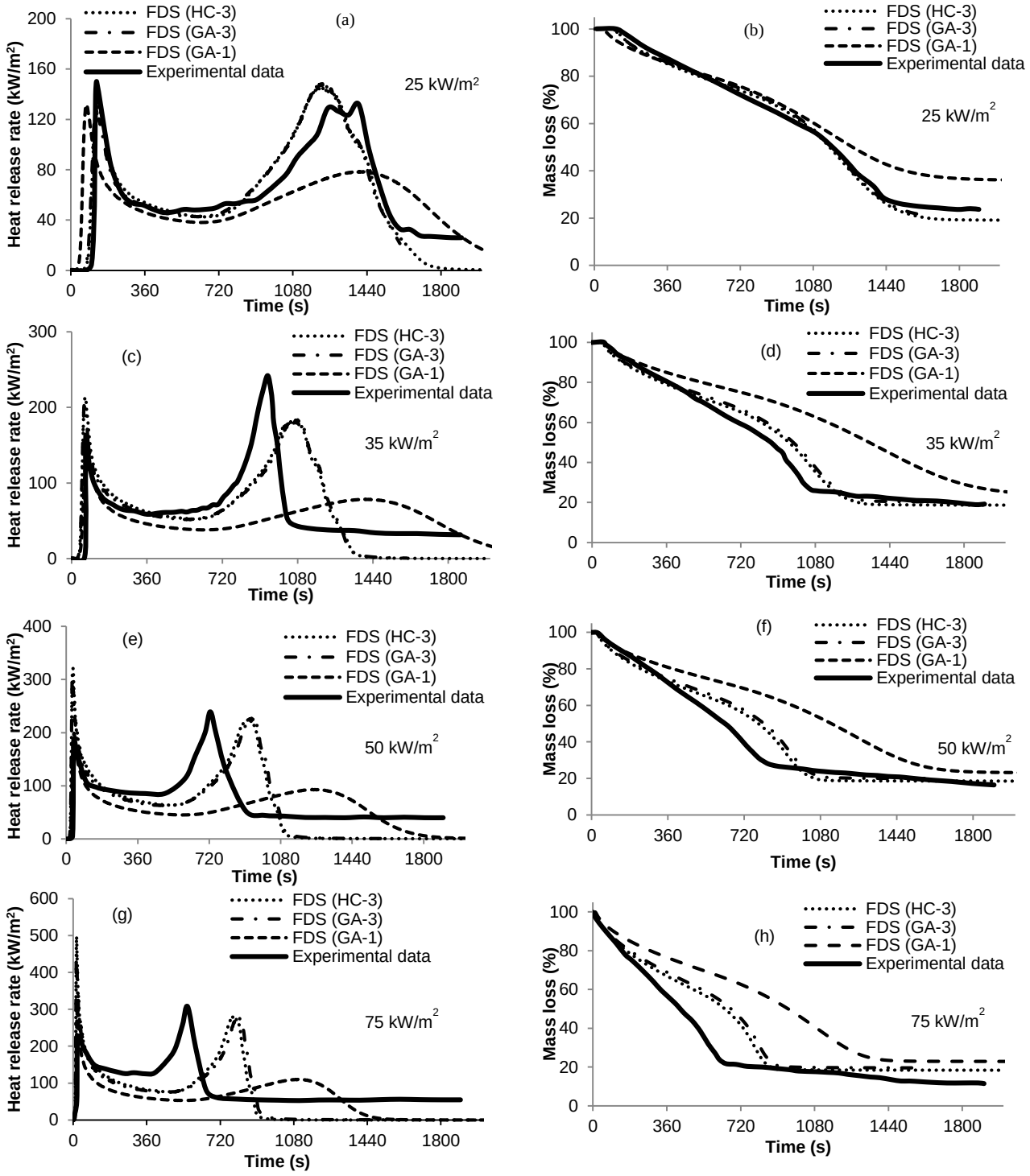

Figure 4-11: Comparison of HRR and mass fraction curves from the wood sample cone calorimeter simulations using the different schemes and experimental results at the indicated incident heat fluxes.

Figure 4-11(a) and (b) are the comparisons of the HRR and mass loss curve at 25 kW/m^2 incident heat flux. In Figure 4-11(a) the simulation results for the HC-3 and GA-3 schemes demonstrate comparable results to the experimental curve. However, the results from the GA-

1 scheme demonstrates a much longer burning period from t_1 to t_2 and a smaller Q_2 compared to the experimental result. In Figure 4-11(b), the mass loss curves for HC-3 and GA-3 are similar to the experimental mass loss curve. For the GA-1 scheme the mass reduction rate is significantly slower than the rate indicated on the experimental curve after ~1080 s.

The simulation results for HRR and mass loss curves at the 35 kW/m^2 incident heat flux are plotted in Figure 4-11(c) and (d). The simulation results for HRR using the HC-3 and GA-3 schemes effectively predict the experimental HRR over the burning period of ~ 0 to 720 s. For the comparisons of mass loss curves in Figure 4-11(d) schemes HC-3 and GA-3 have slightly higher values than the mass loss in the experiment after ~ 720s. The FDS results under scheme GA-1 has a long burning period at very low burning rate which does not represent the burning behaviour in the experiment.

When the external heat fluxes 50 and 75 kW/m^2 are used in the simulations the predictions demonstrate significant variations. As shown in Figure 4-11(e) and (f), for the HC-3 and GA-3 schemes the values of Q_1 are over-predicted; the predicted burning periods are much longer than the experimental results. The predicted mass loss curves in Figure 4-11(g) and (h) also demonstrate the significant burning delays in the simulations for the case of schemes HC-3 and GA-3. FDS is not able to predict the wood sample cone calorimeter experiment using the one-component GA-1 scheme when the external heat flux is 50 and 75 kW/m^2.

4.3.5 Discussions on the Cone Calorimeter Simulation Results

According to the FDS cone calorimeter results for the plastic and wood samples, it is found that the variations in simulation results based on the kinetic properties using the multiple-component scheme from the HC and GA methods are negligible.

For plastic, the FDS predictions based on the two-component scheme at an external heat flux of 25 kW/m^2 cannot adequately represent the burning behaviour obtained from the experiment. The production of the gaseous products and the whole burning process are slower in the simulations than in the experiment, which indicates that the heat transfer based on the defined thermal properties in simulations is too slow for the decomposition of the plastic. Since the thermal properties of the fuel are optimised based on the experimental result at 35 kW/m^2 the corresponding predictions for the HRR results are comparable to the experimental curve. When the external heat flux is increased to 50 kW/m^2 or 75 kW/m^2, higher values of HRR are obtained in the simulations than in experiments. The possible explanation for these differences

is due to the use of the estimated thermal property values of the plastic in simulations which determines the heat transfer calculations in the pyrolysis model.

The one-component scheme for plastic can only sufficiently predict in FDS the burning behaviour of cone calorimeter experiments at high heat fluxes when applying the thermal settings proposed in this work. The one-component scheme does effectively represent the major reaction which occurs at a high temperature in the decomposition of the plastic. So in the FDS simulations, when the external heat flux is high enough, the temperature in the solid can be quickly raised to accelerate the major reaction for the decomposition of the plastic. Therefore, the FDS results based on the one-component scheme at high external heat fluxes can demonstrate the burning behaviour similar to the two-component scheme.

For wood cone calorimeter simulations it is also found that applying a consistent set of thermal properties for the wood and char at different external heat fluxes gives the predictions that are not always comparable to the experimental results. For instance, the predictions under external heat fluxes of 25 and 35 kW/m^2 can more effectively represent experimental results than the predictions under higher external heat fluxes of 50 and 75 kW/m^2. The predictions based on the one-component scheme are not favourable in the cone calorimeter simulations for the wood samples with the use of the same thermal properties for the multiple-component scheme.

Overall, the limitations in the FDS cone calorimeter predictions in this work are mainly due to the uncertainties in the materials. A more detailed parametrisation study by using experimental analysis methods or by optimising the properties under several heat fluxes instead of one heat flux may improve the results. It is suggested to adopt a simple and known material for the detailed parameterisation study and to test the improvements in FDS predictions.

4.4 Conclusions

This chapter applies the pyrolysis model in FDS6 to simulate the decomposition and burning behaviour of plastic and wood based on three decomposition schemes which are: GA one-component scheme, GA multiple-component scheme and hand calculation multiple-component scheme. Two components are used to represent the plastic material and three components are used to represent the wood material.

Based on the results for the TG experiment simulations, it is found that the differences are negligible for GA multiple-component scheme and hand calculation multiple component scheme when the same multiple components are applied. In the application of the GA one-

component scheme, the major decomposition of plastic can be predicted. For wood, only an 'averaged' reaction in between the reaction regions of hemicellulose and cellulose can be demonstrated in the TG simulations.

In the simulations for cone calorimeter experiments, detailed analyses are introduced to determine the thermal properties of plastic and wood samples. The thermal properties chosen in this work are derived based on a series of parametric analyses. The influence of back face condition on HRR curves is investigated in this work. It is found that the effects of the back face conditions are particularly noticeable on the second peak of HRR curves. In this study the properties for a fibre blanket material have been used for the main body of simulations to be consistent with the experiments. However, the default settings representing 'an air gap' at ambient gave a reasonable match with the HRR measurements for the plastic sample and an adiabatic setting gave the best match with the HRR measurements for the wood sample. Different cell size limits for the solid phase are also studied, with no significant difference in results found when different limits are applied.

In the case of using multiple-component scheme to simulate cone calorimeter experiments, the variation in the HRR predictions based on the different kinetic properties determined by the hand calculation and the GA method are minor. The predictions of HRR curves are not always comparable to the experimental HRR curves under different external heat fluxes when a consistent set of thermal properties is used. The best simulation results are obtained at 35 kW/m^2 for plastic and at 25 kW/m^2 for wood.

When the GA one-component scheme is applied to simulate the cone calorimeter experiments, the predicted HRR for plastic samples at high external heat fluxes is similar to the predictions using two-component scheme, while the predictions for wood samples are not favourable. However, it is believed that effective predictions can still be achieved based on the one-component scheme when the thermal properties are altered accordingly for the purpose of fitting to the experimental results.

This study has generated a representative set of material properties for the two materials used in the LTA large-scale tunnel experiment that will be applied to a future FDS modelling study. A practical approach has been necessary in this work to get these kinetic properties given the range of component scheme and parameter selection method options that can be applied and the unavailability of a detailed knowledge of the materials used in the large-scale experiments.

Chapter 5 Comparison of Results from Large-scale and Small-scale Tunnel Experiments

The content of this chapter is reproduced according to the paper titled ‘Comparison of results from large-scale and small-scale tunnel experiments’ submitted to ‘Fire Safety Journal’. Some additional information, which is not included in the paper, is also presented in this chapter.

5.1 Introduction

As introduced in Chapter 1 and Chapter 2, fires involving HGVs in tunnels can have a major impact on the life safety of people and cause extensive damage to the structure as exemplified by the Mont Blanc tunnel incident [1]. Various large-scale road tunnel HGV and simulate HGV cargo fire experiments [73] have been carried out to obtain information on HRR, flame lengths, gas temperatures etc. and also to understand the influences of different factors such as the impact of forced ventilation and fire suppression systems. The information obtained from such large-scale tunnel experiments can represent the burning phenomena in an actual incident however they are usually expensive and time consuming. It is generally impractical to carry out large-scale experiments in order to conduct parametric studies of the burning behaviour of tunnel fires which can be used to assess the capability of numerical models, for example. Instead small-scale tunnel fire experiments have been used such as the studies on the influence of forced ventilation [15, 74] and the effect of tunnel cross-section area [30]. The relatively low cost of doing small-scale tunnel experiments allow the flexibility to conduct more extensive experimental analyses and to also ensure a level of repeatability. However, it is important to evaluate whether the measurements from small-scale experiments can sufficiently represent the burning phenomena in a large-scale tunnel, thus, it is useful to compare the results obtained from corresponding sets of experiments.

A series of small-scale tunnel experiments are described which are a scaled down representation of the LTA large-scale tunnel experiment has been carried out by Cheong et al. [39]. In the small-scale experiments a gas burner and cribs have been adopted as the fuel source to represent the cargo load of a burning HGV that was simulated in the large-scale tunnel experiment. Both the gas burner and cribs were specifically configured to have a comparable energy profile to the large-scale experiment. In the burner experiments the flow of gas to the burner was controlled to produce a scaled HRR curve to match the results from the large-scale experiment. In order to assess the ability of the small-scale tunnel experiments to reproduce the results at the large-scale the temperature results are recorded from the gas burner experiment and are compared with the corresponding results from the large-scale tunnel experiment. Since the majority of the fuel source adopted in the large-scale tunnel experiments comprised of wood materials, the use of wood-based material in a crib arrangement as fuel source in the small-scale tunnel experiments can evaluate the ventilation influence on the fuel for further parametric studies at forced ventilation velocities other than that used in the large-scale experiment. In the experiments introduced in this chapter the cribs are specifically designed to have the comparable energy profile and geometrical shape to the simulated cargo load in the large-scale experiment.

Measurements of HRR, temperature and velocity from the small-scale experiments are reported and discussions are carried out in terms of using the different fuel sources. The results presented in this chapter are to be used in follow-up work to compare with numerical simulations. The numerical simulation work is introduced in Chapter 7. The objective of the experiments presented in this chapter is to use the gas burner experiments to confirm the scaling is appropriate and the crib experiments provide a relevant set of data to further compare with planned modelling exercises.

5.2 Theory and Experiment Design

5.2.1 Scaling Theory

In order to achieve similarity between the small-scale and full-scale experiments, Froude number scaling is applied in this study, a technique that has been widely applied to conduct small-scale tunnel fire experiments [15, 30, 74]. Based on the Froude scaling theory, the HRR, the velocity, the energy content, time and temperature are scaled following Equations 5.1 to 5.5. The influence of thermal inertia of the material, turbulence intensity and radiation are not considered in this work.

Parameter	Scaling equation	
Heat release rate (kW)	$\dot{Q}_s / \dot{Q}_L = (l_S / l_L)^{5/2}$	(5.1)
Velocity (m/s)	$v_S / v_L = (l_S / l_L)^{1/2}$	(5.2)
Energy (kJ)	$Q_S / Q_L = (l_S / l_L)^3 (\Delta H_{c,L} / \Delta H_{c,S})$	(5.3)
Time (s)	$t_S / t_L = (l_S / l_L)^{1/2}$	(5.4)
Temperature (K)	$T_S / T_L = (l_S / l_L)^0$	(5.5)

5.2.2 Large-Scale Tunnel Experiments

The small-scale tunnel experiments in this study are based on one experiment from a series of seven large-scale simulated HGV cargo tunnel fire experiments conducted on behalf of the Land Transport Authority of Singapore in a tunnel test facility in Spain. The tunnel test facility represented a two lane road tunnel and was built of concrete in which the section used for the experiments was rectangular in shape with minimum dimensions of 7.3 m wide and 5.2 m high. The total length of the tunnel was 600 m and measurement points were located from 30 m

away from the upstream edge of the fire to 170 m away from the downstream edge of the fire. An overall view of the tunnel section is shown in Figure 5-1(a) together with the instrumentation locations. Temperatures were measured using thermocouples at the different cross-sections shown in Figure 5-1(a) and gas concentrations of O_2, CO_2 and CO were measured at location D170. The cross-sections with the thermocouples at the D10, D15 and D30 locations are illustrated in Figure 5-1(b). The detailed thermocouple arrangements for other cross-sections can be found in Cheong et al. [39].

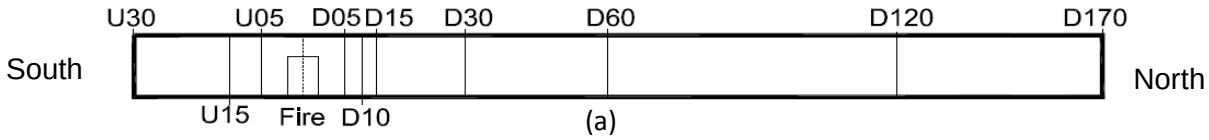

(a)

(U*x*/D*x* defines a position *x* m away from the upstream/downstream edge of the fire)

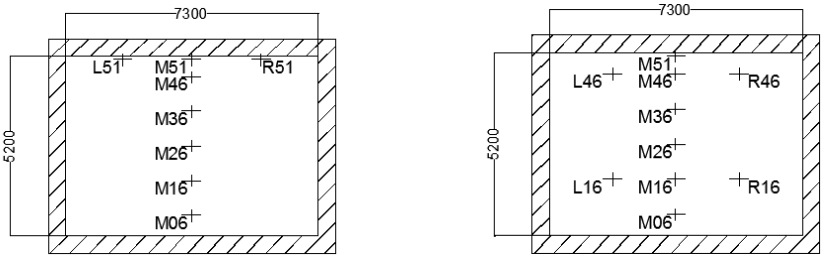

D10 (b) D15 & D30

(M is located at the centreline of the cross section, L/R denote 2 m away from the centreline towards left/right side, e.g. M51 denotes a sensor that is 5.1 m above floor on the centreline)

Figure 5-1: (a) Large-scale tunnel with the measurement locations, (b) tunnel cross-sections.

In the LTA-sponsored large-scale experiment the fuel source consisted of wood and plastic pallets (arranged in 12 stacks and 19 layers) to represent the cargo of a fully loaded HGV (7.5 m (L) × 2 m (W) × 3 m (H)). The fuel source was raised 1 m above the tunnel floor on a concrete support. Two trays (0.35 m × 0.70 m), with 1 L gasoline in each were positioned inside the upstream side of the pallets as the ignition source. A target with two pallet stacks, which had the same height as the cargo load, was located 5 m downstream from the rear of the fuel source.

Jet fans at one end of the tunnel were used to generate an average air velocity of 3 m/s along the centreline of the tunnel for the entire duration of all of the experiments. Of the seven experiments, six were conducted with the activation of a deluge system over the simulated HGV cargo fuel source. This system was designed to activate two zones simultaneously with each suppression zone 25 m in length. One experiment did not use the deluge system but a

water spray was applied around 9 min (540 s) after ignition at the D45 location to cool down the tunnel structure. The temperature results at the D10, D15 and D30 locations were not influenced by the discharge of this water spray. In this study, only the experimental results without the operation of the deluge system is used as a comparison with the small-scale tunnel experiments.

The HRR curve from the large-scale experiment using data measured at the D170 location is shown in Figure 5-2. The fire had a total energy release of 99.2 GJ. The sudden increase in the HRR from the approximately steady 120 MW to the peak of 150 MW at around 770 s was due to the increase in burning area from the collapse of some of the pallet stacks [39]. The target pallet stack ignited at 7 min 50 s (470 s) and also contributed to the overall recorded HRR in the experiment.

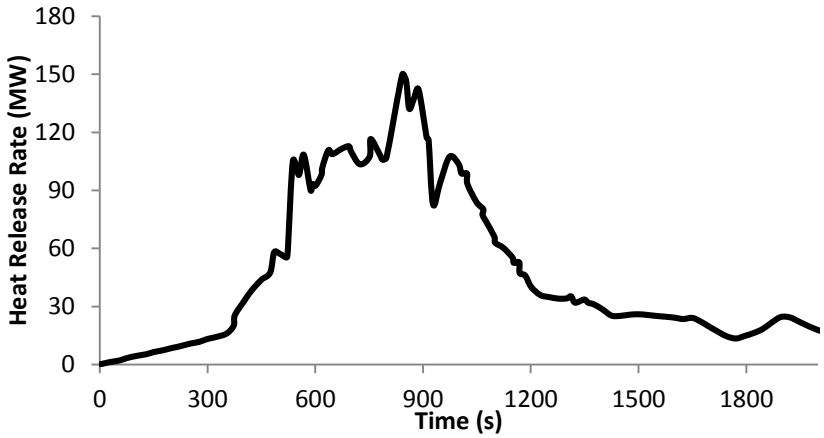

Figure 5-2: HRR curve of the large-scale tunnel experiment (adapted from [39]).

5.2.3 Small-Scale Tunnel Geometry

The series of small-scale experiments described in this paper was conducted in the medium-scale fire laboratory at the University of Canterbury. The geometry of the small-scale tunnel was scaled down based on the tunnel section illustrated in Figure 5-1. In order fit the small-scale tunnel into the laboratory a scaling ratio of 1:20 was adopted in this work. The 1:20 scaling ratio is different from the 1:23 adopted by Ingason [15], other work by Ingason and Li [74] showed that this ratio gives good agreements between small-scale and large-scale based on many applications.

The body of the small-scale tunnel was divided into nine separate sections. Each tunnel section had an inner dimension of 0.365 m (W) × 0.26 m (H) × 1.22 m (L) to give a total length of approximately 11.9 m. One section was used as the combustion chamber where the fire was

located. The ceiling, floor and rear wall of the combustion chamber were made of 0.9 mm thick stainless steel 304, with a 15 mm thick insulation material (density: 336 kg/m3, thermal conductivity: 0.07 W/m/K, specific heat: 1.08 J/g/K), while the front of the chamber had fire resistant glazing for observation purposes and was also accessible for the replacement of the fuel source. Inside the combustion chamber a platform connected to a load cell is used to locate fuel source in the experiments. This platform could also be replaced by a gas burner. The remaining sections were all constructed of 0.9 mm thick stainless steel sheets with 5 mm thick insulation. According to the manufacturer the insulation material has a density of 336 kg/m^3, heat capacity of 1.08 kJ/kg/K and thermal conductivity of 0.07 W/m/K at ambient temperature.

An electrical fan was attached to the upstream end of the tunnel with a section of half metre long flow straighteners to establish a uniform longitudinal ventilation system. In all of the experiments the fan was controlled to give a 0.68 m/s forced air velocity along the centre-line of the tunnel scaled from the large-scale tunnel experiment at 3 m/s using Equation 5.2.

A vertical circular duct (300 mm in diameter and 1.3 m tall) was installed at the downstream end of tunnel, where flue gases were sampled for measurement by gas analysis equipment. The circular duct was placed under the hood of a furniture calorimeter which was simply used to extract the flue gases. When the tunnel was assembled, all connections were sealed and insulated to reduce heat losses. Figure 5-3 illustrates the geometry of the small-scale tunnel.

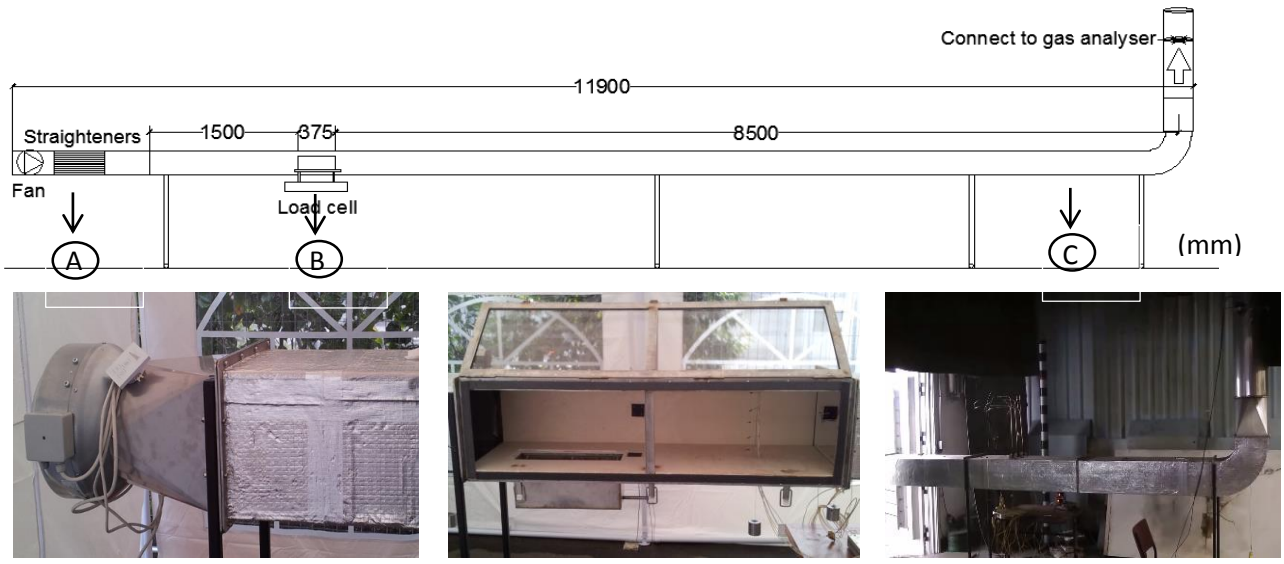

A B C

Figure 5-3: Small-scale tunnel set-up.

5.2.4 Fuel Sources in the Small-Scale Experiments

Medium density fireboard (MDF) was used to construct the crib fuel source. Since the material properties of MDF have been comprehensively investigated by Li et al. [35, 71, 75], the use of the MDF as fuel materials is convenient for further computer modelling purposes. The cribs were scaled to the profile of the large-scale HGV cargo load and configured to achieve the equivalent fuel load. Some detailed information regarding the choosing of MDF as the fuel material are further discussed in Chapter 6. The cribs were geometrically scaled to the profile of the simulated large-scale HGV cargo and the internal configuration of the cribs was specifically designed. Each crib was comprised of five layers with three 375 mm long-sticks, six 100 mm short-sticks equally spaced and the thickness of each stick of 15 mm. Applying Equation 5.1 and 5.3 to the recorded total energy release and steady-state HRR shown in Figure 5-2, the crib was designed to give corresponding total energy and HRR values of 17.6 MJ and 67 kW respectively. However it is important to note that scaling the internal configuration of the large-scale pallets using the small-scale cribs was wholly impractical with likely consequent effects on the dynamics of flame spread and air flow.

The LPG gas burner fuel source had the same length and width as the crib and was mounted flush with the tunnel floor. A control valve was installed in the supply pipe to regulate the mass flowrate of the gas in order to generate the scaled HRR curve equivalent to the large-scale tunnel experiment results.

The target stack of pallets located in the large-scale experiment was not included in the small-scale tunnel experiments as it is difficult to separate the HRR contributed by it from the overall HRR. However based on the amount of pallets used for the target its energy content was less than 8% of the energy content of fuel used to represent the HGV. The omission of the target in terms of its potential effect on the measurements is discussed later.

5.2.5 Instrumentation

The mass loss data in the crib experiments was measured by a weighing system installed under the combustion chamber. This system consisted of a non-combustible board platform with dimensions of 300 mm (W) × 500 mm (L) × 30 mm (H) within the chamber and a weighing scale underneath the chamber connecting to the platform. The platform and the weighing scale were connected by four steel rods through the floor of the chamber and all connections were sealed by fire resistant materials. The height of the supporting steel rods was adjustable and in the experiments the board was raised 20 mm above the tunnel floor to correspond to the

concrete support used to raise the simulated HGV in the large-scale experiment. The mass loss was recorded every second by a data acquisition system.

Gas temperatures were measured by a series of bare type K, of 0.25 mm diameter, thermocouples. Surface temperatures were recorded using plate thermocouples installed on the insulated tunnel walls. Each plate thermocouple consisted of a 50 mm × 50 mm stainless steel plate painted black on the front side and a type K, of 0.25 mm diameter thermocouple welded on backside of plate. In order to carry out comparisons with the results recorded in the large-scale experiments, the locations of the thermocouples corresponded to the measurement locations in the large-scale tunnel. The detailed arrangements of thermocouples and plate thermocouples are illustrated in Figure 5-4.

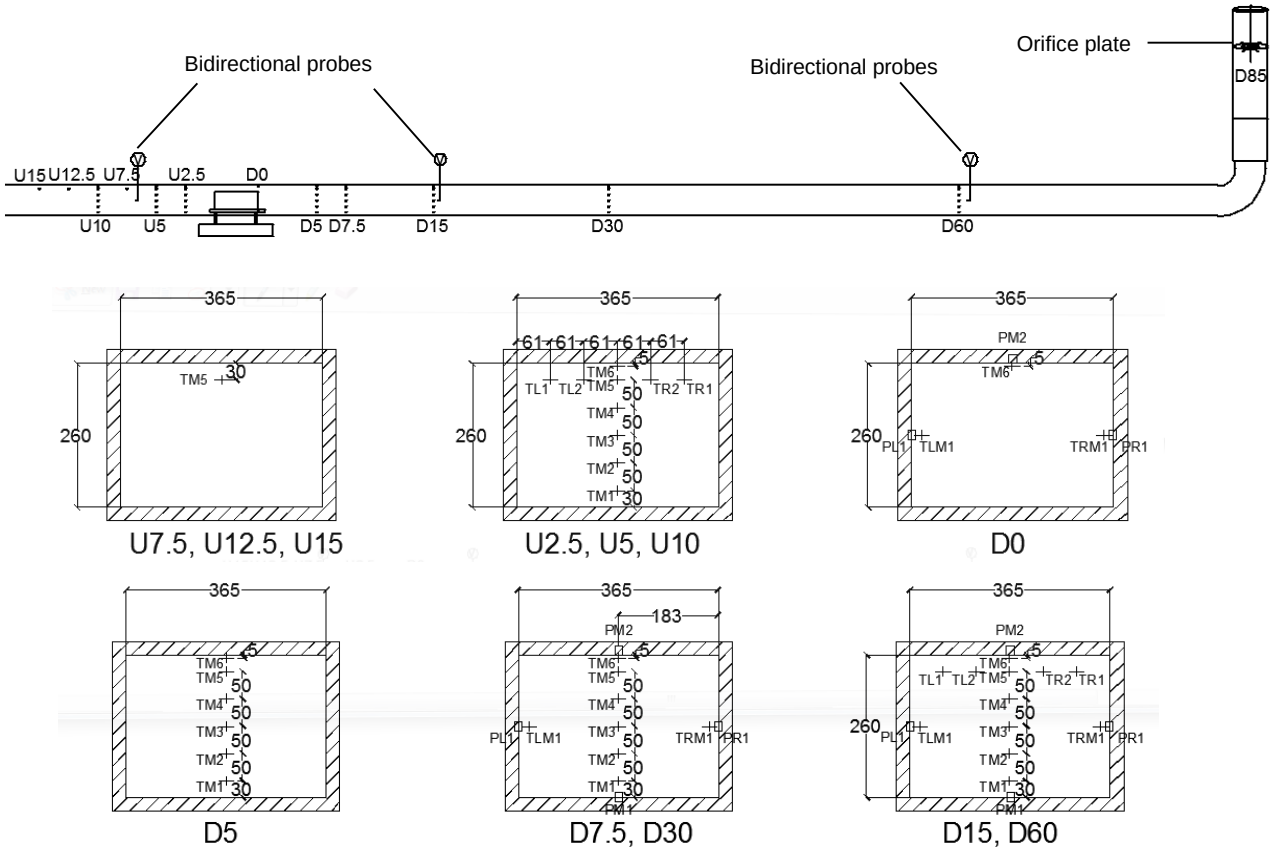

Figure 5-4: Instrumentation locations of the small-scale tunnel with upstream (U) and downstream (D) distances in 10^{-1}m and all other dimensions in mm.

The Ux/Dx designation corresponds to the location in the small-scale tunnel at a position x 10^{-1} m. away from the upstream/downstream edge of the fire. TMn and PMn define the thermocouples and plate thermocouples at the centre-line locations of the cross-sections; PLn and PRn denote the plate thermocouples at half height of the cross-sections on the left and right side walls; TLMn and TRMn refer to the thermocouples that are above the locations of

PLn and PRn; TLn and TRn refer to the horizontal thermocouple trees at 230 mm above the tunnel floor. The letters 'T' and 'P' are the abbreviation for thermocouples and plate thermocouples, 'n' is the thermocouple number, and 'M', 'L' and 'R' denote the centre-line, left and right side of the tunnel, respectively.

The velocity calculations and HRR calculations introduced below are not included in the original paper.

Due to the considerable soot production in wood crib fires, bidirectional probes were used in experiments to record the pressure differences for the calculation of velocity. The bidirectional probes were installed at locations U7.5, D5 and D60 indicated in Figure 5-4. The velocity is determined through Equation 5.6:

$$v = \sqrt{\frac{2\Delta P}{\rho_e}} \Big/ f(\mathrm{Re}) \tag{5.6}$$

In the Equation 5.6, $\rho_e = \rho_a T_a / T_e$ is the density of the airflow at the measured temperature T_e (K) where T_a and ρ_a are the ambient temperature (293 K) and density of air 1.21 kg m^{-3} and $f(Re)$ is the Reynolds number correction [76]. When the Reynolds number is in the range of 40< Re < 3800, $f(Re)$ can be calculated from:

$$1.533 - 1.366\times10^{-3}\,\mathrm{Re} + 1.688\times10^{-6}\,\mathrm{Re}^2 - 9.705\times10^{-11}\,\mathrm{Re}^3 + 2.555\times10^{-13}\,\mathrm{Re}^4 - 2.484\times10^{-17}\,\mathrm{Re}^5 \tag{5.7}$$

To determine the HRR in the experiments using the oxygen depletion method, the concept of this method is based on the difference in oxygen concentration between the incoming ambient air and the exhaust gases to determine HRR [77]. The accuracy of the result can be improved by adding the measurements of CO_2 and CO. Equation 5.8 and 5.9 are used to derive the heat release rate based on this method.

$$\dot{Q} = \left[E\phi - (E_{CO} - E)\frac{1-\phi}{2}\frac{X_{CO}^{A^e}}{X_{O_2}^{A^e}} \right] \frac{\dot{m}_e}{1+\phi(\alpha-1)} \frac{M_{O_2}}{M_a}(1 - X_{H_2 0}^{a}) X_{O_2}^{A^a} \tag{5.8}$$

$$\phi = \frac{x_{O_2}^{A^a}(1 - x_{CO_2}^{A^e} - x_{CO}^{A^e}) - x_{O_2}^{A^e}(1 - x_{CO_2}^{A^a})}{(1 - x_{O_2}^{A^e} - x_{CO_2}^{A^e} - x_{CO}^{A^e}) x_{O_2}^{A^a}} \tag{5.9}$$

where $\dot{m}_e$ is the mass flow rate of the flue gases, E is the heat release rate per unit mass of O_2 consumed (13.1 MJ/kg of O_2), E_{CO} heat release per unit mass of O_2 consumed for combustion of CO to CO_2 (17.7 MJ/kg), $X_{H_2O}^{a}$ is the actual mole fraction of water vapour in the incoming air, $X_{O_2}^{A^a}$ and $X_{CO_2}^{A^a}$ are the mole fraction of O_2 and CO_2 in the incoming air, respectively. $X_{O_2}^{A^e}$, $X_{CO_2}^{A^e}$ and $X_{CO}^{A^e}$ are the measured mole fraction of O_2, CO_2, and CO in the exhaust flow, respectively. α is the volumetric expansion factor, M_{O_2} and M_a are the molecular weight of oxygen and incoming air, which are 32 g/mol for oxygen and 29 g/mol for dry air, respectively.

In order to obtain the mass flow rate for the flue gases passing through the circular duct, the pressure drop across an orifice plate and the temperature at the orifice plate were recorded. The corresponding calculation for $\dot{m}_e$ is written as:

$$\dot{m}_e = C\sqrt{\frac{\Delta p}{T_e}} \tag{5.10}$$

The C in is the orifice plate coefficient, which needs to be calibrated at each velocity.

Three gas probes were also installed at the circular duct, where were prior to the orifice plate, connecting to gas analysers to record the mole fractions of O_2, CO_2, and CO. Figure 5-5 demonstrates the locations of the orifice plate and gas probes at the circular duct.

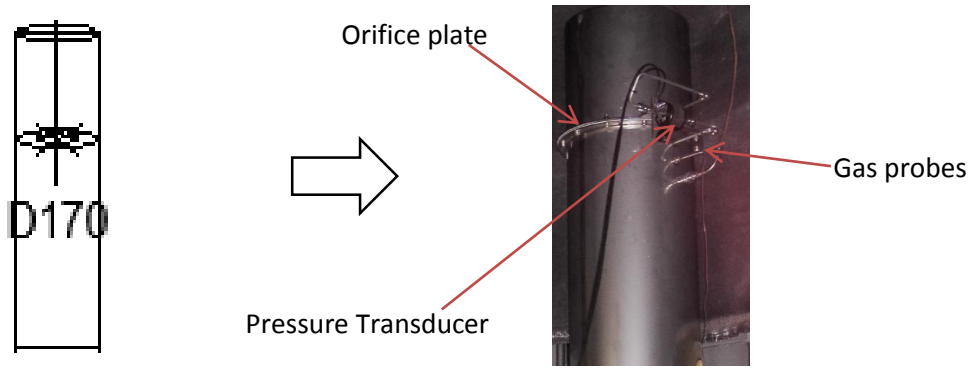

Figure 5-5: Measurements at the circular duct.

5.2.6 Experimental Procedure

As part of the calibration procedure a 20 kW steady state gas burner fire was used to obtain the orifice plate coefficient and also to monitor the responses from the sensors in the flue. The calibration procedure consisted of a three-minute period to ensure all the sensors were working normally followed by the activation of the fan for another minute to obtain a stable ventilation velocity. The 20 kW fire was allowed to run for 15 min followed by another 3 to 4 min to ensure the completion of the data recording. During an experiment the procedure for the initial four-minute baseline was the same as the calibration procedure. The completion of the data recording in the crib experiments was 3 to 4 min after the fuel source burnt out.

When the cribs were used as the fuel source, they were conditioned overnight in an oven at 60 ^{0}C to control the moisture content to be less than 3%. A circular pan in a diameter of ~80 mm contained 20 ml methylated spirits was put under the front end of the crib as the ignition source. The methylated spirits fire burned for about 2 min based on observations. Figure 5-6(a) and (b) illustrate an experiment using the gas burner and a crib as the fuel sources respectively.

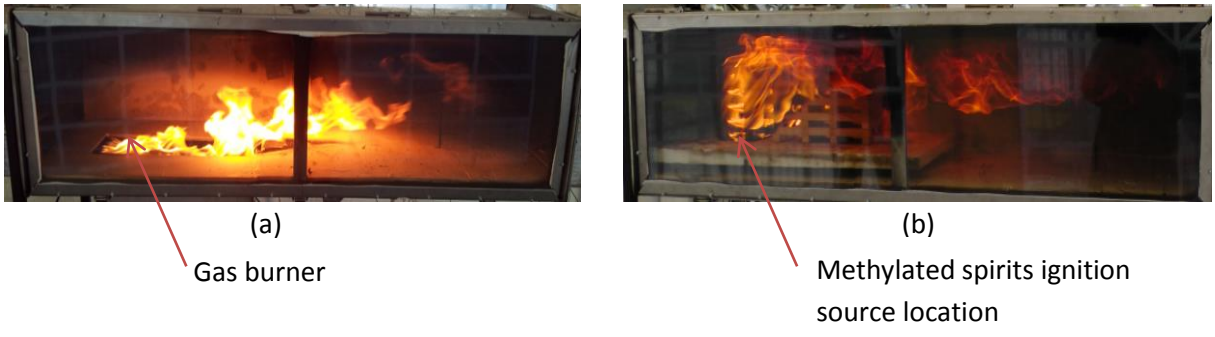

Figure 5-6: Photographs of (a) gas burner fire; (b) crib fire.

5.3 Results

5.3.1 Gas Burner Experiment Measurements

The measured velocity profiles at the three locations of U7.5, D15 and D60 for the gas burner experiment are presented in Fig. 6, where a moving average at 5s interval is adopted to smooth the velocity curves. The calibration time for the baseline has been excluded from the results. As seen, the changes in velocities relate to the development of the fire. The measured flow upstream of the fuel load shows lower values than the flow on the downstream side with and without the fire effects, which may be caused by the buoyancy effects in the chimney at the downstream end. It is also observed that higher velocities on the downstream side were obtained than the upstream side due to the expansion of the hotter gases. However, a velocity of ~ 0.68 m/s is able to be achieved when the influence from the fire is not significant.

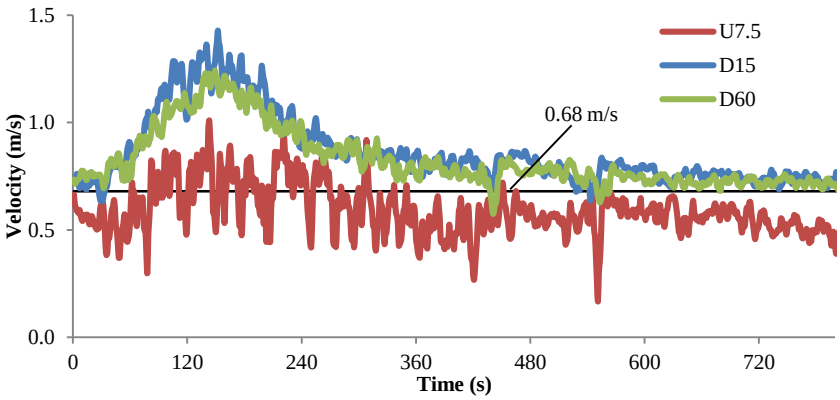

Figure 5-7: Velocity for the gas burner small-scale experiment.

Figure 5-8 shows that the HRR curve from the gas burner experiment was able to represent the scaled HRR results and so it is appropriate to compare the temperatures measured in the small-scale experiment with the corresponding temperatures at large-scale using Equation 5.4 and Equation 5.5.

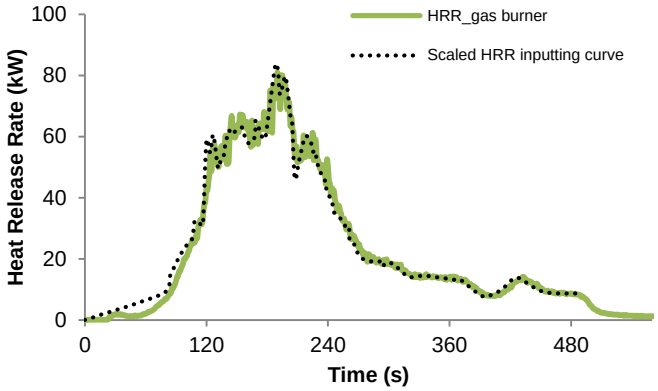

Figure 5-8: HRR for the gas burner small-scale experiment.

As part of the comparison it is noted that there is a time difference between the temperature measurements results at large- and small-scale. The time difference is due to the instantaneous fire in the small-scale experiment using the HRR results measured at the D170 location in the large-scale experiment. Therefore, the time at which the temperatures were measured in the small-scale tunnel have been adjusted to match the time in the large-scale experiment. Using the small-scale tunnel experiment gas transport time from the fire location to the flue sensors of ~ 12 s (further discussed in the crib experiment measurements section) an estimated time adjustment of 40 s to 50 s is derived from Equation 5.4. This is used to adjust for the temperature measurement offset in the large-scale experiment. With the corresponding data adjustment, the temperatures obtained at the D5, D7.5 and D15 locations from the small-scale experiments, where the data were converted to the large-scale using Equation 5.4 and Equation 5.5, are compared with the temperature results at the D10, D15 and D30 measured locations in the large-scale tunnel experiment. Temperature measurements at D60 are not examined here since the activation of the water spray in the large-scale experiment affected the results.

Figure 5-9 presents the temperature results at TM1, TM3 and TM6 for the three cross-sections obtained from the small-scale tunnel and the temperature results at the corresponding M06, M26 and M51 positions.

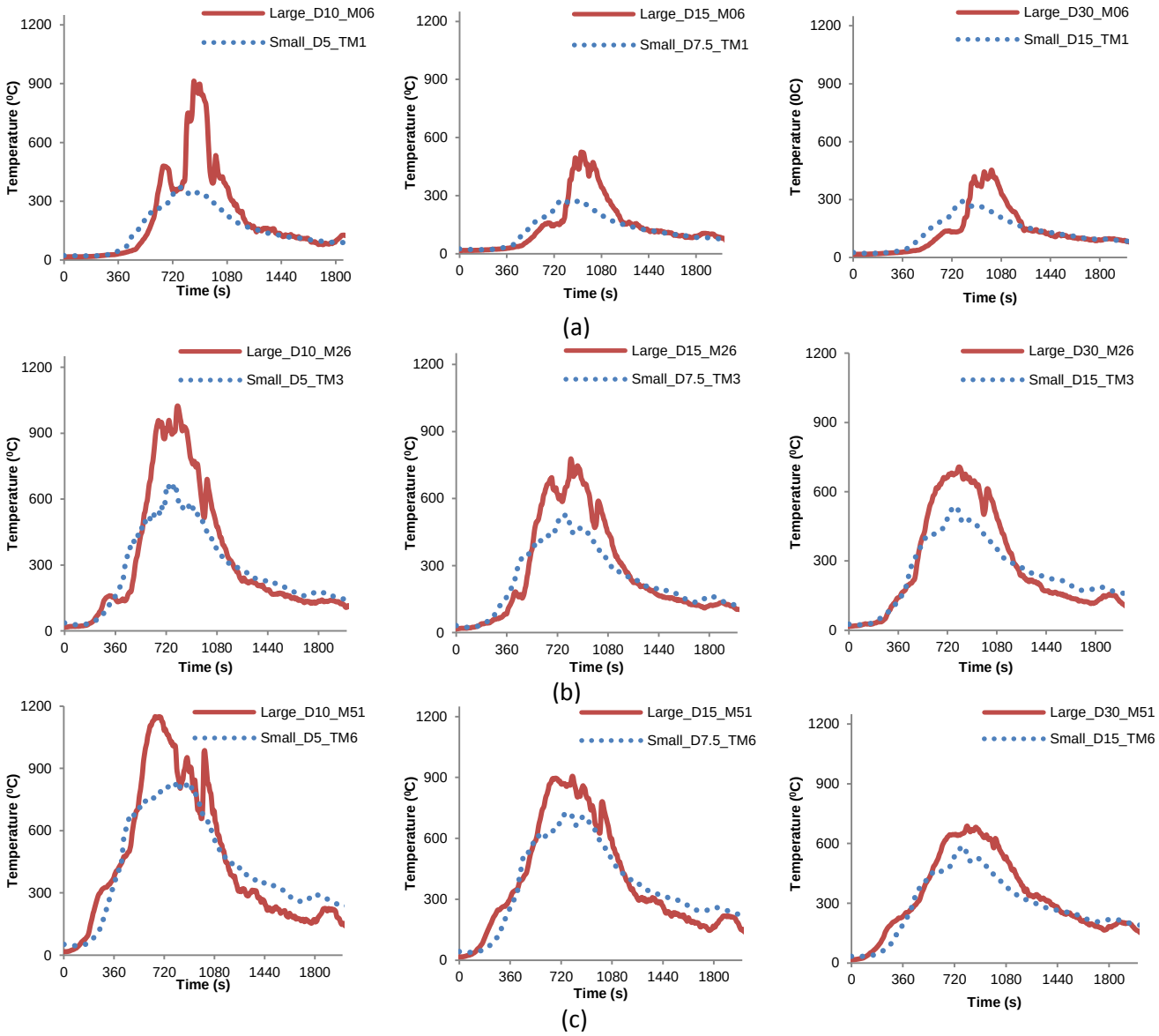

Figure 5-9: Temperature comparisons between the results derived from the small-scale gas burner experiment and the results measured from the large-scale experiment (a) at TM1 and M06 positions, (b) at TM3 and M26 positions, (c) at TM6 and M51 positions.

Figure 5-9 (a) shows the results for the positions closer to the tunnel floor at TM1 and M06. Here the shapes of the temperature curves from the small-scale tunnel results do not closely follow the large-scale curves particularly during the middle periods of the experiments. The peak temperatures at locations of D10, D15 and D30 in the large-scale tunnel experiments are about 2.5, 1.8 and 1.5 times higher than those obtained in the small-scale tunnel experiment at locations of D5, D7.5 and D15, respectively. The time to reach the peak temperature in the large-scale tunnel experiment is slightly later than the adjusted small-scale results. The differences are possibly due to the different fuel source set-ups used in the two experiments.

In the large-scale experiment, the fuel source was raised 1 m above the tunnel floor on a concrete support while the gas burner was at floor level in the small-scale experiment.

For the results at the TM3 and M26 measuring points shown in Figure 5-9 (b), located at the middle positions in both tunnels, the shapes of the curves are similar during the growth phase (0 s to ~600 s) and the decay phase (~1200 s to 1800 s). The peak temperature values from the large-scale experiment at the three cross sections are now ~1.5, 1.4 and 1.3 times higher than the temperatures at the corresponding three cross sections in the small-scale experiment.

The results at the high measuring positions given in Figure 5-9 (c) show that the shapes of the temperature profiles have a closer match when compared to those at the lower heights and similar to the middle positions, only minor differences are observed during the growth and decay phases. The difference in peak temperatures between the large-scale and the small-scale experiments has reduced to a factor of ~1.4, 1.3 and 1.2 at the three cross sections, respectively.

In order to examine the temperatures during the different fire development phases the flame lengths at the large-scale are estimated using an equation given by Ingason et al. [78]. The calculated large-scale flame length is ~6 m for the growth and the decay phases and ~33 m during the fully developed phase. Comparing with the observations from the small-scale experiments, the flame lengths observed from the small-scale experiment at the growth and decay phases are comparable to the estimated flame lengths at large-scale. However, the flame length during the fully developed phase in the small-scale experiment extended beyond the edge of the observation window which is ~750 mm downstream of the fuel. Therefore, the value of 33 m flame length at the large-scale is used to estimate a flame length of ~1650 mm at the small-scale, which suggests that the temperature locations of D5, D15 and D30 were all likely affected by the fire flame to different extends at fully developed fire stage.

Based on the analysis by Li and Ingason [79], the flame temperatures are determined by the boundary conditions. It is noted that more heat is lost in the small-scale experiments than large-scale experiments due to the differences in lining materials. Another reason is that due to the scaling the duration of the large-scale fire was much longer than the small-scale fire so that the tunnel lining in the large-scale experiment was heated up over a longer time. By the time the fire HRR reached the peak values, the temperatures in the large-scale tunnel lining were higher than the temperature of the small-scale tunnel lining. In addition, in the LTA large-scale experiment, the energy from the burning target located at D5 also contributed to the temperatures at the large-scale. As a result of these effects, the temperatures measured in the

small-scale experiments are less than the small-scale experiments consistent with the results in Li and Ingason's work. However in terms of the initial and decay phases, the flame effects, re-radiation effect from the tunnel lining and the influence from the burning target were much less significant such that the differences in the temperatures results at these two stages were minor.

5.3.2 Crib Experiment HRR and Mass Loss

For the three repeated crib fire experiments the transport time lag and the response time lag [80] for the measurement of species concentrations, temperature and pressure are accounted for to ensure that the calculated HRR results reflect the instantaneous fire energy release.

The 20 kW steady state gas burner fire was used for the time lag calibration and the normalised full-scale deflection (FSD) method [80] is adopted. The normalised FSD of O_2 and CO_2 with time are plotted in Figure 5-10. The initial four-minute baseline has been removed, hence the zero time is the time that the burner is ignited. The two separate time lags can be seen in the Figure 5-10: (transport lag) the time required for the change to travel to the instrument and (response lag) time required for the instrument to reach 63% of the FSD. As introduced in Figure 5-10 the time for the O_2 and CO_2 analyser to start to response is ~17 s which includes the travel time within the tunnel and the time for the sample to move through the conditioning system. The response time was also taken Figure 5-10 as 14 s for O_2 and 21 s for CO_2.

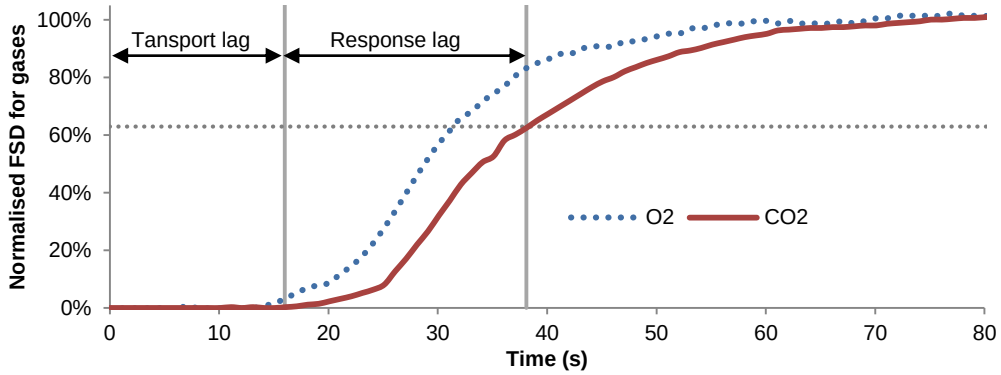

Figure 5-10: Time delays for normalised FSD data of O_2 and CO_2.

It is noted that the fuel in the tunnel was ignited ~8.5 m away from the pressure and temperature measurements at the orifice plate. It is assumed the transport of the combustion products was only due to the 0.68 m/s forced ventilation which gives a transport time of ~12 s. For the pressure transducer the response time is taken 0 s in comparison with response of the thermocouple which was 12 seconds as given Enright's calibration [80].

Using the time lag information shown in Figure 5-10, the experimental data from one of the crib experiments is used to analyse the influence of the time delays on the HRR calculations. The experimental data are shifted based on the transport time delays and the total time delays, respectively, the corresponding HRR curves are shown in Figure 5-11. The instantaneous mass loss rate curve from this experiment is also presented in Figure 5-11.

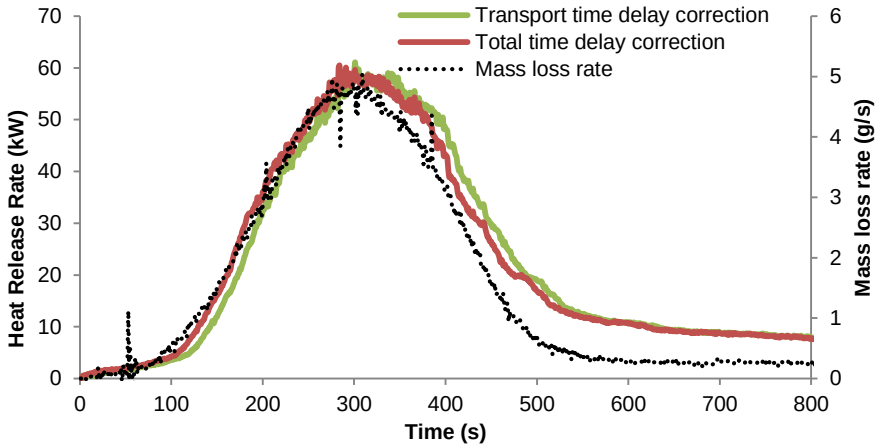

Figure 5-11: Data reduction to calculate HRR using a crib fire in the small-scale tunnel.

As shown in Figure 5-11, when the transport time delays are used, the calculated HRR curve still demonstrates an offset with respect to the instantaneous mass loss rate curve. When the total time delays are applied to the data reduction, the calculated HRR curve shifts forward to the start of the mass loss curve such that the corrected HRR curve is comparable to the mass loss rate curve. Therefore, the HRR curve based on the total time delay corrections can effectively represent the instantaneous fire size of the fire.

The same corrections are also made to the data from other two cribs where the HRR results for the three repeated experiments are plotted in Figure 5-12(a) and the mass loss rate curves are shown in Figure 5-12(b). The results demonstrate that good repeatability is obtained in the three experiments.

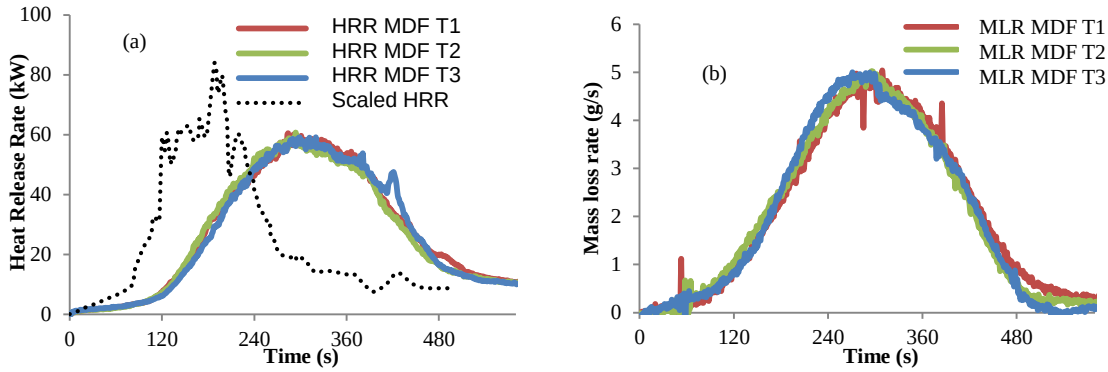

Figure 5-12: Experimental results from the MDF crib (a) HRR; (b) mass loss rate.

The scaled HRR curve from the large-scale experiment is plotted in Figure 5-12(a) to compare with the HRR curves obtained from the crib experiments. A comparable energy profile to the large-scale HGV cargo energy profile is obtained from the crib experiments in terms of a maximum HRR of ~60 kW and a total energy of 19 MJ (compared to the desired values of 67 kW and 17.6 MJ). However, the HRR curves from the crib fires have a limited ability to fully represent the detailed HGV cargo burning behaviour in the large-scale experiment. The crib curves do not show the same rapid increase in HRR 80 s after ignition and the short period of increased burning at around 180 to 205 s where the scaled HRR peaks at ~84 kW. The decay phase in the HRR is later in the crib than the equivalent large-scale experiment data.

5.3.3 Crib experiment velocity and temperature measurements

Due to the good repeatability in the three crib experiments the measured velocities and temperatures from one set are presented in this section. Figure 5-13 shows the velocity data (smoothed through the moving average at 5s interval) at the U7.5, D15 and D60 locations excluding the initial four-minute baseline period, The velocities at the three locations all maintain at a relatively stable value of 0.68 m/s for the first 120 s. The changes in the downstream velocities (D15 and D60) between ~120 s to 720 s were caused by the changes in temperatures (and hence gas density) during the different fire development stages. However, the velocity data measured upstream (U7.5) were relatively stable suggesting the changes in upstream temperatures were minor.

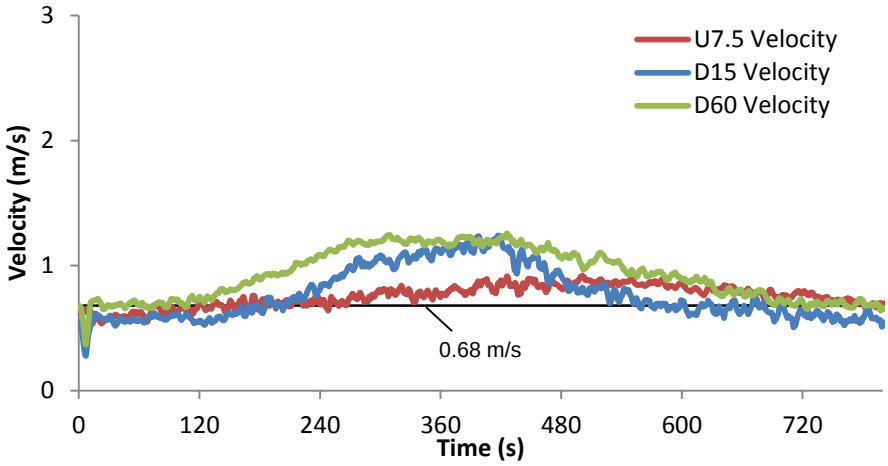

Figure 5-13: Velocity measurements at the U7.5, D5 and D60 locations.

According to the recorded data, the temperatures at the U2.5 location were <200 ℃, the temperatures at the U5 location were <60 ℃ and the temperatures at the U7.5 and U15 locations were around 20 ℃, which suggests that the influence of back layering is effectively controlled when the 0.68 m/s forced ventilation velocity was applied. As expected, the downstream temperatures were higher than those measured upstream. Figure 5-14 gives the detailed gas temperature profiles at the D5, D7.5, D15, D30 and D60 locations. The temperature profiles obtained from the gas burner experiment for positions of TM1, TM3 and TM6 at the corresponding locations are also plotted in Figure 5-14.

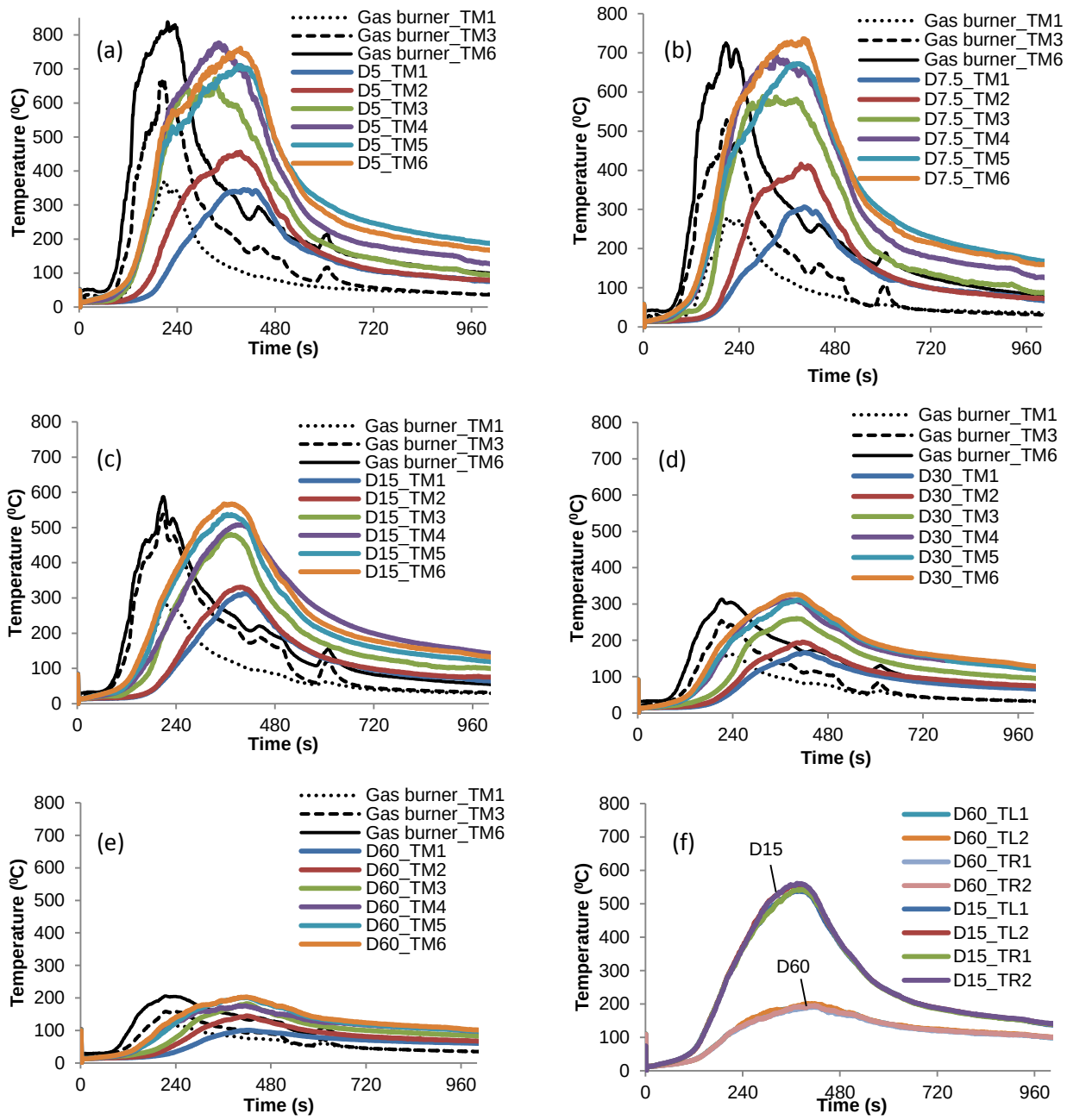

Figure 5-14: Gas temperature profiles at the D5, D7.5, D15, D30 and D60 locations.

The results in Figure 5-14(a) to (e) demonstrate a common temperature development trend where temperatures decrease with the increase in distance from the fuel source. For example, the maximum temperatures of TM6 are 770 ℃ at D5, 730 ℃ at D7.5 and it reduces to 200 ℃ at D60. In terms of the temperature gradients at each cross-section, the results in Figure 5-14 show that the temperatures at upper locations of the cross-section were higher than the lower locations due to buoyancy. The temperature profiles obtained from the gas burner experiment at positions of TM1, TM3 and TM6 for each cross-section demonstrate comparable peak

temperature value to the peak temperature obtained from the wood crib experiment. However, the times to reach the peak temperature in the two set of experiments are different.

Figure 5-14(f) shows that the temperatures measured at 230 mm above the tunnel floor horizontally across the D15 and D 60 locations. As seen, the temperature difference is negligible in the horizontal direction at the same location. The temperatures at D15 location are significant higher than the temperatures at D60 location.

5.4 Discussion

5.4.1 Fuel Sources

The use of the gas burner as fuel source is able to replicate HRR profile based on the large-scale HRR results. The scaled-up temperatures based on the gas burner experiment can effectively represent the temperatures at the large-scale when the fire flame radiation influence on temperatures is not significant. This suggests that the 1:20 scale tunnel provides an appropriate representation of the large-scale experiment within the constraints of the Froude number approximations. However one limitation of the gas burner experiment is that it cannot provide sufficient insight on the influence of ventilation on fires due to the use of the pre-defined HRR curve. Changing the forced ventilation velocity will likely alter the flame extension and downstream temperatures but any effect on the combustion would be minor.

When the cribs are used as the fuel source, the influence of forced ventilation, fuel porosity and three-dimensional geometry can be more directly reflected in the experiments, which allows for the opportunity to carry out parametric analyses. Clearly the representation of the pallet stacks used in the large-scale experiment using a crib of MDF sticks is an approximation. To more closely create the arrangement would require the construction of scaled-down stacked wood and plastic pallets which is simply impractical. So although the equivalent large-scale HRR curve is not able to be accurately obtained through the crib fuel sources, the information from the crib experiments is useful to conduct the planned pyrolysis modelling simulations, where the HRR is expected to be predicted based on the fuel properties, ventilation effects, etc.

5.4.2 Omission of the Target

As noted earlier the target stack of pallets used in the large-scale experiments was not included in the small-scale experiments. The influence of the stack in terms of HRR has been discussed

above but it is also possible that the target could have affected the velocity and temperature profiles. Such effects are exemplified in Chapter 8, where FDS is applied to model the large-scale tunnel experiment. The modelling shows that the target may have an effect on the temperature distributions at the downstream side of the fire in the fully development stage but the influence is minor during the initial fire growth and fire decay stages. However the modelling has to be treated with care as the target is simulated by a solid obstruction whereas in reality it would have been semi-porous.

In these experiments only the temperature measurements using the gas burner can be meaningfully compared to the large-scale experiment since the HRR curves are equivalent. However the gas burner is flush with the tunnel floor and not a three-dimensional object so although including the target may have affected the comparisons it still would have only been an approximation of the large-scale experiment arrangement. The cribs are more characteristic of the three-dimensional, porous simulated cargo load and so including the target would have been a closer representation of the geometry but, as shown above, the HRR from the crib was not equivalent to the cargo load so that any temperature comparisons are not practical whether the target is present or not.

In retrospect it would have been useful to have repeated some experiments with a target to gauge whether it affected the temperature measurements in the small-scale tunnel but the resources to do this were not available at the time. Even then the target would have to have been represented by an array of sticks that would not likely to have the same porosity as the original target and given the small-scale target would have to be placed 0.25 m away from the crib it is possible that turbulence effects would be different as this does not scale in Froude modelling. Furthermore there might need to be a debate on whether the sticks should be combustible or non-combustible since ignition of the small-scale target would unlikely match the large-scale experiment.

5.5 Conclusions

In this work, small-scale tunnel experiments were carried out by using a gas burner and cribs constructed of MDF as the fuel source. The velocity, temperature and the corresponding data for HRR calculations were obtained the experiments.

The time delays in the data for the calculations of HRR values are highlighted. The corresponding data reduction procedure for the time delays is presented. The data reduction based on the total time delays can effectively represent the instantaneous HRR results.

According to the comparisons of the HRR curves obtained from the crib and gas burner small-scale tunnel experiments with the scaled the large-scale HRR curve, the use of the designed crib as the fuel source has limits to fully represent the HGV cargo load burning in the large-scale tunnel experiment, while the HRRs from the gas burner small-scale tunnel experiment can closely reproduce the scaled large-scale tunnel HRR results.

Based on the comparison between the temperature results from the gas burner experiment and the temperatures measured in the large-scale tunnel experiment, the temperatures from the gas burner experiment can effectively represent the temperatures in the large-scale tunnel experiment, especially during the growth and decay phases. Since the radiation effect is not scaled, the temperature results from the small-scale experiment do not correlate so well with the temperatures from the large-scale experiment due to the differences in radiation effects from the flame and boundary conditions. The temperatures results from the crib experiment demonstrate a common temperature development trend where temperatures decrease with the increase in distance from the fuel source, while it is not practical to make any comparison with the large-scale temperatures.

Chapter 6 The Influence of Tunnel Ventilation on Crib Fires in Small-scale Experiments

Following the experiments introduced in Chapter 5, a series of tunnel experiments at different ventilation velocities were carried out. Cribs using a wood-based material were used as the fuel source and forced ventilation velocities from 0.23 m/s to 1.90 m/s were used.

The major content of this chapter is based on the paper ‘Investigation of the effect of tunnel ventilation on crib fires through small-scale experiments’ published in ‘Fire Safety Journal’

6.1 Introduction

The effect of longitudinal forced ventilation on HGV fires in tunnels has been widely investigated through different approaches. The most direct approach is to use large-scale tunnel experiments, such as the Benelux tunnel test series [10], in which HGV mock-ups were simulated using wood pallets and three different ventilation velocities of ~0.5 m/s, between 4 and 6 m/s and 6 m/s were used to observe the influence on the fires. The obtained peak heat release rates (HRR) of 13.5 MW, 19 MW and 16.5 MW for the three different scenarios show changes in fire size when velocity is altered.

In the work of Carvel and Beard [14], a Bayesian probabilistic method has been applied to analyse data from the limited number of tunnel fire experiments then available in the literature. Their work quantified the influence of forced tunnel ventilation on the enhancement of the HRR. For example, they estimated that the HRR increases up to 2 times and 3 times respectively, compared to a corresponding natural ventilation scenario for a two-lane tunnel HGV fire when ventilation velocity is at 3 m/s and 10 m/s. Carvel and Beard's analysis also suggests there is an enhancement to the HRR when velocities are more than 6 m/s.

SP Technical Research Institute of Sweden has carried out several series of small-scale tunnel experiments to further explain the ventilation impact on tunnel fires. Initially, Ingason [15] used a 1:23 small-scale tunnel to study the influence of longitudinal ventilation on fires in which wood cribs were adopted to represent HGVs. Velocities of 0.42 m/s, 0.52 m/s ,0.62 m/s and 1.04 m/s (corresponding to large-scale velocities of 2 m/s, 2.5 m/s, 3 m/s and 5 m/s respectively) were used in the experiments. The maximum HRR was found to increase by a factor of 1.4 to 1.55 under forced ventilation conditions compared to natural ventilation conditions, and these findings are lower than what is obtained from the Carvel and Beard approach. Furthermore, Lönnermark and Ingason [30] conducted another series of small-scale tunnel experiments using different porosity wood cribs to represent HGVs in tunnels. Four ventilation scenarios (1 m/s, 2 m/s, 3 m/s and 5 m/s for the corresponding large-scale velocities) were investigated. They found that when different ventilation velocities were used then low porosity fuels showed greater changes in the maximum HRR than for high porosity fuels. Ingason [15] concluded that the reason for these differences when compared with Carvel and Beard's approach was due to fuel porosity.

Given the findings discussed above with regard to the influence of forced ventilation on the HRR, the topic is still open to further analysis. Since using small-scale experiments is a cost-effective method to obtain quantitative results and to monitor fire behaviour this work adopts

the small-scale tunnel introduced in Chapter 5 to conduct a series of experiments for the study of the impact of forced ventilation on fires.

Cribs give consistent HRR results in fire experiments and there are many applications using wood cribs to represent fuels in tunnel experiments [15, 30, 74, 81]. In this work cribs using a wood-based material have been used to represent fuel source and these have been subjected to forced ventilation velocities from 0.23 to 1.90 m/s (1.0 to 8.5 m/s for the corresponding large-scale velocity) in addition to a natural ventilation (i.e. no forced ventilation) condition. Details of the impact of forced ventilation on the tunnel fires, particularly the results on the peak fire HRR are presented and the reason for this impact is explained. The consistencies and differences between the results from this work and previous studies are also discussed.

6.2 Small-scale Tunnel Experiments

6.2.1 Small-scale Tunnel Geometry

As introduced in Chapter 5, the small scale tunnel was built at a scaling ratio of 1:20 based on the original large-scale tunnel experiments conducted on behalf of the Land Transport Authority of Singapore in a tunnel test facility in Spain [39]. In the experiments, the Froude Scaling theory was adopted to scale the HRR, the velocity, the energy content, time and temperature. The dimensions of the small-scale tunnel were 0.365 m (W) × 0.26 m (H) × 11.9 m (L). An electrically powered fan was attached to the upstream end of the tunnel. The fan was 470 mm long, with a diameter of 250 mm and a maximum capacity of 1070 m^3/h. A control device was attached to the fan motor which allowed the fan speed to be varied over its full range. Following the fan, half metre long flow straighteners were installed within a steel box connecting to the main tunnel body to provide a uniformly mixed airflow. As introduced in Chapter 5, a combustion chamber was designer to locate the fuel and all the flue gases were collected at the downstream end of the tunnel through a circular duct, which had dimensions of 1.3 m (H) × 0.3 m (D). The illustration of the geometry of the small-scale tunnel can be found in Figure 5-3. Table 6-1 summarise the geometric characteristics of the tunnel.

Table 6-1: Small-scale tunnel geometric characteristics.

Items	Characteristics
Ventilation fan	0.47 m (L) × 0.25 m (D), 1070 m^3/h
Straighteners	0.365 m (W) × 0.260 m (H) × 0.500 m (L)
Main tunnel	0.365 m (W) × 0.260 m (H) × 10.375 m (L)
Circular duct	1.3 m (H) × 0.3 m (D)

6.2.2 Fuel Sources

Wood cribs are commonly used as fuel source in many small-scale tunnel experiments [15, 74, 82], since they give consistent results for a given geometry and stick configuration. The majority of the fuel source used in the large-scale tunnel experiments comprised of wood pallets and therefore cribs using a wood-based material are chosen to represent the solid fuels in this study. As said in Chapter 5, MDF is adopted to construct the cribs. The material properties of MDF have been comprehensively investigated by Li et al. [35, 71, 75]. In the numerical simulations of the experiments the solid phase are modelled using the method developed in Chapter 3 to derive the pyrolysis kinetics for the same MDF that was used to in this work. According to the investigation in Cheong's modelling analyses [11] and the observation from Lönnermark and Ingason's [30] experiments, varying the ignition location results in different burning behaviour and maximum HRRs in tunnel fires. In this work the ignition location is limited to the upstream end of cribs which is consistent with the ignition location in the large-scale tunnel experiments.

6.2.3 Energy Release

In order to achieve the similar energy release profile to the large-scale experimental data it was desirable that the cribs in the small-scale experiments produce comparable values of total energy and peak HRR to the values calculated from the scaling equations presented in Chapter 5. In the large-scale experiments, the recorded total energy was 99.2 GJ [39]. According to Equation 5.3, the scaled total energy for the small-scale tunnel experiments is 17.6 MJ. In the calculation, a combined effective heat of combustion 17 MJ/kg for the fuel source in the large-scale tunnel based on the LTA's data and an effective heat of combustion 12 MJ/kg for MDF [75] are used.

The recorded maximum steady heat release rate of 120 MW and the 3 m/s forced ventilation in the large-scale tunnel experiment was used to obtain the required peak HRR for the cribs. Using Equation 5.1 and Equation 5.2, a peak heat release rate of 67 kW at a 0.68 m/s forced ventilation velocity was necessary in the small-scale tunnel experiment. The corresponding peak HRR for a natural ventilation scenario is 45 kW derived from $\dot{Q}_{fv} = k\dot{Q}_{nv}$ [14]. In the calculation for $\dot{Q}_{nv}$, a k value of 1.5 for a fully involved HGV fire at 3 m/s forced ventilation in a two-lane tunnel [14] has been adopted.

6.2.4 Crib Geometrical Form

The configuration of cribs was geometrically scaled from the simulated HGV cargo fuel used in the large-scale experiments. Based on the scaling ratio of 1:20, a dimension of 100 mm (W) × 375 mm (L) × 150 mm (H) for the fuel load in small-scale experiments was calculated.

The internal-spacing between sticks (or porosity) has significant effects on crib fires [15]. Therefore, the porosity as well as the configuration of the cribs needed to be taken into account for the determination of their geometrical form. The influence from the porosity of cribs on mass loss rate has been comprehensively discussed in the literature [15, 83-86]. Ingason [15] proposed an equation to quantitatively define the influence of crib porosity on its mass loss rate based on the data from Croce and Xin [86] in free burn experiments for Sugar Pine wood cribs, such that:

$$\dot{m}'' = \frac{\dot{m}}{A_s} = 1.11\times10^{-3} b^{-\frac{1}{2}} \left(1 - e^{-6.28P}\right) \tag{6.1}$$

where A_s is the exposed fuel surface area and P is the porosity factor [15]. The detailed calculations for P can be found in Appendix B.

As discussed by Ingason [15], when P is larger than 0.7 mm, the mass loss rate is independent of P as the term $1 - e^{-6.28 \cdot P}$ is nearly equal to 1. Equation 6.1 is consistent with Block's equation [84]:

$$\dot{m} = CA_s b^{-0.5} \tag{6.2}$$

The fuel property constant C has been determined for different wood species and a value of $0.88 \times 10^{-3}\ g/s\ cm^{1.5}$ for Sugar Pine was obtained by Block [84]. However, it is important to

note that critical porosity factor (P) of 0.7 mm was derived under a quiescent environment and not in forced ventilation conditions.

To ensure the porosity factor in this work was greater than 0.7 mm and also meet the requirement of total energy, the geometrical form of the cribs was 5 layers each with three 375 mm long-sticks, six 100 mm short-sticks equally spaced and the thickness of each stick of 15 mm. Figure 6-1 illustrates the geometry and the dimensions of the crib where each portion of the crib between two sets of short sticks is defined in this paper as a 'bay'.

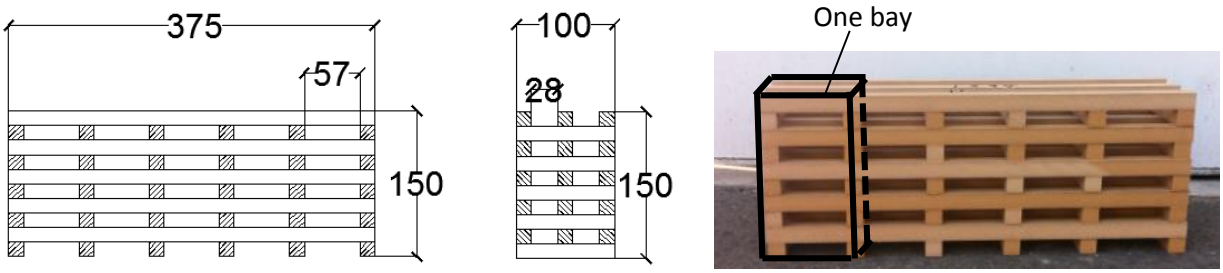

Figure 6-1: Crib geometrical form.

Based on the modified equations for rectangular shape wood cribs from [15], the porosity factor is calculated to be 0.8 mm and the corresponding $\mathrm{A_s}$ of the crib is 0.46 m^2. The total energy of the crib, calculated from $\mathrm{Q} = m \times \Delta H_e$, is 17.4 MJ where m is the mass of the crib (1.45 kg) and ΔH_e is the effective heat of combustion for MDF.

6.2.5 Free-burn and Natural Ventilation Experiments

Theoretically, the maximum mass loss rate for a scenario, where all exposed surface area of the crib is involved in a fire at the same time, can be derived through Equation 6.2 if the value of C for MDF is known. In order to estimate the maximum mass loss rate of the crib used in this work, an experimental approach is adopted. Due to the rectangular geometrical form of the crib the fire was unable spread evenly in each of the different directions to get the whole of the surface area involved simultaneously to reach the maximum mass loss rate. However, it was possible to get individual bays fully involved in fire and therefore a series of free-burn experiments were conducted to record the mass loss rate for each individual bay. The maximum loss rate of the whole crib is then taken as the summation of the maximum mass loss rate of each bay and the number of bays. A load cell system was installed to measure the mass loss rate. This system consisted of a non-combustible board platform with dimensions of 300 mm (W) × 500 mm (L) × 30 mm (H) and a weighing scale underneath connected to the

platform. The connections between the platform and the weighing scale were through four steel rods through the floor of the chamber. The height of the supporting steel rods were adjustable. The mass loss during an experiment was recorded every second by a data acquisition system. In the free-burn experiments, the crib was placed on the board platform in an open environment without any forced airflow influence and the fire was ignited at one end of the crib with a small pan (~ 80 mm in diameter) containing 20 ml of methylated spirits. The fire spread naturally from one bay to another bay until the entire crib was burnt out. Figure 6-2 shows the mass loss results and time series photographs for the 3 replicate experiments. Table 6-2 is the summary of the observations from the experiments and the corresponding mass loss rates at the times where the maximum values were reached.

Table 6-2. Summary of results when the free burn fires reach the peak mass loss rates.

Experiment number	Sum of bays	Total peak mass loss rate (g/s)	Average peak mass loss rate for a bay (g/s)	Peak mass loss rate for crib (g/s)
1	4.3 bays	4.7	1.09	5.45
2	4.1 bays	4.7	1.14	5.70
3	3.4 bays	4.2	1.23	6.15

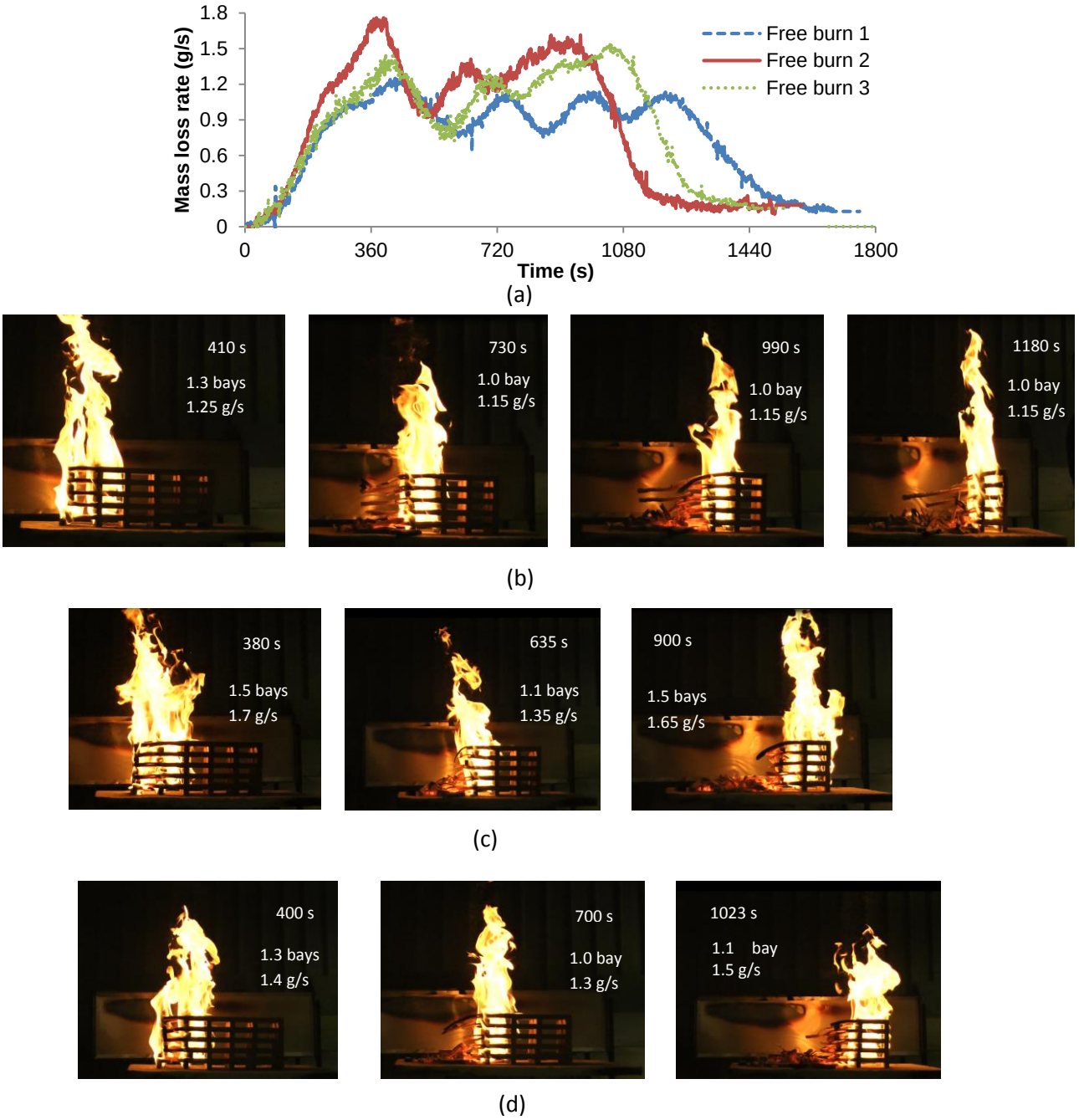

Figure 6-2: Crib free burn experiment: (a) recorded mass loss rate; (b) photographs of fire spread in bays in free burn experiment 1; (c) photographs of fire spread in bays in free burn experiment 2; (d) photographs of fire spread in bays in free burn experiment 3.

In each experiment the number of bays burning at each instance of measured peak mass loss was estimated from the video records. As illustrated in the photographs in Figure 6-2 the estimated number of bays burning at each peak mass loss rate was not constant and not unity. The estimated number of bays and measured peak mass loss values were summed in columns 2 and 3 for each experiment as thus an average peak mass loss per bay is shown in column 4 in Table 6-2. As shown the average maximum mass loss rate for a bay is 1.09 ~1.23 g/s,

which is effectively the mass loss rate for a bay with all of its exposed surface area involved in fire. The maximum mass loss rate of the crib is calculated as 5.45 ~ 6.15 g/s as the crib consists of five bays, which gives an average value of 5.8 g/s. Based on the geometrical form of the cribs used in this work, the C value for MDF is found to be $1.44 \times 10^{-3} \sim 1.62 \times 10^{-3}$ $\mathrm{g/s\,cm^{1.5}}$ through Equation 6.2, which is higher than natural wood species investigated in [84] (from 0.88×10^{-3} to 1.33×10^{-3} $\mathrm{g/s\,cm^{1.5}}$).

Subsequent to the free-burn scenario two repeated experiments were conducted to assess the energy profile of the crib in the small-scale tunnel under natural ventilation conditions. Had the small-scale tunnel been used without forced ventilation being provided, the flow of available oxygen would have been limited to the burning crib because of the blocked fan at one end and the flue at the other. Hence, in this set of experiments a shortened tunnel using just the combustion chamber without blockages at both ends was used. Since the combustion products were allowed to flow freely from both ends of the shortened tunnel, only the mass loss rates were measured. The same load cell system used for free-burn experiments was installed. The difference was that the platform board was within the chamber raised 20 mm above the tunnel floor and the weighting scale was installed underneath of the combustion chamber. The connections between them were sealed by fire resistant materials. The crib was placed on the load cell platform and 20 ml methylated spirits was used as the ignition source, located under one end in order to consistent with the ignition location in the large-scale experiments. The measurement variability between the two experiments was less than 7%, showing a good repeatability. Figure 6-3 illustrates the mass loss result from one of the experiments. The measured peak mass loss rate for the crib was 3.5 g/s and the total integrated energy for the fire was 15.2 MJ. The other experiment gave similar values.

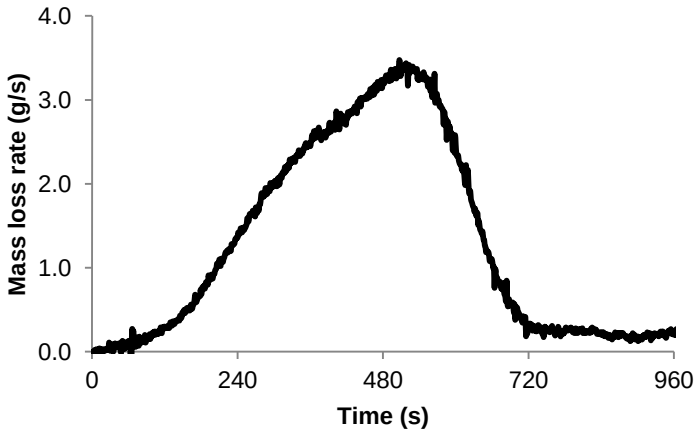

Figure 6-3: HRR curve for the crib under natural ventilation conditions in the shortened tunnel.

Table 6-3: Summary of results from the analysis of the ideal and natural ventilation scenarios.

Parameter	Scaled results from the large-scale tunnel for natural ventilation	Theoretical values under an ideal burning scenario*	Experimental results for natural ventilation in the shortened tunnel
$\dot{m}_p$ (g/s)	-	5.8	3.5
Q (MJ)	17.6	17.4	15.2
$\dot{Q}_p$ (kW)	45	70**	42**

*The ideal burning scenario is a fire involving all the exposed surfaces simultaneously of the crib, while the burning scenario for natural ventilation may not involve all the exposed surface area.

** The peak HRR is calculated using 12 MJ/kg for the effective heat of combustion.

As indicated in Table 6-3, the results obtained from the experiment under the natural ventilation scenario have comparable values to those from the scaled down from the large-scale experiment.

6.2.6 Forced Ventilation Experiments

In this study, a wide range of forced ventilation velocities have been applied to observe the influence on the fire. As the upper limit velocity requirement in PIARC (1999) [24] is 8-10 m/s for tunnels with a longitudinal ventilation system, a maximum velocity of 1.9 m/s was used for the fan at its highest available speed in the small-scale tunnel, which corresponds to 8.5 m/s at full-scale. A velocity of 0.68 m/s was investigated as this is the scaled down value for 3 m/s in the corresponding full-scale tunnel experiments is specifically investigated as this value happens to be the critical velocity to prevent the forming of back layering based on the empirical formula of Thomas [27]. The minimum velocity of 0.23 m/s is determined by the lowest fan speed in the experiments. In addition, scenarios with velocities of 0.40 m/s, 0.57 m/s, 0.90 m/s, 1.10 m/s, 1.20 m/s and 1.60 m/s were selected in between the minimum and maximum values to obtain a detailed profile of the influence on fire behaviour. In the experiments Table 6-4 lists the schedule for the small-scale tunnel experiments. One to three experiments were conducted for the different forced ventilation scenarios.

Table 6-4: Schedule of small-scale tunnel experiments.

Fan velocity (m/s)	Equivalent large-scale velocity (m/s)	Repetitions	Average percentage HRR variability	Average percentage mass loss variability
0.23	1.0	2	6.8%	9.3%
0.40	1.8	2	5.3%	16.2%
0.57	2.5	2	5.4%	20.4%
0.68	3.0	3	4.1%	9.3%
0.90	4.0	2	3.5%	13.5%
1.10	4.9	2	6.4%	14.6%
1.20	5.4	2	6.1%	11.9%
1.60	7.2	1	n/a	n/a
1.90	8.5	3	3.8%	11.4%

6.2.7 Instrumentation and Experimental Procedure

In the experiments, mass loss, gas temperature, wall surface temperature, velocity and heat release rates were measured.

Gas temperatures were measured by a series of bare type K, with 0.25 mm wire diameter, thermocouples. Surface temperatures were recorded through plate thermocouples installed on the insulated tunnel walls. Each plate thermocouple consisted of a 50 mm × 50 mm stainless steel plate painted black on the front side and a type K, 0.25 mm wire diameter thermocouple welded onto the backside of plate. In order to carry out further comparisons with the results recorded in the large-scale experiments, the locations of the thermocouples corresponded to the measurement locations in the large-scale tunnel experiments. Due to the considerable soot production in the crib fires, bidirectional probes were used in experiments to record the velocity data.

To determine the heat release rate using the oxygen depletion method the mass flow rate of flue gases was determined using an orifice plate and the mole fractions of O_2, CO_2, and CO were recorded via a probe installed prior to the orifice plate. As various air flow rates were used in the experiments, calibrations for the orifice plate coefficient were carried out and corrections made to account for the system time delays [80] between the mass loss, gas specie, temperature and velocity measurements.

All of the cribs were conditioned in an oven at 60 °C for overnight. In each experiment, the first three minutes was used as experimental baseline to record the background condition. After this the ventilation system was turned on for another minute in order to obtain a stable ventilation velocity. A ~80 mm diameter circular pan containing 20 ml methylated spirits was put under the upstream end of the crib as the ignition source. The methylated spirits was ignited a minute after the fan was started and this is taken as time zero in terms of the analysis. After the crib had burnt out, another three to four minutes of data was recorded.

6.3 Results and Discussion from the Experiments with Varied Velocities

6.3.1 Influence of Tunnel Ventilation Velocity on Fires

In the experiments the HRR results were recorded. Even though some forced ventilation velocities in the experiments were smaller than the calculated critical velocity [27], no appreciable smoke was observed coming out from around the fan area. However a very small amount of smoke leakage was noted in the experiments at the velocity of 0.23 m/s around some of the tunnel joints near the fan. Table 6-4 shows that the variability in the HRR results in the repeated experiments at the different forced ventilation scenarios are from 3.8% to 6.8%. Due to the good repeatability, the HRR results from one exemplar experiment at each different forced ventilation velocities (from 0.23 m/s to 1.9 m/s) are plotted in Figure 6-4. The HRR curve for the natural ventilation experiment is calculated from the mass loss rate results and effective heat of combustion. Since the 20 ml of methylated spirits used as the ignition source burnt out within the first 2 min of the experiment, the influence on the overall burning behaviour of the crib fire was minor.

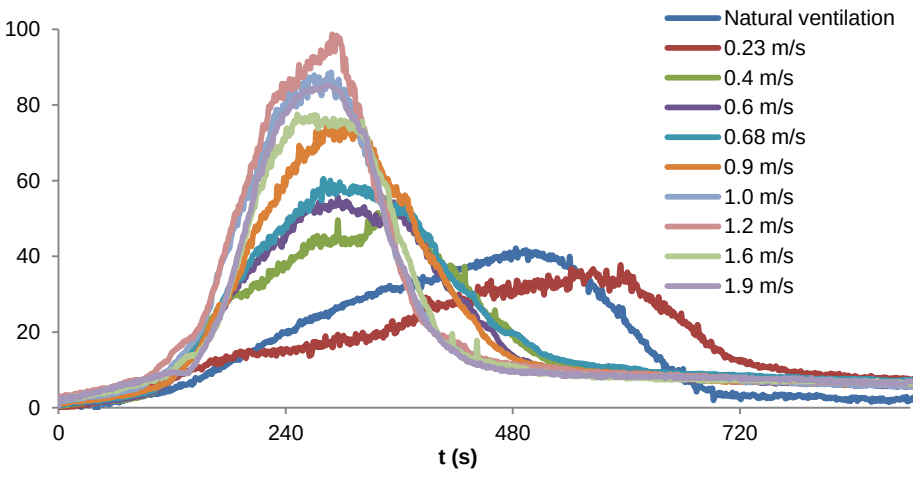

Figure 6-4: HRR curves at different velocities.

As shown in Figure 6-4, the peak HRR values vary with forced ventilation velocity. The peak HRR for natural ventilation and the scenario with velocity of 0.23 m/s occur at 480 s and 520 s after ignition. The peak value of HRR in natural ventilation is slightly higher than the peak value in using ventilation velocity at 0.23 m/s. Two reasons for this are considered: the first reason is possibly because the shortened tunnel without blockage at both ends for natural ventilation scenario provides a better combustion environment; the second reason may be due to the loss of energy from the back layering smoke leakage which was not captured by the calorimeter. For the scenarios using velocities of 0.4 m/s to 1.9 m/s the peak values appear at a similar time over the range from 240 s – 285 s. In order to further observe the differences, the average peak HRR values at the different velocities are presented in Figure 6-5.

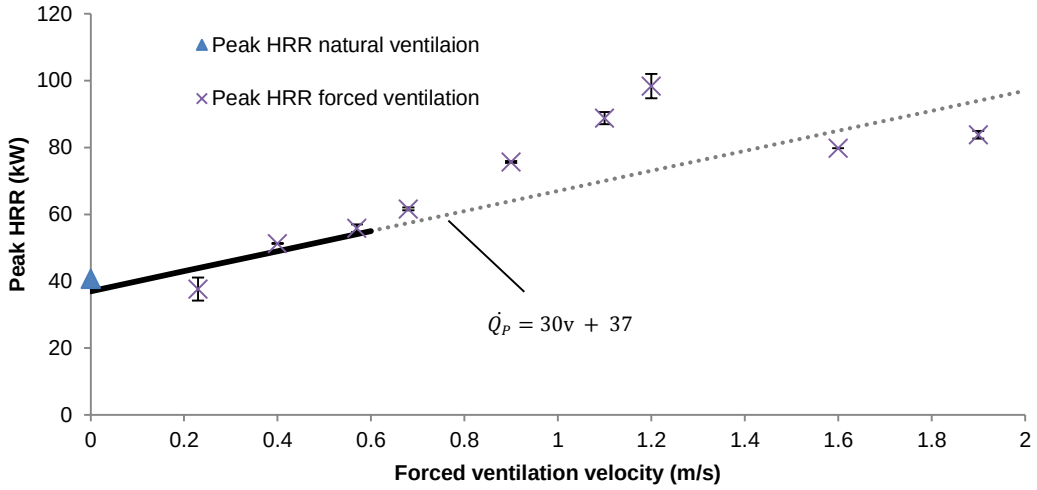

Figure 6-5: Averge peak HRR at different forced ventilation velocities.

The results in Figure 6-5 demonstrate that the peak HRR increases with the increase in forced ventilation velocity in the cases where the velocity is less than 1.2 m/s. When the forced ventilation velocity is above 1.2 m/s, the peak HRR no longer continues to show an increase but reduces to a constant rate of around 80 kW. A linear fit ($\dot{\mathrm{Q}}_{\mathrm{P}} = 30\mathrm{v} + 37$, where $\dot{\mathrm{Q}}_{\mathrm{P}}$ is the peak HRR and v is the ventilation velocity) is indicated to show the changes in peak HRR values, which will be further discussed in Section 6.3.2. According to calculations of the air/fuel equivalence ratio ø [13], when the forced ventilation is applied to the experiments, the values of ø are found to be more than one, which means the fires are fuel controlled and are not restricted by the available air. For fuel controlled fires, the energy release is independent of the oxygen supplied, so an investigation is carried out to examine why the forced ventilation velocity affects the HRR in the experiments. The series of images in Figure 6-6 shows the

burning behaviour of the cribs at the time the fires reach the corresponding peak HRR at the different forced ventilation velocities.

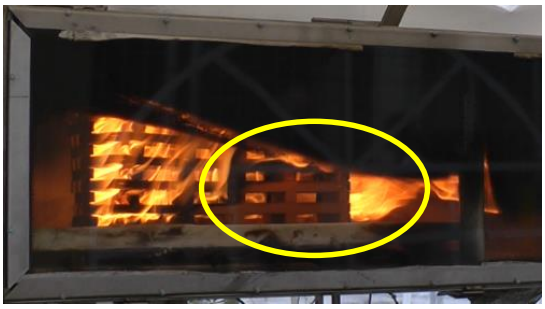

(a) Forced velocity at 0.4 m/s at 310 s, $\dot{Q}_p$ 51 kW

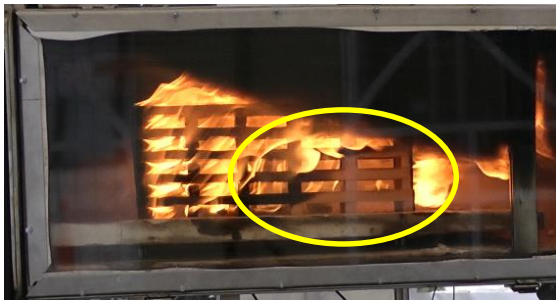

(b) Forced velocity at 0.6 m/s at 280 s, $\dot{Q}_p$ 56 kW

(c) Forced velocity at 0.9 m/s at 290 s, $\dot{Q}_p$ 76 kW

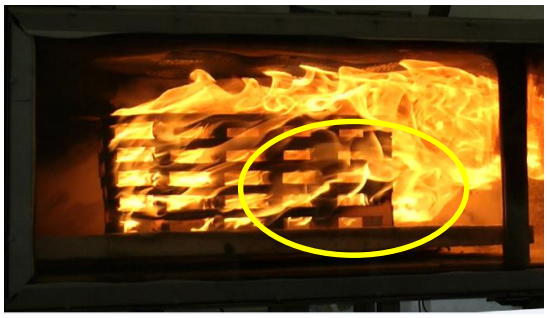

(d) Forced velocity at 1.2 m/s at 285 s, $\dot{Q}_p$ 98 kW

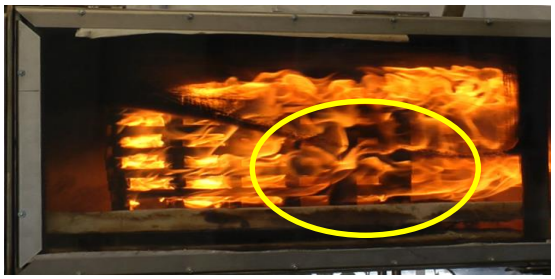

(e) Forced velocity at 1.6 m/s at 270 s, $\dot{Q}_p$ 80 kW

(f) Forced velocity at 1.9 m/s at 290 s, $\dot{Q}_p$ 84 kW

Figure 6-6: Burning behaviour of cribs at the time for the peak HRR.

Figure 6-6 (a), (b) and (c) are for the 0.4, 0.6 and 0.9 m/s velocity conditions respectively in which the peak HRR increases with the increase in velocity. As shown, the cribs in (a), (b) and (c) are not fully involved in the fire when the peak HRR values have been reached. Figure 6-6 (d) is for the 1.2 m/s velocity condition in which the highest peak HRR is obtained among the experiments. As shown in (d), the crib is almost completely covered by the flames at the time the HRR reaches the peak value. Figure 6-6 (e) and (f) are for the 1.6 and 1.9 m/s velocity conditions in which the cribs are completely engulfed by flames.

In order to more clearly show the mass loss data, a moving average at 20 s intervals is applied to smooth the experimental results. Figure 6-7 is a plot for the averaged mass loss rate curves at different forced ventilation velocities where the variability for each set of experiments is from 9% to 20% as listed in Table 6-4.

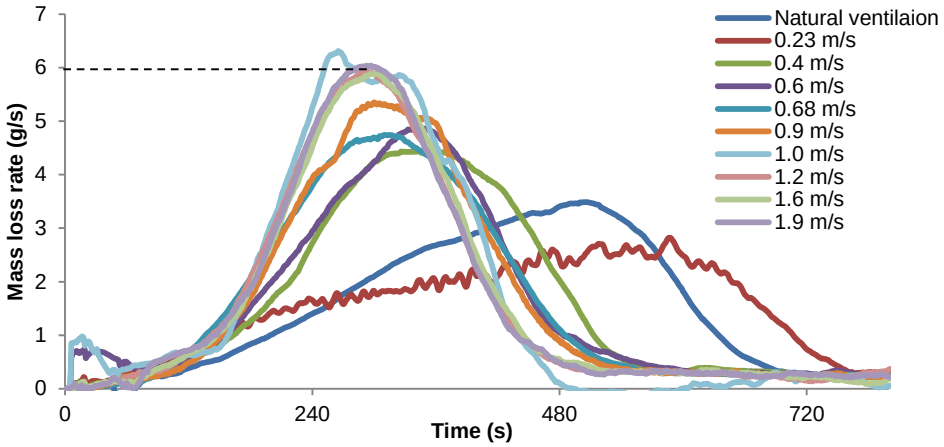

Figure 6-7: Smoothed mass loss rate curves at different forced ventilation velocities.

As shown in Figure 6-7, when forced ventilation velocities are less than 1.2 m/s, the increase in velocity increases the maximum mass loss rate. For forced ventilation velocities greater than or equal to 1.2 m/s, the curves for the 1.2 m/s, 1.6 m/s and 1.9 m/s conditions overlap at the same peak mass loss rate of ~ 6 g/s. This is within to the range of ideal values found to be 5.45 – 6.30 g/s based on the entire exposed surface area of the crib involved in a fire as discussed in Section 6.2.2.2.

According to the mass loss rate and heat release rate data, a series of consistent values for the effective heat of combustion at different velocities can be obtained over the burning period of the crib fires, which are presented in Appendix C. The results over the burning period from the repeated experiments are plotted in Figure 6-8 in which there are two dashed lines for the heat of combustion for MDF obtained from cone calorimeter (12 MJ/kg [75]) and bomb calorimeter (18.6 MJ/kg [87]). As shown, the burning efficiency behaves differently with the changes in the forced ventilation velocity. When the air velocity is less than ~ 0.6 m/s, the value of effective heat of combustion is the same as that obtained from the cone calorimeter. With the increase of air velocity, the burning efficiency gradually increases until a 90% efficiency is obtained when the forced ventilation velocity reaches to 1.2 m/s. However, the burning efficiency does not increase any further after 1.2 m/s but instead shows a decreasing trend to around 75%. This decrease in efficiency at high forced ventilation velocities may be the result of a cooling effect on the flame front, which decreases the fire spread rate and further

reduces the burning efficiency [88]. The results from the experiments suggest that the burning efficiency is a function of forced ventilation velocity. Three linear trend lines are shown in the figure to demonstrate the changes in effective heat of combustion with the change of velocities and details will be introduced in Section 6.3.2.

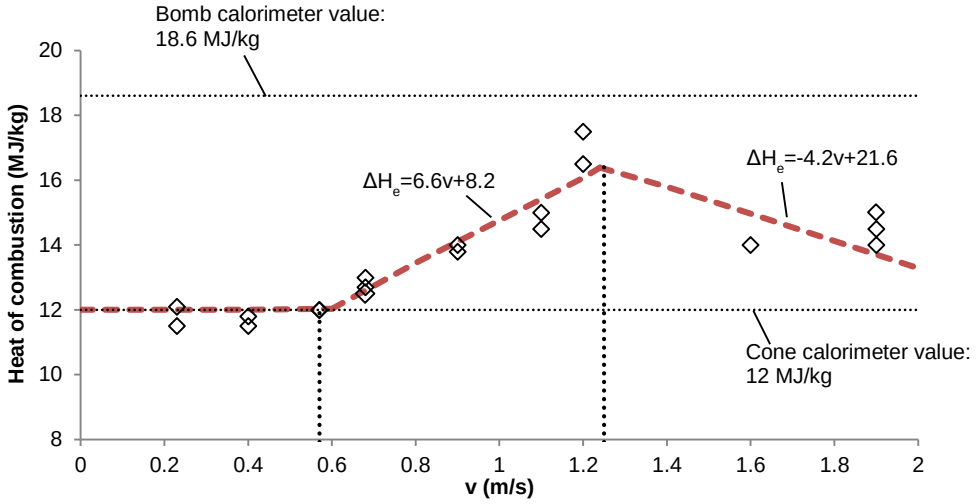

Figure 6-8: Effective heat of combustion at different forced ventilation velocities.

From all the above experimental results, it is clear that the forced ventilation airflow controls the development of tunnel fires. An increase in airflow increases the fire spread rate and further increases the burning surface area. When a larger burning surface area is involved, a higher peak HRR and peak mass loss rate is obtained. However, once the entire crib is engulfed in a fire, the increase in forced ventilation airflow is not able to enhance the burning surface area anymore. With the increase in air velocity, the peak mass loss rate remains at the same value, while the peak HRR value shows a decreasing trend from the highest peak value. The reason that the fire reaches a maximum peak value (HRR or mass loss rate) is because the fuel is fully involved and no more fuel is available. However, if a longer fuel package were used, it seems likely that the peak values of HRR and mass loss rate would be able to increase as there would be additional fuel for the flames to spread to. The role of the forced ventilation system is to increase the burning surface area rather than supplying more oxygen to the fire.

However, the forced airflow also affects the burning efficiency of the fire. Due to the decrease in burning efficiency after velocity of ~ 1.2 m/s, the peak HRR values show a decreasing trend at high velocities in the experiments. The reduction in burning efficiency after ~ 1.2 m/s has no effect on the mass loss rate, which remains a constant value of ~ 6 g/s. Therefore, when a crib is fully engulfed in a fuel controlled fire, which means no more fuel is available, the extra airflow through forced ventilation will not increase the rate of combustion. In contrast, the

burning efficiency might be reduced due to the cooling effect from the high speed airflow blowing towards the fire. Further experiments would be needed to confirm whether the burning efficiency will be further reduced or remain constant when a small-scale velocity of higher than 2 m/s is applied.

6.3.2 Analysis of Peak HRR Enhancement

In order to investigate the enhancement in peak HRR at different forced air velocities, a simplified mathematical model is developed based on the results shown in Figure 6-5 and Figure 6-8. As discussed, the forced ventilation affects fire spread rate and burning efficiency and then further affects the values of peak HRR. However, the extent of the influences is different with the changes in forced ventilation velocities. When the air velocity is less than 0.6 m/s, the forced ventilation influence on burning efficiency is negligible; while it increases the fire spread rate and the peak HRR values. When the air velocity is greater than 0.6 m/s, the effective heat of combustion varies with the changes in forced ventilation velocities. At this stage, the peak HRR is both affected by the burning efficiency and fire spread rate until the fuel is fully engulfed by the fire. Once the fuel is fully engulfed, there is no further fuel available for the flame to spread to and so the peak HRR is only affected by the burning efficiency. The three stages can be mathematically expressed as:

When $v \leq 0.6\ \mathrm{m/s}$, then $\dot{Q}_p = \gamma_{fs}\dot{Q}_{p,nv}$, while $\dot{Q}_p < \dot{Q}_{p,engfuled}$

otherwise

$\dot{Q}_p = \dot{Q}_{p,engfuled}$

When $v > 0.6\ \mathrm{m/s}$, then

$\dot{Q}_p = \gamma_{fs}\gamma_{be}\dot{Q}_{p,nv}$, while $\dot{Q}_p < \dot{Q}_{p,engfuled}$

otherwise

$$\dot{Q}_p = \gamma_{be}\dot{Q}_{p,engfuled} \tag{6.3}$$

where, γ_{fs} and γ_{be} are the enhancement factors due to the fire spread rate and the burning efficiency, respectively. The parameter $\dot{Q}_{p,nv}$ is the peak HRR for the natural ventilation scenario and $\dot{Q}_{p,engfuled}$ is the peak HRR if the fuel is fully engulfed in the fire.

The parameter γ_{fs} can be represented by a linear relationship for the peak HRR against air velocity when $v \leq 0.6\ \mathrm{m/s}$ as shown in Figure 6-5 such that:

$$\dot{Q}_{p,v} = 30v + 37 \tag{6.4}$$

Using this linear correlation, $\dot{Q}_{p,v}$, the peak heat release rate at different forced ventilation velocities can be calculated so that γ_{fs} is calculated by:

$$\gamma_{fs} = \dot{Q}_{p,v} / \dot{Q}_{p,0} \tag{6.5}$$

In terms of γ_{be}, the expressions in different regions can be obtained from Figure 6-8 for the effective heat of combustion values which are:

$$\Delta H_{e,v} = 12,\ 0 \leq v \leq 0.6 \text{ m/s}$$
$$\Delta H_{e,v} = 6.6v + 8.2,\ 0.6 < v < 1.24 \text{ m/s}$$
$$\Delta H_{e,v} = -4.2v + 21.6,\ v \geq 1.24 \text{ m/s} \tag{6.6}$$

In the experiments, when the forced ventilation velocity is zero, the effective heat of combustion is the same as the 12 MJ/kg value measured in the cone calorimeter [75] and therefore, γ_{be} is taken to be:

$$\gamma_{be} = \Delta H_{e,v} / 12 \tag{6.7}$$

Ingason and Lönnermark [82] highlight the important effect of the fuel porosity on the peak HRR in a tunnel fire involving wood cribs. In their study, two different porosities of wood cribs, denoted as P1 = 2.1 mm and P2 = 0.62 mm, were used as the fuel sources to carry out a series of experiments in a small-scale tunnel (0.45 m (W) × 0.25 m (H) × 10 m (H)). The HRR curves for the two different porosity wood cribs in different forced ventilation scenarios of 0.22 m/s, 0.67 m/s and 1.12 m/s corresponding to 1 m/s, 3 m/s and 5 m/s in large-scale were compared. The mass loss curve for the P1 wood crib under natural ventilation scenario was also recorded. The conclusion regarding fuel porosity in their work is that very high changes in peak HRR are expected for a low porosity fuel source ($P \leq 0.7$ mm) when the forced ventilation airflow rate is altered, while only weak changes in peak HRR for a high porosity fuel source is found [82].

Details for the experiments and results are listed in Table 6-5 where values for $\dot{Q}_{p,engulfed}$ are estimated from Equation 6.1 and the corresponding heat of combustion value of 17 MJ/kg obtained from free burning tests [30]. Values for $\dot{Q}_{p,nv}$ were not measured in Lönnermark and

Ingason's experiments but a reported ratio of $\mathrm{MLR_{ratio}/HRR_{ratio}}$ is given as 1.26 and the value of $\mathrm{MLR_{ratio}}$ is 1.4 [30]. The parameters $\mathrm{MLR_{ratio}}$ and $\mathrm{HRR_{ratio}}$ are the ratios of the maximum mass loss rate and maximum HRR for the natural ventilation scenario and the free burn scenario. Since the values for $\dot{Q}_p$ in the free burn scenarios are known for wood crib P1 (50 kW) and wood crib P2 (53 kW) [30], values for $\dot{Q}_{p,nv}$ for P1 and P2 are derived based on the ratios giving 55 kW and 58 kW, respectively.

Table 6-5: Details of the small-scale tunnel and cribs for the comparison.

No.	Cross section W × H (mm)	P (mm)	Fuel dimensions W × L× H (mm)	B (mm)	A_s (m^2)	$\dot{Q}_{p,nv}$ (kW)	$\dot{Q}_{p,engulfed}$ (kW)	Reference
P1	450 × 250	2.10	150 × 500 ×105	15	0.54	55	83	[82], [30]
P2	450 × 250	0.62	150 × 500 × 90	10	0.8	58	147	[82], [30]
P3	375 × 260	0.80	100 × 375 ×150	15	0.48	42	70	This work

Using Equation 6.3, the $\dot{Q}_p$ values at different velocities for the three different porosity cribs can be calculated. In order to demonstrate the enhancement to the fire size, k the ratio of the peak HRR under forced ventilation (*fv*) conditions and the peak HRR under natural ventilation (*nv*) conditions is introduced in this study, which was firstly adopted in Carvel and Beard's [14] work. Therefore, the enhancements to peak HRR for different porosity cribs at different velocities, which are represented by k, are plotted in Figure 6-9.

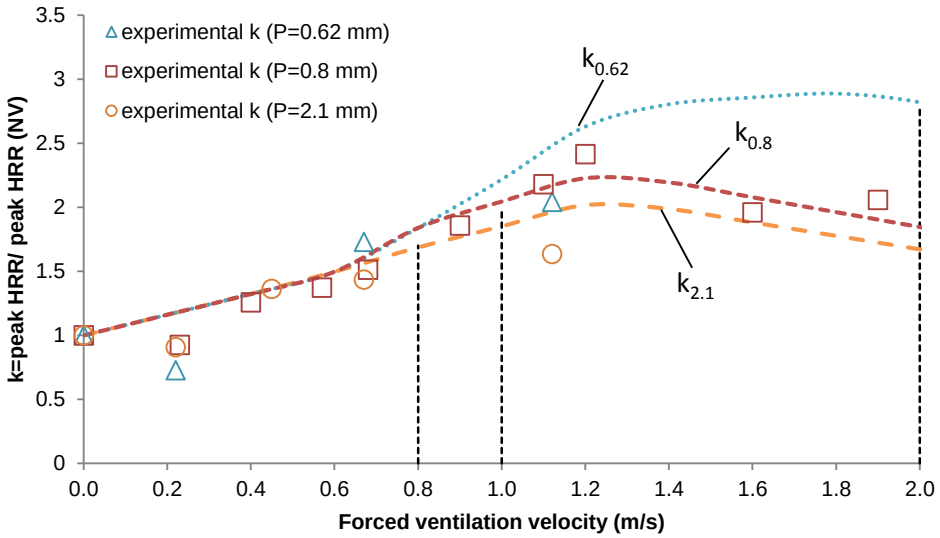

Figure 6-9: Influence of fuel porosity on the enhancement to peak HRR.

In Figure 6-9, the three k curves ($k_{0.62}$, $k_{0.8}$ and $k_{2.1}$) illustrate the enhancement trend for cribs at the different porosity factors of 0.62 mm, 0.8 mm and 2.1 mm. Vertical dotted lines indicate the calculated velocity at which the crib is fully engulfed in flame. As shown, the peak HRR enhancement using a low porosity wood crib of 0.62 mm is larger than the cases using porosity values of 0.8 mm and 2.1 mm, which is consistent with Ingason and Lönnermark [82] in that high changes in peak HRR are more likely to occur using a low porosity crib than using a high porosity crib at different forced ventilation velocities.

The corresponding experimental data for the three different porosity cribs are also indicated in the plot. Since the available data points for P = 0.62 mm and P = 2.1 mm are limited in terms of forced ventilation velocity and only a single experiment at each velocity was referred to by Lönnermark and Ingason [30]) then some experimental points do not closely follow the ′k′ curves. For instance, the experimental data point for P = 0.62 mm at ~1.1 m/s has a similar value to the experimental point for P = 0.8, which is much higher indicated on the $k_{0.62}$ curve. However, the overall enhancement trend of peak HRR based on the data points for different porosity cribs demonstrate a similar developing trend as the k curves. According to the calculations from Equation 6.3, it is also found that the different porosity cribs start to become fully engulfed by the fire at different forced ventilation velocities. The lower the porosity of the crib then the higher the forced ventilation velocity that is required for the fire to spread over the entire fuel surface. As indicated in Figure 6-9, a forced ventilation velocity of 0.8 m/s is needed for the fire to engulf the crib having a porosity of 2.1 mm, whereas 1 m/s and 2 m/s are required for the fire to spread over the crib having a porosity of 0.8 mm and 0.62 mm respectively. The results suggest that different porosity fuels in a fire will result different involvements of burning surface area in a fire and further affect the corresponding peak HRR.

The involvement of burning surface area in a fire can also be modified by providing more available fuel either by having a longer HGV or additional neighbouring vehicles. For a tunnel fire scenario with multiple fuel packages the fire is able to spread from the original fuel source towards the downstream fuel packages under forced ventilation conditions and the peak HRR will also be increased. The involvement of multiple fuel packages can be simplified by increasing the length of a crib since the work by Hansen and Ingason [81] showed that under forced ventilation there is no significant delay to the time to ignition among fuel packages that are placed within short distances of each other. Based on this concept, two different cribs of lengths 1.2 times and 2 times of the original crib (L) used in this study are applied to investigate the enhancement to the peak HRR when more fuel is available where the 1.2 and 2 factors have been arbitrarily selected to illustrate the approach.

By scaling-up the work by Hansen and Ingason [81] it suggests that an adjacent pallet target 9 m or further downstream away from the fuel source would not ignite under a low forced ventilation of 1.2 m/s then the $\dot{Q}_{p,nv}$ values for the different length cribs are considered to be the same as the original crib. Since the A_s values are increased with regard to the ratios of the crib lengths, the values of $\dot{Q}_{p,engufled}$ are 84 kW and 140 kW for the $1.2L$ crib and $2L$ crib.

The $\dot{Q}_p$ values for the three different length cribs are obtained from Equation 6.3 and corresponding values of k are calculated by dividing by $\dot{Q}_{p,nv}$. By converting the small-scale values to the large-scale equivalent values using the 1:20 ratio a plot of k curves (k_L, $k_{1.2L}$, and k_{2L}) for the different length cribs is shown in Figure 6-10.

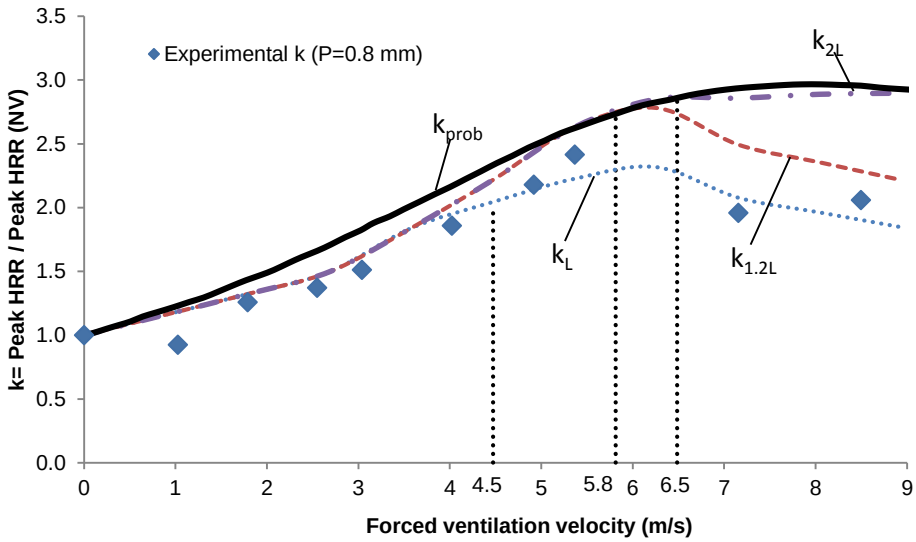

Figure 6-10: Influence of length of fuel on the enhancement of peak HRR.

As shown in Figure 6-10 with the increase in the length, the forced ventilation velocity required to initially engulf the cribs is increased and the values of the maximum enhancement k are also increased. The engulfing velocity is 4.5 m/s when original crib length is used however when the length is increased by a factor of 1.2 the engulfing velocity is increased to 5.8 m/s (shown on Figure 6-10 as the two vertical dotted lines at the two corresponding velocities). When the crib is twice the original length the fire will not be able to engulf the fuel within the ventilation design range while at the same time the peak HRR will not keep increasing either as the burning efficiency will reach a maximum value at ~ 6.5 m/s (again shown on Figure 6-10) and will even be reduced thereafter due to the cooling effect from flame front. Therefore, a maximum enhancement factor of ~3 is obtained based on this study. The same trend is found for cribs with porosity factors of 0.62 mm and 2.1 mm when the length of the cribs is altered.

The results of Carvel and Beard in Figure 6-10 are denoted as curve k_{prob}, which demonstrate the fire size enhancement trend for a fully involved HGV fire in a two-lane tunnel [14]. The values of k_{prob} are the probabilistic results based on a series analysis of tunnel fire tests data including ones with wood cribs and HGVs. There is approximately a 50% probability to achieve these values [14]. Interestingly, the 50% probabilistic curve effectively estimates the enhancement in fire size for the scenarios in which available fuels are sufficient and forced ventilation conditions are available.

From the above comparisons it is found that the difference between the conclusions from Lönnermark and Ingason and those from Carvel and Beard is because the two studies describe the enhancement in fire size for different characteristic fuels used in tunnel fires. Different porosity factors of fuels result in significant differences in the involvement of burning surface area, higher changes in peak HRR for low porosity cribs can be obtained than for high porosity cribs. However, for the fuels with similar burning surface area the trends of enhancement on fire size are similar. In the condition that the fuels are sufficiently large and ventilation is available, the enhancement curve for crib-type fuels derived from this study has a good match with the results of Carvel and Beard. Further experiments would be needed to confirm whether the burning efficiency will be further reduced or remaining constant when a velocity of higher than 2 m/s (at the small-scale) is applied and also whether the geometry of the crib has any influence on the results.

6.4 Different Length and porosity Cribs

Based on the small-scale tunnel set-up presented previously, Cateley and Crum [89] conducted some extra tunnel experiments using MDF crib length of 500 mm and 750 mm, crib porosities of 1.0 mm, 1.5 mm and 2.0 mm and forced ventilations of 0 m/s, 1.4 m/s, 1.7 m/s and 2.0 m/s at the University of Canterbury. Based on the experimental data collected by them, it is found that the burning behaviour is affected by the crib length. The experimental data for the crib porosity of 1.0 mm, which is similar to the crib porosity 0.8 mm in the previous work, are presented in Figure 6-11 in order to investigate the influence of the wood crib length.

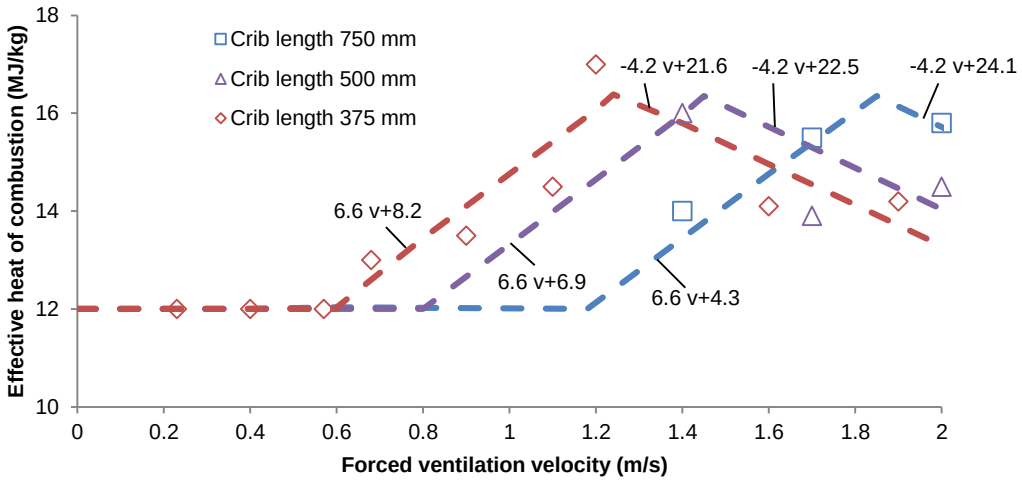

Figure 6-11: Effective heat of combustion for different length cribs.

As seen in Figure 6-11, when the crib length is increased from 375 mm to 500 mm and 750 mm, the heat of combustion values at high velocities do not follow the changing trend suggested previously. The results for the 500 mm cribs show a high value at 1.4 m/s and similar values at 1.7 m/s and 2.0 m/s, while the results for 750 mm cribs clearly demonstrate an increasing trend from 1.4 m/s to 1.7 m/s. Based on the trends indicated on the figure, an assumption is made that the longer the crib is, the higher the velocity needed, initially, to influence the burning efficiency in the crib fire. Because crib length is then considered as a factor influencing the burning efficiency, the previous Equation 6.6 is revised as below:

$$\Delta H_{e,v}=12,\ 0 \le v \le 0.6L/L_0$$

$$\Delta H_{e,v}=6.6v+12.2-3.96L/L_0,\ 0.6L/L_0 < v < 0.64+0.6L/L_0$$

$$\Delta H_{e,v}=-4.2v+2.52L/L_0+19.1,\ v \ge 0.64+0.6L/L_0 \qquad (6.8)$$

where L_0 is the initial crib length (375 mm in this study) and L is the actual crib length. When the crib is 500 mm long, the burning efficiency starts to increase after the velocity reaches 0.8 m/s and it starts to decrease after the velocity reaches 1.44 m/s. When a 750 mm long crib is applied, the burning efficiency is not influenced by the velocity until 1.2 m/s. As seen in Figure 6-11, the linear relationship between the velocity and heat of combustion is shifted with the changes in crib lengths. The measured heat of combustion for cribs with porosities of 1.5 mm and 2 mm are compared with the linear lines derived from Equation 6.8, in Figure 6-12.

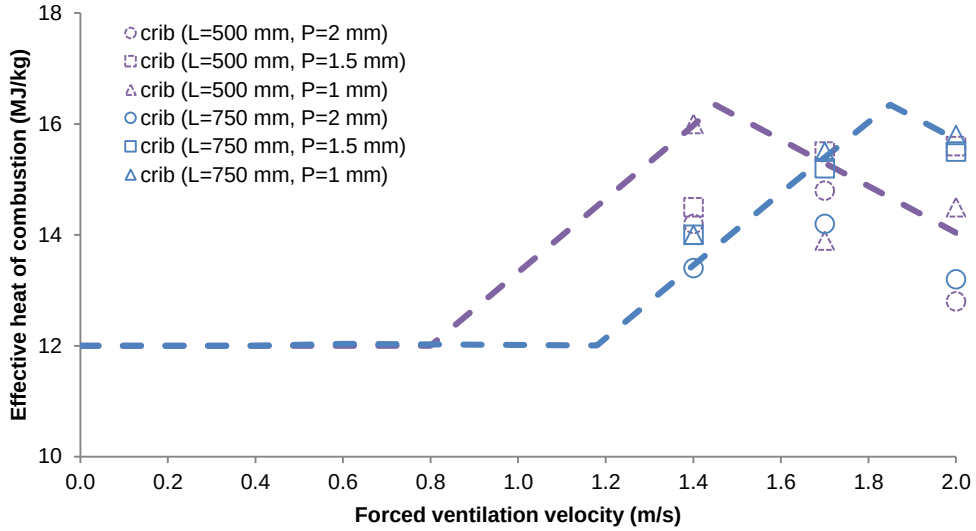

Figure 6-12: Effective heat of combustion for different length cribs.

As demonstrated in Figure 6-12, the linear relationship derived from Equation 6.8 is limited fully representing the heat of combustion values for 500 mm long crib when the crib porosity factors are 1.5 mm and 2 mm. However, the heat of combustion values for 750 mm long crib match well with the calculation results based on Equation 6.8 except one single data point at 2 m/s and P = 2 mm. Even though there are limitations in this revised equation, it is still interesting to expand this assumption to investigate the influence on the peak HRR at different velocities from the effect of crib length on burning efficiency. Therefore, the velocity limits in Equation 6.3 are updated accordingly after considering of the effect from crib length:

When $v \leq 0.6L/L_0$, then

$\dot{Q}_p = \gamma_{fs}\dot{Q}_{p,nv}$, while $\dot{Q}_p < \dot{Q}_{p,engfuled}$

otherwise

$\dot{Q}_p = \dot{Q}_{p,engfuled}$

When $v > 0.6L/L_0$, then

$\dot{Q}_p = \gamma_{fs}\gamma_{be}\dot{Q}_{p,nv}$, while $\dot{Q}_p < \dot{Q}_{p,engfuled}$

otherwise

$$\dot{Q}_p = \gamma_{be}\dot{Q}_{p,engfuled} \quad (6.9)$$

Based on Equation 6.9, the peak HRR at different velocities can be predicted. Figure 6-13 is the comparison between the predicted HRR in Equation 6.9 for different experiment scenarios and the measured peak HRR from the corresponding experiments. As shown in Figure 6-13,

the predicted peak HRR values in the new proposed Equation 6.9 can effectively predict peak HRR for different experimental scenarios.

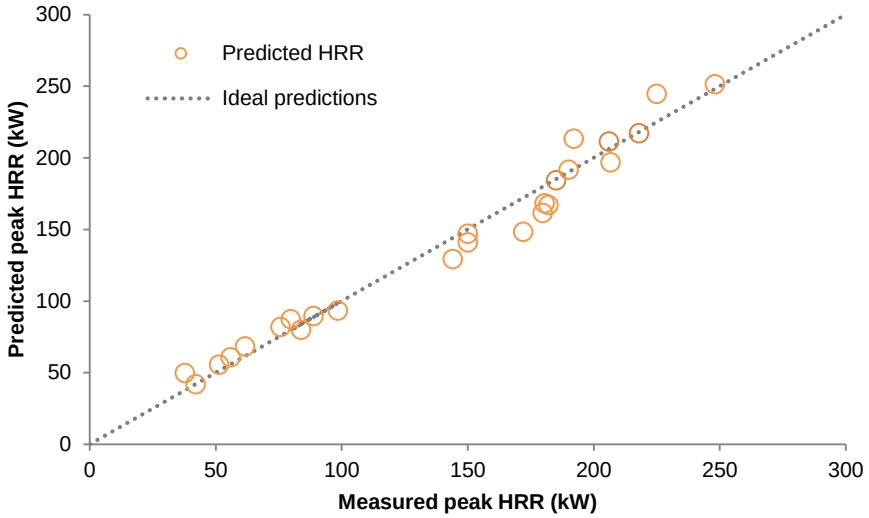

Figure 6-13: Comparison between peak HRR predictions and measured values.

In Equation 6.9, there are two critical parameters $\dot{Q}_{p,nv}$ and $\dot{Q}_{p,engulfed}$. In the previous analysis, the value of $\dot{Q}_{p,nv}$ was obtained experimentally and the value $\dot{Q}_{p,engulfed}$ was calculated through Equation 6.1. Carvel and Beard's suggest a relationship between the HRR for tunnel fires under natural ventilation and in an open space, which is written as $\dot{Q}_{nv} = \varphi \dot{Q}_{open}$, where φ is determined by the width of a tunnel and a fuel object. Based on the fire size in the free burn experiment and the φ value obtained in this work, the calculated $\dot{Q}_{p,nv}$ from this equation is only around 20 kW, which is only half of the measured value in the experiment. The factor φ in this equation may not fully represent the tunnel geometry influence on fire size based on the experimental data from this work.

According to the results presented in Table 6-3, the value of $\dot{Q}_{p,nv}$ is 60% of the $\dot{Q}_{p,engulfed}$. When comparing the experimental data from Cateley and Crum's work, it is also found that the ratio between $\dot{Q}_{p,nv}$ and $\dot{Q}_{p,engulfed}$ is approximately 0.6. The calculated ratio and experimental values from Cateley and Crum's work are listed in Table 6-6. Since these experimental results suggest that there is a fixed ratio of 0.6 between $\dot{Q}_{p,nv}$ and $\dot{Q}_{p,engulfed}$, the $\dot{Q}_{p,nv}$ values derived from 60% $\dot{Q}_{p,engulfed}$ is also presented in the table.

Table 6-6: Experimental data from Cateley and Crum [89]

P (mm)	L (mm)	$\dot{Q}_{p,nv}$ (kW)*	$\dot{Q}_{p,engulfed}$ (kW)	Ratio (-)	$\dot{Q}_{p,nv}$ (kW)**	$\dot{Q}_p$ (1.4 m/s) (kW)	$\dot{Q}_p$ (1.7 m/s) (kW)	$\dot{Q}_p$ (2.0 m/s) (kW)
2	750	96	150	0.64	90	182	190	207
	500	-	100	-	60	135	118	147
1.5	750	108	165	0.65	99	185	206	219
	500	79	110	0.71	66	150	149	144
1.0	750	108	191	0.57	115	191	225	248
	500	72	126	0.57	76	181	180	173

* $\dot{Q}_{p,nv}$ are measured in the experiments; ** $\dot{Q}_{p,nv}$ are derived from 60% $\dot{Q}_{p,engulfed}$.

Figure 6-13 has demonstrated that the Equation 6.9 can give effective predictions in $\dot{Q}_p$ at different velocities. In order to demonstrate the enhancement of HRR due to the ventilation influence, the k curves ($\dot{Q}_p/\dot{Q}_{p,nv}$) based on the results shown in Table 6-6 are calculated. Figure 6-15 (a) shows the k curves derived from the calculated $\dot{Q}_{p,nv}$ (60%$\dot{Q}_{p,engulfed}$) values and Figure 6-14 (b) shows the k curves based on the measured $\dot{Q}_{p,nv}$ values in the experiments. The k values at velocities of 1.4 m/s, 1.7 m/s and 2.0 m/s, derived from the experimental results, are indicated on the two plots.

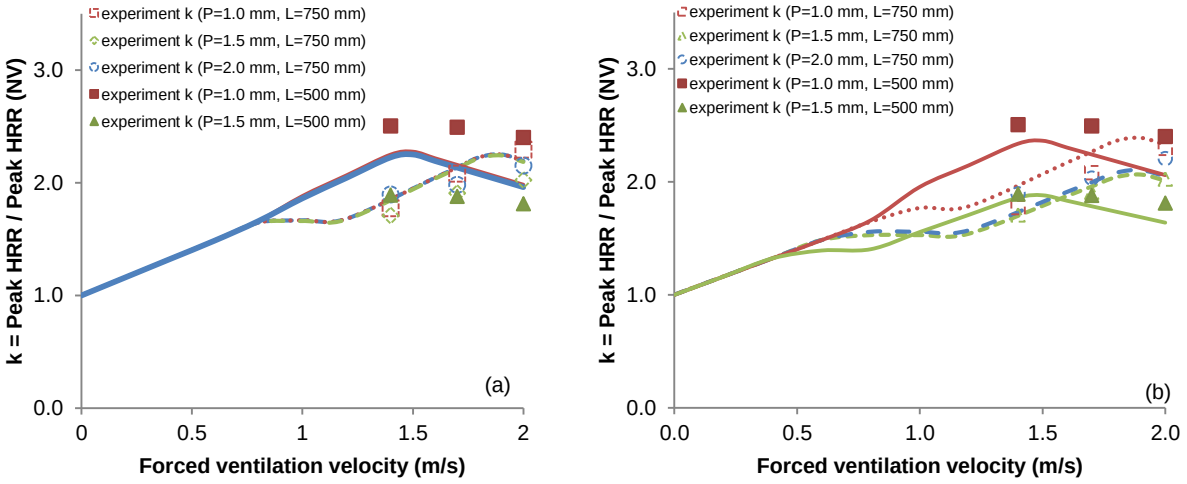

Figure 6-14: Comparison of experimental results and model predictions: (a) k curves derived from calculated $\dot{Q}_{p,nv}$; (b) k curves derived from measured $\dot{Q}_{p,nv}$.

Comparing the results between Figure 6-14 (a) and Figure 6-14 (b), the model predicted k curves based on the calculated $\dot{Q}_{p,nv}$ in Figure 6-14 (a) for cribs with the same length but different porosities are overlapped onto each other. The k values obtained from the experiments at 1.4 m/s, 1.7 m/s and 2.0 m/s are within the 25% deviation to the predicted k curve for 500 mm long crib and within 2% deviation to the predicted k curve for the 750 mm

long crib. The model-predicted k curves in Figure 6-14 (b) based on the experimentally measured $\dot{Q}_{p,nv}$ demonstrate the clear differences in k results when the cribs are the same length but have different porosity factors. As shown, the differences in k curves are noticeable when crib porosities are changed from 1.0 mm to 1.5 mm for both 500 mm long crib and 750 mm long crib, while the differences in k curves are negligible between the cribs with porosity factors of 1.5 mm and 2 mm for 750 mm long crib. The experimental k values at 1.4 m/s, 1.7 m/s and 2.0 m/s match the model-predicted k curves in Figure 6-14 (b) better than in Figure 6-14 (a). However, the model-predicted k curves in Figure 6-14 (a) still demonstrate reasonable predictions with the simplified estimation of $\dot{Q}_{p,nv}$. Therefore, it is considered that $\dot{Q}_{p,nv}$ can be estimated through 60%$\dot{Q}_{p,engulfed}$ when the crib porosity is more than 0.7 mm as the crib porosity influence on HRR is negligible when it is beyond this value.

In Figure 6-9, the influence of different porosities on HRR is compared. It is noted that different crib length were applied in the comparison. Equation 6.9 is applied to replot the k curves. Due to the different tunnel cross sections and crib sections in the experiments for cribs with porosity of 0.62 mm and 2.1 mm [30], the values of $\dot{Q}_{p,nv}$ measured from the corresponding experiments are applied to the calculations of k curves. Figure 6-16 shows the predicted k curves are based on Equation 6.3 and Equation 6.9, respectively. (Figure 6-15 (a) shows the original model predictions and Figure 6-15 (b) presents the revised model predictions).

There are significant changes in the predictions for curve $k_{0.62}$ in Figure 6-15 (b) where the enhancement on peak HRR at high velocities is not as pounced as the results shown in Figure 6-15 (a). The predicted curve $k_{2.1}$ in Figure 6-15 (b) shows lower k values at high velocities than the results on curve $k_{2.1}$ in Figure 6-15 (a). The predicted curves are improved based on Equation 6.9.

The influence of low porosity factors on the enhancement of HRR is consistent with the previous results. The values on curve $k_{0.62}$ is higher than the values on curve $k_{2.1}$ in both figures, which indicates that the enhancement on peak HRR for low porosity fuel (P = 0.62 mm) is higher than high porosity fuel (P = 2.1 mm) in terms of the same length cribs. When the cribs with different length are used, the influence on the enhancement of HRR for the crib with porosity factor of 2.1 mm is lower than the crib with porosity factor of 0.8 mm, which still corresponds well with the previous results. However, it is difficult to conclude whether the crib with a low porosity factor of 0.62 mm enhances peak HRR more or the crib with a high porosity factor of 0.8 mm enhances peak HRR more.

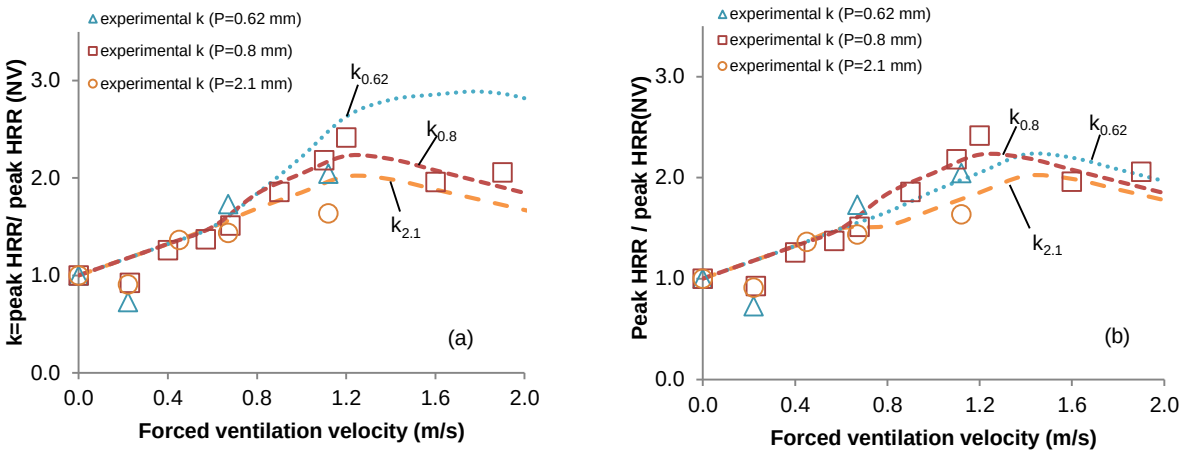

Figure 6-15: k curves predictions: (a) based on Equation 6.3; (b) based on Equation 6.9.

In addition to the porosity factor influence, the influence of crib length on the enhancement of peak HRR at different velocities was investigated based on Equation 6.3 previously. Because of the limited information for the peak HRR for different length of cribs under natural ventilation, a tunnel fire scenario with multiple fuels was introduced to explain the consideration of $\dot{Q}_{p,nv}$ values for different length cribs, while the enhancement on burning efficiency caused by the crib length itself was ignored. Based on the previous results, it was found that there was an enhancement limit on the peak HRR at high velocities when the crib length reaches twice that of the original crib length and this limit matches the 50% probabilistic k_{prob} curve proposed by Carvel and Beard.

Based on the revised Equation 6.9, the new k curve predictions for different length cribs are plotted in Figure 6-16. The $\dot{Q}_{p,nv}$ used in the calculations is based $60\%\dot{Q}_{p,engulf}$ suggesting the porosity of the fuel in this comparison is larger than 0.7 mm and its influence on the HRR is negligible. The curve k_{prob} representing 50 % probabilistic results is shown in the plot.

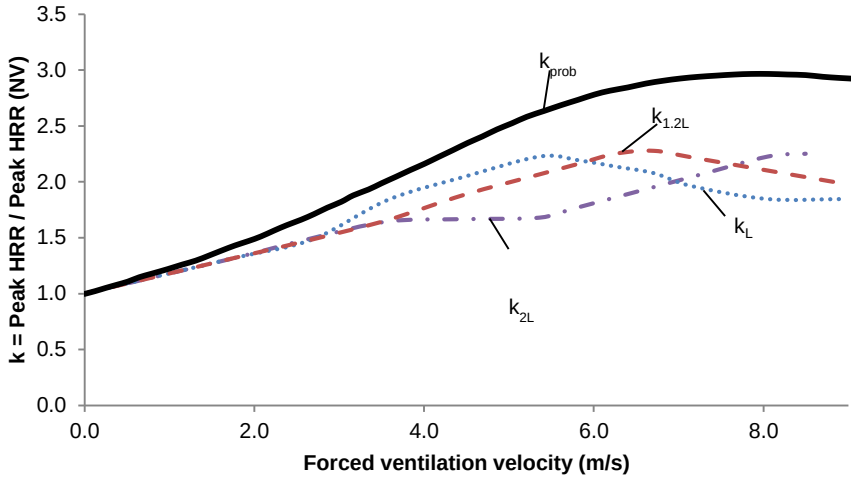

Figure 6-16: k curve predictions for different length cribs.

In Figure 6-16, the predicted values for k_L, $\mathrm{k}_{1.2L}$ and k_{2L} curves are lower than the results shown on k_{prob} curve. It can be seen from the figure that the maximum enhancement for the peak HRR is around a factor of 2.2 for the different length cribs, while a higher velocity is required to reach the maximum enhancement for a longer crib. However, this comparison does not include the results for low porosity factor cribs (P < 0.7 mm).

6.5 Conclusions

This work uses a series of small-scale tunnel experiments, which have been scaled from a large-scale tunnel simulated HGV cargo fire experiment, to carry out an investigation of the burning of cribs under different forced ventilation velocities. Due to the advantages in doing the small-scale tunnel experiments the burning of the fuel source is effectively captured together with the recorded data of heat release rate and mass loss rate.

The results from the experiments reveal that the increase in forced ventilation air velocity in a tunnel fire affects the fire spread rate and burning efficiency, and further affects the peak HRR and peak mass loss rate.

From the original set of experimental results, when the velocity is less than 0.6 m/s, the fire spread rate is mainly affected by the forced ventilation system such that the peak HRR increases linearly with the increase in air velocity. When the velocity exceeds 0.6 m/s then the forced ventilation affects both the fire spread rate and burning efficiency until no more fuel is available to spread to. At this stage, the peak mass loss rate and peak HRR reach maximum values. As per the experiments, once the forced ventilation velocity exceeds ~1.2 m/s, the increase of air velocity does not enhance the fire spread rate anymore so that the forced

ventilation only changes the burning efficiency of the fire. Therefore, the peak mass loss rate remains the same, while the peak HRR even decreases due to the reduction in burning efficiency. Using the results from the experiments a simple mathematical model is proposed that combines the effect of the forced ventilation velocity on the spread of fire with the changes in burning efficiency. The model reproduces the variation in peak HRR with ventilation velocity and crib porosity as previously noted by Ingason [15]. The model also allows an assessment to be made of what the effect of increasing the available fuel has on the peak HRR.

According to the experimental results where different length cribs were used, it is found that the influence of ventilation on burning efficiency is also affected by the crib length. A revised mathematical model is proposed where the influence due to the changes in crib length is included. Based on the revised mathematical model, informative predictions of peak HRR can be obtained for different scenarios. In addition, it is found that the $\dot{Q}_{p,nv}$ can be derived from $60\%\dot{Q}_{p,engulf}$ when the porosity factor of the fuel source is larger than 0.7 mm, however, the relationship between $\dot{Q}_{p,nv}$ and $\dot{Q}_{p,engulf}$ for low porosity factor fuels is not discussed due to the insufficient data. The new model is also applied to reassess the previous discussion in terms of the crib porosity factor influence on the enhancement of peak HRR. The new predicted enhancement ratios match the experimental results better than the previous model predictions. Finally, the effect of crib length on the enhancement of peak HRR is discussed and a maximum enhancement factor of 2.2 is obtained.

Chapter 7 Comparison of Heat Release Rate Prediction Methods Using FDS for Small-scale Tunnel Experiments

In this chapter, two different methods (the pyrolysis model method and the multiple gas burner method) in FDS6 are applied to simulate the small-scale tunnel experiments at different tunnel ventilation conditions. The analysis of the pyrolysis model method is reproduced from a paper submitted to Fire Technology titled ‘Applying the FDS pyrolysis model to predict heat release rate in small-scale tunnel experiments’.

7.1 Introduction

As discussed in Chapter 2, one of the most important parameters in the selection of design fire scenarios is the HRR. This input provides information for the evaluation of fire hazard severity, the tenability conditions for occupants and tunnel ventilation design parameters, etc. Various tunnel fire safety standards and guidance provide design fire HRR values. However, the use of these recommended design fires has limitations when representing different tunnel fire scenarios where a range of vehicles may be involved and the influences on the fire from the tunnel size and ventilation conditions may be different to those in the original experiments.

There are generally three methods to investigate tunnel fire size, which are through large-scale experiments, small-scale experiments and computational modelling techniques. In previous chapters, the experimental methods have been introduced. Large-scale tunnel experiments can reflect the actual fire sizes in real tunnel fires and small-scale experiments are suitable to conduct parametric studies. However, there are always limits when using experimental methods to carry out analysis, such as the time and costs of performing repeated experiments. As stated in Chapter 1, the widely used FDS software in fire engineering is a cost-effective method to predict HRR for tunnel fires. In this chapter, the modelling approach is adopted to study tunnel fire size although prediction of HRR for tunnel fires is not used in practice.

Different approaches in FDS to simulate fires have been briefly introduced in Chapter 1. As discussed, the HRR of a solid fuel fire can be estimated using an ignition temperature and subsequent burning rate for the fuel in FDS, hereafter referred to as the multiple gas burner method in this chapter. In this method, the fuel surface is divided into individual elements each with a defined ignition temperature and burning rate history. The fuel is assumed to ignite when the surface reaches the ignition temperature. Once ignited the element releases energy following the specified rate. Consequently, the multiple gas burner method requires the user to specify the ignition temperature of the material elements and to pre-define the burning rate rather than allowing the material to pyrolyse as a result of the local environmental conditions. Obtaining material ignition temperatures is not always simple and burning rate values are often measured in free-burn conditions under quiescent conditions. However, previous work [11] has used the multiple gas burner method in which the ignition properties were determined through cone calorimeter experimental data to simulate the burning and fire spread within a single fuel package. The method has also been used to simulate fire burning and spread among different fuel items [37].

FDS provides an alternative modelling method to allow the description of the pyrolysis reactions that occur within solids when they are burning. Different from the multiple gas burner method, the use of the pyrolysis model in FDS can reflect the environment influence on a solid fuel to predict the HRR of a fire based on the decomposition reactions within the solid. The predicted HRR is not controlled by the user specified burning rate but is the simulation of the burning material decomposition reactions. In this method, the burning rate and ignition temperature of the fuel items do not need to be specified in advance. However, the properties of the fuels and environmental conditions (such as velocity, temperature and etc.) are required in order to determine the decomposition rate and then to further predict the HRR of the fire. The decomposition rate is given in the form of the Arrhenius equation and the heat transfer in the solid is taken to be one-dimensional. This is referred to as the pyrolysis model method in this chapter. As mentioned the literature review discussed in Chapter 2, the main applications of the pyrolysis model are for material- and bench-scale experiments where the heat transfer can be simply modelled in one-dimension [20, 36]. The use of the pyrolysis model to simulate a more realistic fire has not been widely studied although it is known [37] that the accuracy of the HRR prediction from the FDS pyrolysis model is limited due to the assumptions (such as one-dimensional heat transfer and simplified pyrolysis reactions) it contains. However, it is still useful to investigate the predictive capability of the pyrolysis model for more complex fire scenarios than the material or bench-scale fire scenarios and to investigate where its limits may be.

This chapter includes two main parts. The pyrolysis model is firstly applied to simulate the small-scale tunnel experiments introduced in the previous chapters. The derivation of the fuel properties have been evaluated with a series of cone calorimeter experiments. The predicted HRR results of the tunnel experiment are presented and the improvements in the predictions are discussed. In the second part, the multiple gas burner method is also used to simulate the small-scale tunnel experiments. The determination of the ignition properties including the ignition temperature and the burning history for the fuel source are discussed. The predicted HRR results obtained from the multiple gas burner method are presented.

7.2 Small-scale Tunnel Experiments

Since the details of the small-scale tunnel experiments can be found in Chapter 5 and Chapter 6, this chapter only briefly describes the experimental set-ups and some results, which are critical to the modelling work.

The constructed small-scale tunnel had dimensions of 0.365 m (W) × 0.26 m (H) × 11.9 m (L). The downstream end of the horizontal tunnel connected to a circular duct for the measurement of the flue gases. An electrically powered fan, which was attached to the upstream end of the tunnel to provide a longitudinal ventilation system, was 2580 mm away from the fuel load.

The tunnel had a combustion chamber for the fuel. The rear wall, ceiling and floor of this chamber were constructed using 0.9 mm thick stainless steel and internally insulated with 15 mm thick insulation board. The insulation material had a density of 336 kg/m3, heat capacity of 1.08 kJ/kg/K and thermal conductivity of 0.07 W/m/K at ambient temperature. The front of the chamber had fire resistant glazing. The rest of the tunnel was constructed of the same stainless steel and covered with a 5 mm thick insulation material.

Cribs MDF were used as fuel (the average weight for the cribs was 1.44±0.05 kg). The cribs were constructed with 5 layers of 15 mm thick sticks comprised of three 375 mm long-sticks and six 100 mm short-sticks equally spaced.

Results and analysis of the experiments found that the forced ventilation affected the fire spread as well as burning efficiency of the crib, and further affect the HRR. Figure 7-1 presents the measured effective heat of combustion for the MDF cribs at different ventilation velocities. When the air velocity is less than ~ 0.6 m/s the effective heat of combustion is found to be 12 MJ/kg which is the same as that obtained from the cone calorimeter experiments discussed in the next Section. At this stage, the increase of HRR is majorly due to the increase of fire spread rate by the forced ventilation. Thereafter an increase in air velocity up to 1.2 m/s gradually increases the burning efficiency; however the burning efficiency then falls when the velocity exceeds 1.2 m/s.

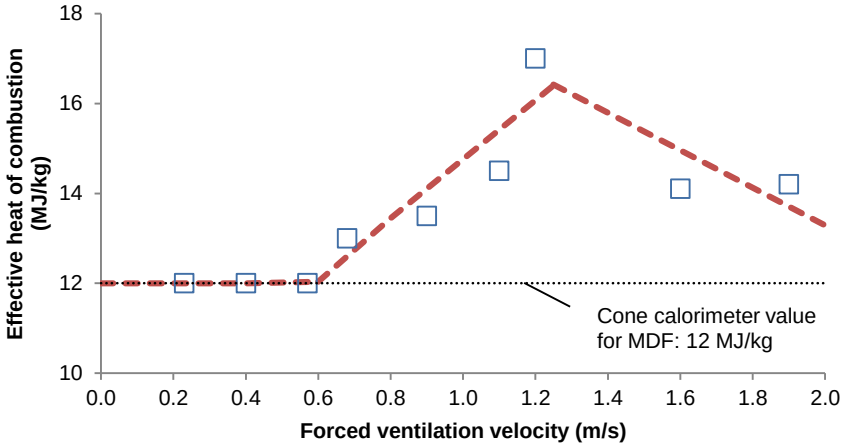

Figure 7-1: Effective heat of combustion at different forced ventilation velocities. (Reproduced from Chapter 6).

7.3 Investigation of MDF Properties

7.3.1 Thermal Properties

The thermal properties of MDF required in the pyrolysis model are density, specific heat and thermal conductivity. Li *et al*. [71] have carried out a series of studies on the same MDF adopted in the small-scale tunnel experiments. In Li et al.'s [71] study, the specific heat and thermal conductivity for both virgin and charred MDF have been investigated as functions of temperature (T) and moisture content (MC) with the results shown in Table 7-1.

Table 7-1. Thermal properties for virgin MDF and char MDF [71].

MDF, specific heat (J/kg/K)	$c_p(dry) = 2.5T + 1080$
MDF, thermal conductivity (W/m/K)	$k_0^{30} = 4.86\times10^{-8}\rho^2 + 4.63\times10^{-5}\rho + 4.38\times10^{-2}$ $\Delta k = 4.9\times10^{-3} MC\times100 + (1.1\times10^{-4}\rho + 4.3\times10^{-5} MC\times100)(T-30)$ $k = k_0^{30} + \Delta k$
Char, specific heat (J/kg/K)	$c_{p,ch}(dry) = 3.7T + 547.86$
Char, thermal conductivity (W/m/K)	0.09 W/m/K at ambient temperature and 7% increase per 10 K

7.3.2 Kinetic Properties

In the work of Li *et al*. [35], the kinetic properties (activation energy (E), pre-exponential factor (A) and reaction order (n)) of MDF have been analysed through an advanced computational searching method. They used four components to correspond to resin, hemicellulose, cellulose and lignin to represent MDF. The kinetic properties of each component were derived inversely from three differentiated thermogravimetric (DTG) curves at heating rates of 5, 20 and 60 K/min. However, the suitability of these kinetic properties to model decomposition behaviour in FDS was not part of the original research. In this chapter, the kinetic properties of the MDF are re-analysed by using the hand calculation method developed in Chapter 3 using the DTG experimental curves for the application of these properties to FDS modelling. This analysis consists of two steps: the first step is to obtain a linear relationship based on Equation 7.1 to derive E and A.

$$\ln\left(\frac{\beta}{T_{i,p}^{\ 2}}\right) = -\frac{E_i}{RT_{i,p}} + \ln\left(\frac{A_i R}{E_i}\right) \tag{7.1}$$

The same four-component scheme proposed by Li *et al*. [35] is adopted for this analysis. According to the relationships of $ln(\beta/T_{i,p}^2)$ and $1/T_{i,p}$ for each component in Figure 7-2, the value of E and A for each component can be calculated based on the slope and the intercept of each line.

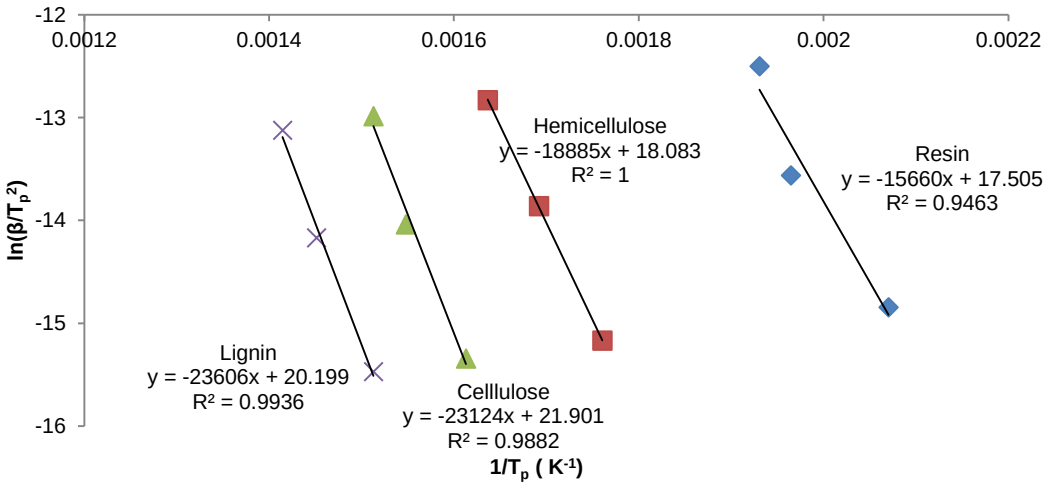

Figure 7-2: linear relationships of $ln(\beta/T_{i,p}^2)$ and $1/T_{i,p}$ for each component in MDF [35].

The second step is to develop a mathematical model according to the decomposition rate presented in Equation 7.2 in order to depict the reaction rate curves at different heating rates.

$$r_{i,j} = \sum_{\substack{i=1 \\ j=0}}^{N,t_e} (1-\nu_{s,i}) c_i A_i \exp\left(-\frac{E_i}{RT_j}\right)\left(Y_{i,j}\right)^{n_i} \tag{7.2}$$

The values of n_i and c_i can be determined through visual comparisons between the model and corresponding experimental results. In this analysis, an average of 20% residue for ν_s based on the TG experiment data in Li *et al*. [35] is considered. Due to the different mathematical expressions for the decomposition rate between the hand calculation and the FDS pyrolysis model, a further modification on the pre-exponential factor obtained from the hand calculation method is required in order to apply it in FDS. Table 7-2 summarises the final results of the kinetic properties for the four components of MDF for the application in the FDS6 pyrolysis model.

Table 7-2: Kinetic properties for MDF.

Components	E_i (J/mol)	A_i (s^{-1})	n_i	c_i
Resin	1.30×10^5	6.24×10^{15}	5.0	0.10
Hemicellulose	1.57×10^5	7.64×10^{12}	3.0	0.42
Cellulose	1.92×10^5	6.78×10^{13}	0.9	0.36
Lignin	1.96×10^5	3.90×10^{19}	8.0	0.12

FDS6 simulations of the TG experiments at the heating rates of 5, 20 and 60 K/min were conducted using the kinetic properties in Table 7-2 by applying the methods described in Chapter 3. Figure 7-3 is the comparison of DTG curves obtained from the simulations and from the experiments. The predictions for the DTG curves indicate that the kinetic properties derived in this section can satisfactorily represent the decomposition behaviour of the MDF.

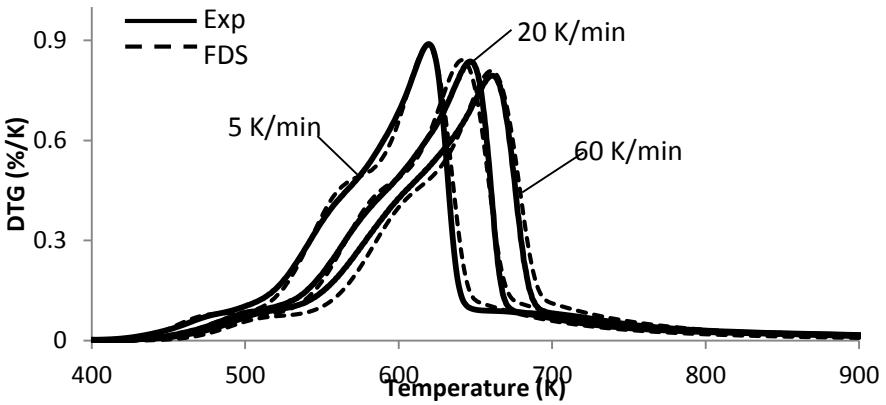

Figure 7-3: Comparison of DTG curves between simulations and experiments.

7.3.3 Evaluation through FDS Cone Calorimeter Simulations

In the TG simulations the heat transfer within solids is not included. However, when using the pyrolysis model to simulate a fire the thermal properties have a significant influence on the heat transfer results and consequently the HRR predictions will be affected. Therefore the thermal properties and the kinetic properties of the MDF are evaluated and optimised using FDS simulations of the cone calorimeter experiments.

Cone calorimeter ignition, mass loss and HRR results at incident heat fluxes of 25, 35 and 50 kW/m^2 are adopted. In the experiments, conditioned samples with dimensions of 100 mm $\times$ 100 mm $\times$ 18 mm thick were used. The MDF samples were dried at 60 ˚C for 12 hours similar to the conditions used for the cribs in the small-scale tunnel experiments. Experimental procedures were based on AS/NZ 3837:1998 [65] and each experiment was repeated three times.

The average initial bulk density of the MDF samples was 710 kg/m^3 and the remaining mass from the experiments gave an average bulk density of 180 kg/m^3 for the char. According to the measured HRR and mass loss data, the average effective of heat of combustion is 11 to 12 MJ/kg which is consistent with the value obtained from Li *et al.* [75].

To evaluate the MDF properties for the FDS predictions of HRR, simulations for the three cone calorimeter experiments at each incident heat flux were conducted. The sample was represented by the top surface of a solid block (100 mm × 100 mm). The thermal conductivity and specific heat for the MDF and char were defined according to the values listed in Table 7-1 and the density as discussed previously. The back face was defined according to the properties of the insulation board used in the cone calorimeter experiments (density 336 kg/m^3, thermal conductivity 0.07 W/m/K and specific heat 1.08 kJ/kg/K) and the side surfaces are defined as inert. The incident heat flux from the cone heater was specified as a constant external heat flux to the surface.

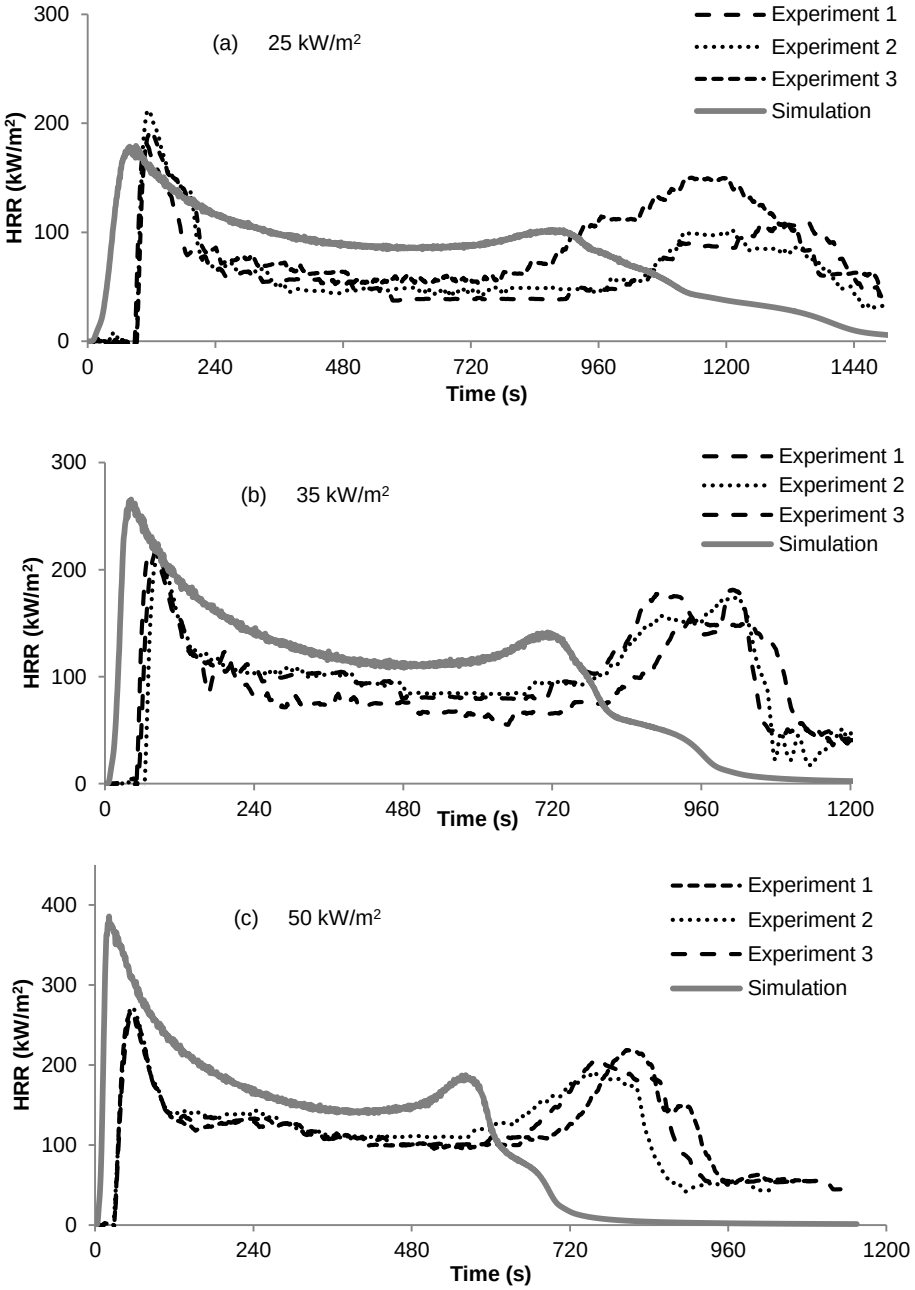

Figure 7-4: Simulations for cone calorimeter experiments at incident heat fluxes of (a) 25 kW/m^2, (b) 35 kW/m^2, (c) 50 kW/m^2.

The corresponding predicted HRR curves from cone calorimeter simulation at the three incident heat fluxes are plotted in Figure 7-4 and are compared with the experimental results. The first peak HRR for all three fluxes occur at times are comparable to the experiments and the predictions at 25 and 35 kW/m^2 showing similar magnitudes to the experimental results. The all three predictions show comparable decay curves to the experimental curves. The values of the second peak HRR are all close to the experimental values, while the predictions for the burning duration are not successful. The ignition in the simulations are much faster than

the ignition in the experiments under the three heat fluxes. Although the simulation results cannot precisely match the experimental HRR curves, the FDS results shown in Figure 7-4 can still demonstrate the general burning behaviour in MDF cone calorimeter experiments with limited sucess.

7.4 Simulations Based on the Pyrolysis Model Method

7.4.1 Basic Settings

According to the FDS user's guide[16], the parameter D^* can be obtained from Equation 7.3, where $\dot{Q}$ is the heat release rate, and ρ_0, c_0, T_0 are the properties of ambient air.

$$D^* = \left(\frac{\dot{Q}}{\rho_0 c_0 T_0 \sqrt{g}} \right)^{2/5} \tag{7.3}$$

The maximum $\dot{Q}$ obtained in the small-scale tunnel experiments was less than 100 kW so that the corresponding D^* is 0.383 m. As suggested by Li and Ingason [17] $0.075D^*$ is a reasonable value for the simulation of tunnel fires and $0.05D^*$ has been used by Zhang *et al*. [90] to simulate the behaviour of a wood crib fire in a confined space. With a uniform cell size of 15 mm adopted for the simulations in this work, this gives about 25 cells spanning the characteristic diameter of the fire which gives $0.039D^*$ and this is smaller than used in [17, 90].

After a sensitivity analysis using cell size of15 mm, 7.5 mm and 3.75 mm (corresponds to about 25 cells, 51 cells and 102 cells spanning the characteristic diameter of the fire, respectively), it was found that a numerical instability occurred at ~100 s when 7.5 mm and 3.75 mm cell sizes were applied. The simulation with 15 mm cell size (resulting 0.45 million cells based on the dimensions of the domain) took about one week to complete a burning duration of 1000 s on a personal computer with the specification of i7 CPU @ 3.3 GHz and 32 GB RAM. In order to achieve a numerically stable simulation within a reasonable computational time and give sufficiently accurate predictions of the small-scale tunnel fire simulations, the cell size of 15 mm was adopted in this study. For the solid phase, a stretch factor of one and cell size factor of 0.5 were applied to have a more uniform and smaller cell size for the solid phase calculations. The discussion for the influence for the stretch factors and cell size factors can be found in Chapter 4. The calculated cell size limit in the solid phase is 0.185 mm based on thermal properties at the initial state in FDS.

Since the dimensions of the small-scale tunnel was 360 mm (W) × 260 mm (H) × 11900 mm (L), a domain with dimensions of 420 mm (W) × 300 mm (H) × 12645 mm (L) was used in the simulations to ensure sufficient volume to represent the entire tunnel and to accommodate the 15 mm cell size set-up. In the simulations the insulated platform was represented as a solid block adjusted to a dimension of 300 mm (W) × 495 mm (L) × 45 mm (H) and the surfaces of the block were assigned the insulation material thermal properties. The tunnel walls were given the thermal properties of the insulation material used in the experiments and the thin steel sheets were omitted. The observation window glass was not specifically simulated because of the insignificant thermal influence on the results.

The ventilation fan was represented by a supply air vent at 2585 mm upstream away from the fuel location. The circular duct for the collection of flue gases was not modelled, while the downstream end of the tunnel was initially modelled as being directly open to ambient conditions. A Smokeview image of the simulated tunnel is shown in Figure 7-5.

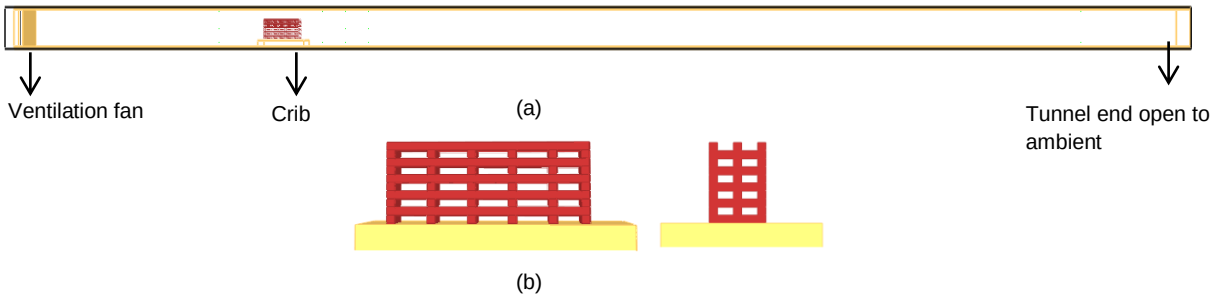

Figure 7-5: Simulation geometry set-ups for (a) tunnel; (b) crib geometry.

In the simulations, the crib was constructed as obstructions through the OBST Namelist group in FDS [16]. The dimensions of the crib were defined as those used in the experiments except that the length of the short stick was modified to 105 mm so it could correspond to the 15 mm cell size. The representation of the crib geometry in FDS is shown in Figure 7-5 (b).

For the application of the pyrolysis method the decomposition reactions of the MDF has to be defined. A surface line in the FDS input file was defined to prescribe the boundary conditions for the obstructions that corresponded to the crib. The four different components (resin, hemicellulose, cellulose and lignin) were used to represent the fuel with the corresponding mass fraction of each component described in order to specify the kinetic properties, thermal properties and heat of combustion for each component. In FDS6, the burning efficiency can be controlled though the heat of combustion parameter. In order to investigate the influence of burning efficiency on HRR predictions, the heat of combustion of 12 MJ/kg based on cone

calorimeter results and the heat of combustion obtained from the small-scale tunnel experiments were applied to conduct corresponding simulations.

Another important parameter is the thermal thickness of solids for heat conduction and in FDS6, only one-dimensional heat transfer in solids is available. Therefore, the actual solid thickness could not be simply adopted to represent the thermal thickness for the heat conduction calculation. In order to effectively reflect the heating conditions, an approximation was to use ¼ thickness of wood stick (3.75 mm) represents a scenario in which the wood stick is heated evenly over all of the surfaces excluding the ends.

7.4.2 Ignition Source

In the experiments 20 ml of methylated spirits was placed in an 80 mm diameter circular pan as the ignition source for the cribs. The burning of this fuel lasted for approximately 120 s. By using a density of 789 kg/m^3 and heat of combustion 26.8 MJ/kg [88] to 28.9 MJ/kg [91] for the fuel the corresponding steady-state heat release rate was calculated as 3.5 kW to 3.8 kW and the total energy content as 423 to 456 kJ.

In the simulations, the ignition source was simplified to a rectangular area with a dimension of 60 mm × 90 mm. 3.8 kW maximum HRR was obtained based on 700 kW/m^2 HRRPUA. To represent the burning of the methylated spirits the ignition source was set to linearly grow to 3.8 kW over the first 10 s and the value was kept constant for a further 110 s. By using this specification it was found that the ignition source would not ignite the crib over the 120 s duration. In order to investigate the ability to ignite the crib, different burning times of 120 s, 240 s, 360 s and 1500 s (the full simulation time) were used to simulate the ignition source for the tunnel scenario with a 0.23 m/s forced ventilation velocity. The ignition source in this experiment lasted for about 120 s and the experiment was stopped at 1500 s when the crib residue was in a smouldering stage. The corresponding simulation results are plotted in Figure 7-6.

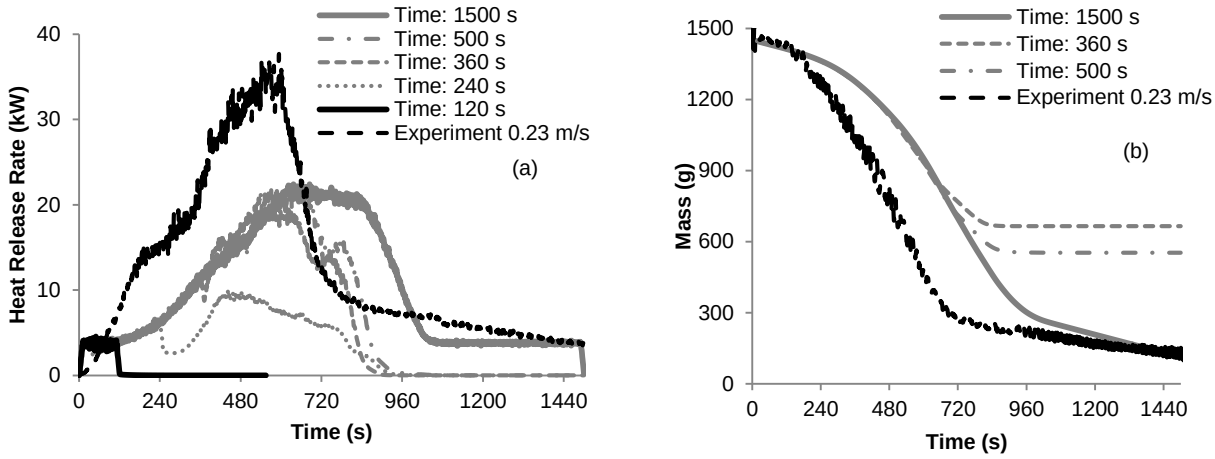

Figure 7-6: Crib predictions in using different ignition source burning durations: (a) HRR; (b) mass loss rate.

From these results, it can be seen that when the 120 s duration was used the HRR curve has an average value of 3.8 kW which lasted about 120 s and then it dropped to zero, which suggested that the crib had not been ignited. When the ignition duration time was extended to 240 s, 360 s, 500 s and 1500 s, the crib in these simulations was ignited so that the HRR values increased after the ignition source burned out. As seen in Figure 7-6 (a) the HRR for the 240 s duration ignition source was lower than the estimates results when longer ignition source durations were applied, which indicated that the crib had not fully ignited in this case. For the cases of the 360 s, 500 s and 1500 s durations the predicted peak HRR values were similar while the burning period increased with the increase of ignition duration. Figure 7-6 (b) plots the mass consumption situations for the cases of using 360 s, 500 s and 1500 s ignition duration where the longer ignition duration is used, the more crib is consumed.

In order to reflect the results from the small-scale tunnel experiments the influence of the ignition source on the crib needs to be minimised. Simulations found that a 360 s ignition source duration can effectively ignite the crib under different ventilation conditions from 0.23 m/s to 1.2 m/s when an effective heat of combustion (ΔH_e) of 12 MJ/kg is used for the MDF, while the duration of ignition needs to increase to 480 s for the scenario of 1.6 m/s. However as discussed previously, different values of ΔH_e can be obtained when different forced ventilation velocities are applied. Simulations have found that a 240 s ignition source duration is sufficient to ignite crib when the correspondingly higher values of ΔH_e are applied. Table 7-3 gives the ignition source duration times for the different forced ventilation conditions when a heat of combustion of 12 MJ/kg (referred to as Fixed HoC) is used and the revised durations (referred to as Modified HoC) when the modified heat of combustion values are applied.

Table 7-3: Ignition source durations and assumed effective heats of combustion for different forced ventilation velocity simulations.

Velocity (m/s)	Fixed HoC		Modified HoC	
	ΔH_e (MJ/kg)	Duration (s)	ΔH_e (MJ/kg)	Duration (s)
0.23	12	360	12	360
0.40	12	360	12	360
0.68	12	360	13	240
0.90	12	360	14	240
1.20	12	360	17	240
1.60	12	480	15	240

7.5 Results and Discussion by Using the Pyrolysis Model Method

7.5.1 HRR Estimations

The HRR estimations for the Fixed HoC, the Modified HoC groups and the corresponding experimental curves at different forced ventilation velocities are plotted in Figure 7-7. The HRR generated from the ignition source has been subtracted from the HRR curves. The heat of combustion values calculated from the estimated values of HRR and mass loss rate are consistent with the set-up values in the FDS data file, which indicate that all of the available fuel is burned within the simulation domains. The corresponding heat of combustion outputs for each velocity are plotted in Figure 7-8.

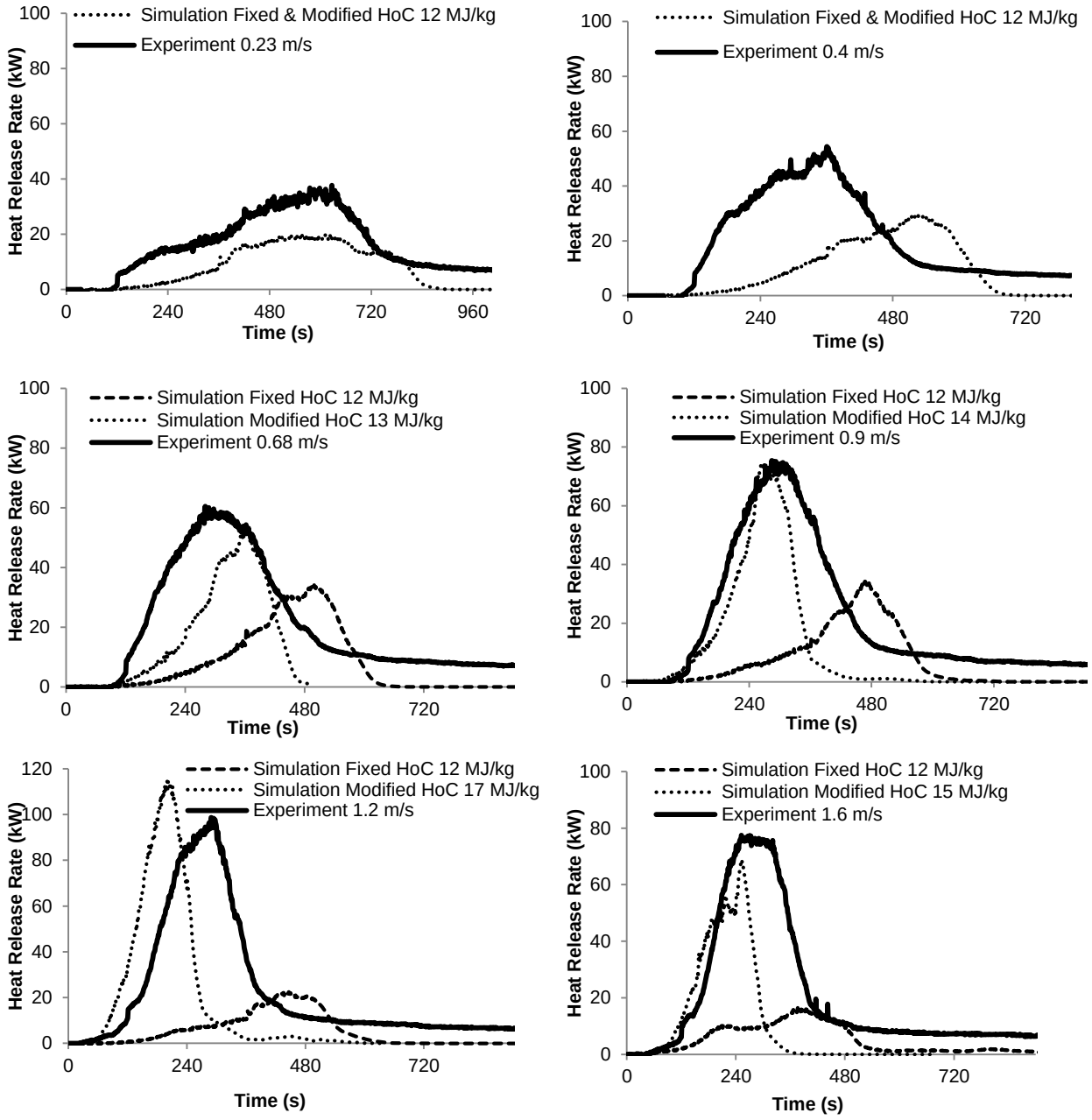

Figure 7-7: Estimations of HRR curves at different velocities using different values of heat of combustion.

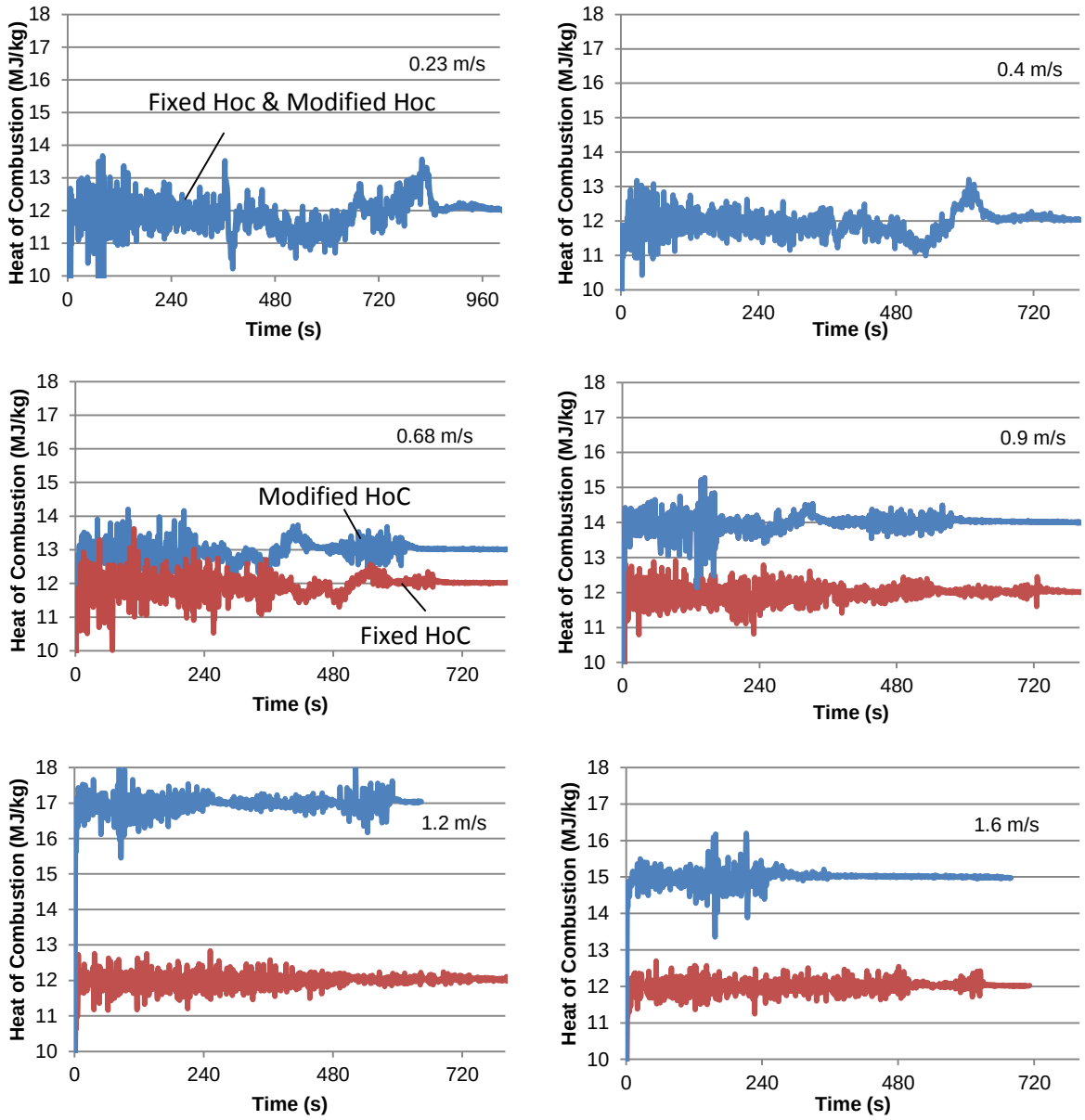

Figure 7-8: Outputs of heat of combustion under different forced ventilation velocities.

For the simulations using the fixed heat of combustion conditions, as the forced ventilation velocity changes from 0.23 m/s to 0.4 m/s, the burning duration reduces from 800 s to about 650 s and the peak HRR increases from 18 kW to 27 kW. However, the estimated HRR curves demonstrate similar burning behaviour in terms of burning duration and peak HRR when the 0.4 m/s, 0.68 m/s, 0.9 m/s and 1.2 m/s forced ventilation velocities are examined. When the velocity increases to 1.6 m/s, the burning duration and the peak HRR are both less than those estimations at the 0.4 m/s to 1.2 m/s forced ventilation velocities. In general the estimated peak HRR value for each scenario are noticeably less than the results from the experiments.

As shown in Figure 7-7, when the values for the heat of combustion are modified, the estimated HRR values largely improve when compared with the fixed value simulations. The estimated peak HRR values are similar to the experimental values at the 0.68 m/s, 0.9 m/s and 1.2 m/s forced ventilation velocities. However, the predictions of the fire growth and the entire burning duration at each forced ventilation velocity are unsatisfactory when compared to the experimental results.

When the total energy release results are considered, there are significant differences between the experiments and simulations. As shown in Figure 7-9, less than half of the energy is estimated in the simulations for each forced ventilation scenario compared with the energy released in the corresponding experiment.

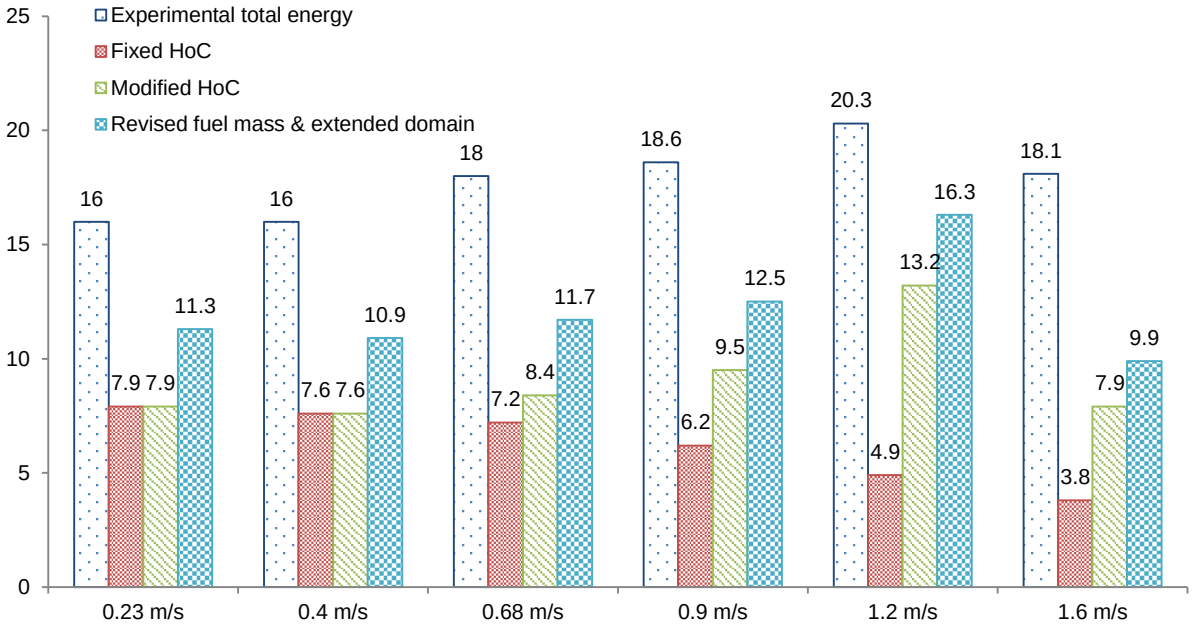

Figure 7-9**:** Measured and estimated total energy released at different forced ventilation velocities based on different simulation set-ups.

7.5.2 Improvements to Estimations

In order to improve the estimations from FDS an investigation into the mass and energy consumption is carried out for the 0.68 m/s forced ventilation velocity scenario. Figure 7-10 shows MDF burning at different times along with the corresponding HRR and mass loss curves. The fire in the experiment reached its peak heat release rate at around 260 s when the crib was partially engulfed by the fire the some parts of the fuel surface was noticeably charred. At 420 s the crib has started to collapse and the burning showed in the figure involving the burning of both wood and char. The fuel was almost burnt away when time reached 480 s. In the

experiment, the initial mass of the crib was measured as 1.4 kg and the remaining mass of the residue material (char and ash mixture) after burning was measured as ~ 0.2 kg, which was about 14% of the original fuel mass.

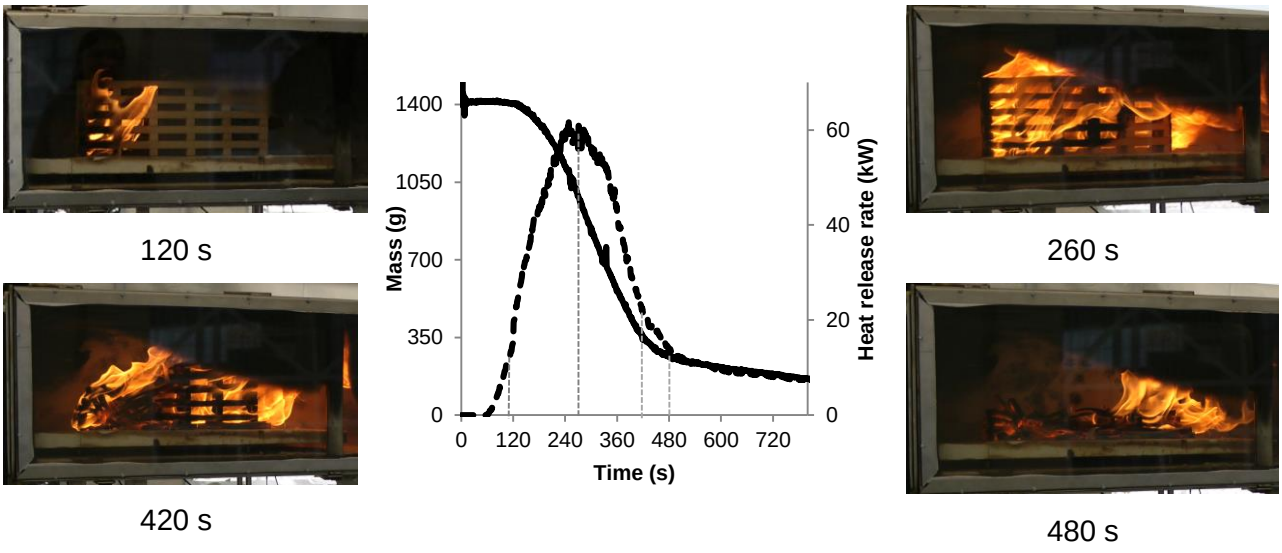

Figure 7-10: Experimental mass loss and HRR curves and crib burning at different times under 0.68 m/s forced ventilation velocity conditions.

When the crib with the geometrical form was applied to the simulations, the available fuel surface for burning could not be as large as in the experiments due to the overlapping sections of the sticks. FDS uses the surface properties of one side obstruction only when two obstructions overlap each other [16]. As a result of the available surface area (0.51 m^2), thermal thickness (3.75 mm) and density (710 kg/m^3) applied in the simulations, the available mass was 1.36 kg rather than 1.40 kg. In addition, 20% of MDF was set to covert to char in the simulations, which means that no combustion reaction occurs for this component proportion. Therefore, the available burnable fuel mass in the simulations was less than that in the experiments.

In order to obtain a comparable fuel mass between FDS and the experiments some modifications were made to the 0.68 m/s forced ventilation simulation case to re-assess the results. The thermal thickness of sticks was increased from 3.75 mm to 3.90 mm to compensate for the 'missing' fuel mass due to the overlapping area and also in order to maintain the same fuel density and crib geometrical shape as the experiments. No residue was considered in this case, which means all of the exposed fuel was available to be consumed in the simulation. Thus a total of 1.4 kg of fuel was available as a result of these modifications. The revised simulation results are plotted in Figure 7-11(a) for the HRR curves and Figure 11

(b) for the mass loss curves along with the experimental data and the previous simulation results using the 3.75 mm thickness.

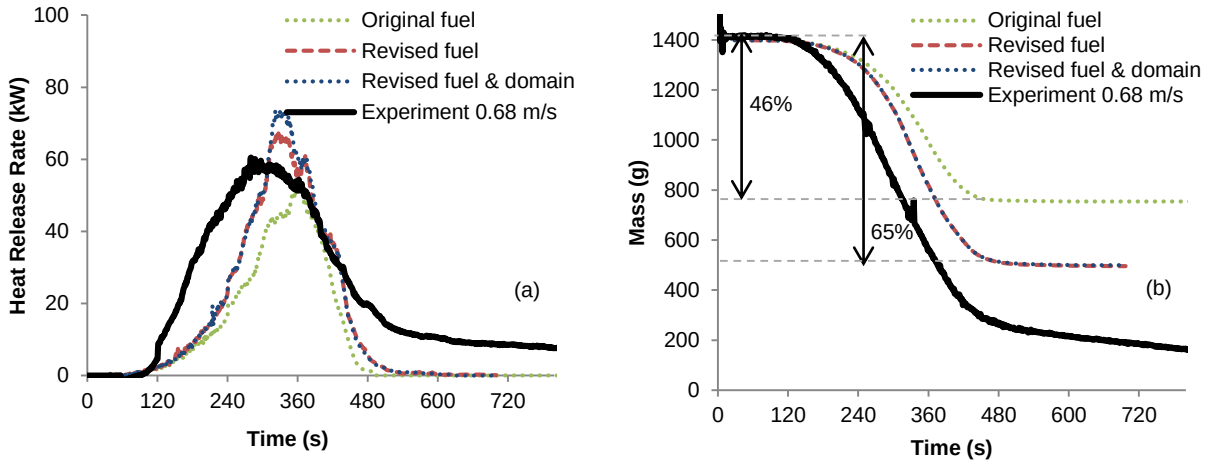

Figure 7-11: Simulation results with the modification of the available fuel mass for: (a) HRR curves; (b) mass loss curves.

As shown in Figure 7-11 (a), the estimated shapes of the fire growth curve are similar in both cases albeit with a delayed time shift when compared to the experiment. However, the increase in fuel mass improves the estimation of the peak HRR, where a value of 62 kW is obtained for the modified case (~60 kW was obtained in the experiment) compared with 47 kW with the previous case. The consumption of the fuel has improved from 46 % to 65 % in the mass loss curves shown in Figure 7-11 (b). For the original mass loss curve there is still about 32 % remaining after subtracting the unavailable mass for burning and the mass that converts to char. This remaining mass indicates that the fuel is still not completely consumed in the simulation. The same as the revised mass loss curve, there is ~ 35 % fuel remaining for the modified case even though the fuel was set up to be fully consumed in this case. Based on the simulation results for the revised fuel mass, the estimated heat of combustion values (the estimated HRR / the estimated mass loss rate) obtained from this simulation are not fully consistent with the set-up value of 13 MJ/kg, which are plotted in Figure 7-12.

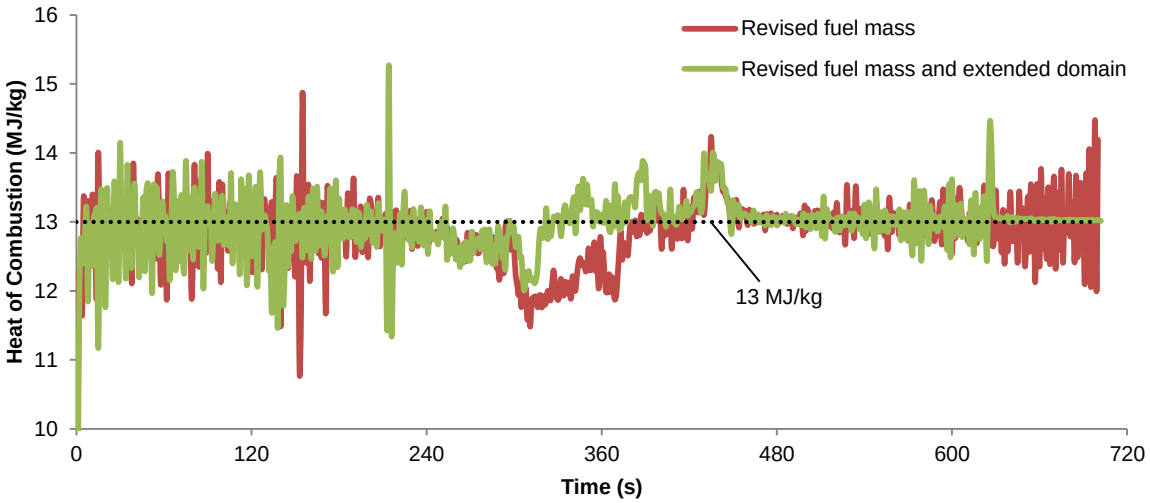

Figure 7-12: Heat of combustion results obtained from simulations

As seen in Figure 7-12, the values of heat of combustion obtained from the simulation with the revised fuel mass drops to about 11.5 to 12 MJ/kg between 280 s and 360 s, which indicates that the fuel is not effectively burnt in the simulation and some unburned fuel is lost out of domain. In order to overcome this, an extra mesh with 15 mm cell size was at the end of the original domain with sufficient height and length (as shown in Figure 7-13) to allow the unburned fuel to burn. The estimated heat of combustion values based on the extended domain is also plotted in Figure 7-12 and the results of mass loss rate and HRR are plotted in Figure 7-11. The heat of combustion values over 280 s to 360 s are improved after the changes in the domain as shown in Figure 7-12. The HRR curve for the revised domain shown in Figure 7-11 (a) also demonstrates a higher peak HRR values over this time period, while no change is shown on the mass loss curve.

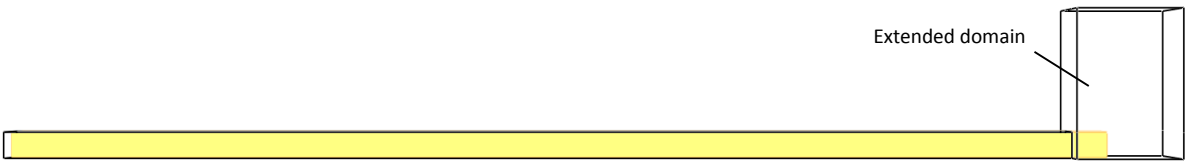

Figure 7-13: The modified domain with an extended mesh.

Based on the improvements obtained above, the modifications to the fuel mass and domain were applied to the other forced ventilation scenarios. The corresponding results are shown in Figure 7-14, which demonstrate a general improvement in the peak HRR and total energy estimations. Even though the simulation results have been improved after the increase of the available fuel mass, the estimated HRR curves at different velocities are still not ideal. The

initial fire growth phase at each forced ventilation velocity is not improved. Significant ignition delays and slower fire growth rates are still found at 0.23 m/s, 0.4 m/s and 0.68 m/s. The earlier ignition and faster fire growth rates are obtained for at 1.2 m/s and 1.6 m/s. The estimated total energy is still less than the experimental value at each velocity based on the comparison of the area the under curve between the simulation and experimental result. The corresponding comparison is shown in Figure 7-9.

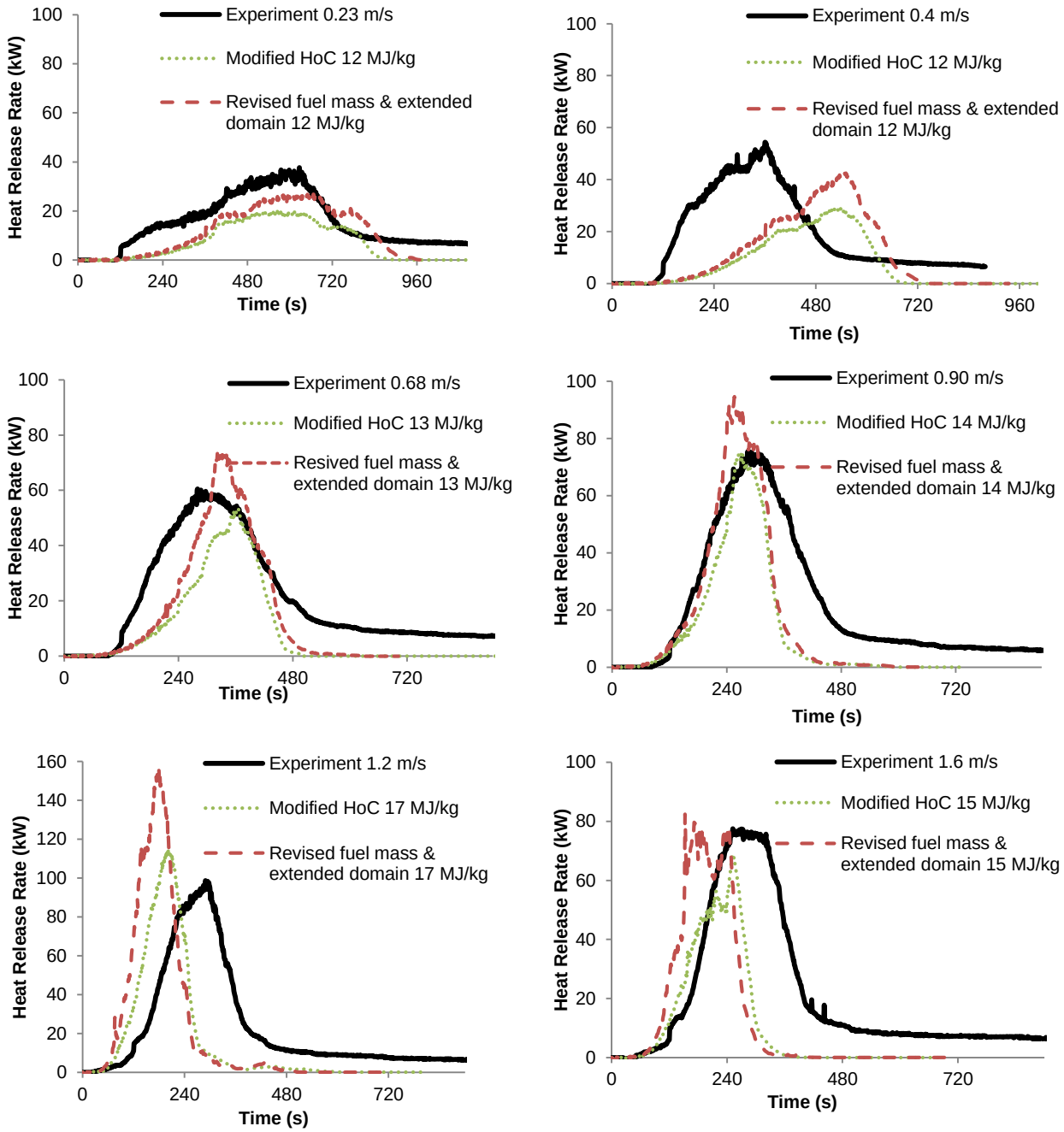

Figure 7-14: HRR estimations using different available fuel mass set-ups.

Overall, the estimations in HRR for the small-scale tunnel fires at different forced ventilation velocities through the application of the FDS6 pyrolysis model are disappointing. The assumption of one-dimensional heat conduction in the solid may over simplify the heat transfer and the increase in temperatures therefore hindering the pyrolysis reactions, slow down the ignition of the fuel and so reducing the growth rate of the fire. Another reason for the limited estimations may be the specified pyrolysis reactions are not wholly able to represent the decomposition reactions in the presence of air. The pyrolysis rate adopted in this study was under a nitrogen environment, which represents the scenarios where the decomposition reactions occur under flame without the presence of oxygen. When forced ventilation conditions are present, the heat may be imposed on the downstream side of the fuel. Therefore, the fuel surface may be heated first without being covered with flame and the pyrolysates may mix with vitiated air before reacting. However, the description of decomposition in two different environment conditions is beyond the current version FDS estimation ability. It is also noted that some burning phenomena are not simulated in the FDS. The collapse of fuel during the burning is not modelled, which may increase burning surface area. In addition, the burning of char is not modelled. The heat of combustion for char is normally higher than the wood material (MDF), however, this value is not able to be defined separately in FDS.

7.6 Simulation of the Fuel Source Using the Ignition Burner Method

In this section, the multiple gas burner method is applied to simulate the same series of experiments.

7.6.1 Determination of Fuel Properties in Ignition Burner Method

The crib in this method is built by the OBST Namelist group in FDS [16]. Surface lines are required to assign to the obstructions with the description of the ignition properties of the fuel (such as the ignition temperature, the burning rate and the thermal thickness). The thermal properties (density, specific heat and, thermal conductivity) of the fuel are defined under a material line (MATL).

The ignition temperature in FDS is the temperature of a surface which reaches a defined value and then the surface starts burning. As discussed in Li's work [37], the ignition temperature in a real fire varies with the external conditions. For instance, the fuel may be ignited by radiation

(auto-ignition) or by a flame (piloted ignition) where the auto-ignition temperature can be twice that of the pilot ignition temperature. In this study, a forced ventilation system was applied in the experiments and the flame was blown towards the downstream side of the fuel. The ignition mechanism for the crib in the experiment is mainly from the flame front and therefore a piloted ignition temperature is used here.

In order to obtain the ignition temperature, the time to ignition (t_{ig}) for the cone calorimeter experiments at three different incident heat fluxes introduced in section 7.3.3 are adopted, which are 100±2 s, 55±2 s and 22±3 s at the incident heat fluxed of 25, 35 and 50 kW/m^2, respectively. There are several mathematical models [92-95] available to calculate the corresponding apparent ignition temperature (T_{ig}) at the time to ignition. The relationship between T_{ig} and critical incident heat flux, $\dot{q}_{cr}''$ required to sustain piloted ignition of a material is written in Equation 7.4 as

$$\dot{q}_{cr}'' = \sigma(T_{ig}^4 - T_0^4) + h_c(T_{ig} - T_0) \tag{7.4}$$

where h_c is the convective heat transfer coefficient and ε is assumed to be 1. Since the long-time ignition assumption is used in the above equation, a value for h_c can be obtained through Equation 7.5. As suggested by Spearpoint [95] where

$$h_c = -2.04\dot{q}_{cr}'' + 19.58 \tag{7.5}$$

A value for $\dot{q}_{cr}''$ can be found from the plot of $1/\sqrt{t_{ig}}$ and incident heat flux $\dot{q}_e''$ shown in Figure 7-15. By plotting a best-fitting straight line, the critical heat flux can be estimated.

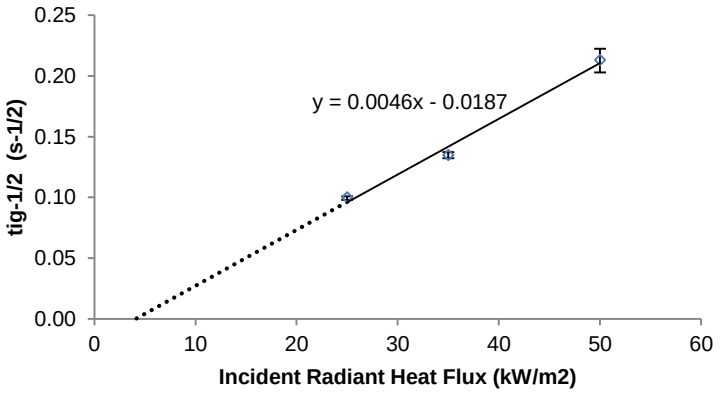

Figure 7-15: Ignition data at different incident heat fluxes.

Based on Figure 7-15, a critical incident heat flux $\dot{q}_{cr}''$ of 4.1 kW/m^2 is obtained. If the corresponding heat transfer coefficient h_c is 11.4 W/m^2/K calculated from Equation 7.5 then, T_{ig} is 195 ˚C using Equation 7.4, which is close to the results in Ngu's [96] calculation for MDF based on the model proposed by Mikkola and Wichman [93]. However, the directly measured T_{ig} in Henderson's [97] cone calorimeter experiments was 340 ˚C. Table 7-4 lists several values of ignition temperature investigated by Ngu for two different thickness MDF boards (20 mm and 40 mm). As seen, the thickness of the MDF only has very limited influence on ignition temperature.

Table 7-4: Ignition temperature for MDF using different calculation procedures, adapted from [96].

Calculation procedure	T_{ig} for 20 mm MDF	T_{ig} for 40 mm MDF
Mikkola and Wichman [93]	202 ˚C	197 ˚C
Quintiere and Harkleroad [92]	389 ˚C	389 ˚C
Spearpoint and Quintiere [95]	240 ˚C	233 ˚C

The set-up of burning rate is to use a time-dependent burning history to describe the burning situation of the fuel after ignition. The heat release rate per unit area (HRRPUA) data obtained from cone calorimeter experiments for the corresponding fuels are often used to describe the burning histories for single fuel package [11, 90]. Cheong [11] adopted the cone calorimeter burning histories of wood samples at an incident heat flux of 50 kW/m^2 and plastic samples at an incident heat flux of 75 kW/m^2 to simulate the Runehamar tunnel fire under 3 m/s forced ventilation in FDS . However, there was no specific discussion regarding the thickness of the sample used for the cone results in his work. In Zhang et al's work [90], a wood crib fire was simulated using FDS where the thickness of the wood stick was 2 cm. The wood surface in the simulation was defined as 1 cm, while the corresponding burning rate was based on 2 cm thick sample cone calorimeter results. In consideration of the one-dimensional heat conduction in FDS6 [16], it is reasonable to use half thickness of the stick on the surface line to describe the heat conduction calculation when both side surfaces are defined. Since the half thickness fuel is used to define the fuel surface, the burning rate for the fuel surface is more reasonable when it is based on the cone results for the half thickness fuel than based on the full thickness fuel.

In this work, the HRR of 7.5 mm thick and 15 mm thick MDF board at incident heat flux of 50 kW/m^2 are measured through cone calorimeter experiments. Since 7.5 mm thick MDF is

not manufactured, samples were prepared by cutting the 15 mm thick MDF board into 7.5 mm thick board for the HRR measurement in cone experiments. In order to keep the sample shape during the burning, a retaining frame with a wire grid was used in the experiments for 7.5 mm MDF samples and a retaining frame was used for 15 mm MDF samples. Two repetition experiments for each thickness MDF were carried out at 50 kW/m^2 and consistent HRR curves were obtained. Figure 7-16 presents the corresponding experimental results for different thickness of MDF board at 50 kW/m^2 incident heat flux.

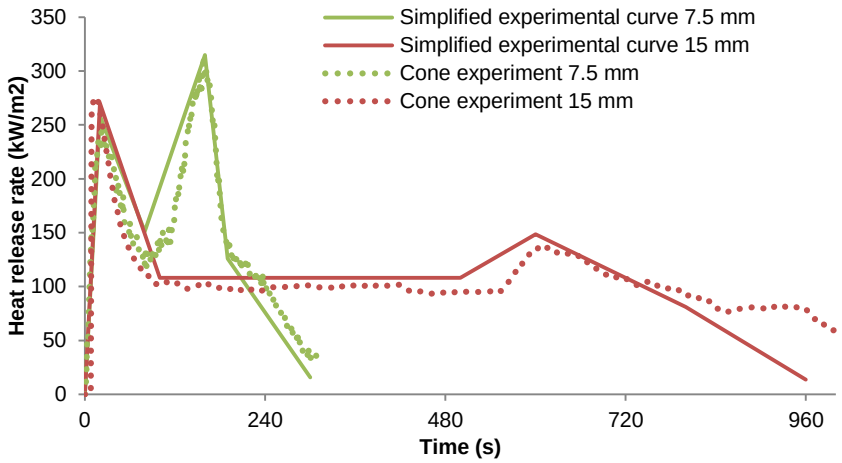

Figure 7-16: Measured cone calorimeter HRR results for different thicknesses of MDF boards.

Based on the measured HRR curves for the 7.5 mm and the 15 mm MDF board, a sensitivity analysis was carried out through a simulation for the small-scale tunnel experiment at 0.68 m/s in order to select the most suitable burning rate curve to estimate the HRR.

The tunnel geometry set-ups shown in Figure 7-5 and 15 mm cell size were adopted for the simulations. The ignition source was represented by a simplified rectangular vent giving a maximum HRR of 3.8 kW. The HRR was allowed to linearly grow to 3.8 kW over a period of 10 s and then remain at the peak value for 120 s before being terminated. In this method, it was found that the cribs could be effectively ignited during the 120 s duration. The ignition properties were applied to define the burning of the fuel accordingly. Since the HRR data were based on the cone experiments, the corresponding heat of combustion of 12 MJ/kg was specified on the REAC line for both simulations. The REAC line in FDS is used to model a fire with the defining of the basic fuel chemistry and the post-combustion yields of CO and soot. The estimated HRR curves are plotted in Figure 7-17. As shown in the comparison, the use of 7.5 mm thick MDF cone results can give more reasonable estimations compared with estimations based on 15 mm thick MDF cone values.

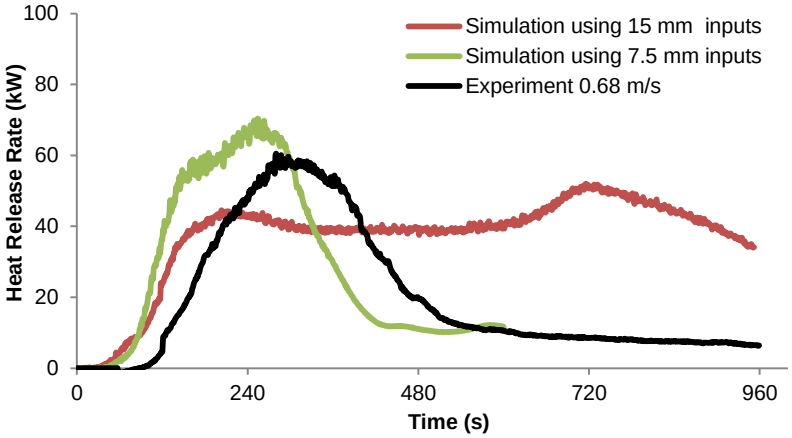

Figure 7-17: FDS estimations for 0.68 m/s small-scale tunnel experiment based on the burning rate for 7.5 mm thick MDF and 15 mm thick MDF

However, it is found the heat of combustion values from the estimations significantly deviate from input value. The deviation is demonstrated in Figure 7-18(a). The modified tunnel domain shown in Figure 7-13 was applied to re-simulate the tunnel experiment with the use of 7.5 mm thick MDF cone data. The corresponding heat of combustion values and HRR results are plotted in Figure 7-18.

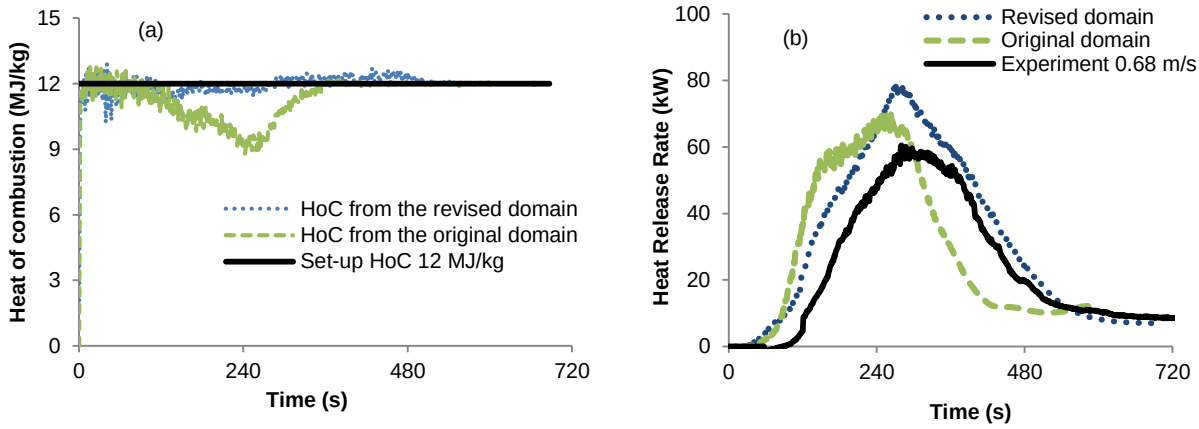

Figure 7-18: FDS estimations for 0.68 m/s small-scale tunnel experiment based on different domain set-up: (a) heat of combustion; (b) HRR estimations

The heat of combustion values based on the revised domain are consistent with the 12 MJ/kg over the burning time and the over estimations in HRR are larger than the results using the original domain.

7.7 Results and Discussion for the Multiple Gas Burner Method

Following the sensitivity study, the enlarged domain and the burning rate for 7.5 mm thick MDF measured from the cone experiments are applied to simulate the tunnel experiments at different ventilation conditions. Figure 7-19 are the comparison of the estimated HRR curves with the experimental results a numerical instability occurred in the simulation for the case of 0.23 m/s when two meshes were aligned. However, the simulation was able to run to completion when meshes were partially overlapped near the exterior boundaries.

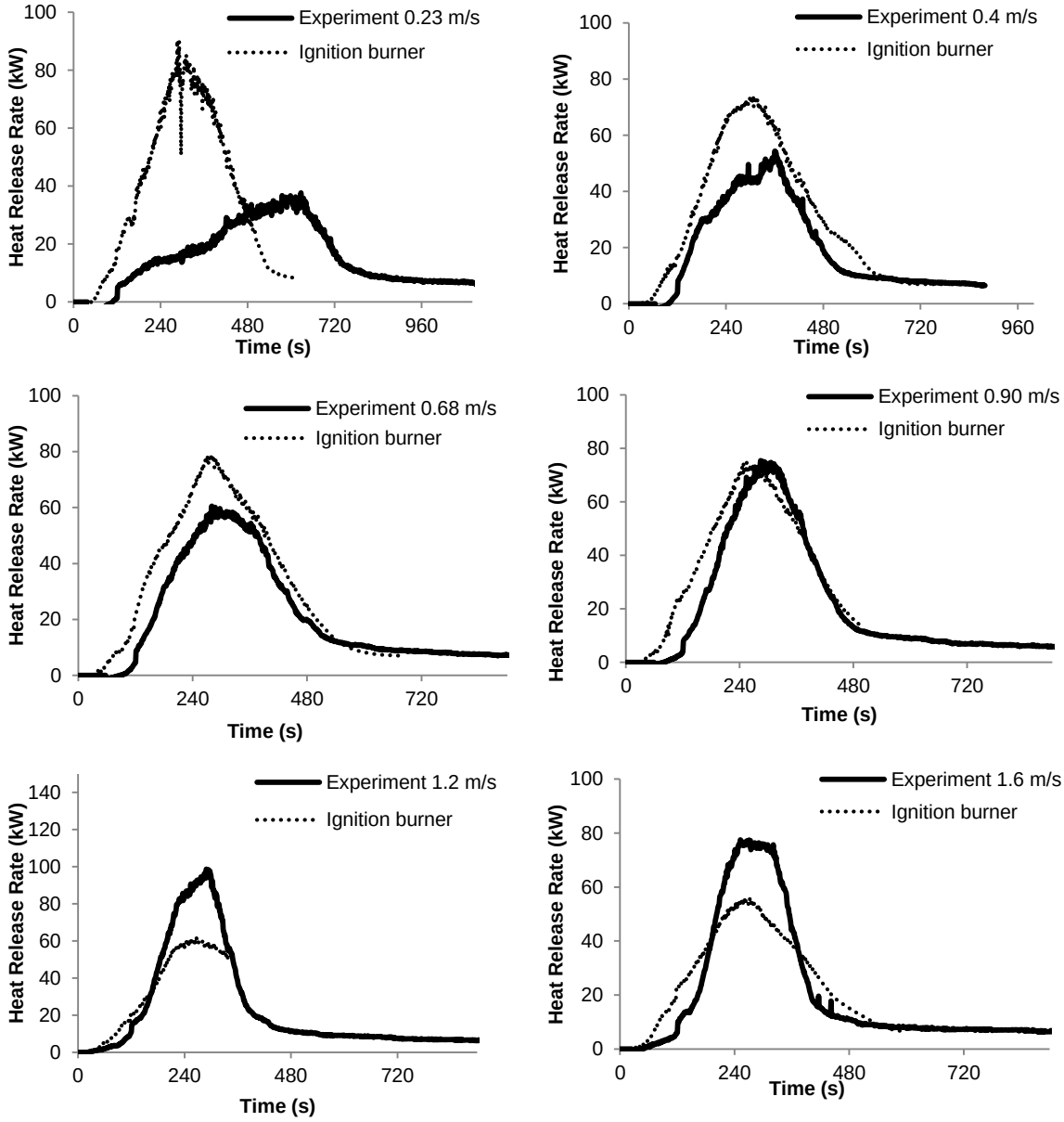

Figure 7-19: FDS HRR estimations for small-scale tunnel experiments at different forced ventilation velocities.

As shown in the above comparisons, except the estimations for velocity of 0.23 m/s experiment, the burning duration at each velocity based on the multiple burner method is effectively estimated. When comparing the estimated HRR curves for 0.23 m/s, 0.4 m/s, 0.68 m/s and 0.9 m/s, only minor difference in HRR results are found. The limited difference in these HRR curves indicates that the influence from these velocities on the HRR cannot be represented in the simulations. The ventilation influence on HRR results are more significant at high velocities (1.2 m/s and 1.6 m/s), whereas the estimated peak HRR values are much lower than the experimental values at these two velocities.

Although the estimations at the forced ventilation conditions are not favourable in the use of the multiple burner method, some suggestions are listed based on the current understanding to the method:

1. The ignition temperatures are varied based on different calculation methods or measurements. A careful study is suggested to choose the most effective ignition temperature to represent the ignition of the fuel during the burning.
2. The appropriate thickness of sample should be considered when cone calorimeter experimental results are applied to define the burning history.
3. The ignition properties determined under quiescent conditions may have limitations to represent burning under ventilation conditions.

7.8 Conclusions

This work applies the pyrolysis model in FDS to simulate a series of small-scale tunnel experiments under different ventilation velocities. The material properties of the MDF used in the small-scale tunnel experiments are investigated and evaluated through simulations of TG and cone calorimeter experiments. It is found that the kinetic properties for MDF obtained in this work can effectively represent the decomposition behaviour in FDS. The FDS cone simulation results cannot precisely match the experimental results, however the FDS can still demonstrate the general burning behaviour for MDF cone experiments.

Based on the simulation results for the tunnel experiments, some factors are found to have significant influence on the estimations: the ventilation influence on burning efficiency must be defined in the use of the pyrolysis mode method; the available fuel mass for burning in the simulations needs to be equivalent to the actual fuel mass; the use of appropriate domain is important in order to prevent the loss of energy during the burning. Because of some limitations in FDS, the burning phenomena of crib fires are still unable to be fully represented.

According to the predictions for the cone experiments and the burning of MDF cribs, the application of the FDS pyrolysis model in this work lacks of the ability to effectively describe the important mechanisms of ignition of the fuel source and the fire growth behaviour.

In the application of the multiple gas burner method, the ignition properties of ignition temperature and burning history are specifically investigated. However, the estimated HRR results for the small-scale tunnel fire experiments cannot represent the ventilation influence on fire size effectively.

Chapter 8 Influence of Fuel Geometrical Shape on FDS Predictions

This chapter is reproduced according to the published paper titled ‘Assessing the influence of fuel geometrical shape on FDS predictions for a large-scale heavy goods vehicle tunnel fire experiment’ in Case studies in Fire Safety.

8.1 Introduction

Fires in tunnels are often caused by vehicle accidents that occur inside them. The characteristics of the fire depend on the various types of vehicles involved and for road tunnels these could include passenger cars, utility vehicles, buses and/or HGVs. HGVs usually have much larger dimensions and carry goods that can cause more severe fires than normal passenger cars. Therefore HGV fires can pose a greater risk to life safety and property protection than fires caused by other types of vehicles.

FDS6 [16] is a commonly used tool in fire engineering to simulate fires. In FDS, a typical way to simulate a given HRR fire is to represent it as the ejection of gaseous fuel from a solid surface by a 2D 'gas burner'. In previous work Li et al. [17] used a simple 2D gas burner with a dimension of 3 m × 10 m to represent the HGV to simulate the Runehamar tunnel fire experiment using FDS. This 2D gas burner representation of a fire is also specified in the New Zealand Verification Method: Framework for Fire Safety Design [98]. The results in the study of Li et al. showed that the simplified 2D gas burner of HGV could give reliable predictions of ceiling temperatures along the tunnel length however, Li et al. did not predict temperature profiles at different tunnel cross section locations. In the work of Cheong et al. [18] a more complex fuel representation was used to simulate the Runehamar simulated HGV cargo fire experiment where the fuel package surface area in the simulation was equivalent to the fuel surface area in the experiment and the inputted HRR curves were based on cone calorimeter experimental results. The approach used in their work was mainly for the prediction of HRR of tunnel fires using FDS and the influence on temperature distributions due to the geometrical shape of the HGV was not investigated in their work.

For an HGV fire that occurs under a forced ventilation condition, the burning behaviour will be affected by the airflow [13, 14]. The physical dimensions of the HGV will also interact with the airflow so that the behaviour of the fire and the downstream temperature distribution in the tunnel will likely be further affected. Any changes in the shape of the fuel package due to material burning away or the collapse of the fuel package will result in additional effects on the fire and hence the temperature distributions. Therefore, it is important to take into account the large geometrical vehicle shape in the simulations of HGV fires.

In this chapter, a series of simulations are carried out to model a large-scale simulated HGV cargo tunnel fire experiment by using different simple geometrical shapes to represent the HGV cargo in order to investigate the influence of the shape of fuel package on flame

extensions, the distributions of temperature and gas concentrations. Several simplifications have been made in order to carry out the simulations in a practical manner.

8.2 The LTA Tunnel Fire Experiment

The details of the LTA experiment have been introduced in Chapter 2. Some specific information of the experiment is repeated in this chapter.

A series of large-scale simulated HGV cargo tunnel fire experiments [39] were conducted on behalf of the LTA of Singapore in a tunnel test facility in Spain. A rectangular shape test section was used for all the experiments, which had a minimum cross section of 7.3 m (W) × 5.2 m (H) and 1% longitudinal gradient. The length of the test tunnel was 600 m and the fire was located 350 m away from the south portal. Measurement points in the tunnel were installed from 30 m away from the upstream edge of the fire to 170 m away from the downstream edge of the fire.

The tunnel section in which the measurements were made is shown in Figure 8-1 together with the instrumentation locations. Temperatures were measured using thermocouples at the different cross sections shown in Figure 8-1(a) and gas concentrations of O_2, CO_2 and CO were measured at location D170. The cross sections with the thermocouple locations at D10, D15 and D30 are illustrated in Figure 8-1(b). More detailed information of tunnel measurement locations and tunnel cross sections can be found in Chapter 2.

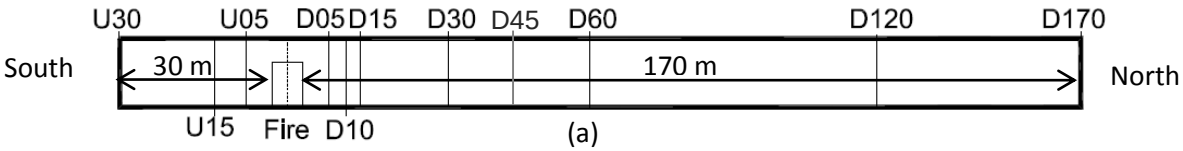

(a)

(U*x*/D*x* defines a position *x* m away from the upstream/downstream edge of the fire)

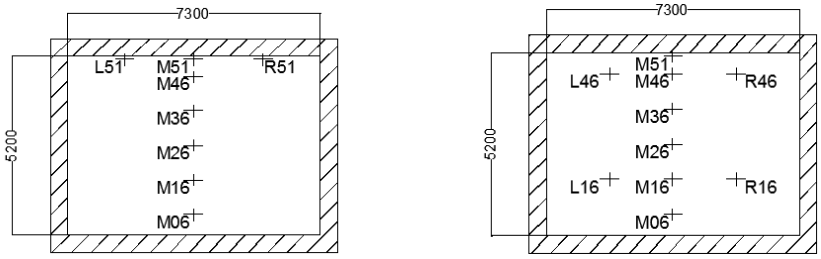

D10 (b) D15 & D30

(M represents the centreline (middle) of the cross section, L/R denote 2 m away from the centreline towards left/right side, e.g. M51 denotes a sensor that is 5.1 m above floor on the centreline)

Figure 8-1: (a) Tunnel with the measurement locations, (b) tunnel cross sections.

The fuel source consisted of 228 pallets with 48 plastic pallets (20% by volume) and 180 wood pallets (80% by volume) [99], in a configuration representative of a fully loaded HGV (7.5 m (L) × 2 m (W) × 3 m (H)). According to the averaged densities of the plastic (1376 kg/m^3) and wood (566 kg/m^3) from the LTA, the mass fractions of plastic and wood pallets are ~38% and 62%, respectively. The fuel source was elevated 1 m above floor and in addition, the top side, the front side and the back side of the fuel source were covered by steel plates to represent a typical HGV configuration. During the experiment the fuel source collapsed as the pallets burned away.

In addition to the fuel source, a target consisting of a stack of pallets with dimension of 1.2 m (L) × 2 m (W) × 3 m (H) was used in the experiments that was located 5 m from the downstream edge of the fuel source.

Jet fans at the southern end of the tunnel were used to generate longitudinal air flow with a desired velocity of 3 m/s in all of the experiments. According to the measurements [39] at the upstream side of the fire, an average of 3 m/s was maintained in the upper cross section of the tunnel, while lower velocities were obtained in the lower cross section. A total of seven experiments were conducted, six with a water suppression system in the vicinity of the simulated HGV cargo and one without. In this study, only the results without the operation of water suppression system are used. The corresponding HRR curve is shown in Figure 8-2. According to the information provided by the LTA, water spray was used to cool down the tunnel structure at the D45 location 9 minutes after ignition. However, the water discharge had no influence on the temperature results recorded at locations of D10, D15 and D30 and no influence on the burning and hence the HRR of the simulated HGV cargo (measured O_2, CO_2 and CO concentrations).

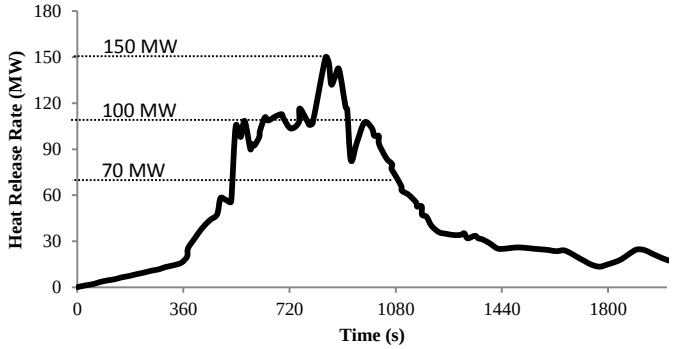

Figure 8-2: HRR curve in the large-scale experiment, adapted from [39].

8.3 FDS Simulation Set-up

8.3.1 Tunnel Geometry and Basic Settings

As indicated in Figure 8-1, the test section had dimensions of 7.3 m (W) × 5.2 m (H) × 210.5 m (L). In order to minimise any influence on the simulation results of sudden changes in temperature at the open ends, the tunnel section in FDS is extended to 240 m including 35 m upstream and 205 m downstream from the centre of the fire. Walls, ceiling and floor are defined as concrete having thermal conductivity of 1.2 W/m.K, specific heat of 0.88 kJ/kg.K and density of 2000 kg/m^3 [88]. A radiative fraction of 35% is used as a reasonable estimate in this work. The 1% longitudinal gradient is modelled through the gravitational vector (GVEC) function in FDS6. Thermocouple devices are set up at the D10, D15 and D30 locations to correspond with the measurement locations in Figure 8-1(b). Thermocouple devices were not included at the D45 location or further downstream because of the influence of the water spray. In addition, the concentrations of O_2, CO_2 and CO are determined at the D170 location.

In order to simulate the experiment several simplifications are made. A 3D solid block with adjusted dimension of 1.2 m (L) × 2.19 m (W) × 3.12 m (H) based the grid resolution is used to represent the target stack of pallets, however, the porous nature of the pallet stack is not modelled as a much finer subgrid size is needed, which is beyond the scope of this work. A uniform velocity of 3 m/s is applied to a solid surface at the upstream end of the tunnel blowing air towards the tunnel to represent the forced ventilation condition and the downstream boundary condition is specified as ambient. The complexity of simulating the measured velocity profile is not attempted in this work.

8.3.2 Fuel Source

The four different fuel package shapes shown in Figure 8-3 are used to represent the HGV cargo fire. The 2DF scenario simplifies the HGV fire to a 2D gas burner on the tunnel floor; in scenario 2DT a 3D solid block is used to represent the HGV and the gas burner is set up on the top surface of the solid block; scenario 3DS mimics the actual fuel source arrangement in the experiment, where the top, upstream, and downstream surfaces of the HGV were covered by the steel plates such that a 3D solid block is used with only the longitudinal surfaces of the block assigned as the gas burners. Scenario 3DA uses the top and all four vertical surfaces but not the bottom surface of a 3D block to simulate the HGV fuel package. To simplify the modelling no attempt is made to simulate the collapse of the fuel source during the experiment.

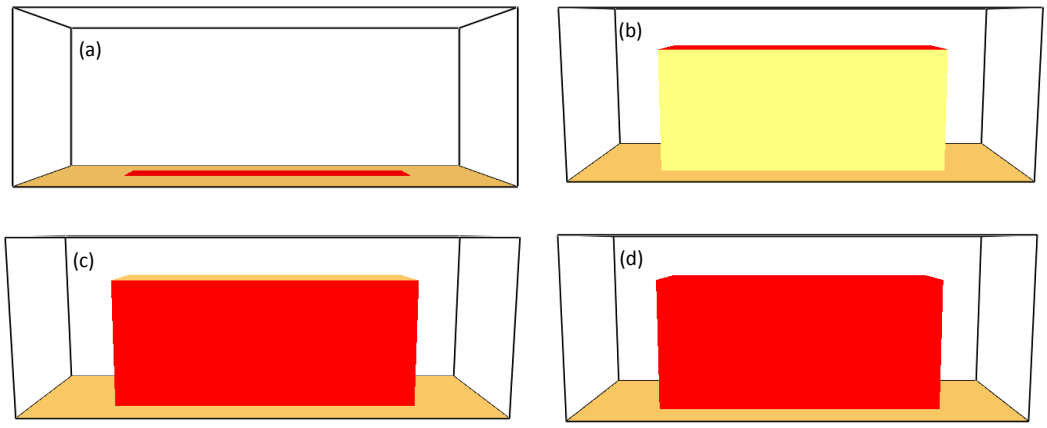

Figure 8-3: Different gas burner surface arrangements: (a) Scenario 2DF; (b) Scenario 2DT; (c) Scenario 3DS; (d) Scenario 3DA;

In order to describe the gas phase combustion reaction, the 'simple chemistry' [16] approach is used. The chemical formula in the simulations is specified as $CH_2O_{0.62}$ which combines values for 38% plastic $(CH_2)_n$ [100] and 62% wood $(CH_2O)_n$ [88]. The yields of CO (y_{co}) and soot (y_s) are defined as 0.012 g/g and 0.012 g/g, respectively which are derived from combining 38% y_{co} and y_s yields for plastic and 68% y_{co} and y_s yields for wood [100]. The combined heat of combustion for the fuel is 20 MJ/kg based on the information provided by the LTA.

8.3.3 Grid Size

According to the FDS6 user's guide [16], the quantity $D^*/\delta x$ represents the number of computational cells spanning the characteristic diameter of the fire, where δx is the nominal size of a mesh cell and D^* is a characteristic fire diameter defined through the HRR of a fire and the thermal properties of ambient conditions. In general the more cells spanning the fire, the better resolution in the simulation.

In the work of Li et al. [17] $0.075D^*$ was shown to be a reasonable value to determine the cell size and a 20 cm uniform cell size was used to simulate Runehamar tunnel Test 1, where the maximum HRR was 202 MW. Cheong et al. recommended 30 cm mesh size in their FDS simulations of the Runehamar tunnel experiment [18].

With consideration of the numerical accuracy, the computational time and the actual tunnel dimensions, a rectangular mesh size is proposed in all of the simulations in this work, which is less than $0.075D^*$ in the x, y and z directions. Table 8-1 lists the relationships between D^* and $\delta x, \delta y, \delta z$ when different fire heat release rates are applied (where $\delta x, \delta y$ and δz are the cell

sizes in the x, y and z directions). The cell sizes in Table 8-1 are determined from the length, width and height of the tunnel to ensure that there are an integral number of cells in each direction. Three different heat release rates (150 MW, 100 MW and 70 MW) from the curve shown in Figure 8-2 are used to calculate characteristic diameter of the fire to correspond to the instantaneous peak, 'average' maximum steady state and value during the growth and decay phases.

Table 8-1: Relationship between D^* and $\delta\mathrm{x}, \delta\mathrm{y}, \delta\mathrm{z}$ for different fire heat release rates and different cell sizes.

$\delta x, \delta y, \delta z / D^*$		150 MW	100 MW	70 MW
		D^* (7 m)	D^* (5.9 m)	D^* (5.2 m)
δx	30 cm	$0.043D^*$	$0.034D^*$	$0.058D^*$
δy	36.5 cm	$0.052D^*$	$0.062D^*$	$0.070D^*$
δz	26 cm	$0.037D^*$	$0.044D^*$	$0.050D^*$

Based on the cell sizes for the *x*, *y* and *z* directions given in Table 8-1, the dimensions of the experimental fuel package (7.5 m (L) × 2 m (W) × 3 m (H)) are adjusted to obtain an integral number of cells for the four different geometrical fuel shape scenarios as shown in Table 8-2. The FDS RAMP_Q function is adopted to specify the heat release rate curve (Figure 8-2). As different fuel surface areas are used in the four different scenarios, the values of heat release rate per unit area (HRRPUA) are different as shown in Table 8-2. The FDS HRR results based on different scenarios are verified, which all match to the experimental HRR curve. The values for 2DF and 2DT are higher than values seen for real fuels but are inevitable when a complex 3-dimensional fuel geometry like the HGV cargo, which were constructed by wood and plastic pallets, are reduced to a 2-dimensional footprint within a model.

Table 8-2: Fuel dimensions and HRRPUA in different fuel geometrical shape scenarios.

Scenario	Fuel dimensions	HRRPUA (kW/m^2)
2DF	7.5 m (L) × 2.19 m (W)	9140
2DT	7.5 m (L) × 2.19 m (W)	9140
3DS	7.5 m (L) × 2.19 m (W) × 3.12 m (H)	3205
3DA	7.5 m (L) × 2.19 m (W) × 3.12 m (H)	1949

8.4 Results and Discussion

8.4.1 Flame Extension

The FDS6 output quantity 'HRRPUV' is rendered through Smokeview to provide a means to visualise the flame boundary. Figure 8-4 shows the predicted flame extension for the four different fuel package geometrical shapes at 360 s, 720 s and 1860 s, which represent burning behaviour during the initial fire growth phase, fully developed phase and the decay phase.

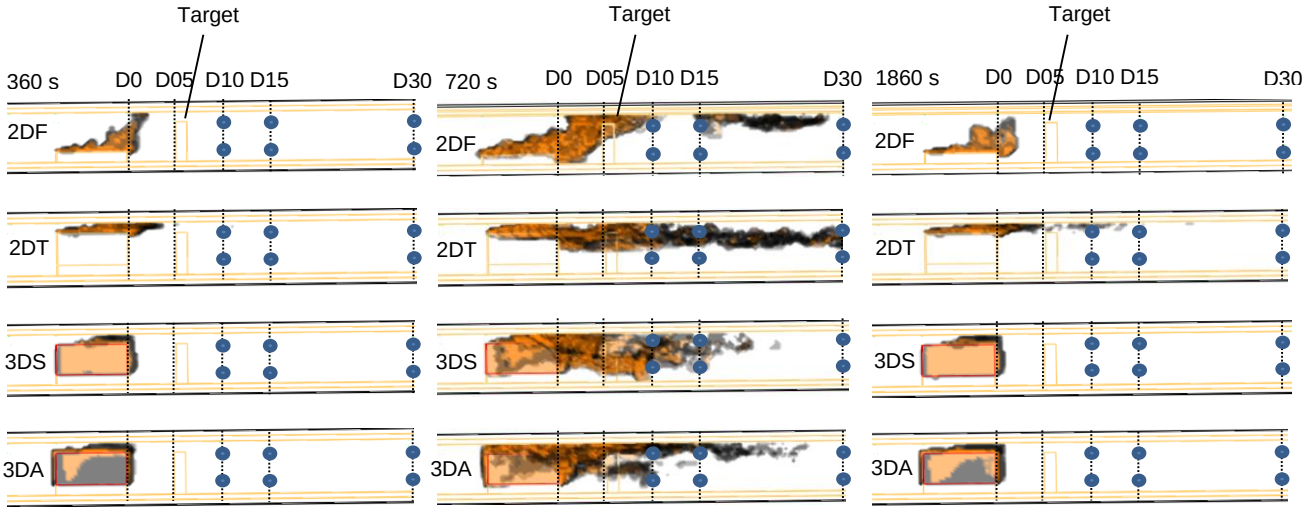

Figure 8-4: Flame extension images at different fire development stages for the four scenarios.

Flame extension lengths are determined from FDS over the time periods 345 to 375 s, 705 to 735 s and 1845 to 1875 s, to correspond to the initial fire growth, fully developed and decay phases respectively. The flame length is defined as the horizontal flame length, where is the distance from the impingement point of the fire source centre to the flame tip [78]. The overall predictions for flame length during the initial fire growth phase and the decay phase are similar

such that there is no obvious flame extension beyond the fuel burning surface area. The significant differences in the predictions of flame extension mainly occur during the fully developed fire phase. In the 2DF scenario the flame extends along the floor to a downstream location 14 m away the fuel centre. In the 2DT scenario the flame extends to more than 30 m away from the fuel centre location. In scenario 3DS and scenario 3DA, the entire 3D block is surrounded by the fire and the flame length extends to ~25 to 30 m on the downstream side.

According to the equation in Tunnel Fire Dynamics [78], the flame length of an HGV fire can be predicted from:

$$L_f = 5.5HQ_f^* \tag{8.1}$$

where L_f is the horizontal flame length, H is the tunnel height and Q_f^* is dimensionless heat release rate. Based on the HRR curve in Figure 2, the $\dot{Q}$ values at the initial fire growth phase, fully developed phase and decay phase are 20 MW, 100 MW and 20 MW, respectively and therefore, the corresponding L_f is calculated as 6 m, 33 m and 6 m. Comparing the results obtained from this mathematical model with the predictions from FDS, it is found that Equation 8.1 gives values close to the FDS6 predictions for the 3DS and 3DA scenarios in the fully developed fire phase. However, since the actual flame length in the experiment was not recorded it is not possible to verify whether the predicted values match reality.

8.4.2 Gas Temperature

The corresponding predicted temperature results for the three different fire development phases at the D10, D15 and D30 cross sections are shown in Figure 8-5 along with the experimental temperature results. The plotted temperatures at 360 s 720 s and 1860 s are average and standard deviation values for the time periods 345 to 375 s, 705 to 735 s and 1845 to 1875 s, respectively.

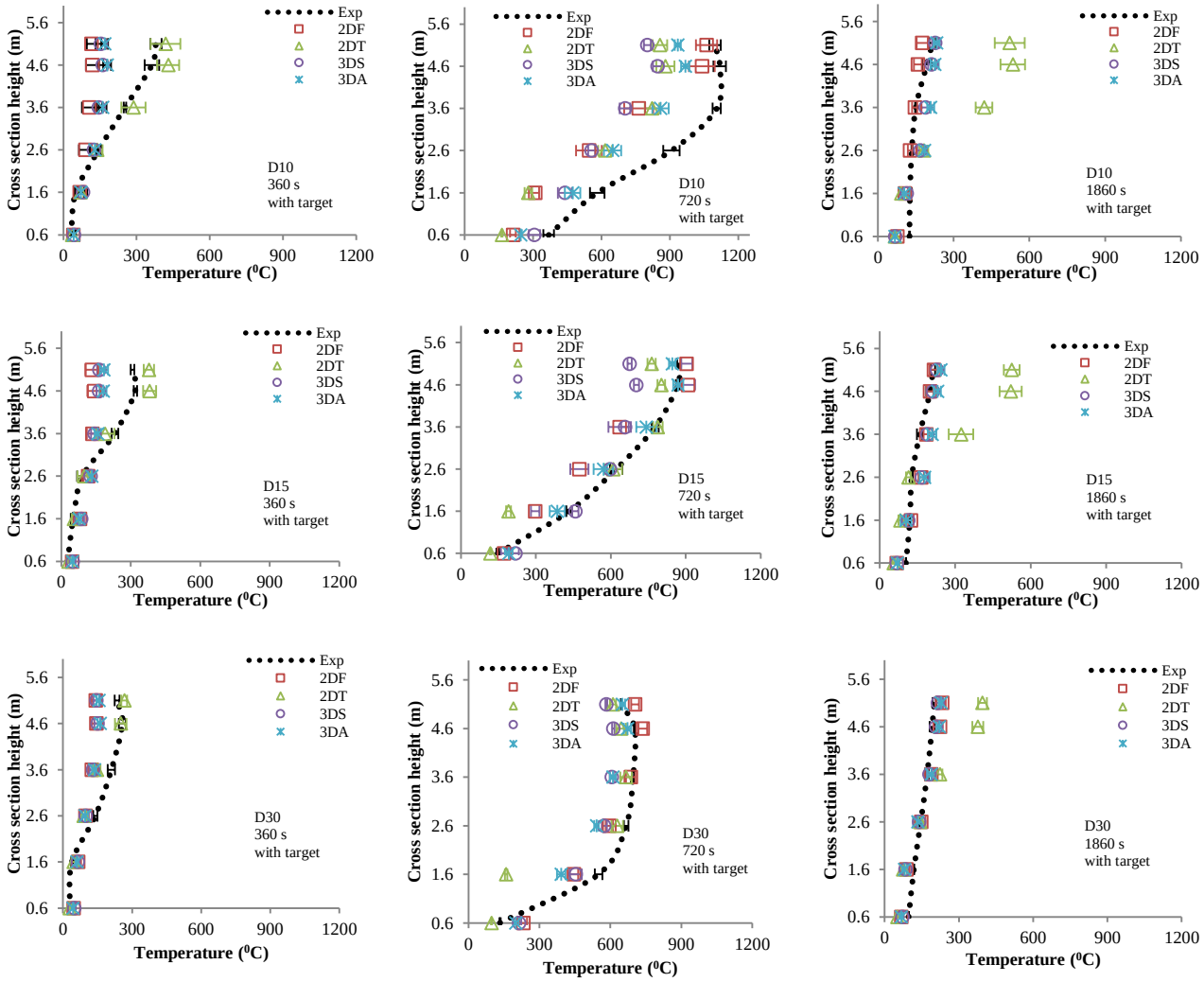

Figure 8-5: Temperature results at different fire development stages for the four scenarios with the downstream target.

As shown in Figure 8-5, during the initial fire development phase, scenario 2DT gives the most effective temperature predictions at the D10, D15 and D30 cross sections. The temperature results for the other scenarios at the upper locations are all slightly underpredicted. During the fully developed phase the predicted temperatures for the four scenarios can all represent the temperature gradients in the experiment at the different cross sections. In particular, the predictions at locations D15 and D30 are closer to the experimental results than the predictions at location D10. The temperature results at D10 are all underpredicted. During the decay phase the results from scenarios 2DF, 3DS and 3DA are all similar, and all match with the experimental temperature curves at the different cross sections. Scenario 2DF may physically demonstrate the actual fuel geometrical shape due to the collapse of the fuel package in the decay phase, while the difference in temperature profiles based on the three scenarios is negligible. The results from scenario 2DT have much higher temperature values at the upper

locations for the different cross sections suggesting the set-up of a gas burner on a 3D block top surface does not represent the temperature profiles due to the collapse of the fuel package in decay phase.

Overall, the results in Figure 8-5 shows that when the target obstacle is present on the downstream side of the fire, the different fuel geometrical shapes only weakly affect the temperature distributions downstream of the obstacle. It is interesting to compare the simulation results for the situation in which the target behind the fire is removed. Figure 8-6 illustrates the temperature predictions at D10, D15 and D30 cross sections without the presence of the target in the simulations. In order to compare with the results in Figure 8-5, the experimental temperature profiles are also plotted.

As seen in Figure 8-6, the predicted temperature distributions during the initial fire growth phase and the fire decay phase are similar to those shown in Figure 8-5. However, the predicted temperatures for the four scenarios show distinct differences during the fully developed phase and of the four scenarios it appears that 3DA gives the closet match with the experimental results.

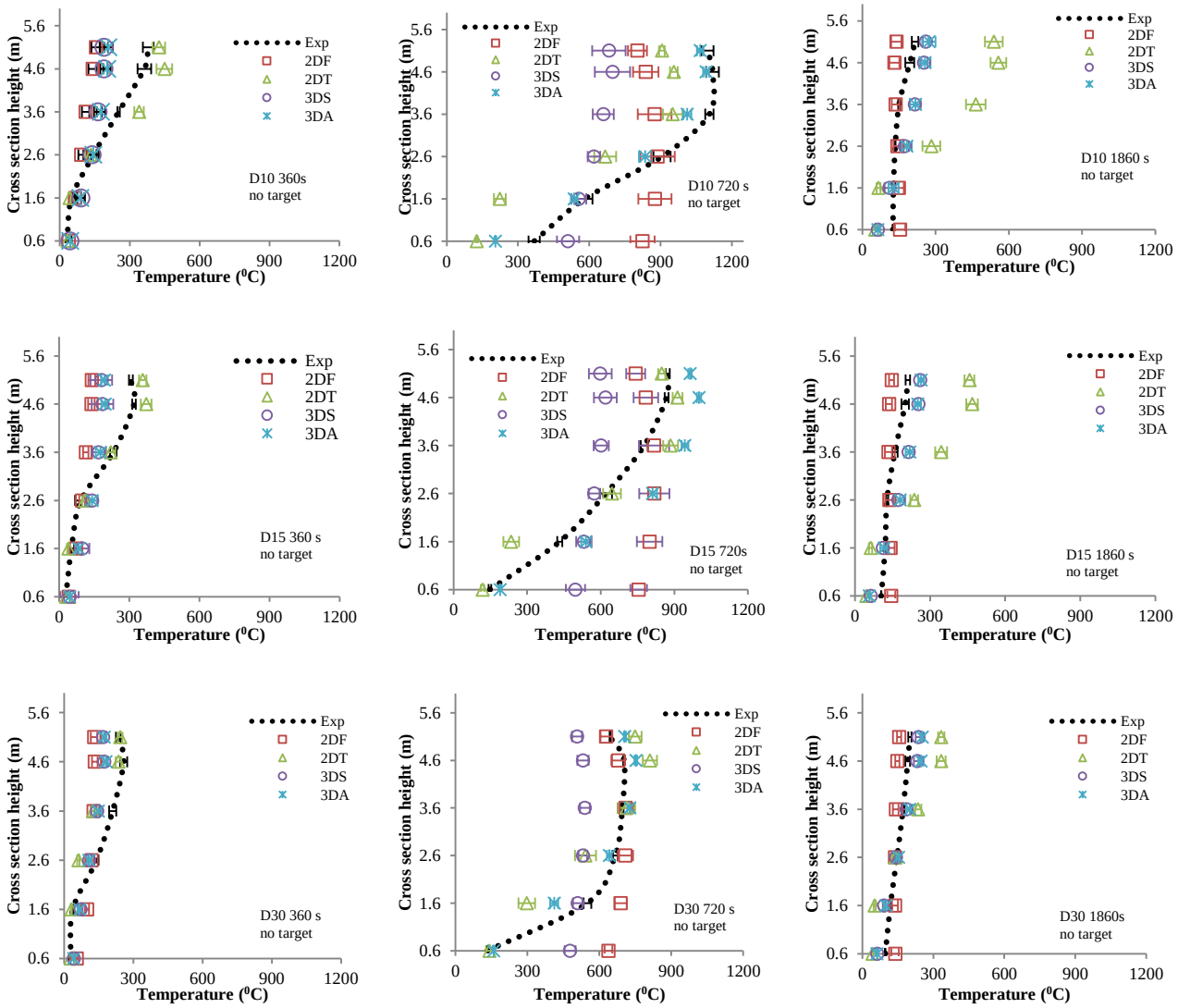

Figure 8-6: Temperature results at different fire development stages for the four scenarios without the downstream target.

8.4.3 Gas Species Concentration

In FDS, the predictions of gas species (O_2, CO_2 and CO) are determined by the chemical formula and the given values of y_{co} in the input file. In this study, the chemical formula of the fuel and y_{co} are estimated based on the previously discussed mass fractions of plastic and wood pallets. In the experiment, the concentrations of O_2, CO_2 and CO were measured at location D170. Since the different fuel geometrical shapes result in different flame extension behaviour and different temperature distributions it is also instructive to observe the influence on the gas concentration predictions. Figure 8-7 presents the comparisons for the concentrations of O_2, CO_2 and CO between the simulation results from the four different fuel shape scenarios and the experimental results. A moving average technique is used to smooth the curves for the FDS6 predictions.

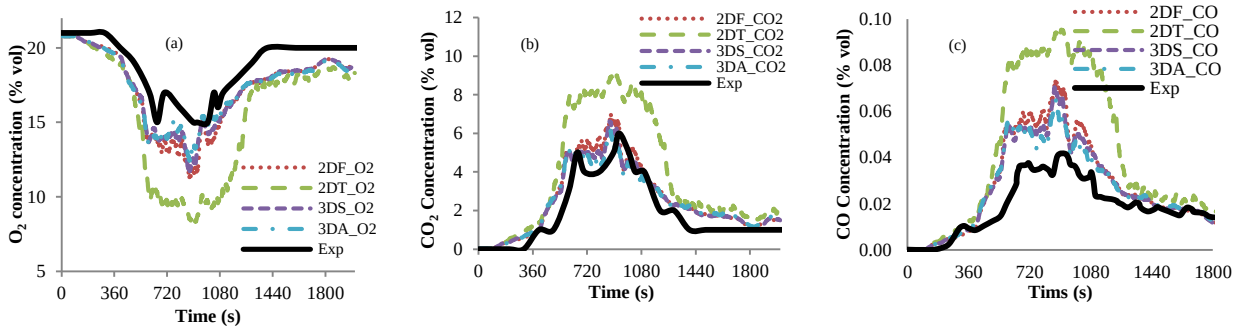

Figure 8-7: Predictions of gas concentrations (a) O_2, (b) CO_2, (c) CO.

As shown in Figure 8-7, different concentration predictions of O_2, CO_2 and CO are obtained in scenario 2DT compared with the predictions from the other three scenarios. The negligible differences in gas concentrations based on scenarios 2DF, 3DS and 3DA suggests that the predicted gas species are sufficiently mixed at the downstream D170 location and are not affected by the three different geometrical shapes. However, when the scenario 2DT is applied, the different gas concentrations profiles shown in Figure 8-7 indicate that the 2DT geometrical shape considerably affects the gas species distributions even when the location is 170 m away from the fire.

Comparing the predicted concentrations of O_2, CO_2 and CO from the scenarios 2DF, 3DS and 3DA to the experimental concentration curves, the predicted O_2 and CO_2 concentration curves are close to the experimental curves, while the concentration curve of CO is significantly overpredicted. The results suggest that the values of O and C based on mass fractions of plastic and wood pallets can give adequately accurate predictions in FDS6. However, the value of 0.012 g/g CO yield in the simulations is higher than the CO yield in the experiments, which results overpredicted CO concentration values.

Overall, the predictions in Figure 8-7 can effectively demonstrate the changes in the concentrations of O_2, CO_2 and CO with the development of fire. However, the species measurements should be viewed caution due to the unknown quantity of water vapour included in the combustion products from the water spray which has not been included in the simulations.

8.5 Conclusions

This work uses four different simplified geometrical shapes in FDS6 to simulate a fuel package that represents a large-scale simulated HGV cargo tunnel fire which includes the influence of a forced ventilation system. It is found that flame extension predictions are affected by the use of fuel geometrical shapes when the fire is fully developed. During this phase the predicted

values of flame length (~25 to 30 m) in scenarios in which vertical as well as horizontal surfaces are burning (3DS and 3DA) are similar to the values calculated from the Ingason et al's model. The use of the different geometrical shapes only weakly affects the predicted temperature distributions in the presence of the large target located downstream of the fire. However significant differences are obtained during the fully developed phase using the different fuel shapes without the presence of the target. Finally the 2D burner on the top of the fuel package scenario (2DT) results in different predicted gas distribution profiles at location D170 when compared with the three other geometrical scenarios.

In summary this case study highlights the influence of using different fuel geometrical shapes on flame extension, temperature distributions and gas species concentrations during different fire development phases. Depending on the objective the results from this work suggest that the use of 'a 2D gas burner' in fire engineering simulations using FDS may not always be suitable in cases involving a fuel package that creates a blockage within a tunnel that is subject to a forced ventilation. The work also illustrates the potential importance of including any large target items that are located downstream of the fire.

8.6 Different mass fractions

In Chapter 9, a detailed analysis of the actual mass plastic and wood pallets was carried out and the mass fractions of the two pallets were found to be 19% and 81%. Therefore, the chemical formula of the fuel was revised as $CH_2O_{0.81}$ and the yields of CO (y_{co}) and soot (y_s) were defined as 0.024 g/g and 0.0088 g/g accordingly. The corresponding predictions of gas concentrations are plotted in Figure 8-8.

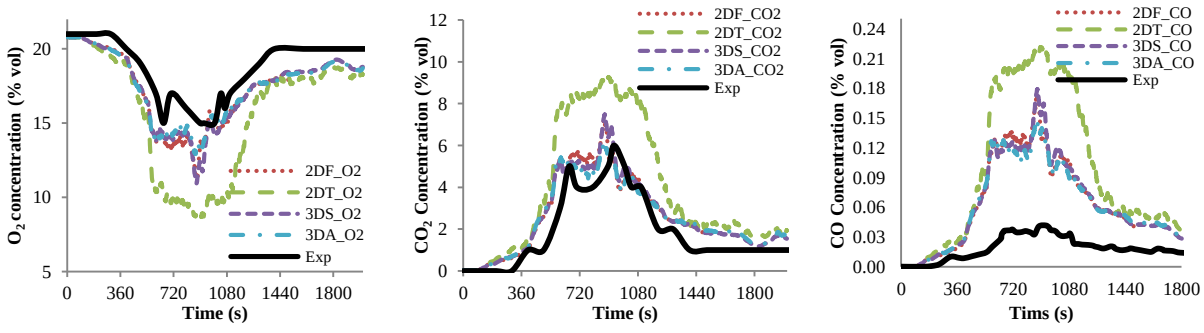

Figure 8-8: Predictions of gas concentrations (a) O_2, (b) CO_2, (c) CO.

There is no significant difference in the results of the concentrations of O_2 and CO_2 shown in Figure 8-8 (a), (b) and Figure 8-7 (a), (b). However, the predictions of CO concentration are

noticeably higher than the predictions shown in Figure 8-7 (c) suggesting that a much lower value of CO yield was obtained in the experiments.

Chapter 9 Large-scale Tunnel Pyrolysis Simulations

9.1 Introduction

In Chapter 8, the single gas burner method of defining heat release rate inputs in FDS was adopted to simulate the simulated HGV cargo fire in the LTA large-scale tunnel experiment through four different simplified fuel geometric shapes. The importance of choosing the appropriate fuel geometry was highlighted in the discussion. However, in the simulations by using the single gas burner method, the HRR data was required to be available. The interaction between the fire and environment conditions could not be represented. The influence from the detailed fuel arrangement and the porous feature of the fuel were not considered. In order to overcome these limitations, the pyrolysis model in FDS6 is applied to simulate the same HGV fire experiment in this chapter since the pyrolysis model is able to predict HRR and to reflect the influence from the fuel geometrical arrangements and the environment conditions.

The pyrolysis model has been adopted to predict HRR in Chapter 7 for a series of small-scale tunnel experiments, the significant influence from the burning mass, the burning surface area and the burning efficiency on the predictions was observed. In order to achieve the equivalent burning surface area and burning mass to the experimental values, the details of the fuel geometrical arrangements and porous feature of the pallets in this work are carefully considered. The material properties of for the LTA wood and the recycled plastic samples are defined from the results discussed in Chapter 3 and Chapter 4. The ventilation influence on burning efficiency is also taken into account through the set-up for the heat of combustion. Because of the length of the tunnel and the fine cell size required to describe the fuel geometry, only the tunnel section from upstream 45 m away from the fire, where the velocity profiles were obtained in the experiment, to 30 m downstream from the fire, where the measurements were recorded in the experiment, is simulated through two meshes. The HRR results obtained from the simulation are compared with the experimental data. The fire spread snapshots from the simulations are demonstrated.

9.2 The LTA Experiment Investigation

In Chapter 2 and Chapter 8, the details of the LTA experiment are introduced. The testing tunnel section had a rectangular shape with minimum dimensions of 7.3 m wide and 5.2 m

high with a length of 445 m. The temperature measurements were located at 30 m upstream away from the fuel (U30) to 170 m downstream away from the fuel (D170). Since the geometrical form of the fuel source and the arrangement of the pallets have been introduced in Chapter 2 and Chapter 8, detailed description of the fuel source used in the LTA large-scale experiment is not repeated in this chapter. However, it is worthwhile to mention that a target consisting of a stack of pallets with dimensions of 1.2 m (L) × 2 m (W) × 3 m (H) was located 5 m from the downstream edge of the fuel source. The target was also elevated by 1 m on a concrete support. Figure 9-1 illustrates the arrangement of the wood and plastic pallets [39].

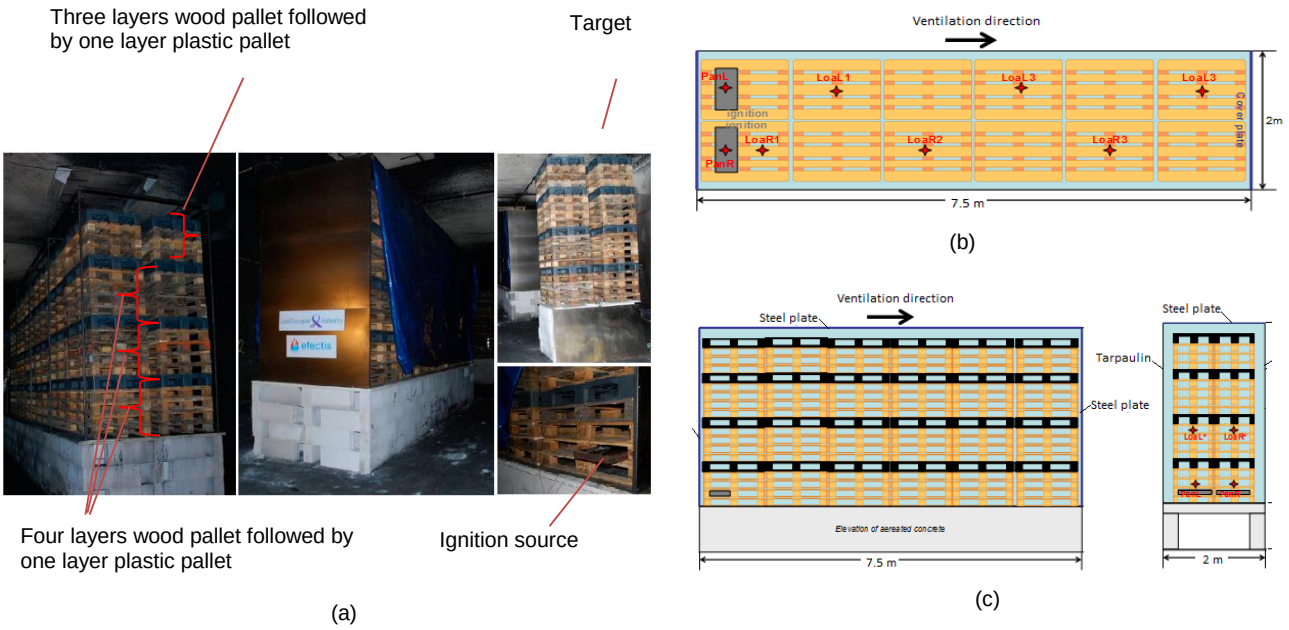

Figure 9-1: The simulated HGV fuel source in the LTA experiment: (a) Detailed arrangement of wood and plastic pallets; (b) Top view of the fuel source; (c) Side view of the fuel source. (reproduced from [39])

The pallets used in the large-scale experiment were Euro pallets which have dimensions of 1.20 m × 0.80 m. The detailed dimensions of a typical Euro wood pallet are shown in Figure 9-2, which are reproduced from [101]. Based on the dimensions in the figure, the total volume of a wood pallet is calculated to be 0.045 m^3. Since the averaged density for the LTA wood sample is 566 kg/m^3, the weight for each wood pallet is 25.4 kg.

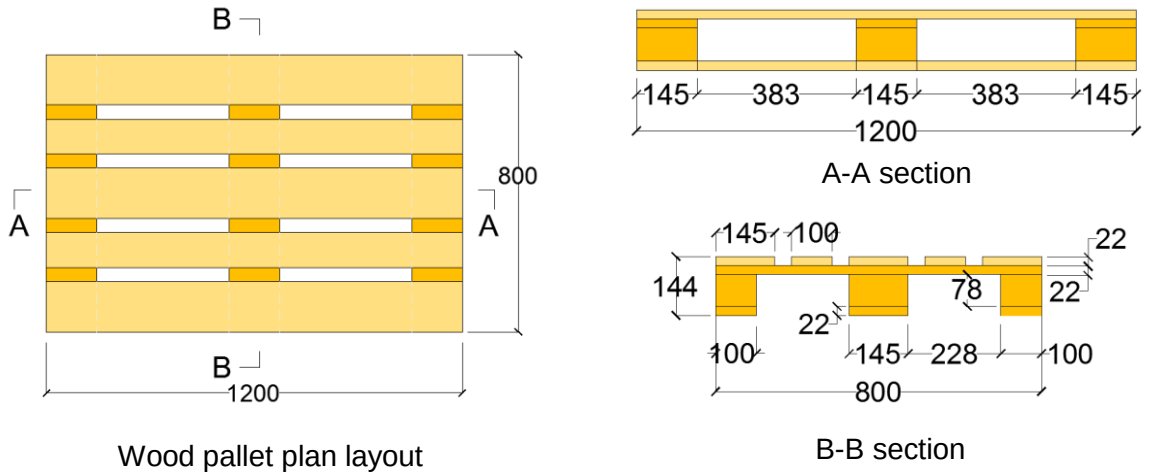

Figure 9-2: Dimensions for wood pallets (reproduced from [101]).

The dimensions for Euro plastic pallets are taken from reference [102] as shown in Figure 9-3.

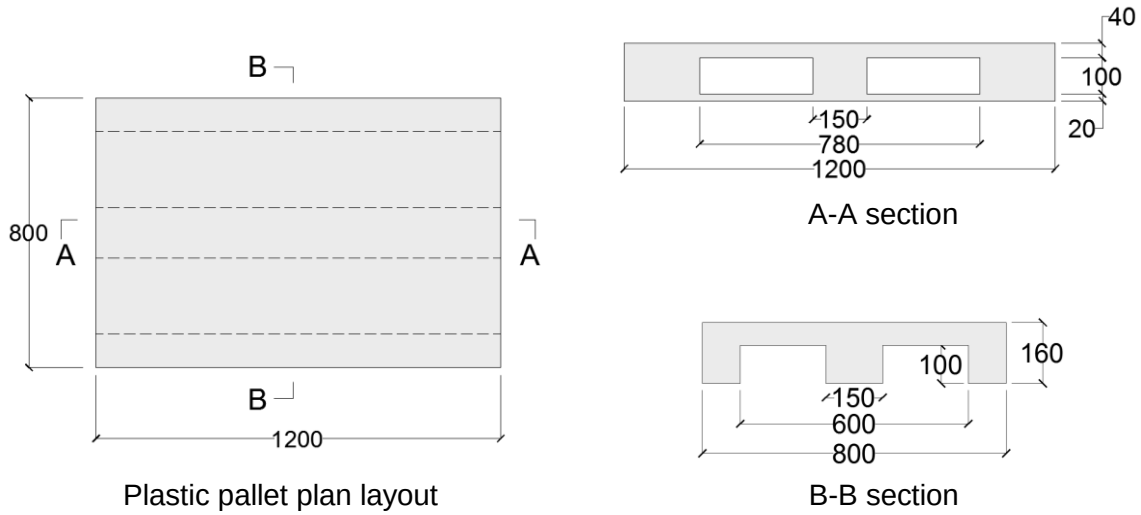

Figure 9-3: Dimensions for plastic pallets (Reproduced from [102]).

The Euro plastic pallets provided in [102] is 20.5 kg/pallet and reported to be HDPE (970 kg/m^3); therefore the actual volume of the Euro plastic pallet is 0.0211 m^3. Based on the LTA plastic sample density (1376 kg/m^3), the weight for each recycled plastic pallet is 29 kg.

Jet fans at the southern end of the tunnel were used to generate longitudinal air flow in the experiment. From the measurements [39] at 45 m upstream (represented by U45) away from the fire, an average of 3 m/s was maintained in the upper cross section of the tunnel, while

lower velocities were obtained in the lower cross section. The details of the velocity at the cross section of U45 can be found in Chapter 2.

9.3 FDS Simulation Set-ups

9.3.1 Determination of Meshes and Cell Sizes

In Chapter 8, the cell size of 30 cm × 36.5 cm × 26 cm is adopted to simulate the simulated HGV cargo fire. In this chapter, the fuel set-ups in the simulations need to represent the actual geometrical details of the pallets in order to reflect the actual surface area and mass in the experiment. Based on the dimensions of wood and plastic pallets presented in Figure 9-2 and 9-3, a much finer cell size of 15 cm × 10 cm × 5 cm is adopted to represent the geometrical details of wood and plastic pallets. The actual details of the pallets would be more accurately represented by a smaller cell size, on the order of 2 cm, however, the computational time would be prohibitive.

As introduced in Chapter 8, only the temperatures measured ahead of the location 30 m downstream (denoted as D30) of the fire were not affected by the water discharges used in the experiments. Therefore, a location of D32 is considered as the downstream boundary of the simulation. The inlet air velocity data was measured at U45 location, thus U45.5 is defined as the upstream boundary of the domain in the simulation.

A separated domain from location of U45.5 to U11.5 with a coarser cell size of 50 cm × 20 cm × 10 cm is used for the upstream tunnel section. The cell size for remainder of the tunnel from location of U11.5 to D32 is defined as 15 cm × 10 cm × 5 cm, where the fuel is located and more importantly, the information of the burning behaviour can be obtained from this section. In terms of the width and height of the two domains, 7.8 m for the width and 5.6 m for the height were considered, which are 0.5 m wider and 0.4 m higher than the tunnel width and height. The dimensions of the tunnel in the simulation are consistent with the dimensions in the experiment. The same as Chapter 8, the 1% longitudinal gradient is modelled through the gravitational vector (GVEC) function in FDS6. Based on the domain dimensions and the cell sizes adopted, a total number of 3.1 million cells for the two meshes were obtained. This simulation took at least two months to complete for a 30 min fire duration on a personal computer with specification of 3.30 GHz CPU (with eight cores) and 32 GB RAM.

9.3.2 Tunnel Boundary Conditions

During the experiment, velocity results at the U45 location showed significant fluctuations in the burning phase and the velocities near the floor were lower than maximum velocity seen near the ceiling. In order to minimise the influence from the fire and to represent the actual ventilation situations, the averaged air velocities over time period from 300 s to 400 s are simulated. Figure 9-4 (a) shows the detailed velocity profile at different heights. The corresponding velocities at U45 location in the simulation are plotted in Figure 9-4 (b). As seen, the simulated velocity profile can effectively represent the velocity range in the experiment. The downstream boundary condition is set as ambient. Walls, ceiling and floor are defined as concrete having thermal conductivity of 1.2 W/m.K, specific heat of 0.88 kJ/kg.K and density of 2000 kg/m^3 [88]. A radiative fraction of 35% is used.

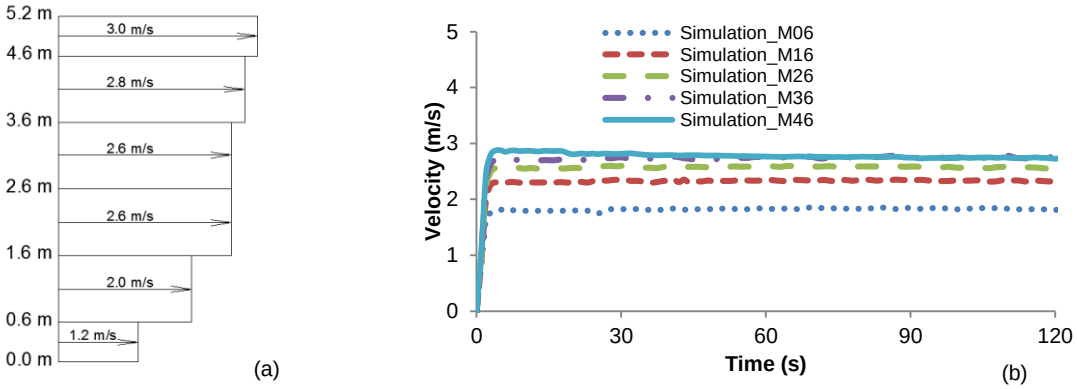

Figure 9-4: Velocity profiles: (a) simplified input velocity; (b) simulated profile.

9.3.3 Fuel Geometry

In order to achieve the equivalent surface area and mass of the fuel to the actual area and mass used in the experiments and to accommodate the cell size, some simplifications of the wood and plastic pallets in the simulations are made. The pallet is simplified to two elements based on different obstacle thicknesses: the wood deckboard obstacle with a 0.05 m thickness and the wood block obstacle with a 0.1 m thickness. The detailed dimensions for each wood and plastic pallet in the simulations are illustrated in Figure 9-5.

Based on the dimensions shown in Figure 9-6, the total available surface area for a wood pallet in the simulations is 2.53 m^2, which is close to the surface area of 2.74 m^2 measured from the actual wood pallet. Since the available mass calculated in the simulations is based on the available surface area and the thermal thickness, the surface area for the wood block and

wood deckboard are derived separately with the use of different thermal thicknesses for these two elements. The surface area for the short wood block is 0.39 m^2 and the total surface area for the thin wood deckboard is 2.14 m^2. In order to have a comparable mass to the experimental value for each wood pallet, 0.025 m thick for the wood block and 0.0018 m for the deckboard are used to calculate the total available mass for burning, which is 27 kg.

The total surface area for the blocks and deckboards in each plastic pallet are 0.39 m^2 and 2.44 m^2, respectively. The mass of each plastic pallet is 31.2 kg when 0.009 mm thickness is considered for both elements.

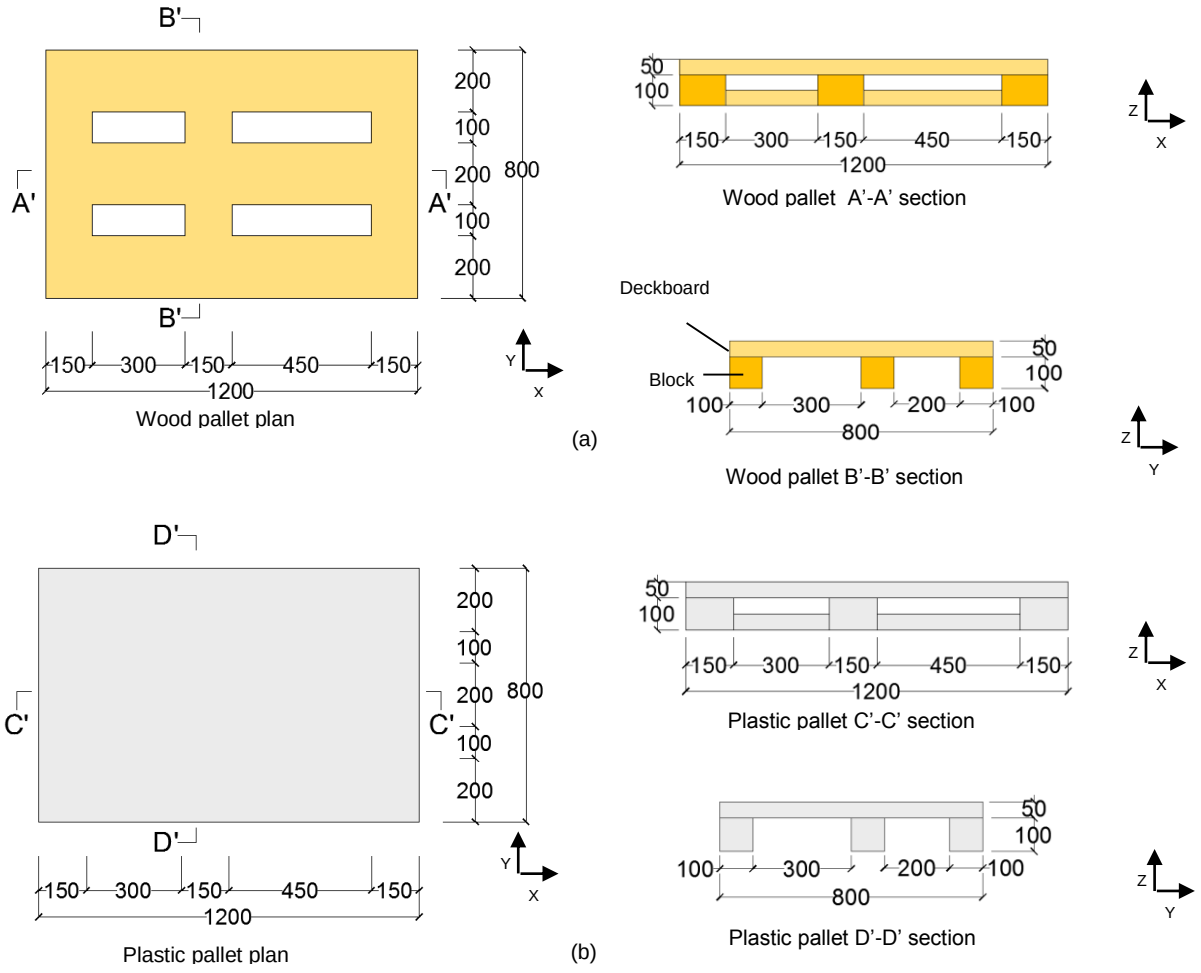

Figure 9-5: Dimensions of pallets in the simulations: (a) wood pallets; (b) plastic pallets.

In the construction of the HGV cargo, the surface area of each are reduced since the surface properties for one side overlapping area is chosen only [16]. With the subtraction of one side overlapped area of each pallet in the cargo, the total surface area for each wood and plastic pallet is 2.38 m^2 and 2.68 m^2, respectively. The mass of each wood pallet is 26 kg and the

mass for each plastic pallet is 29.6 kg. Table 9-1 is the summary of the surface area and mass for each wood and plastic pallet for the fuel load in the simulations.

Table 9-1 Available surface area and mass for the fuel load in the simulations

Items	Wood pallet			Plastic pallet		
	Experiment	Simulation		Experiment	Simulation	
		Block	Deckboard		Block	Deckboard
Surface area (m^2)	2.74	0.36	2.02	2.82	0.36	2.32
Hole area (m^2)	0.146	0.15		-	-	
Mass (kg)	25	26		29	29.6	
Number of pallets	228			48		
Total HGV mass (kg)	5768	5928		1392	1420	

Based on the dimensions of pallets in Figure 9-5, the HGV and the target in the experiment were constructed in the simulations. The steel sheet cover with 1 mm thickness at the front, back and top sides is also modelled. The overall view for the simulated tunnel and fuels are illustrated in Figure 9-6.

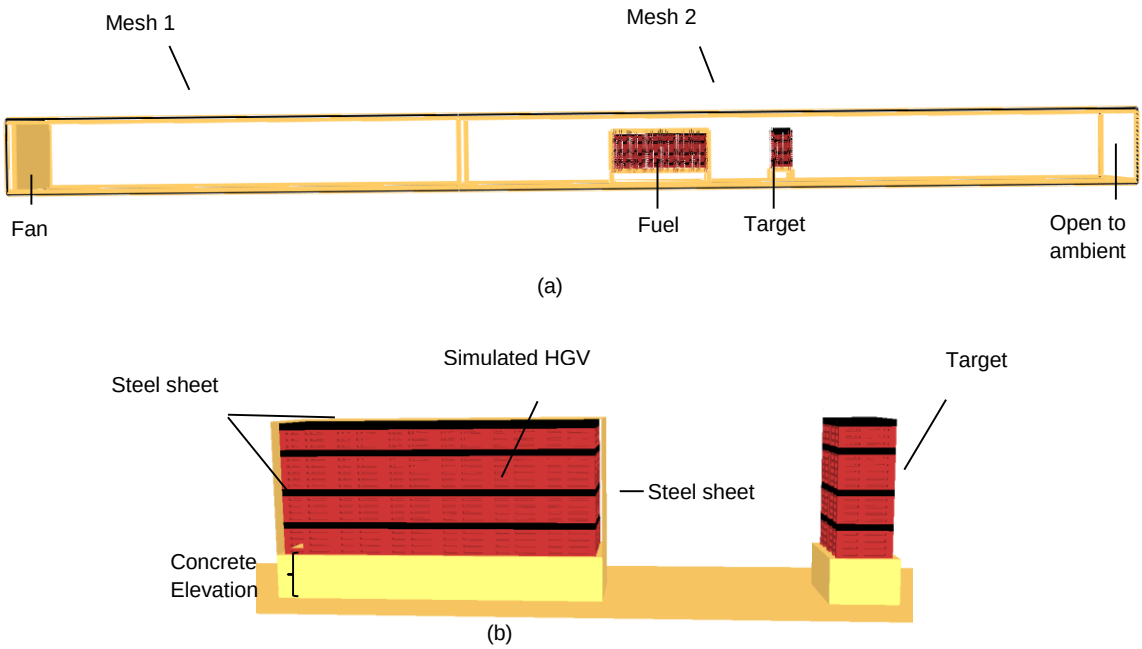

Figure 9-6: Overall view in the simulations: (a) Tunnel geometry; (b) Fuel source and target.

9.3.4 The Properties of Fuels

The material properties of the LTA fuels have been investigated in Chapter 3 and Chapter 4. In the simulation of the wood and plastic pallets, multiple-component schemes are employed to describe the decomposition for wood and plastic pallets, where four components (water, hemicellulose, cellulose and lignin) and two components (P1 and P2) are used to represent the wood and plastic, respectively.

The pallets in FDS are constructed through OBST, which is the namelist group containing parameters used to define obstructions [16], by assigning the corresponding surface lines to represent wood and plastic pallets. Two surface lines are defined to describe the wood pallets: “wood_block” and “wood_board”. The two surface lines are both comprised of four material lines to specify the details of the properties of the four components. The difference between the two surface lines is the definition of thermal thickness, where 0.025 m and 0.018 m were adopted. For plastic pallets, a surface line of ‘plastic’ is used, which consists of two material lines. The thermal thickness is 0.009 m.

9.3.5 Gas Phase Reactions

Based on the calculated mass fraction of plastic and wood pallets, the yields of CO (y_{co}) and soot (y_s) are defined as 0.024 g/g and 0.0088 g/g, respectively. The details can be found in Chapter 8.

The effective heats of combustion for the LTA recycled plastic (35 MJ/kg) and wood (12 MJ/kg) were measured in the cone calorimeter by a third party on behalf of the LTA. Based on the analysis in Chapter 5, the ventilation can significantly enhance the burning efficiency of wood. Since the effective heat of combustion for the wood-based cribs was enhanced from 12 MJ/kg to 13 MJ/kg at 0.68 m/s in the small-scale experiment, the same enhancement on the heat of combustion for the wood pallets at 3 m/s in large-scale experiment is used. According to Harmathy’s work [103], the ventilation effect on the majority of synthetic polymers (for non-charring fuels) was found to be negligible. The charring effect of the plastic fuel is considered to be insignificant based on the very limited residue observed after burning, discussed in Chapter 4. Therefore, there is no enhancement effect on burning efficiency for the plastic pallets. A combination heat of combustion of 17.4 MJ/kg is defined on the reaction line.

9.3.6 Ignition Source and Duration Time

Two trays (0.35 m × 0.70 m) with 1 L gasoline in each were used as the ignition source to ignite the pallets in the experiment. Based on the properties of gasoline 740 kg/m^3, 43.7 MJ/kg and 0.055 kg/m^2/s, the heat release rate generated from each gasoline tray is assumed to be 580 kW and lasts for 55 seconds. In the simulation, each gasoline tray is represented by a vent with dimensions of 0.3 m × 0.8 m at a specified HRRPUA of 2417 kW/m^2 to generate the same fire size as in the experiment. As the simulations demonstrated in Chapter 7, the solid fuels in the pyrolysis model simulations required a much longer ignition duration to be effectively ignited. Based on a preliminary testing for the ignition durations of 1 min, 2 min and 3 min, the pallets in the simulations could not be ignited using these times. Because of the limited computer resources and the extremely long computational time, the ignition duration of 480 s is adopted in the simulation.

9.4 Results

9.4.1 HRR Predictions

The predicted HRR curve from the simulation with 480 s ignition duration is plotted in Figure 9-7. Three αt^2 fire growth curves for ultra-fast, fast and medium are plotted to compare with the predicted and experimental curve. As can be seen, the experimental HRR curve shows an ultra-fast fire growth rate, while the predicted fire growth rate lies in between the fast fire growth rate and the medium fire growth rate. The maximum steady HRR value shown on the experimental curve is about 110 MW. After this value, the HRR suddenly jumps to a peak value of 150 MW, which was due to the collapse of pallets in the burning process [99]. The maximum peak HRR indicated on the predictions is approximately 60 MW, which is only about 55 % of the maximum HRR at the steady state. The total energy integrated from the area under curve is 99.2 GJ for the experiment and is about 100 GJ for the predicted curves. The similarity of the total energy to the experimental result suggests that the set-up fuel in the simulation is mostly consumed.

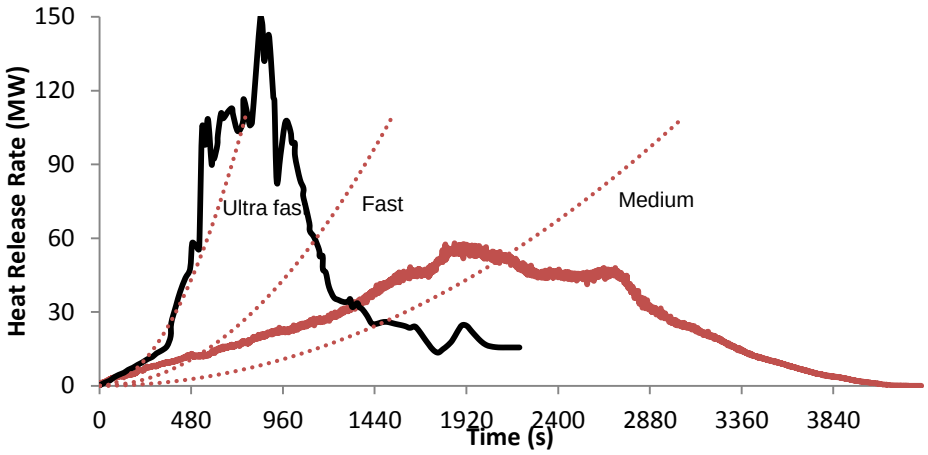

Figure 9-7: Comparison of the predicted HRR curve and the experimental HRR curve.

9.4.2 Flame Spread Behaviour on the Fuel Source

One of the advantages of the simulation for the large-scale tunnel experiment is being able to observe the flame spread behaviour. The predicted fire growth rate and the peak HRR are significantly less than the experimental results, and the burning duration is extensively longer in the simulation. However, the fire spread behaviour from the upstream end of the fuel to the downstream end of the fuel can be clearly observed in the smokeview through the form of HRRPUV. The target set-up in the simulation is successfully ignited in the simulation. Figure 9-8 shows the smokeview images for the HRRPUV at different fire growth stages.

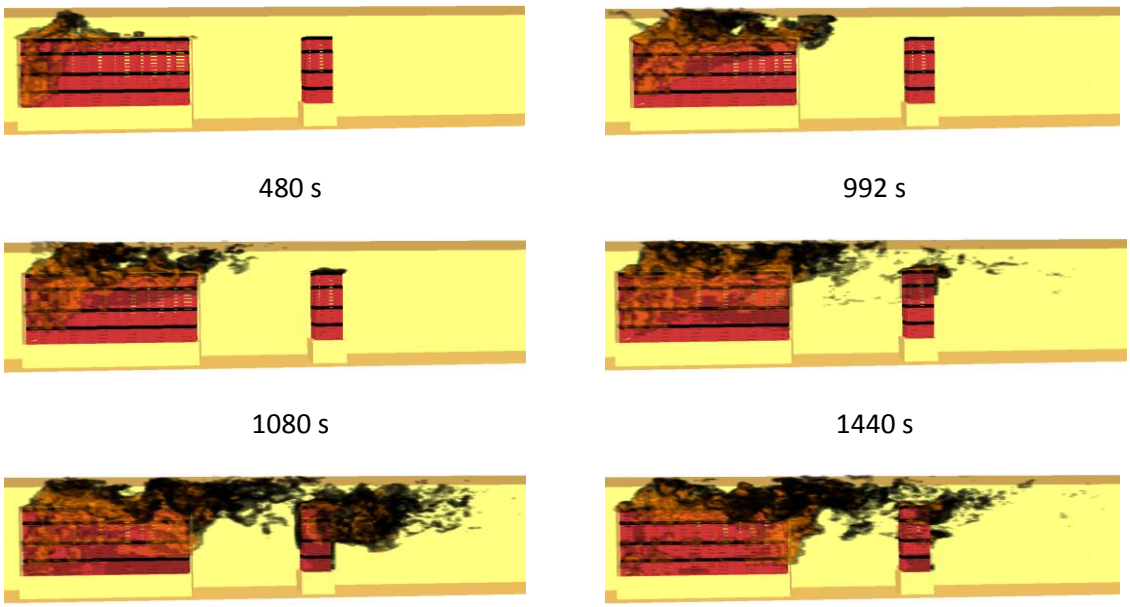

480 s 992 s

1080 s 1440 s

1920 s 2400 s

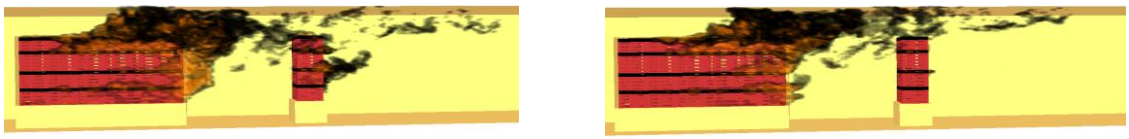

2880 s 3134 s

Figure 9-8: Fire spread behaviour in the simulations at different fire development times.

As shown in the snapshots in Figure 9-8, the fire initially spread vertically in the first stack of pallets before spreading downstream along the upper layers of pallets and finally spreading into the lower layers of pallets. The target ignites at 992 s, when smoke is able to be observed from the top layer of the plastic pallets. The corresponding heat flux on the target at 992 s is 20 kW/m^2. In the experiment, the target was regarded as being ignited when the heat flux reached 10 kW/m^2 at 470 s. In the simulation, the heat flux reaches 10 kW/m^2 at 810 s. The spread of the fire on the target is from the top layers down into the lower layers of pallets. The fire size in the simulation reaches the maximum value at 1920 s and the corresponding snapshot at 1920 s shows that the fuel source is not fully engulfed in flame at that time. The snapshots at 2400 s and 2880 s show that the fire behaviour during the decay phase of the fire. As revealed, the fire starts to extinguish from the upstream side of the pallets towards the downstream side of the pallets and from the lower layers to the upper layers of pallets. Since the fuel shape is not set to be changed in the simulation, the ventilation influence from the changes in fuel geometry in the experiments is not fully represented. The fire flame eventually disappears from the target at 3134 s. There is no image available from the large-scale tunnel experiment to compare the fire spread behaviour in the simulation.

9.4.3 Temperature Comparisons

Temperatures measured at different cross sections of D10, D15 and D30 in the simulation are compared with the temperature results from the experiment. (The detailed experimental temperature measurement set-ups can be found in Chapter 8.) Figure 9-9 illustrates the temperature profiles at the three cross sections.

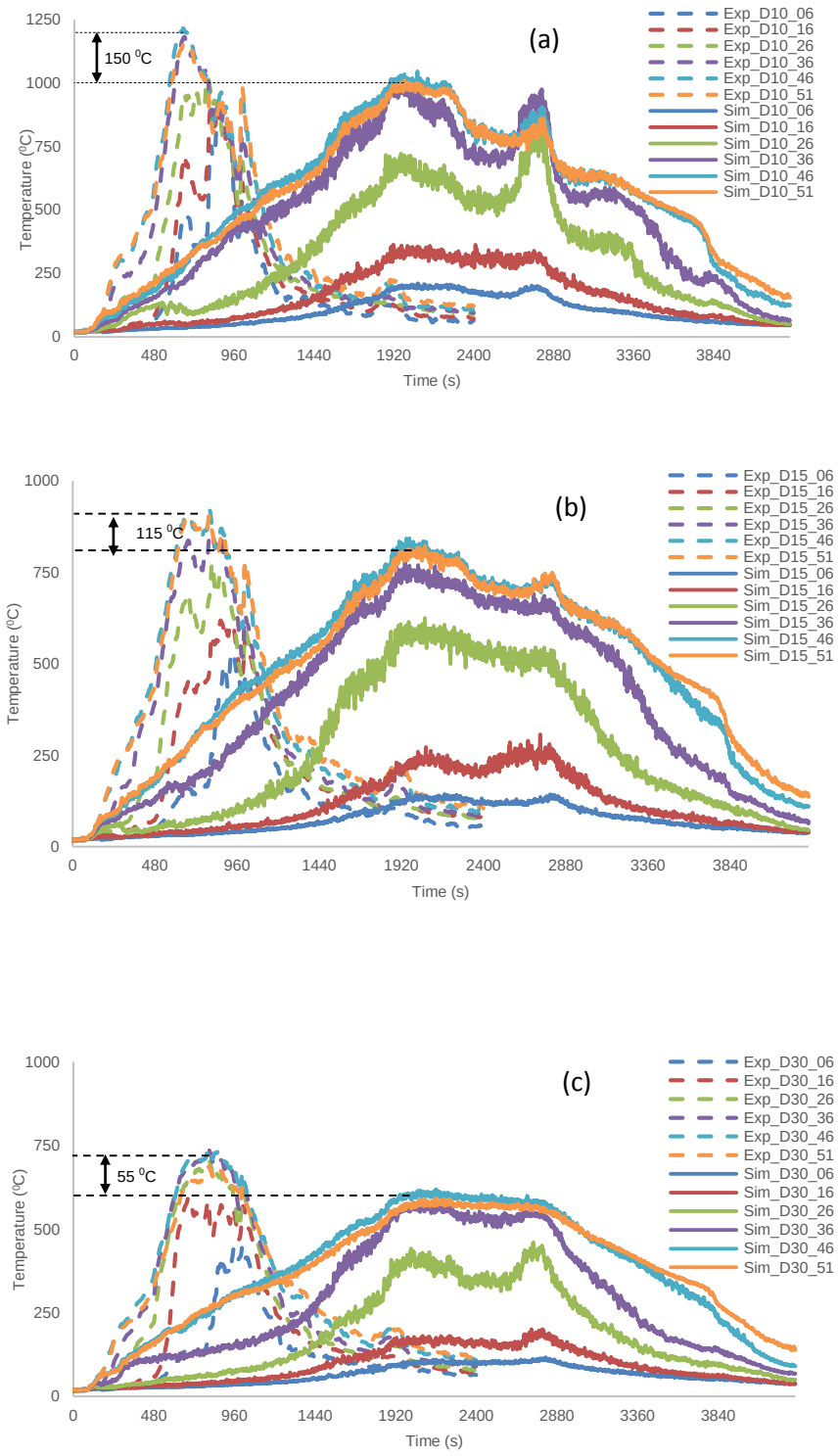

Figure 9-9: Temperature curves at different cross section: (a) D10; (b) D15; (c) D30.

As shown in Figure 9-9 (a), (b) and (c), there are significant differences in temperature curve shapes between experimental results and simulation results due to the differences in HRR. However, there are some similarities in temperature distributions. In both experiments and simulations, the temperature curves measured at high positions (e.g. M36, M46 and M51) at

the cross sections of D10, D15 and D30 closely overlap on each other. The peak values obtained at the three positions in simulations do not demonstrate significant differences. The peak temperature is only ~150 ^{0}C higher in the simulation at location D10 than the peak temperature from the experiment. The differences in peak temperatures are even smaller where the measurement locations are further from the fire source. The differences in the peak values are ~115 ^{0}C for D15 and ~ 55 ^{0}C for D30. The temperature predicted curves at lower positions (e.g. M06, M16 and M26) at the three cross-sections don't shown similar temperature distribution behaviour to the experimental curves.

9.5 Discussion

The results from the simulations suggest that there are still many limitations in using the pyrolysis model to predict the HRR for a large-scale tunnel simulated HGV cargo fire although comparable temperature predictions to the experimental results at high positions of D10, D15 and D30 were obtained. This part discussion is mainly to explain the possible reasons behind the unfavourable HRR predictions.

The limited predictions in HRR may be affected by the kinetic properties defined for the fuel materials. The kinetic properties adopted in this study are based on the analysis of the decomposition under a nitrogen environment, where the air is not considered to be present during the decomposition process. However, the decomposition environment for the fuel in reality, might involve the presence of air. As the fire spread on the fuel is from the upstream side towards the downstream side, the fuel on the downstream side is heated up first and starts to decompose before the fuel is ignited. The ignition of the target shown in the Figure 9-8 is a good example, where the smoke is visible on the target before the flame appears. This phenomenon suggests that the top layer plastic pallet of the target starts to decompose first in the air environment and then the generated gases are ignited. According to some experimental results for the fuel decomposition under air (such as wood and polyurethane materials [56, 104]), it has been found that higher decomposition rate and lower reaction temperatures could be obtained than the results under a nitrogen environment. Therefore, the overall decomposition behaviour for the simulated HGV fire demonstrates a very complex manner. It combines partial of the decomposition in the presence of the air and partial of the decomposition under flame without the presence of the air.

Another reason for the limitations in the predicted HRRs is that the influence from the changes in fuel shape during the burning cannot be fully captured in the simulation. The fuel was actually consumed and burnt away in the experiments. Notably, the fuel collapsed before reached the

peak HRR, which increased the burning surface area. In the simulation, the initial complicated porous geometry of the HGV cargo is carefully considered. However, the collapse of the fuel and the increase in the burning area are not modelled, which may result in low predicted HRR results.

The oversimplified radiative fraction in FDS, where the 0.35 default value is used, might be another cause for the underpredictions. The radiation effects on fires are more significant within tunnels than compartment fires or open fires. In this particular simulated HGV cargo fire experiment, the porous feature of the pallets acting as many small compartments may result in much higher radiation effect than other type fuels. However, this increase in radiation effect is not considered in the simulation.

Some other limitations in FDS, which have been discussed in the simulations for the small-scale tunnel experiments, are also applied to this simulation.

9.6 Conclusions

In this chapter, the pyrolysis model was applied to simulate the LTA large-scale tunnel simulated HGV cargo fire experiment. The complex porous features of the plastic and wood pallets were modelled in the simulation. According to the simulation results, the HRR curve was significantly underpredicted, as it had much slower fire growth behaviour and lower peak HRR values than the experimental results. The total energy obtained from the simulation was close to the experimental value. The fire spread behaviour on the HGV cargo was observed in the simulation. However, there is no available image from the experiments to compare with. Some possible reasons for the limited predictions in HRR are discussed: the kinetic properties adopted in the simulation could not represent the decomposition reactions in the immediate area of the decomposition reaction; the geometrical form of the fuel in the simulation did not change with the development of fire and the increasing burning area caused by the fuel collapse could not be represented in FDS. The increase in radiation effect due to the tunnel geometry and the porous feature of the fuel was not modelled in FDS.

It is worthwhile to mention that even though the HRR predictions are unfavourable in this simulation, some peak temperature values are effectively predicted.

Chapter 10 Conclusions and Recommendations

10.1 Conclusions

10.1.1 Conclusions for material property studies

In this research, the material properties of plastic and wood, which were the same materials used in the LTA experiments, were investigated through a series of material-scale and bench-scale experiments.

Based on the TG experiments, a simple hand calculation method was proposed to derive the kinetic properties for the plastic and wood samples. A multiple-component scheme to describe a complex decomposition for a material was adopted in this method, where two components and three components were used to represent the plastic and wood material. Due to the different definitions of normalised mass for each component in the pyrolysis rate calculation between the proposed method and FDS6, the kinetic properties derived from the method were modified accordingly in order to apply the results to FDS6. In the comparison to the experimental data for TG simulations in FDS6 showed that the kinetic properties derived from the hand calculation method were effective.

The heat of reaction for plastic and wood materials were analysed from the measured DSC heat flow data. In the analysis for the DSC heat flow data for the plastic samples, an approximate baseline method was used. It was found that the change in energy was negligible for the first decomposition reaction of the plastic and the heat of reaction for the second decomposition reaction was $\sim$ 670 to 875 J/g.

Due to the significant charring characteristic for wood, a study was carried out to investigate the influence of using lids in DSC experiments on the heat of reaction for the LTA wood sample. Differences in the absorption and release of energy during the decomposition of wood were found in the experiments with lids and without lids. The values of heat of reaction varied from experiment to experiment. An overall trend was concluded from these values that more energy is gained and released in the experiments with lids than without lids. However, the differences in the predictions of HRR for cone calorimeter simulations in FDS6 using these various heat of reaction values were minor.

In addition, the kinetic property results based on one and multiple-component schemes obtained from the GA searching method were compared with the kinetic properties obtained from the hand calculation method proposed in this research through the simulations for TG experiments. The differences in the TG simulation results were negligible when the multiple-component kinetic properties derived from the GA method and the hand calculation were applied. However, only limited accuracy were obtained when the kinetic properties derived from the GA one-component scheme were used.

In order to apply the pyrolysis model to predict burning behaviour, the required material properties of the plastic and wood materials were analysed from a series of manual optimisation studies. The simulations for cone calorimeter experiments were used to examine the ability of the pyrolysis model to predict the burning behaviour. According to the predictions, the backface conditions defined for the cone simulations had significant effects on HRR predictions. The influence for different cell size limits in the solid phase was found to be minor in the simulations for cone experiments. When the kinetic properties based on the multiple-component schemes obtained from GA and hand calculation methods were applied, only insignificant differences were observed on the predicted HRR curves for the two methods. In terms of the accuracy of the predictions, the HRR curves were not always comparable to the experimental HRR curves under different heat fluxes. The best predictions were obtained at 35 kW/m^2 for plastic and 25 kW/m^2 for wood. When kinetic properties based on the one-component scheme were applied, the predicted HRR curves for plastic and wood samples had different degrees of success in representing the basic burning future for the two materials in the cone experiments.

10.1.2 Conclusions for the small-scale tunnel experiment studies

A series of small-scale tunnel experiments were carried out which was scaled at a ratio of 1:20 based on the large-scale tunnel simulated HGV cargo fire experiment carried out by the LTA.

In order to assess the ability of the small-scale tunnel experiments to reproduce the results at the large-scale, two types of fuel sources which a gas burner and cribs constructed of MDF were adopted to represent the burning HGV in the large-scale experiment. The velocities, temperatures and the corresponding data for HRR calculations were measured from the small-scale experiments.

According to the comparison of the HRR curves obtained from the crib and gas burner small-scale experiments with the scaled HRR curve from the large-scale experiment, the HRR curve

from the gas burner experiment could closely reproduce the scaled HRR curve obtained from the large-scale experiment. However, the HRR curves obtained by using the cribs as the fuel source cannot fully represent the HGV burning in the large-scale experiment. Comparing the temperature results obtained from the experiments, the temperatures from the gas burner experiment effectively represented the temperatures at the large-scale during the growth and decay phases. However, the maximum temperature results didn't match the correspond temperatures at the large-scale due to the different effects from the boundary conditions on temperatures.

Following the assessment of using different fuel sources to represent the HGV burning in the large-scale experiment, a parametric study with regards to the ventilation influence on fire burning behaviour in tunnels was further conducted. In this parametric study, a series of small-scale tunnel experiments at different ventilation velocities from 0.23 m/s to 1.9 m/s were carried out MDF cribs 375 mm long as the fuel source. The HRR and mass loss rate data were obtained from the experiments. According to the analyses of peak HRR and maximum mass loss rate data at different velocities, it was found that the influence of forced ventilation on peak HRR was from two aspects: fire spread rate and burning efficiency. The influences could be described through three different stages. When the velocity was less than 0.6 m/s, the forced ventilation mainly affected the fire spread rate. When the velocity was beyond 0.6 m/s, the forced ventilation affected both the fire spread rate and burning efficiency of the crib fire until no more fuel was available to spread to. Based on the experiment, when the air velocity reached 1.2 m/s, the fuel was engulfed by the fire and the ventilation velocity only affected the burning efficiency of the fire. A simple mathematical model was proposed to explain the effect of the force ventilation on the spread of fire and the burning efficiency.

Analysis was also conducted on some tunnel experiments by using different lengths of cribs at high velocities. It was found that the crib length also had significant influence on burning efficiency. Therefore, the previous mathematical model was modified by taking into account the influence of the crib length on fires and good predictions in peak HRR could be obtained based on this new model. The relationship between the $\dot{Q}_{p,nv}$ and $\dot{Q}_{p,engulf}$ could be described as $\dot{Q}_{p,nv}$ =60%$\dot{Q}_{p,engulf}$ for the fuel source with a porosity factor larger than 0.7 mm. The model was applied to assess the effect of crib length on the enhancement of peak HRR for cribs with porosity factor more than 0.7 mm. It was found the maximum enhancement ratio was around 2.2 for different length cribs, while a higher velocity was required to reach the maximum enhancement for a longer crib.

10.1.3 Conclusions for the numerical simulations for the small- and large- scale tunnel experiments

Two different simulation methods (the pyrolysis model method and the multiple ignition burner method) were applied to simulate the small-scale tunnel experiments. In order to apply the pyrolysis model, the material properties of the fuel source were investigated and evaluated through different experimental and modelling analyses. According to the simulations for the small-scale tunnel experiments, some significant influences on the predictions from different factors were noted. Much longer ignition duration was required to ignite the MDF crib in the simulations than in the experiments; the effect on the burning efficiency by the forced ventilation should be taken into account; the available mass and area for burning should be equivalent to the experimental values; a sufficient domain should be used in order to obtain effective predictions. Although efforts have been made to modify the simulation set-ups based on the observed factors, only limited improvements in the predictions of HRR and consumption of fuel mass in the simulations were obtained. In the application of the ignition burner method, the determination of the ignition temperature and burning history were specifically discussed and applied to simulate the small-scale tunnel experiments. The predicted HRR curves based on this method could not effectively represent the influence from ventilation on burning.

In the simulation of the LTA large-scale tunnel experiment, the single gas burner method in FDS6 was initially adopted to investigate the influence of using different geometrical shape fuel packages on flame extensions, temperature distributions and gas concentrations in FDS simulation. The LTA fuel source was represented by four different fuel package shapes. A 2D gas burner on the tunnel floor; a solid block with a 2D gas burner on the top surface of the block; a solid block with assigning gas burners on the top, upstream and downstream surfaces of the block; a solid block with assigning gas burner on all surfaces except the bottom surface. The target located on the downstream side of the fuel in the experiment was also considered in the simulations. According to the results, similar flame length predictions based on the scenarios using different burning surfaces on the solid block to the flame lengths calculated from Ingason et al's model were obtained. The temperature distributions on downstream side were only weakly affected by the use of different geometrical shapes in the presence of the target, while the differences were significant at fully developed phase when the target was not presented. The scenario of using a gas burner on the top of the solid fuel block resulted different predictions in gas concentrations from other scenarios. This work highlighted the importance in considering the use of appropriate fuel representation in tunnel fire simulations.

Finally, the pyrolysis model was applied to simulate the large-scale tunnel experiment. In the simulations, the equivalent burning surface area and burning mass to the experimental values were considered and the complex porous features of the pallets were represented. The predicted HRR results demonstrated considerably slower fire growth behaviour and lower peak HRR than the experimental results. The reasons for the inaccurate predictions were discussed: the limitation in the kinetic properties; the limitation in representing the changes in the fuel geometrical shape while burning and the limitation in adopting appropriate radiation effect.

Overall, this research extensively discussed the methods of obtaining material properties and the importance of using the appropriate properties in the application of the pyrolysis model. A mathematical model was proposed to explain the comprehensive tunnel ventilation influence on crib fires. The capability of the current pyrolysis model in FDS to accurately predict HRR for tunnel fires is limited. However, the advantages in using the pyrolysis model to reflect the interactions between the environmental conditions and the development of the fire are demonstrated and the approaches from different aspects to improve the pyrolysis model predictions are highlighted.

10.2 Recommendations and future work

According to the results of using the FDS pyrolysis model to simulate different scales experiments, it is recommended that the FDS pyrolysis model can be applied to simulate material-scale and bench scale experiments. Effective results can be obtained when appropriate material properties are adopted in the simulations. However, the application of using the pyrolysis model to simulate tunnel fires with complex fuel geometrical shapes is not suggested.

From the studies of the fundamental material properties, small-scale tunnel experiments and the FDS pyrolysis simulations, it is also found that there are many aspects in this research which are worth extending through further investigations.

In terms of material properties, it would be worthwhile applying experimental methods suggested in [54, 55] to further understand the thermal properties for the LTA recycled plastic and wood materials. In addition, studies to define decomposition reactions in FDS for both reactions in the presence of air and in the absence of air are suggested. It is of interest to further examine the influence of lid in DSC experiments for non-charring materials

Some future small-scale tunnel experiment studies are recommended as below:

- To repeat some small experiments with a target to study the influence on temperatures.
- To use pallets stacks in the small-scale experiment to effectively represent the porous feature of the HGV cargo fuel.
- Experiments with forced ventilation > 2 m/s are suggested in order to demonstrate the ventilation influence on burning efficiency at higher velocities.
- Experiments to be conducted using the same crib lengths and lower forced ventilation velocities (such as from 0.2 m/s to 1.2 m/s) to verify the influence of crib length on burning efficiency.
- Further research is needed on the relationship between $Q_{p,nv}$ and $Q_{p,engulf}$ for cribs with porosity factors less than 0.7 mm.

With regards to the modelling work, it is recommended to explore the radiation applications in FDS to specify the effects for more satisfactory predictions. The approach of using the multiple gas burners to predict HRR still remains of interest for further studies. More studies on using the appropriate ignition properties in this approach to define the burning of fuels are suggested. It is also recommended to carry out simulations for a relatively simple pallet stack fire with single type fuel to further observe the factors affecting the HRR predictions.

Some suggestions for the improvements to FDS:

1. It is suggested to improve the heat transfer algorithm in FDS as the one-dimensional heat transfer in FDS cannot fully represent the heat transfer for complex burning,
2. Since charring materials may have different heat of combustion values over the burning period, it is suggested that the definition of the heat of combustion in FDS should be more flexible (such as allowing for time-dependence of the property).
3. A further suggestion is to develop a methodology within FDS to account for the increase in burning surface area due to the collapse of fuel and other factors.

Chapter 11 Reference

1. Carvel, R. and Marliar, G., *A history of fire incidents in tunnels*, in *Handbook of tunnel fire safety* R. Carvel and A. Beard, Editors. 2011, ICE.

2. Amunsen, F., *Data on Large Tunnel Fires*, in *Report prepared for the OECD study on transport of dangerous goods through tunnels*. 2000, Norwegian Public Road Administration: Oslo.

3. Lacroix, D. *The Mont Blanc Tunnel Fire: what happened and what has been learned.* in *The 4th International Conference on Safety in Road and Rail Tunnels*. 2001. Madrid, Spain.

4. Eberl, G. *The Tauren Tunnel incident: what happened and what had to be learned*. in *The 4th International Conference on Safety in Road and Rail Tunnels*. 2001. Madrid, Spain.

5. Bajwa C, Mintz T, Huczek J, Axler K, and K, D., *FDS simulation of the Newhall Pass tunnel fire*, in *NFPA World Safety Conference* 2009: Chicago, IL, USA.

6. Ingason, H., Li, Y.Z., and Lönnermark, A., *Heat Release Rate in Tunnels*, in *Tunnel Fire Dynamics*. 2015, Springer New York: New York, NY.

7. *Fires in Transport Tunnels: Report on Full-Scale Tests (1995)*, Studiensgesellschaft and Stahlanwendung e. V., Editors.: Düsseldorf, Germany.

8. Brousse B, Perard M, Voeltzel A, and YL, B., *Ventilation and fire tests in the Mont Blanc Tunnel to better understand the catastrophic fire of March 24th, 1999*, in *Third international conference on Tunnel Fires and Escape from tunnels*. 1999: Washington DC,USA. p. pp 211–222.

9. Lemaire A and van de Leur PHE, K.Y., *Safety Proef: TNO Metingen Beneluxtunnel—Meetrapport. TNO*. 2002.

10. Ingason, H. and Lönnermark, A., *Heat release rates from heavy goods vehicle trailer fires in tunnels.* Fire Safety Journal, 2005. **40**(7): p. 646-668.

11. Cheong, M.K., *Assessment of Vehicle Fire Development in Road Tunnels for Smoke Control Ventilation Design, PhD thesis*. 2009, University of Canterbury.

12. *NFPA 502 Standard for Road Tunnels, Bridges, and Other Limited Access Highways*. 2014.

13. Ingason, H., *Fire dynamics in tunnels*, in *The handbook of tunnel fire safety Second Edition*. 2012, Thomas Telford: London.

14. Carvel, R. and Beard, A., *The influence of tunnel ventilation on fire behaviour*, in *Handbook of tunnel fire safety* R. Carvel and A. Beard, Editors. 2012, ICE.

15. Ingason, H., *Model Scale tunnel fire tests-longitudinal ventilation* SP Swedish National Testing and Research Institute, 2005. **SP Report 2005:49**.

16. McGrattan, K., McDermott, R., Hostikka, S., and Floyd, J., *NIST special publication 1019 Fire Dynamics Simulator User's Guide Version 6*. 2015: National Institute of Standards and Technology.

17. Li, Y.Z. and Ingason, H., *Numerical Simulation of Runehamar Tunnel Fire Tests*, in *6th International Conference 'Tunnel Safety and Ventilation'*. 2012: Graz. p. 203-210.

18. Cheong, M.K., Fleischmann, C.M., and Spearpoint, M.J., *Calibrating an FDS Simulation of Goods-vehicle Fire Growth in a Tunnel Using the Runehamar Experiment.* 2009.

19. Matala, A., *Methods and applications of pyrolysis modelling for polymeric materials, PhD thesis*, in *School of Science*. 2013, Aalto University Finland. p. 84.

20. Pau, D.S.W., *A comparative study on combustion behaviours of polyurethane foams with numerical simulations using pyrolysis models, PhD thesis*, in *Civil and Natural Resources Engineering* 2013, University of Canterbury: Christchurch, New Zealand.

21. Ingason, H., Li, Y.Z., and Lönnermark, A., *Design Fire Curves*, in *Tunnel Fire Dynamics*. 2015, Springer New York: New York, NY.

22. Ingason, H., Li, Y.Z., and Lönnermark, A., *Tunnel Fire ventilation*, in *Tunnel Fire Dynamics*. 2015, Springer New York: New York, NY.

23. Bendelius, A., *Tunnel ventilation: state of the art*, in *Handbook of tunnel fire safety* R. Carvel and A. Beard, Editors. 2012, ICE.

24. PIARC, *Technical Report on Fire and Smoke Control in Road Tunnels*, in *Report 05.05.B. PIARC(World Road Association)*, L. Defense, Editor. 1999: France.

25. Services, R.a.M., *Road Tunnel Ventilation Systems*. 2014.

26. *Memorial Tunnel Fire Ventilation Test Program – Test Report*. 1995, Massachusetts Highway Department and Federal Highway Administration.

27. Thomas, P.H., *The movement of smoke in horizontal passage against an air flow*, in *Fire Research Station Note*. 1968, Fire Research Station: UK.

28. Oka, Y. and Atkinson, G., *Control of smoke flow in tunnel fires.* Fire Safety Journal, 1995. **25**: p. 305–322.

29. Kennedy, W.D., Gonzalez;, J.A., and Sanchez, J.G., *Derivation and application of the SES critical velocity equations.* ASHRAE Transactions, 1996. **102**(2).

30. Lönnermark, A. and Ingason, H., *The effect of cross-sectional area and air velocity on the conditions in a tunnel during a fire*. 2007: SP Technical Research Institute of Sweden.

31. Kissinger, H.E., *Reaction Kinetics in Differential Thermal Analysis.* Analytical Chemistry, 1957. **29**(11): p. 1702-1706.

32. McGrattan, K., McDermott, R., Mell, W., Floyd, J., Hostikka, S., and Matala, A., *Modeling the burning of complicated objects using Lagrangian particles*, in *Proceedings of the Twelfth International Interflam Conference*. 2010. p. 743-753.

33. Rein, G., Lautenberger, C., Fernandez-Pello, A.C., Torero, J.L., and Urban, D.L., *Application of genetic algorithms and thermogravimetry to determine the kinetics of*

polyurethane foam in smoldering combustion. Combustion and Flame, 2006. **146**(1): p. 95-108.

34. Pau, D.S.W., Fleischmann, C.M., Spearpoint, M.J., and Li, K.Y., *Determination of kinetic properties of polyurethane foam decomposition for pyrolysis modelling.* Journal of Fire Sciences, 2013. **31**(4): p. 356-384.

35. Li, K.Y., Huang, X.Y., Fleischmann, C., Rein, G., and Ji, J., *Pyrolysis of medium-density fiberboard: optimized search for kinetics scheme and parameters via a genetic algorithm driven by Kissinger's method.* Energy & Fuels, 2014. **28**(9): p. 6130-6139.

36. Matala, A. and Hostikka, S. *Pyrolysis modelling of PVC cable materials*. in *10th International Association for Fire Safety Science (IAFSS)*. 2011. Maryland, USA.

37. Li, Y.Z., *CFD modelling of fire development in metro carriages under different ventilation conditions*. 2015, SP Technical Research Institue of Sweden.

38. Kim, E., Woycheese, J.P., and Dembsey, N.A., *Fire Dynamics Simulator (Version 4.0) Simulation for Tunnel Fire Scenarios with Forced, Transient, Longitudinal Ventilation Flows.* 2008. **44**(Generic): p. 137-166.

39. Cheong, M.K., Cheong, W.O., Leong, K.W., Lemaire, A.D., and Noordijk, L.M., *Heat Release Rate of Heavy Goods Vehicle Fire in Tunnels with Fixed Water Based Fire-Fighting System.* Fire Technology, 2014. **50**(2): p. 249-266.

40. Kalsi, H.S., *Indicators and Display Devices* in *Electronic Instrumentation, Third Edition*, H.S. Kalsi, Editor. 2010: New Delhi p. PP. 25-63.

41. Nikolaev, A.V., Logvinenko, V.A., and Gorbatchev, V.M., *Special features of the compensation effect in non-isothermal kinetics of solid-phase reactions.* Journal of thermal analysis, 1974. **6**(4): p. 473-477.

42. McGrattan, K., Hostikka, S., McDermott, R., Floyd, J., Weinschenk, C., and Overholt, K., *NIST special publication 1018-1 fire dynamics simulator Technical Reference Guide Volum 1: Mathematical Model*. 2015: National Institute of Standards and Technology.

43. Grønli, M.G., Várhegyi, G., and Di Blasi, C., *Thermogravimetric analysis and devolatilization kinetics of wood.* Industrial and Engineering Chemistry Research, 2002. **41**(17): p. 4201-4208.

44. Di Blasi, C., *Modeling and simulation of combustion processes of charring and non-charring solid fuels.* Progress in Energy and Combustion Science, 1993. **19**(1): p. 71-104.

45. Madorsky, S.L., *Thermal degradation of organic polymers.* . 1964, , Interscience Publishers.

46. Cassel, R.B., *How TzeroTM Technology Improves DSC Performance, Part I: Flat Baselines and Glass Transition Measurements*. 2001, TA Instruments: New Castle, DE.

47. Cassel, R.B., *How TzeroTM Technology Improves DSC Performance, Part III: The Measurement of Specific Heat Capacity*. 2001, TA Instruments: New Castle, DE.

48. *Presentation slides Good Laboratory Practice (GLP) in Thermal Analysis*. 2011, Research Instruments: Singapore.

49. Rath, J., Wolfinger, M.G., Steiner, G., Krammer, G., Barontini, F., and Cozzani, V., *Heat of wood pyrolysis.* Fuel, 2003. **82**(1): p. 81-91.

50. Le Parlouër, P., *Thermal Analysis and Calorimetry Techniques for Catalytic Investigations*, in *Calorimetry and Thermal Methods in Catalysis*, A. Auroux, Editor. 2013, Springer Berlin Heidelberg. p. 51-101.

51. Harper, C.A., *Handbook of building materials for fire protection*. 2004: McGraw-Hill.

52. Yang, H., Yan, R., Chen, H., Lee, D.H., and Zheng, C., *Characteristics of hemicellulose, cellulose and lignin pyrolysis.* Fuel, 2007. **86**(12): p. 1781-1788.

53. Carvel, R., Beard, A., Jowitt, P.W., and Drysdale, D., *Fire Size and Fire Spread in Tunnels with Longitudinal Ventilation Systems.* Journal of Fire Sciences, 2005. **23**(6): p. 485-518.

54. Stoliarov, S.I. and Walters, R.N., *Determination of the heats of gasification of polymers using differential scanning calorimetry.* Polymer Degradation and Stability, 2008. **93**(2): p. 422-427.

55. Stoliarov, S.I., Crowley, S., Lyon, R.E., and Linteris, G.T., *Prediction of the burning rates of non-charring polymers.* Combustion and Flame, 2009. **156**(5): p. 1068-1083.

56. Matala, A., *Estimation of solid phase reaction parameters for fire simulation*, in *Faculty of Information and Natural Sciences*. 2008, Helsinki University of Technology: Helsinki University of Technology.

57. Huang, X., Li, K., and Zhang, H. *Modelling bench-scale fire on engineered wood: effects of transient flame and physicochemical properties*. in *Proceedings of the Combustion institute* 2016.

58. Anca-Couce, A., Zobel, N., Berger, A., and Behrendt, F., *Smouldering of pine wood: Kinetics and reaction heats.* Combustion and Flame, 2012. **159**(4): p. 1708-1719.

59. Stoliarov, S.I. and Li, J., *Parameterization and Validation of Pyrolysis Models for Polymeric Materials.* Fire Technology, 2016. **52**(1): p. 79-91.

60. Yang, J., Miranda, R., and Roy, C., *Using the DTG curve fitting method to determine the apparent kinetic parameters of thermal decomposition of polymers.* Polymer Degradation and Stability, 2001. **73**(3): p. 455-461.

61. *Thermal properties of plastic materials*. [cited 2016 02 June]; Available from: http://www.professionalplastics.com/professionalplastics/ThermalPropertiesofPlasticMaterials.pdf.

62. Fujino, J. and Honda, T., *Measurement of the specific heat capacity of plastic waste/fly ash recycled composite using a differential scanning calorimeter.* Heat Transfer—Asian Research, 2007. **36**(7): p. 435-448.

63. Fujino, J. and Honda, T., *Measurement of Thermal Conductivity of Recycled Composite of Plastic Waste and Fly Ash Using Guarded Hot Plate Apparatus.* Netsu Bussei, 2006. **20**(2): p. 75-82.

64. *Morgan Advanced Materials Europe product data book*. [cited 2015 6 July]; Available from: http://www.morganthermalceramics.com/sites/default/files/documents/2014_product_data_book.pdf.

65. *ASNZS3837-1998: Method of test for heat and smoke release rates for materials and products using an oxygen consumption calorimeter*. 1998, SAI Global Limited and Standards New Zealand. p. 54.

66. TenWolde, A., McNatt, J.D., and Krahn, L., *Thermal properties of wood and wood panel products for use in buildings*. 1988: Oak Ridge National Laboratory.

67. Ragland, K.W., Aerts, D.J., and Baker, A.J., *Properties of wood for combustion analysis.* Bioresource Technology, 1991. **37**(2): p. 161-168.

68. Grønli, M.G., *A theoreticl and experimental study of the thermal degradation of biomass, PhD thesis*, in *Norwegian University of Science and Technology*. 1996, Norwegian University of Science and Technology: Norway.

69. Saastamoinen, J. and Richard, J.-R., *Simultaneous drying and pyrolysis of solid fuel particles.* Combustion and Flame, 1996. **106**(3): p. 288-300.

70. Kersten, S.R.A., Wang, X., Prins, W., and van Swaaij, W.P.M., *Biomass pyrolysis in a fluidized bed reactor. part 1: literature review and model simulations.* Industrial & Engineering Chemistry Research, 2005. **44**(23): p. 8773-8785.

71. Li, K.Y., Fleischmann, C.M., and Spearpoint, M.J., *Determining thermal physical properties of pyrolyzing New Zealand medium density fibreboard (MDF).* Chemical Engineering Science, 2013. **95**(0): p. 211-220.

72. Hagge, M.J. and Bryden, K.M., *Modeling the impact of shrinkage on the pyrolysis of dry biomass.* Chemical Engineering Science, 2002. **57**(14): p. 2811-2823.

73. Ingason, H., Li, Y.Z., and Lönnermark, A., *Tunnel Fire Tests*, in *Tunnel Fire Dynamics*. 2015, Springer New York: New York, NY.

74. Ingason, H. and Li, Y.Z., *Model scale tunnel fire tests with point extraction ventilation.* Journal of Fire Protection Engineering, 2011. **21**(1): p. 5-36.

75. Li, K., Pau, D.S.W., Wang, J., and Ji, J., *Modelling pyrolysis of charring materials: determining flame heat flux using bench-scale experiments of medium density fibreboard (MDF).* Chemical Engineering Science, 2015. **123**(0): p. 39-48.

76. Janssens, M., *Measuring rate of heat release by oxygen consumption.* Fire Technology, 1991. **27**(3): p. 234-249.

77. Thornton, W.M., *The relation of oxygen to the heat of combustion of organic compounds.* PHILOSOPHICAL MAGAZINE, 1917. **33**(193-98): p. 196-203.

78. Ingason, H., Li, Y.Z., and Lönnermark, A., *Flame Length*, in *Tunnel Fire Dynamics*. 2015, Springer New York: New York, NY.

79. Ingason, H., Li, Y.Z., and Lönnermark, A., *Tunnel Fire Dynamics*. 2015, New York: Springer New York.

80. Enright, P.A., *Heat release and the combustion behaviour of upholstered furniture. PhD thesis*. 1999, University of Canterbury.

81. Hansen, R. and Ingason, H., *Model Scale fire experiments in a model tunnel with wooden pallets at varying distances*, in *SP Swedish National Testing and Research Institute*. 2010.

82. Ingason, H. and Lönnermark, A., *Effects of longitudinal ventilation on fire growth and maximum heat release rate*, in *Fourth International Symposium on Tunnel Safety and Security*. 2010: Frankfurt am Main, Germany.

83. Gross, D., *Experiments on the burning of cross piles of wood.* Journal of Research, 1962. **66**(2).

84. Block, J.A., *A theoretical and experimental study of nonpropagating free-burning fires.* Symposium (International) on Combustion, 1971. **13**(1): p. 971-978.

85. Heskestad, G., *Modeling of enclosure fires*, in *Proceedings of the Fourteenth Symposium (International) on Combustion*. 1972: Pennsylvania State University,USA. p. 1021-1030.

86. Croce, P.A. and Xin, Y., *Scale modeling of quasi-steady wood crib fires in enclosures.* Fire Safety Journal, 2005. **40**(3): p. 245-266.

87. Günther, B., Gebauer, K., Barkowski, R., Rosenthal, M., and Bues, C.-T., *Calorific value of selected wood species and wood products.* European Journal of Wood and Wood Products, 2012. **70**(5): p. 755-757.

88. Drysdale, D., *An introduction to fire dynamics Second Edition* 2011, Hoboken, N.J: Wiley.

89. Cateley;, M. and Crum, J., *Effects of forced ventilation velocity and crib characteristics on tunnel fires*, in *Final year projects, 2016*. 2016: University of Canterbury.

90. Zhang, S., Ni, X., Zhao, M., Feng, J., and Zhang, R., *Numerical simulation of wood crib fire behavior in a confined space using cone calorimeter data.* Journal of Thermal Analysis and Calorimetry, 2015. **119**(3): p. 2291-2303.

91. *Thermal-FluidsCentral*. Heat of Combustion [cited 2016 13th Sep]; Available from: http://www.thermalfluidscentral.org/encyclopedia/index.php/Heat_of_Combustion.

92. Quintiere, J.G. and Hakleroad, M. *New Concepts for Measuring Flame Spread Properties*. in *Fire safety: Science and Engineering*. 1984. American Society for Testing and Materials.

93. Mikkola, E. and I.S., W., *On the Thermal Ignition of Combustible Materials.* Fire and Materials, 1989. **14**: p. 87-96.

94. Tewarson, A., *Generation of Heat and Chemical Compounds in Fires*, in *The SFPE Handbook of Fire Porotection Engineering, Section 3/Chapter 4*. 1995.

95. Spearpoint, M.J., *Predicting the Ignition and Burning Rate of Wood in the Cone Calorimeter Using and Intergral Model*. 1999, United States Department of Commerce Technology Administration National Institute of Standards and Technology.

96. Ngu, C.K., *Ignition Properties of New Zealand Timber*. 2001, University of Canterbury: Christchurch, New Zealand.

97. Henderson, A., *Predicting Ignition Time Under Transient Heat Flux Using Results from Constant Flux Experiments*. 1998, University of Canterbury: Christchurch, New Zealand.

98. *Verification Method: Framework for Fire Safety Design*. 2014, Ministry of Business Innovation & Employment: Wellington New Zealand.

99. Cheong, M.K., Cheong, W.O., Leong, K.W., Lemaire, A.D., Noordijk, L.M., and Tarada, F., *Heat Release Rate of Heavy Goods Vehicle Fires in Tunnels*, in *15th International Symposium on Aerodynamics, Ventilation& Fire in Tunnels*. 2013: Barcelona, Spain.

100. Tewarson, A., *Generation of heat and chemical compounds in fires*, in *SFPE Handbook of Fire Protection Engineering, Third Edition*. 2002, National Fire Protection Association.

101. *Euro standard wood pallets*. [cited 2016 14 June]; Available from: http://www.totregroup.com/Euro%20Pallets.html.

102. *Plastic pallets*. [cited 2016 14 June]; Available from: http://en.e-catalog.craemer.com/plastic-pallets/euro-pallets-1200-x-800-mm/tc1.

103. Harmathy, T.Z., *Experimental study on the effect of ventilation on the burning of piles of solid fuels.* Combustion and Flame, 1978. **31**(1): p. 259-264.

104. Krämer, R.H., Zammarano, M., Linteris, G.T., Gedde, U.W., and Gilman, J.W., *Heat release and structural collapse of flexible polyurethane foam.* Polymer Degradation and Stability, 2010. **95**(6): p. 1115-1122.

Appendix. A

THE APPLICATION OF DIFFERENT COMPONENT SCHEMES TO PREDICT WOOD PYROLYSIS AND FIRE BEHAVIOUR

Xiaoyun Wang∗ PhD Student, University of Canterbury, New Zealand
Charles Fleischmann Professor, University of Canterbury, New Zealand
Michael Spearpoint Associate Professor, University of Canterbury, New Zealand
Xinyan Huang PhD student, Imperial College London, United Kingdom

ABSTRACT
An analytical method and a genetic algorithm searching method are used to estimate the kinetic properties of wood based on the assumptions of two different multiple-component schemes. The pyrolysis model in Fire Dynamics Simulator is used to model material-scale and bench-scale experiments using the kinetic properties derived from the two methods. It is found that the use of the kinetic properties from the different methods and the different component assumptions cause slight differences in the prediction of pyrolysis behaviour for the material-scale experiments, however, no significant differences are found in the prediction of heat release rate for bench-scale experiments.

Keywords: TGA, genetic algorithm, component schemes, FDS simulations, wood pyrolysis

1. INTRODUCTION

The decomposition kinetics of wood determines the release rate and the composition of flammable pyrolysate, which thereby affects the likelihood of ignition and subsequent flame spread rate. In order to describe the complex decomposition of wood, a multiple-component scheme [1] has been widely adopted to simplify the decomposition into several parallel reactions. Li et al. [1] suggested that the Kissinger method [2] can easily identify the pre-exponential factor and activation energy for each reaction in a multiple-component scheme but the reaction order needs to be determined by other approaches (such as a first reaction order). However, the overall matching condition to thermogravimetric (TG) curves by applying a forced reaction order is not as good as using complex searching methods such as a genetic algorithm (GA) which can find the effective solutions of reaction order [1]. In addition, the suitability of applying the assumption of multiple components for wood to predict the pyrolysis and burning behaviour for real fires is an uncertain factor.

In this study, the Kissinger method, combined with a first reaction order model, is applied to estimate the kinetic properties of wood based on two different multiple-component schemes. A GA searching method is also adopted to find the kinetic properties. Fire Dynamics Simulator, version 6.1.0 (FDS6) [3] is employed to model both material-scale and bench-scale experiments to further evaluate the accuracy and suitability of the estimated properties in predicting the pyrolysis and burning behaviour of real fires.

2. METHODOLOGY

2.1 Wood pyrolysis model

The multiple-component decomposition scheme in this study assumes wood is composed of several major components and each component independently undergoes a reaction over a distinct temperature range, i.e. a parallel reaction scheme. The reaction rate for the i^{th} component is specified by the Arrhenius law:

$$r_i = A_i \exp(-E_i / RT)(Y_i)^{n_i} \quad (1)$$

where Y_i is the normalised mass fraction of the i^{th} component; and A_i, E_i and n_i are the pre-exponential factor (s^{-1}), activation energy (kJ/mol) and reaction order respectively, often referred to as the kinetic triplet. The total pyrolysis rate of wood can be written as Equation 2 [1], where $f_i = m_{i0}/m_0$ is the initial mass fraction of each component.

∗**Autor correspondente – Department of Civil and Natural Resources Engineering University of Canterbury Private Bag 4800 Christchuch, New Zealand Tel: +64 3642987. e-mail:xiaoyun.wang@pg.canterbury.ac.nz**

$$r = d(m/m_0)/dT = \sum_{i=1}^{M} f_i r_i \quad (2)$$

2.2 Methods to derive kinetic properties

In order to determine the decomposition rate for the pyrolysis process, the kinetic triplet for each reaction needs to be defined. A common approach is to use curves from TG experiments which record the changes in mass during decomposition. In this study, two inverse derivation methods are applied to the TG curves: one is an analytical method and the other uses a GA method.

For the analytical method proposed by Kissinger [2], the reaction order n cannot be determined, and for simplicity, all reaction orders are assumed to be one. The Kissinger method uses the value of $T_{i,p}$ for the maximum reaction rate of the i^{th} reaction occurring at different heating rates and to further develop the linear relationship between $ln(\beta/T_{i,p}^2)$ and $1/T_{i,p}$ as:

$$\ln(\beta / T_{i,p}^2) = -E_i / RT_{i,p} + \ln(A_i R / E_i) \quad (3)$$

where E_i and A_i can be identified through the slope and line intercept.

A GA method is a heuristic searching method based on Darwinian survival-of-the fittest theory. GA-based searching methods have been widely used in the decomposition model to search for values for the kinetic and stoichiometric parameters [1, 4]. GA is able to produce a large search space in a complex landscape to avoid being trapped in numerous local maxima and minima and TG experiments conducted under different heating rates can be optimised simultaneously by simply increasing the number of experimental data points.

2.3 Experiments

Two types of experiments are carried out in this work: material-scale (TG) and bench-scale (cone calorimeter) experiments. The wood samples adopted in this study are the same materials used in a large-scale fire testing programme [5]. TG experimental curves for the wood decomposition are obtained through a SDT Q600 thermal analyzer. A sample of about 10 mg of wood is placed in an aluminium crucible (5 mm in diameter) for each experiment. Three sets of experiments are conducted in a nitrogen environment heating up from ambient temperature to 800 K at a constant rate of 5, 20 and 60 K/min respectively. Each experiment is repeated three times. The cone calorimeter experiments are performed using samples in a board-like shape with an approximate exposed area of 100 mm × 100 mm. The unexposed surfaces of the samples are placed on a mineral-based insulation. Two incident heat fluxes of 35 kW/m^2 and 50 kW/m^2 are applied in the experiments and the heat release rate (HRR) is measured.

3. RESULTS AND DISCUSSION

3.1 Kinetic properties estimation for wood

Figure 1 shows an example of mass loss rate curves for wood at three different heating rates: 5, 20 and 60 K/min. The uncertainty of three repeating tests is within 5%, showing an excellent repeatability. All the curves have a shoulder region, a noticeable peak and a long tail region, which indicates the existence of multiple reactions. Therefore, one widely used three-component scheme (hemicellulose, cellulose and lignin) [1], is firstly adopted to analyse the decomposition process of wood.

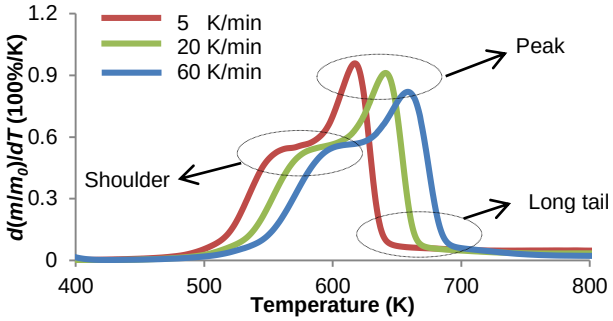

Figure 1 Mass loss rate curves at 5, 20 and 60 K/min

As proposed by Kissinger [2], the reaction rate ($d(m/m_0)/dT$) reaches a maximum value when $d(m/m_0)^2/dT^2$ equals zero. Therefore, the curves $d(m/m_0)^2/dT^2$ are plotted to identify $T_{i,p}$ for the maximum reaction rate of each reaction. Figure 2a illustrates the curves $d(m/m_0)/dT$ and $d(m/m_0)^2/dT^2$ at a heating rate of 5 K/min as an example to locate the $T_{i,p}$ values for each component. When the three-component scheme is applied, the curve $d(m/m_0)^2/dT^2$ is zero at temperatures of 618 K and 665 K, which correspond to the maximum reaction rate of hemicellulose and lignin component respectively. However, there is not a clear zero value on the $d(m/m_0)^2/dT^2$ curve for the hemicellulose region, which is possibly affected by nearby hidden reactions. Thus, a temperature of 572 K for a local minimum value in the hemicellulose region is considered to represent the T_p. In order to further interpret the possible reactions, two components, hemicellulose 1 and hemicellulose 2, are proposed to describe the reaction at the hemicellulose region instead of one component. Hence, a four-component scheme is depicted in Figure 2b, with two assumed components for the hemicellulose reaction regions at $T_{i,p}$ of 550 K and 576 K respectively, while the reactions for cellulose and lignin are the same as the three-component scheme. Table 1 summarises the $T_{i,p}$ values for each reaction at heating rates of 5, 20 and 60 K/min based on the proposed multiple-component schemes.

According to Table 1, the linear relationship of $ln\ (\beta/T_{i,p}^2)$ and $1/T_{i,p}$ for each component is plotted in Figure 3a and Figure 3b. Therefore, the E_i and A_i of each component can be calculated from the slope and intercept of each line based on Equation 3. The mass fraction (f_i) value of each component is determined by comparison of experimental results and the results calculated from Equation 2.

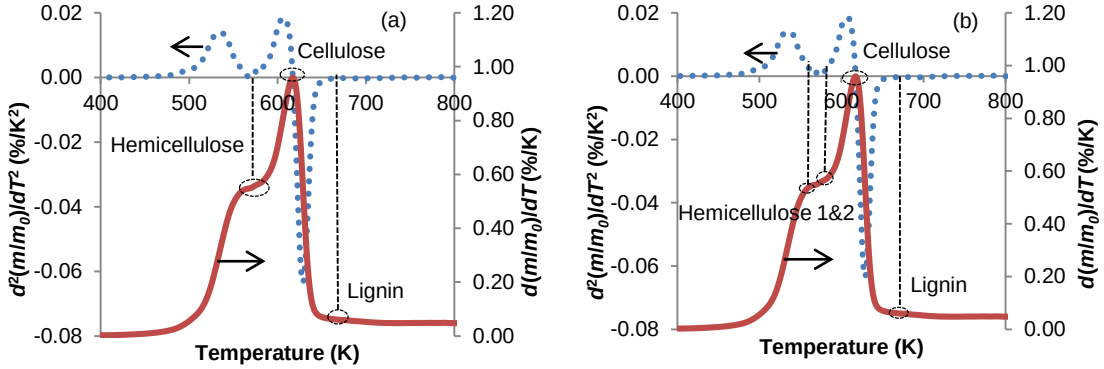

Figure 2 Decomposition curvatures: (a) three-component; (b) four-component.

Table 2 Summary of $T_{i,p}$ for three-component and four-component schemes

β (K/min)	Three-component	Four-component		Three-component & four-component	
	Hemicellulose	Hemicellulose 1	Hemicellulose 2	Cellulose	Lignin
5	572 K	550 K	576 K	618 K	650 K
20	595 K	575 K	600 K	641 K	685 K
60	615 K	595 K	623 K	659 K	706 K

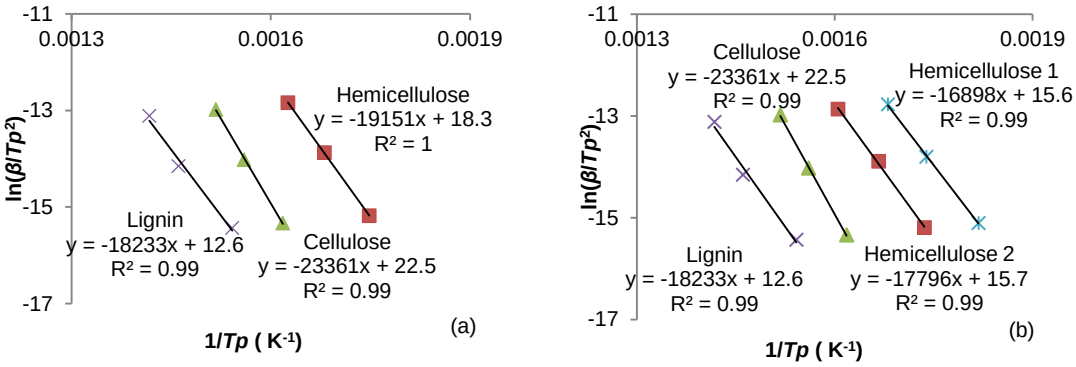

Figure 3 $ln(\beta/T_p^2)$ v.s. $1/T_p$: (a) three-component; (b) four-component.

Table 2 lists the results of kinetic properties and mass fraction for each component based on the analytical method for the three-component scheme and four-component scheme. In addition, the GA searching method is applied to inversely search the kinetic parameters of E, A and n for the three-component scheme. The three sets of TG data under different heating rates of 5, 20 and 60 K/min are chosen for the optimisation. The best solutions are listed in Table 2.

Table 3 Results of kinetic triplet and mass fraction (f_i) for each component

Methods	Components	E_i (J/mol)	A_i (s^{-1})	n_i	f_i
Analytical method four-component scheme	Hemicellulose 1	1.40×10^5	$1.01E\times10^{11}$	1	0.15
	Hemicellulose 2	1.48×10^5	1.20×10^{11}	1	0.17
	cellulose	1.94×10^5	1.30×10^{14}	1	0.45
	Lignin	1.52×10^5	5.57×10^9	1	0.13
Analytical method three-component scheme	Hemicellulose	1.59×10^5	1.70×10^{12}	1	0.32
	cellulose	1.94×10^5	1.30×10^{14}	1	0.45
	Lignin	1.52×10^5	5.56×10^9	1	0.13
GA three-component scheme	Hemicellulose	1.41×10^5	1.54×10^{11}	1.54	0.38
	cellulose	1.87×10^5	3.36×10^{13}	0.94	0.40
	Lignin	1.19×10^5	2.14×10^{10}	4.41	0.12

Note: 10% mass fraction is assumed for the moisture content.

3.2 Simulation results of TG experiments

Based on the TG experiments, FDS6 simulations are conducted in the absence of gas phase computations to represent the decomposition process within a nitrogen environment. The gas temperature is set to ramp up linearly

at 5, 20 and 60 K/min. In the simulations, each component is assumed to undergo a single step reaction to generate gas and solid products. The outputs are recorded in the form of a normalised mass loss rate for comparison with the TG experimental data.

Figure 4 illustrates the comparison of the experimental result and the FDS6 simulation results using the properties derived from the different methods at 5 K/min heating rates. Curves 4C_KA and 3C_KA denote the FDS6 simulations that adopt the kinetic properties derived from the Kissinger analytical method for the four-component and three-component schemes respectively. Curve 3C_GA indicates where the properties used in the FDS6 simulations are those obtained from the GA analysis for the three-component scheme.

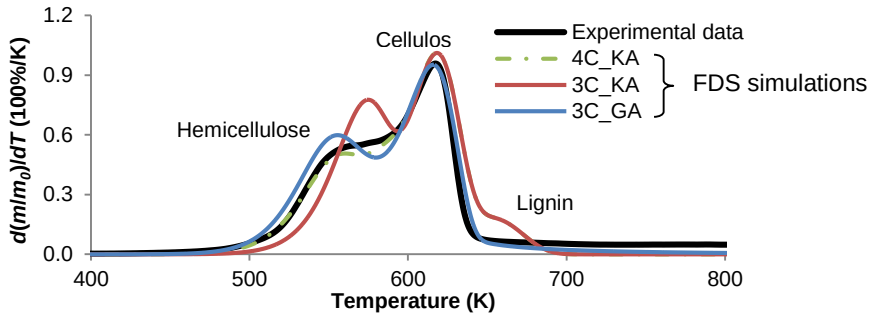

Figure 4 Comparison for TG simulation and experimental results at 5 K/min

Generally, all of the proposed schemes can effectively predict the main features of the decomposition curve of wood. The differences in the FDS6 simulation curves are mainly at the hemicellulose and the lignin reaction regions. Mathematically, the shape of reaction curves is determined by the kinetic triplets. If the values of E and A are fixed, the sharpness of the curve for a reaction is controlled by the reaction order [1, 6] and the magnitude of the peak for the reaction can be changed by the mass fraction of each component. Even though the sharpness of the curve for a reaction is fixed by the first reaction order, the adjustment in the mass fraction of each component can still effectively change the peak value of the reaction to fit the experimental curve. In the application of the Kissinger analytical method (where n=1), it is found that when two components with two small mass fractions are used to describe a reaction, the decomposition curve becomes flatter than the curve based upon one component with a large mass fraction. As shown in Figure 4, the simulation based on the four-component scheme presents the hemicellulose reaction features better than the results from the traditional three-component scheme in the case of using the first reaction model. However, when a free reaction order is applied from GA, the sharpness of the reaction curve can be shaped freely with less effect from the defined mass fraction of the component. For instance, the simulation result for lignin, with a reaction order of 4.41, gives a better fit to the experimental result. Figures 5a and 5b compare the heating rate at 20 K/min and 60 K/min; they demonstrate the same features as shown in Figure 4.

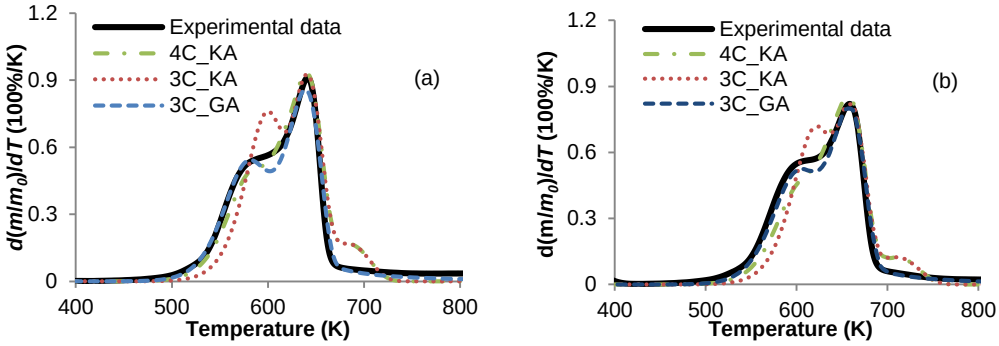

Figure 5 Comparison for TG simulation and experimental results: (a) 20 K/min; (b) 60 K/min.

3.3 Simulation results of cone calorimeter experiments

Two sets of cone calorimeter FDS6 simulations are carried out with external heat fluxes of 35 and 50 kW/m^2. In each simulation, a domain with dimensions of 220 mm × 220 mm × 1200 mm is used to ensure the fire plume can be fully captured and the loss of heat to the outside of domain can be effectively minimised. A simulated 100 mm ×

100 mm × 21.5 mm thick sample is placed at the centre of both the X and Y axes, and 250 mm above the bottom of the domain. In order to compute the reactions and heat transfer in the solid sample, the size of mesh cells for the solid phase is automatically defined to be smaller than the square root of the diffusivity of the samples in FDS6 [3], which is different from the cell size set-up in the gas phase. A 10 mm cell is applied to the gas phase computations which gives results comparable to those produced using a cell size of 5 mm but within a reasonable computational time. The incident heat fluxes from the cone heater used in the experiments are simplified by adding an external heat flux to the surface of the sample rather than simulating the cone heater above the sample. As a result of the aim of this study, the only variations in the simulations are the kinetic parameters. Other parameters are kept fixed in all of the simulations as listed in Table 3.

Table 4 Parameters defined in FDS cone calorimeter simulations

Item	Wood	Char
Thermal conductivity (W/mK)	-0.62 + 0.0038T - $4\times10^{-6}T^2$ [7]	4.43×10^{-2} + 1.48×10^{-4}T [7]
Specific heat (J/kg/K)	3.87T + 101.3 [8]	714 + 2.3T - $8\times10^{-4}T^2$ - $3.7\times10^{-7}T^3$ [8]
Heat of combustion (MJ/kg)	12.1 MJ/kg **	-
Density (kg/m^3)	566 kg/m^3 **	150 kg/m^3, based on [9]

** The lab results are provided by the Land Transport Authority (LTA) of Singapore.

The FDS6 simulation results at incident heat fluxes of 35 and 50 kW/m^2 are shown in Figure 6a and Figure 6b. Comparison shows that there is no significant difference in the HRR predictions by applying different kinetic properties derived from the different component schemes, and there is no obvious advantage in the simulation results with using the GA searched parameters.

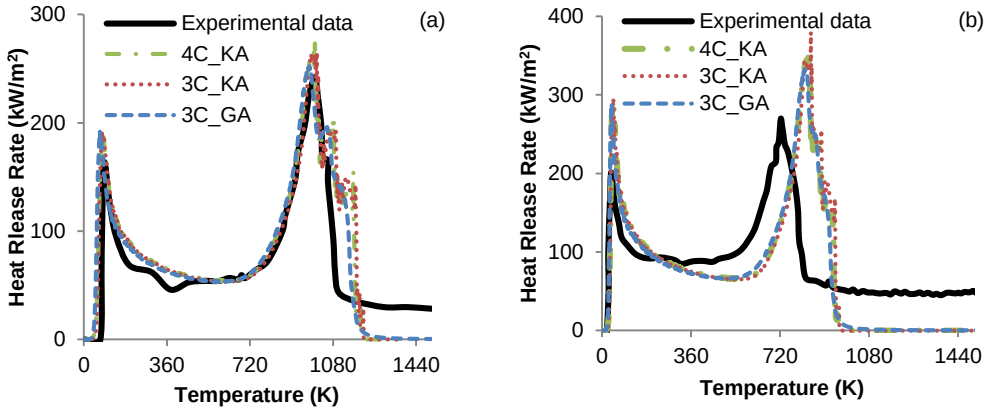

Figure 6 Cone calorimeter simulations and experimental results: (a) 35 kW/m^2; (b) 50 kW/m^2

The similarities in the simulation results obtained by using different model derived kinetic properties suggest that the kinetic properties of wood are not material dependent parameters, which agrees with Matala's [6] interpretation. These parameters are not unique and they can be defined in different ways based on the models or assumptions applied. In terms of the accuracy of the predictions for HRR in FDS6, all the simulations effectively demonstrate the features of the HRR curve for wood obtained from cone calorimeter experiments with the first peak in HRR after ignition and the second peak after a long period of energy dissipation. The FDS6 result for the 35 kW/m^2 heat flux is a close fit to the experimental curve, while the FDS6 result for 50 kW/m^2 gives higher values for the peak HRR and a longer energy dissipation time compared to the results shown in the experimental curve. The simulation results do not show the final char oxidation process. These differences in the burning behaviour of wood between the simulation results and experimental results are due to the HRR predictions in FDS6 are not solely determined by the kinetic properties but also rely on the choice of other parameters, the sensitivity of which needs further analysis.

5. CONCLUSIONS

This study applies the different component schemes to predict the pyrolysis and burning behaviour of wood in FDS6. In the simulations of the TG experiments, the pyrolysis behaviour for the hemicellulose reaction can be more effectively described by two components than one in the case of using the first reaction order model. The parameters determined by the analytical method using the four-component scheme and the GA method give similar results. However, the use of four-component scheme may increase the complexity of simulations and it is difficult to justify the two reactions for the hemicellulose of wood. On the other hand, the free use of the reaction order allows the GA parameters to properly present the lignin reaction. There is no significant difference in the predictions of HRR in the cone calorimeter simulations when applying the different kinetic properties and the different component schemes. For future work it is worth investigating whether the application of the GA method to determine the kinetic properties of wood can result in a simpler component scheme for the predictions of burning behaviour of wood.

6. AKNOWLEDGMENTS

The authors want to acknowledge the LTA of Singapore for the provision of the wood samples.

7. REFERENCES

[1] Li, K. Y., Huang, X. Y., Fleischmann, C., Rein, G., & Ji, J. - *Pyrolysis of Medium-Density Fiberboard: Optimized Search for Kinetics Scheme and Parameters via a Genetic Algorithm Driven by Kissinger's Method*. Energy & Fuels, vol.28, no.9, 2014, p. 6130-6139.

[2] Kissinger, H.E.- *Reaction Kinetics in Differential Thermal Analysis.* Analytical Chemistry, vol. 29, no.11, 1957, p. 1702-1706.

[3] McGrattan, K., McDermott, R., Weinschenk, C., Overholt, K., Hostikka, S., & Floyd, J. -*NIST special publication 1019 Fire Dynamics Simulator User's Guide Version 6*, National Institute of Standards and Technolog, 2014.

[4] Rein, G., Lautenberger, C., Fernandez-Pello, C., Torero, J.L, & Urban, D., - *Application of genetic algorithms and thermogravimetry to determine the kinetics of polyurethane foam in smoldering combustion*, Combustion and Flame, vol. 146, no. 7, 2006, p. 95-108.

[5] Cheong, M.K., Cheong, W.O., Leong, K.W., Lemaire, A.D. & Noordijk, L.M. - *Heat Release Rate of Heavy Goods Vehicle Fires in Tunnels*, 15th International Symposium on Aerodynamics, Ventilation & Fire in Tunnels. Barcelona, Spain. 2013.

[6] Matala, A. - *Methods and applications of pyrolysis modelling for polymeric materials,* PhD Thesis, Aalto University School of Science, 2013. 84 p.

[7] Hankalin, V., Ahonen, T. & Raiko, R. - *On thermal properties of a pyrolysing wood particle.* Finnish-Swedish Flame Days, vol.16, 2009

[8] Harper, C.A. - *Handbook of Building Materials for Fire Protection*. McGraw-Hill, 2004

[9] Ragland, K.W., Aerts, D.J. & Baker, A.J. - *Properties of wood for combustion analysis.* Bioresource Technology, vol.37, no. 2, 1991, p. 161-168.

Appendix. B

In this appendix, the a series of calculations by using three different geometrical form MDF cribs are conducted to determine an appropriate MDF crib for the experiments introduced in Chapter 5 and Chapter 6.

The equations for the calculation of porosity factor to suit rectangular shape cribs modified by Ingason are listed in Table 1:

Table 1 Equations to calculate the porosity factor for rectangular shape cribs

Porosity factor:	$P = \frac{A_v}{A_s} S_p^{1/2} b^{1/2}$
Ventilation area:	$A_v = (L - bn_1)(l - bn_L)$
Total exposed surface area:	$A_s = A_{s,L} + A_{s,l}$
Exposed surface area of the short sticks:	$A_{s,l} = 4 \times b \times l \times N_l \times n_l \times \left(1 - \frac{b}{2l}(n_L - 1)\right)$
Exposed surface area of the long sticks	$A_{s,L} = 4 \times b \times L \times N_L \times n_L \times \left(1 - \frac{b}{2L}(n_l - 1 - \frac{n_l}{N_L})\right)$
Hydraulic diameter of the ventilation area:	$S_p = \frac{2S_l S_L}{S_l + S_L}$
Free distance between the short sticks:	$S_l = \frac{l - n_L b}{n_L - 1}$
Free distance between the long sticks:	$S_L = \frac{L - n_l b}{n_l - 1}$

where L is the length of long stick, l is the length of short stick, b is the stick thickness, n_L is the number of long sticks per layer, n_l is the number of short sticks per layer, N_L is the number of layers for long sticks and N_l is the number of layers for short sticks.

Based on the equations in Table 1, three different geometrical form schemes are proposed to estimate the suitable porosity factor. Scheme A uses 3 numbers of 375 mm long-sticks for

each layer with 5 layers, 4 numbers of 100 mm short-sticks for each layer with 5 layers and the thickness of each stick is 15 mm; Scheme B and C keep the same elements as Scheme A but using 5 numbers and 6 numbers of short-sticks instead of the 4 numbers short-stick proposed in Scheme A.

In addition, the total energy profiles are calculated for the three different form cribs. As introduced in Chapter 6, the total energy can be estimated based on equation: $\mathrm{E} = \mathrm{m} \times \Delta H_e$ where E is total energy (kJ), m is total mass (kg) and ΔH_e is effective heat of combustion (kJ/kg). Table 2 lists the estimates and parameters for the three types of MDF cribs with different geometrical forms.

Table 2 Estimations for the three types of MDF cribs

Items	Scheme A	Scheme B	Scheme C
l (mm)	100	100	100
L (mm)	375	375	375
b (mm)	15	15	15
n_l (-)	4	5	6
n_L (-)	3	3	3
N_l (-)	5	5	5
N_L (-)	5	5	5
S_l (mm)	275	275	275
S_L (mm)	105	75	57
S_p (mm)	43.6	40.2	37.1
A_p (cm^2)	4246.5	4447.5	4648.5
A_v (cm^2)	173.3	165	156.8
P (mm)	1	0.9	0.8
Mass of Fuel (kg)	1.28	1.37	1.45
ΔH_c (MJ/kg)	12	12	12
E Total Energy (MJ)	15.4	16.4	17.4

As seen the results from Table 2, the crib geometrical form C can meet the required criteria, where the porosity factor should be more than 0.7 mm and the total energy should be close to 17.6 MJ as discussed in Chapter 6.

Appendix. C

In this appendix, the effective heat of combustion curves obtained from the small-scale tunnel experiments at different ventilation velocities are plotted. The time periods presented in these plots exclude the first 120 s when the ignition source also contributed to the burning and the mixture burning period when the burning of char started to be largely involved.

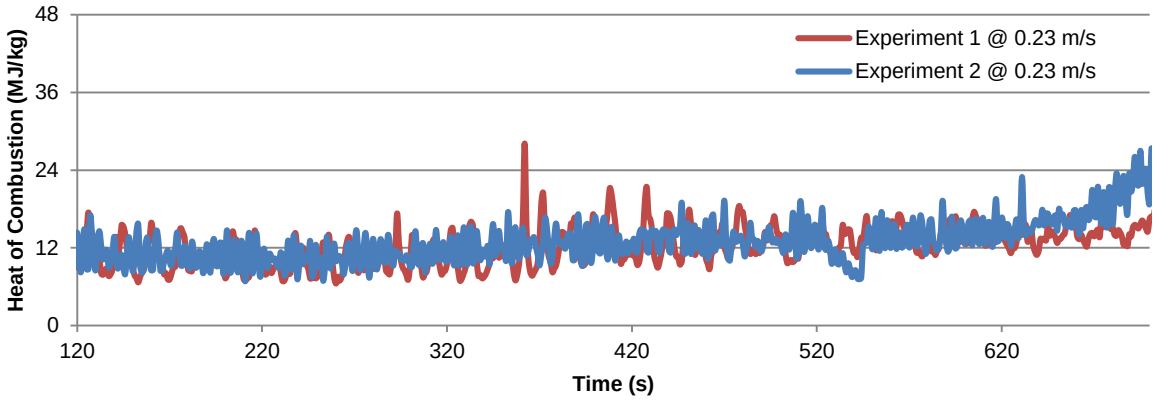

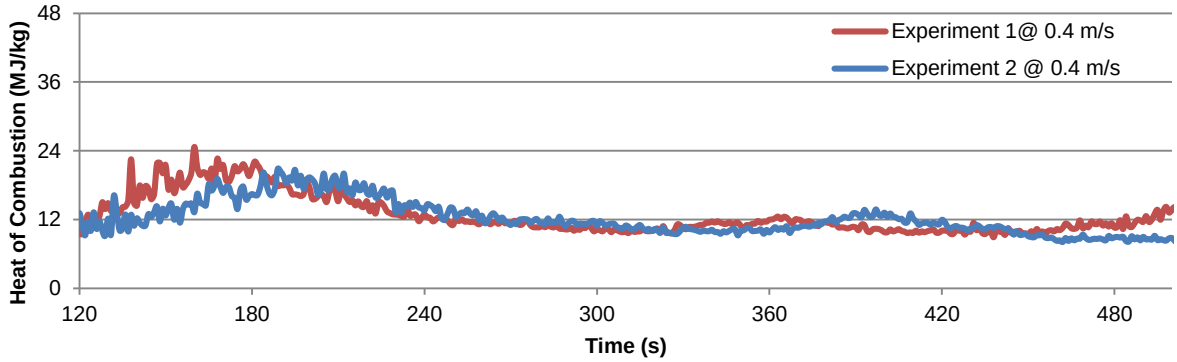

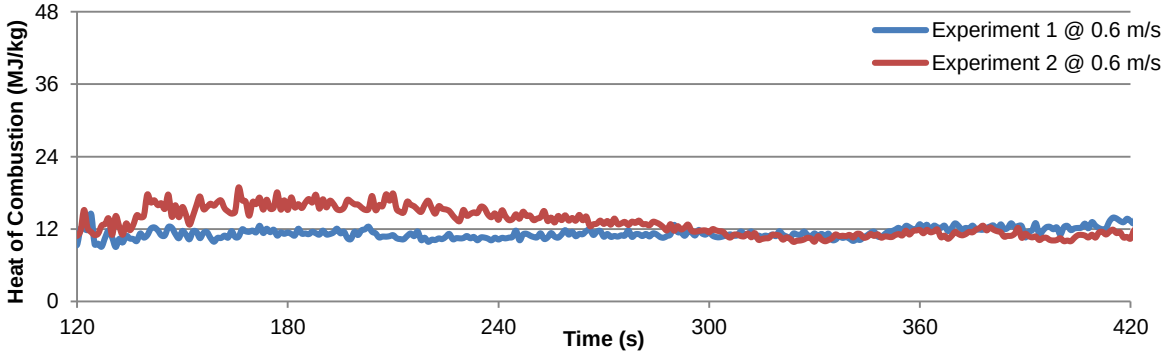

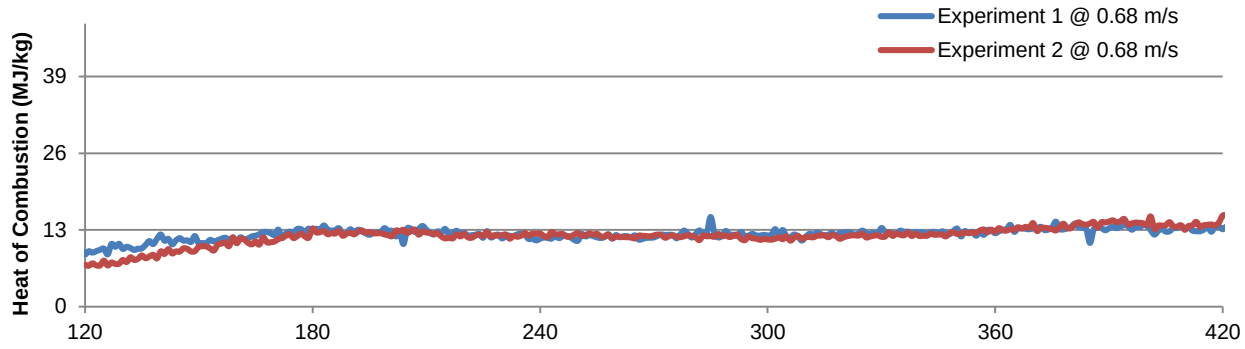
Experiment 1 @ 0.68 m/s
Experiment 2 @ 0.68 m/s
Heat of Combustion (MJ/kg)
0
13
26
39
120
180
240
300
360
420

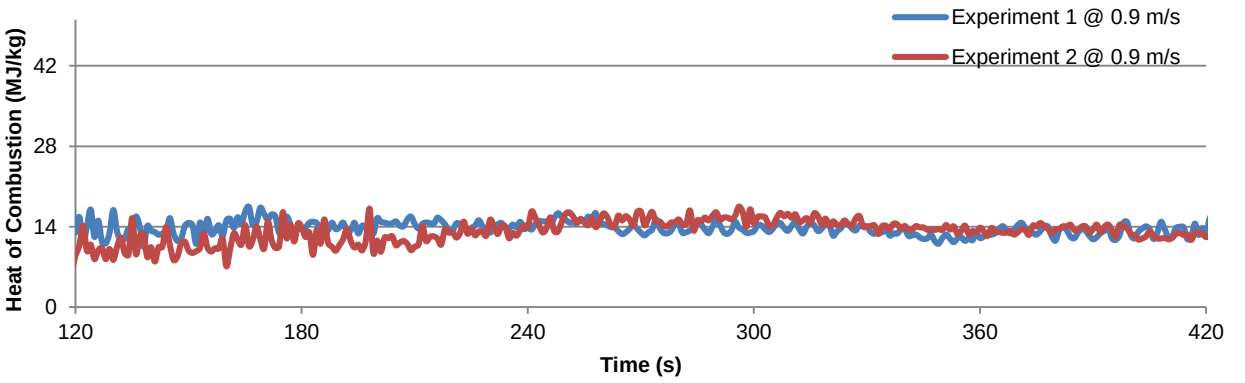
Experiment 1 @ 0.9 m/s
Experiment 2 @ 0.9 m/s
Heat of Combustion (MJ/kg)
0
14
28
42
120
180
240
300
360
420
Time (s)

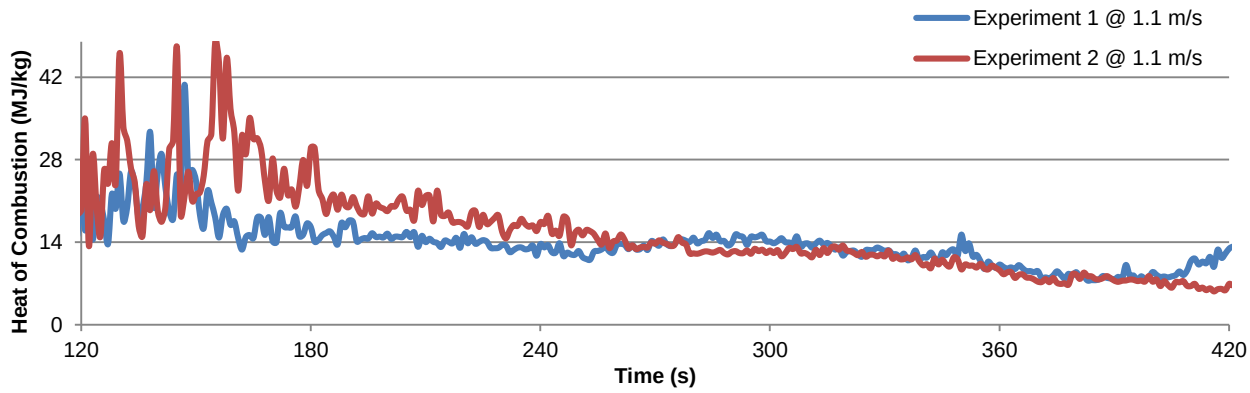
Experiment 1 @ 1.1 m/s
Experiment 2 @ 1.1 m/s
Heat of Combustion (MJ/kg)
0
14
28
42
120
180
240
300
360
420
Time (s)

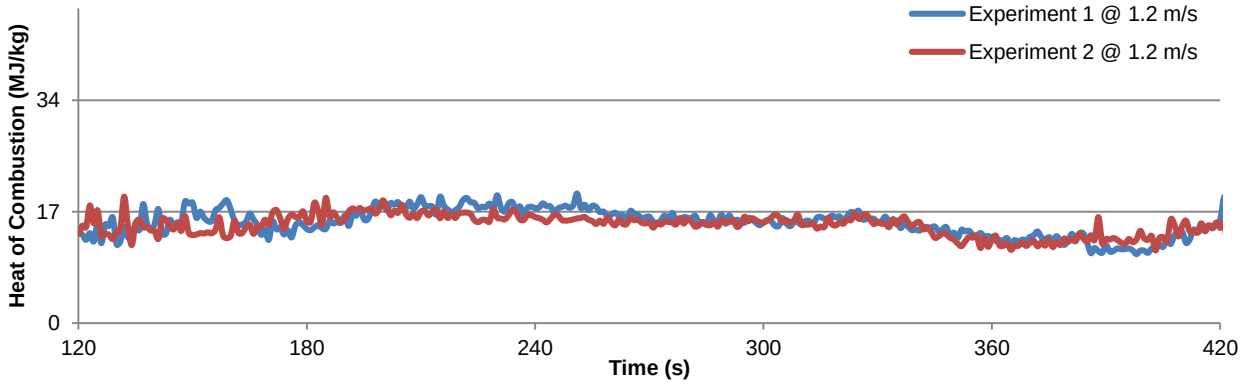
Experiment 1 @ 1.2 m/s
Experiment 2 @ 1.2 m/s
Heat of Combustion (MJ/kg)
0
17
34
120
180
240
300
360
420
Time (s)

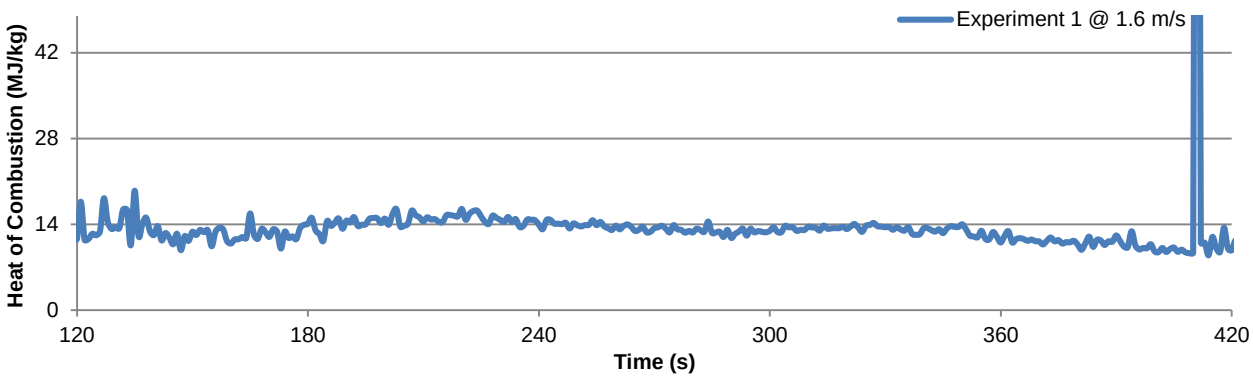
Experiment 1 @ 1.6 m/s
Heat of Combustion (MJ/kg)
42
28
14
0
120
180
240
300
360
420
Time (s)

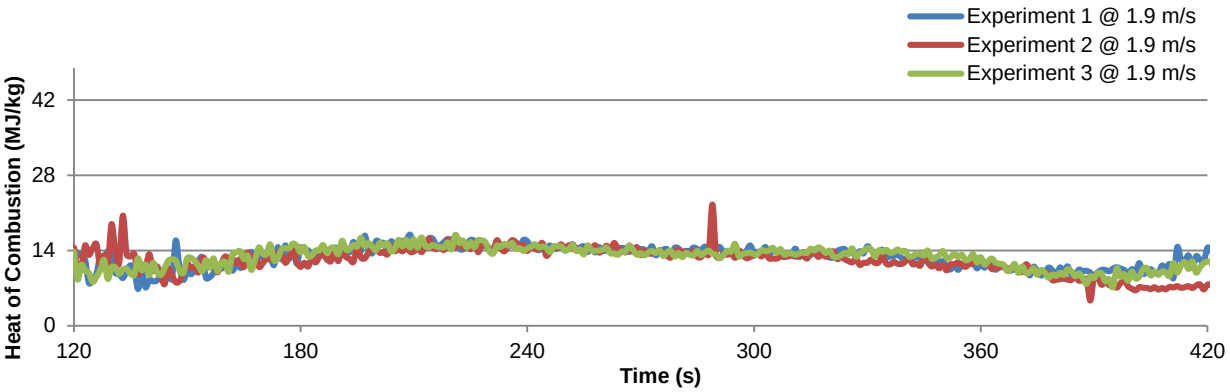
Experiment 1 @ 1.9 m/s
Experiment 2 @ 1.9 m/s
Experiment 3 @ 1.9 m/s
Heat of Combustion (MJ/kg)
42
28
14
0
120
180
240
300
360
420
Time (s)